

**Molecular Footprints in the Deaths and Births of  
Stars: Observing Carbon-rich Chemistry from  
Evolved Stars to Prestellar Clouds**

**Mark Andrew Siebert**

Hollis, New Hampshire

B.A. Astronomy, Cornell University, 2019  
M.S. Astronomy, University of Virginia, 2021

A Dissertation Presented to the  
Graduate Faculty of the  
*University of Virginia*  
in Candidacy for the Degree of  
*Doctor of Philosophy*

Department of Astronomy

University of Virginia  
May 2024

Committee Members:  
Anthony J. Remijan  
L. Ilse-dore Cleeves  
Zhi-Yun Li  
Brooks H. Pate

© Copyright by  
Mark Andrew Siebert  
All rights reserved  
May 19, 2024

# Abstract

Tracing the production and evolution of carbon compounds in astronomical sources is a key piece of understanding the cosmic origins of organic material in the solar system. In the Milky Way, carbon is recycled in the form of dust and aromatics through the mass-loss of evolved stars. Then, after being subject to the energetic, chemically active conditions of the interstellar medium and star formation, this material is incorporated into planetary systems. This progression is crucial to astrobiology; however, many of the processes which shape the composition of interstellar and circumstellar carbon are still largely unconstrained. In this thesis, I present several radio spectroscopic studies of molecular carbon in both dying stars and cold prestellar clouds. The aim of these works is to better-characterize the dominant chemical pathways leading to large carbonaceous species, and understand how this chemistry is linked to the physical/dynamical properties of a particular source.

In Chapters 2–5, I highlight three AGB-related stellar outflows as key case studies for understanding C-rich recycling in complex circumstellar morphologies: CW Leo (IRC+10216), V Hya, and V510 Pup. Though these sources exist at different stages of evolution, they are linked by the presence of a binary companion dynamically perturbing their circumstellar structure. These case studies will detail the rapid growth of hydride species, binary-induced photochemistry, and the unique molecular distributions present in circumbinary disks and jets. In Chapter 6, I investigate the production of large carbon chains in the dark molecular cloud TMC-1, and present the discovery of a new symmetric top molecule  $\text{CH}_3\text{C}_7\text{N}$  through spectral stacking methods. Through this analysis, I show that nitrogen-terminated chains exhibit a distinct chemistry from their pure hydrocarbon counterparts.

## Acknowledgements

None of this work would have been possible without the constant support of my peers, colleagues, and loved ones over the last five years.

To my UVA friends, you have made this a terrific experience full of laughs and happy memories. When I look back on graduate school, I will of course remember the stressful moments of debugging code and putting this dissertation together, but equally I will think of volleyball, board games, and movie nights with you all, so I thank you for that dearly. To my fellow Dark Skies, Bright Kids volunteers, I am so proud of the work we accomplished while I was a member of this organization, and I thank all of you who gave even the smallest amount of their valuable time working towards that with me.

To my colleagues and mentors, thank you for helping me solve uncountable problems that arose over the course of this research. Brett, Ryan, Ceci, Kelvin, thank you for teaching me many of the tools that were essential in this work. And thank you to Tony for encouraging my venture into the field of evolved stars, and for providing invaluable guidance since day one. To my wonderful co-authors over the years, your contributions to this science, as well as my development as a researcher, cannot be overstated. And special thanks to the many employees at NRAO who have maintained the data archives that were absolutely critical to the studies in this thesis.

To my family, thank you for cheering me on throughout this long process. Mom, Dad, and Matthew, I am so lucky to have had you to turn to during the most difficult parts of graduate school. And to my grandparents who have encouraged and supported my education since my earliest memories, I thank you and share this with you.

Leah, there is no way for me to express briefly the impact you have had on this endeavor, so let me instead just say how happy I am that you are in my life. I am so grateful that you have been with me every step of the way, I cherish every moment we spent together during this chapter, and I can't wait to see where we go next.

Finally, to the reader, I thank you for looking at this document at all. It is the result of a great deal of work from myself and many amazing people, and I hope you find the science explored here as exciting as I do.

With love,  
Mark

# Table of Contents

<b>List of Figures</b>	<b>xiv</b>
<b>List of Tables</b>	<b>xv</b>
<b>1 Introduction</b>	<b>1</b>
1.1 The Cycle of Carbon in the Milky Way . . . . .	1
1.1.1 The Major Carriers of Interstellar Carbon . . . . .	3
1.1.2 A Holistic View of Organic Recycling . . . . .	5
1.2 The Mass-loss and Chemistry of Evolved Stars . . . . .	5
1.2.1 The Asymptotic Giant Branch . . . . .	6
1.2.2 Circumstellar Chemistry . . . . .	9
1.2.3 Post-AGB Evolution and Red Supergiant Stars . . . . .	11
1.3 Radio Observations of Interstellar and Circumstellar Molecules . . . . .	14
1.3.1 Rotational Spectroscopy . . . . .	14
1.3.2 Local Thermodynamic Equilibrium . . . . .	16
1.3.3 Non-Thermal Excitation . . . . .	18
1.3.4 Mapping Molecular Lines with Interferometric Observations . . . . .	20
<b>2 Small Hydrides in Circumstellar Envelopes</b>	<b>24</b>
2.1 Introduction . . . . .	24
2.2 Observations . . . . .	28
2.3 Results & Analysis . . . . .	31
2.3.1 IRC+10216 . . . . .	31
2.3.2 VY CMa . . . . .	41
2.4 Discussion . . . . .	43
2.4.1 Iron Chemistry in CSEs . . . . .	45
2.4.2 Si and P Hydrides in CSEs . . . . .	47
2.5 Conclusions . . . . .	49
<b>3 Photochemistry in the Inner Layers of IRC+10216</b>	<b>51</b>

3.1	Introduction . . . . .	51
3.2	Observations and reduction . . . . .	55
3.3	Results . . . . .	59
3.3.1	Spectra, interloping lines, and flux recovery . . . . .	59
3.3.2	Emission Maps . . . . .	61
3.3.3	Radiative Transfer Modeling . . . . .	66
3.4	Discussion . . . . .	72
3.4.1	Chemical modelling . . . . .	76
3.5	Conclusions . . . . .	81
3.6	Appendix: Effect of orbit geometry . . . . .	84
<b>4</b>	<b>Molecules in the Circumbinary Disk of V Hya</b>	<b>87</b>
4.1	Introduction . . . . .	87
4.2	Observations and reduction . . . . .	90
4.3	Results . . . . .	95
4.3.1	Spectra and detected transitions . . . . .	95
4.3.2	Emission maps . . . . .	103
4.3.3	Kinematic structure and radial profiles . . . . .	107
4.4	Discussion . . . . .	113
4.4.1	Summary of detected species . . . . .	113
4.4.2	Excitation analysis of CH <sub>3</sub> CN . . . . .	119
4.4.3	Abundance distributions . . . . .	123
4.5	Conclusions . . . . .	133
4.6	Appendix: Further applications of line stacking . . . . .	137
<b>5</b>	<b>A Spectral Line Survey of the Exotic Proto-Planetary Nebula V510 Pup</b>	<b>141</b>
5.1	Introduction . . . . .	141
5.2	Observations . . . . .	143
5.3	Results & Analysis . . . . .	144
5.3.1	Detected species and line profiles . . . . .	144
5.3.2	LTE modeling . . . . .	146
5.4	Conclusions . . . . .	150
<b>6</b>	<b>Methyl-terminated Carbon Chains in the Taurus Molecular Cloud</b>	<b>153</b>
6.1	Introduction . . . . .	153
6.2	Observations . . . . .	156
6.3	Methods & Analysis . . . . .	156
6.3.1	Molecular spectroscopy . . . . .	156
6.3.2	MCMC modeling . . . . .	159
6.3.3	Spectral line stacking and matched filter . . . . .	160
6.4	Results & Discussion . . . . .	161

6.4.1	Column densities and physical characteristics . . . . .	161
6.4.2	A/E symmetry state populations . . . . .	167
6.5	Chemical modeling of methyl chains . . . . .	169
6.6	Conclusions . . . . .	174
6.7	Appendix: MCMC posterior distributions . . . . .	176
6.8	Appendix: Chemical Model Time Dependence . . . . .	179
<b>7</b>	<b>Conclusions</b>	<b>181</b>
7.1	Future Work . . . . .	184
	<b>References</b>	<b>186</b>

# List of Figures

1.1	Schematic describing the general cycle of carbon in the interstellar and circumstellar medium. At each stage, some examples of known C-bearing species in that environment are listed. . . . .	2
1.2	Post-main sequence evolution of a $2M_{\odot}$ star on the Hertzsprung-Russell diagram. Numbers next to each stage denote the approximate duration (in log-years). Adapted from Herwig (2005). . . . .	6
1.3	Circumstellar structure in the one-dimensional, steady-wind model of an AGB outflow. Major physical and chemical processes are listed on the top and bottom halves, respectively. Adapted from Decin (2021). . . . .	8
1.4	Gallery of observed wind structures surrounding AGB-related stars. <i>Top row:</i> C-rich AGB stars imaged at optical and infrared wavelengths, as well as molecular gas from Cernicharo et al. (2015). <i>Bottom row:</i> Post-AGB nebulae, image credits NASA/ESA. . . . .	12
1.5	LTE simulations of rotational spectra for three molecules ( $\text{CH}_3\text{C}_7\text{N}$ , $\text{HC}_3\text{N}$ , $\text{CN}$ ). Spectral coverage of example radio/far-infrared observatories are included, with band edges indicated for their respective instruments. Intensity units are arbitrary. Image credits: NRAO, ESO, GBO . . . . .	17
1.6	<i>Bottom panels:</i> ALMA channel maps of the $J = 8-7$ transition of $^{29}\text{SiO}$ measured toward CW Leo (IRC+10216) at the envelope expansion velocity ( $v_{\text{exp}}$ ), $v_{\text{exp}}/2$ , and the line center. <i>Top left:</i> ALMA spectrum associated with the images, obtained with a $5'' \times 5''$ diameter circular aperture centered on the position of CW Leo. <i>Top right:</i> Schematic of a spherical expanding AGB outflow, indicating the regions sampled by the three imaged velocity channels. In this example, the systemic velocity of CW Leo ( $v_{\text{sys}} = -26.5 \text{ km s}^{-1}$ ) is subtracted from the spectrum and channel maps. . . . .	22

2.1	Continuum subtracted SOFIA GREAT spectrum of IRC+10216 around targeted 624925 MHz transition of SiH. Emission lines contributed from the rest frequency band are written near the lower x-axis, and those contributed from the image band are written near the upper x-axis. . . . .	31
2.2	Continuum subtracted SOFIA GREAT spectrum of IRC+10216 around targeted 1043918 MHz transition of SiH. Emission lines contributed from the rest frequency band are written near the lower x-axis, and those contributed from the image band are written near the upper x-axis. Unidentified lines are labeled with their observed frequency in the rest band even though they could be contributed from the image band. Corresponding image frequencies for each U line are shown in Table 2.2. . . . .	32
2.3	SOFIA GREAT spectra of IRC+10216 showing targeted emission lines of SiH $J = 3/2 - 1/2$ (top left), SiH $J = 5/2 - 3/2$ (top right), FeH $\Omega = 5/2, J = 5/2 - 7/2$ (bottom left), and PH $J = 4 - 3$ (bottom right). . . . .	40
2.4	SOFIA GREAT spectra of VY CMa showing targeted emission lines of SiH $J = 3/2 - 1/2$ (top row), SiH $J = 5/2 - 3/2$ (middle row), and FeH $\Omega = 5/2, J = 5/2 - 7/2$ (bottom row). . . . .	42
3.1	Coverage of the $uv$ -plane offered by the three ALMA projects utilized in this work. Baselines from compact 12m configurations are shown in blue, those from extended 12m configurations are shown in brown, and 7m ACA baselines are shown in orange. Observations from left to right were used to image the $J = 28 - 27$ , $J = 30 - 29$ , and $J = 38 - 37$ transitions of HC <sub>3</sub> N, respectively. . . . .	58
3.2	Spectra demonstrating the three HC <sub>3</sub> N lines studied in this work (red), in addition to nearby and interloping molecular lines (gray). Spectra were created from image cubes using a 30'' aperture centered on the position of IRC+10216. The lower x-axes denote sky frequencies, while the upper axis shows velocity using the rest frequency of the respective HC <sub>3</sub> N transition. All transitions are from the ground vibrational state unless indicated otherwise. . . . .	60
3.3	ALMA emission maps of three HC <sub>3</sub> N lines toward IRC+10216. Images were created at the systemic velocity of $-26.5 \text{ km s}^{-1}$ with a channel width of $1.69 \text{ km s}^{-1}$ . IRC+10216 is located at the center of the maps at $\alpha_{J2000} = 09^{\text{h}}47^{\text{m}}57.458^{\text{s}}$ , $\delta_{J2000} = +13^{\circ}16'43.90''$ , and a reference circle with diameter 15'' is shown in yellow. Because data from separate observation sets are used, the beam sizes and absolute brightness scales are different for each panel. The shapes of the synthesized beams are shown in the bottom left corner, with sizes $0.48'' \times 0.45''$ , $0.73'' \times 0.52''$ , and $0.85'' \times 0.76''$ from left to right. . . . .	62

3.4	Contour maps of $\text{HC}_3\text{N } J = 28 - 27$ , $J = 30 - 29$ , and $J = 38 - 37$ (white) overlaid on the image of $^{13}\text{CO } J = 3 - 2$ toward IRC+10216. All components are again taken at the systemic velocity and centered at the position of IRC+10216 $\alpha_{\text{J2000}} = 09^{\text{h}}47^{\text{m}}57.458^{\text{s}}$ , $\delta_{\text{J2000}} = +13^{\circ}16'43.90''$ , and the yellow circle denotes a radius of $7.5''$ . Contour levels for each line are shown at 3, 6, 9, and 12 times the rms. . . . .	64
3.5	RADEX models of the three observed transitions of $\text{HC}_3\text{N}$ run with a range of densities at $T_k = 30$ K (dashed lines) and $T_k = 100$ K (solid lines). The shaded region denotes the average gas densities at radii where we observe these lines toward IRC+10216 (between $1''$ and $5''$ ). . . . .	67
3.6	Observed (solid lines) and LIME simulated (dashed lines) brightness profiles of $^{13}\text{CO}$ , $\text{HC}_3\text{N } J = 38 - 37$ , and $\text{HC}_3\text{N } J = 28 - 27$ from top to bottom. Profiles were obtained by taking the azimuthal average of the channel map at the systemic velocity of IRC+10216 centered on the position of the AGB star. Shaded regions denote the standard deviation of the surface brightness in each radial bin. In the top panel, the profile is also shown when a convolution with the synthesized beam of observations is used instead of visibility sampling. In the bottom panel, the expected contaminating emission from $\text{CH}_2\text{NH}$ is shown as well (dotted line). . . . .	71
3.7	Radial abundance with respect to $\text{H}_2$ (top) and volume density (bottom) profiles of $\text{HC}_3\text{N}$ in the envelope of IRC+10216. Solid black line represents the best fit profile resulting from the visibility sampled LIME radiative transfer models, while the dashed gray line is the prediction of a simple kinetic chemistry model (described in Section 3.4.1). The shaded red region represents the radii where the $\text{HC}_3\text{N}$ abundance is best sampled by the observations. . . . .	73
3.8	The retrieved $\text{HC}_3\text{N}$ abundance (black) together with the chemical modelling results. Gray, solid: smooth outflow without a stellar companion. Red, dotted: porous outflow (characterised by $f_{\text{ic}} = 0.40$ , $f_{\text{vol}} = 0.50$ , and $l_* = 2 \times 10^{13}$ cm) without a stellar companion. Orange, dashed: smooth outflow with a solar-like companion and dust condensation radius $R_{\text{dust}} = 5 R_*$ . Blue, solid: porous outflow with a solar-like companion and $R_{\text{dust}} = 5 R_*$ . The shaded red region represents the radii where the $\text{HC}_3\text{N}$ abundance is best sampled by the observations. . . . .	78
3.9	Occultation time of a companion star orbiting with IRC+10216 semi-major axis $a$ as seen by a point on the orbital plane as a function of radius. Magenta and green curves correspond to the semi-major axes proposed in Cernicharo et al. (2015) and Decin et al. (2015), respectively. . . . .	85
4.1	Continued. . . . .	93

4.1	Continued. Full spectrum of V Hya obtained from the ALMA observations. Spectra were extracted using a $4'' \times 6''$ elliptical aperture on the position of V Hya, and shifted to rest frequency using the system velocity $v_{\text{lsr}} = -17.4 \text{ km s}^{-1}$ . All identified transitions are labeled, and insets are provided for bright lines. Not included here is a separate spectral window covering 345.6–346 GHz, which contains only the $^{12}\text{CO } J = 3 - 2$ and $\text{HC}_3\text{N } J = 38 - 37$ lines. . . . .	94
4.2	Demonstration of the parametric model used to fit individual lines. Solid line depicts the original double-peaked model of Wannier et al. (1990) with $S_{\text{pk}} = 1 \text{ Jy}$ , the dashed line represents the result of applying a gaussian top hat filter to model line wings, and the dotted line shows the effect of using a positive non-zero value for the asymmetry parameter $\beta$ (Eq. 4.1). . . . .	97
4.3	Individual line-fitting results for a group of transitions at Band 6. The observed ALMA spectrum of V Hya is shown in black, while the model fits are overlaid in red. The best-fit central frequencies, expansion velocities, and resulting integrated line fluxes are listed in Table 4.2. .	97
4.4	Channel maps of selected C-bearing molecular transitions. All images are overlaid with corresponding channel maps from $^{13}\text{CO } J = 3 - 2$ in white at 20%, 40%, and 60% the peak flux of that image (0.166 Jy). White ellipses denote the synthesized beam for the $^{13}\text{CO}$ window, while yellow ellipses indicate the shape of the beam for the mapped molecule. 103	
4.4	Integrated intensity maps of the brightest transitions detected for all species. Ring structures R1, R2, and R3 are denoted by white arcs in each panel, and the synthesized beams are shown in the bottom-left corners. The compact ring R0 at 160 au is shown in black arcs surrounding the position of V Hya (black cross). The color scale in each image is adjusted to best show emission sub-structure. Maps were integrated over a width of $21 \text{ km s}^{-1}$ centered on the system velocity of V Hya. . . . .	105
4.4	Continued. . . . .	106
4.5	Demonstration of line shifting and stacking algorithm for a strong (top) and weak (bottom) rotational line. Error bars in the corrected spectra denote the standard deviation of flux measurements in a particular velocity bin. Spatial integrations were performed over a deprojected radius range of $0'' - 1.5''$ for $\text{C}_4\text{H}$ and $0'' - 3''$ for $\text{CH}_2\text{CN}$ . . . . .	108

- 4.6 Velocity-integrated radial intensity profiles of unblended, mapped transitions toward V Hya. For each line, two profiles are shown; one corresponding to the average over all angles in the disk (blue), the other extracted over a southward-pointing  $100^\circ$  wedge. Shaded regions around both curves denote the standard deviation in each radial bin. Bin sizes are one quarter the major axis of the synthesized beam. Ring structures R1, R2, and R3 are labeled with arrows. . . . . 111
- 4.6 Continued. . . . . 112
- 4.7 Top: Population diagrams constructed using radial brightness distributions of  $\text{CH}_3\text{CN}$  lines detected toward V Hya. Points correspond to  $K$ -states of the  $J = 18 - 17$  transition, from left to right:  $K = 0, 1$  blend,  $K = 2, \dots, K = 5$ . Dashed lines denote linear fits to the temperature. Bottom: Measured excitation temperature compared with the kinetic temperature profile calculated in Sahai et al. (2022). . . . . 120
- 4.8 LTE-calculated radial abundance profiles of molecules detected toward V Hya. For each transition, two abundances are shown, corresponding to the cool (solid) and warm (dotted) temperature models discussed in Section 4.4.2. The shaded region around each profile denotes the uncertainty, including the standard deviation of flux in the radial bin, the noise level of the integrated image, and the ALMA flux calibration error. Radial spacing of points is one-quarter of the beam size, and values are only shown where the azimuthally averaged line flux is larger than 3 times the rms of the image. . . . . 124
- 4.9 Non-LTE-simulated abundances of molecules in V Hya using RADEX, assuming purely collisional excitation (no vibrational pumping). Radial spacing of points is one-quarter of the beam size, and abundances are only calculated where the disk-averaged line flux is larger than 3 times the rms of the image. Since the uncertainty could not be carried through the forward-modeling process, it is assumed to be 30%, matching the typical error in radial integrated line flux. . . . . 128
- 4.10 Original (solid green) and velocity-stacked (solid black), spatially-integrated line profiles for  $\text{HC}_3\text{N}$  and  $\text{c-C}_3\text{H}_2$  toward V Hya. Dashed red line profile shows a Lorentzian fit to the corrected spectrum. Best fit values for the parameters in Eq. 4.9 are labeled, with last-digit errors shown in parentheses. All spectra were obtained over a deprojected radius range from  $0'' - 1.5''$  (600 au), and therefore neglect emission outside of R1. 138

- 4.11 Application of line shifting and stacking procedure on larger bandwidths covering groups of CH<sub>3</sub>CN (top) and H<sub>2</sub>CS (bottom) transitions. For these molecules, we indicate the catalog rest frequencies (CDMS; Müller et al., 2005) with vertical dashed lines. From left to right, these represent the  $K = 5, 4, 3, \dots, 0$  components of the  $J = 18 - 17$  transition of CH<sub>3</sub>CN, and the  $J_{K_a, K_c} = 10_{4,7} - 9_{4,6}$ ,  $10_{2,9} - 9_{2,8}$ ,  $10_{3,8} - 9_{3,7}$ ,  $10_{3,7} - 9_{3,6}$  lines of H<sub>2</sub>CS. Additional blended species are labeled with arrows. Both the corrected and uncorrected spectra were converted to rest frequency using a modified systemic velocity of  $v_{lsr} = -16.96 \text{ km s}^{-1}$ , and were extracted from the central region of the DUDE ( $0''-1.5''$ ). . . . . 140
- 5.1 Emission line profiles of various molecules measured by the ACA toward V510 Pup. The central velocity (CV), medium-velocity (MV), and high-velocity (HV) components are defined in the left panel. Species that are typically associated with O- and C-rich evolved stellar outflows are shown in the middle and bottom panels, respectively. Spectra were extracted from an aperture with diameter  $10''$  centered on the position of the post-AGB star. Some transitions are scaled for comparison. . . 147
- 5.2 Comparison of integrated molecular line brightness (relative to <sup>13</sup>CO) for SO (red) and HC<sub>3</sub>N (blue) among a sample of nearby PPNe. For V510 Pup, the O-rich central and C-rich medium velocity components are labeled CV and MV, respectively. Hatched regions denote upper limits, while solid regions indicate detected transitions. Data for sources other than V510 Pup adapted from Olofsson et al. (2019), Gallardo Cava et al. (2022), and Pardo et al. (2004). . . . . 148
- 5.3 Examples of LTE emission line fits for SO (left panels) and HC<sub>3</sub>N (right panels). ACA spectrum shown in black, while colored lines represent fitted mol<sub>sim</sub> simulation. For SO, a narrow (magenta dashed) and wide (green dashed) gaussian were needed to reproduce the shape of the CV component. For HC<sub>3</sub>N, one component was used, centered on the red-shifted side of the MV region. . . . . 149
- 5.4 Diagram of the circumstellar environment of V510 Pup as suggested by our ACA analysis of its millimeter spectrum. Includes major morphological structures and their velocities, as well as the observed chemistry in each region. Proposed components include a carbon-rich bipolar outflow (red and blue), and a slowly expanding oxygen-rich equatorial waist surrounding the central binary (brown). . . . . 151

- 6.1 (*First and third rows*) Velocity stacks of the observational (blue) and MCMC simulated (red) spectra. The cross-correlation of the two velocity stacks for each molecule corresponds to the matched filter (MF) spectrum (*second and fourth rows*), which are shown in the second and fourth rows. Though the transitions belonging to *A* and *E* symmetry states were treated with separate MCMC fits, their results are combined here. The peak impulse response are annotated on the MF spectra. . . . . 162
- 6.2 Derived total column densities of methyl-terminated carbon chains in TMC-1 as a function of chain length. Methylcyanopolyynes are shown in red while methylpolyynes are shown in blue. Contributions from the *A* and *E* symmetries of each species are summed, with their errors added in quadrature.  $\text{CH}_3\text{C}_8\text{H}$  is denoted with a triangle as it is an upper limit. Results from Remijan et al. (2006) are overplotted in their respective colors with no connecting line. Additionally, column densities of the linear cyanopolyynes and hydrocarbons radicals published in Loomis et al. (2021) and Brünken et al. (2007) are shown in pink and green, respectively. . . . . 166
- 6.3 Column density ratios toward TMC-1 of *A* and *E* symmetry states for each of the chains studied in this work (colored points), as well as those derived for methyl cyanide and methyl acetylene by Minh et al. (1993) and Askne et al. (1984), respectively (black points). Also plotted in black is the expected ratio of these two populations if the molecules are thermalized to a Boltzmann distribution at a range of kinetic temperatures. The vertical error on the points represents the 95% confidence level from our MCMC modeling results, and the horizontal error bars denote the range of kinetic temperatures observed for gas phase molecules toward the CP region TMC-1 (Fehér et al., 2016). 167
- 6.4 Simulated abundances and column densities of the four carbon chain families studied here at a model time of  $2.5 \times 10^5$  years, with the same colors and markers as Figure 6.2. Observed values are shown as dotted lines and the  $\text{CH}_3\text{C}_8\text{H}$  upper limit is denoted as an unfilled triangle. 172
- 6.5 Corner plot for  $\text{CH}_3\text{C}_7\text{N}$ . The diagonal traces correspond to the marginalized, cumulative posterior distributions for each parameter, and off-diagonal heatmaps represent parameter covariances. Vertical lines in the cumulative distribution plots represent the first, second, and third quantiles. . . . . 177
- 6.6 Corner plot for  $\text{CH}_3\text{C}_8\text{H}$ . The diagonal traces correspond to the marginalized, cumulative posterior distributions for each parameter, and off-diagonal heatmaps represent parameter covariances. Vertical lines in the cumulative distribution plots represent the first, second, and third quantiles. . . . . 178

- 6.7 Simulated gas-phase abundance and column densities of the  $\text{CH}_3\text{C}_n\text{N}$  (*left*) and  $\text{CH}_3\text{C}_n\text{H}$  (*right*) families from **nautilus** chemical models in comparison to the observed values with uncertainties as a horizontal bars. The upper limit of the  $\text{CH}_3\text{C}_8\text{H}$  is shown as green dotted line. The time used in Figure 6.4 is shown as a vertical dashed gray line. . 180

# List of Tables

2.1	Frequency bands observed with SOFIA GREAT . . . . .	29
2.2	List of all detected and targeted rotational transitions toward IRC+10216. . . . . .	35
2.3	List of all detected and targeted rotational transitions toward VY CMa.	44
3.1	Summary and characteristics of the ALMA data utilized in this work.	56
3.2	Physical parameters of the chemical model . . . . .	81
4.1	Summary and characteristics of the ALMA data utilized in this work.	91
4.2	List of all detected transitions . . . . .	99
4.3	Average column densities and abundances of daughter molecules in the disk of V Hya . . . . .	129
5.1	Summary of detected molecules and isotopologues . . . . .	145
5.2	Measurements of physical parameters of optically thin species in the outflow of V510 Pup . . . . .	150
6.1	Spectroscopic properties of stacked CH <sub>3</sub> C <sub>7</sub> N lines covered by the GBT X-band receiver . . . . .	157
6.2	MCMC model results for all observed CH <sub>3</sub> -terminated carbon chains. Uncertainties are listed as the 95% confidence level. . . . .	164

## CHAPTER 1

# Introduction

### 1.1 The Cycle of Carbon in the Milky Way

The long and complex journey carbon takes before it is incorporated into planetary systems is a topic central to the chemical evolution of our Galaxy and the cosmic origins of life. On Earth, carbon is the basis of all biological processes, as the enabler of organic chemistry and the primary constituent of biomolecules like amino acids and proteins. In the solar system, the building blocks of biological compounds have been discovered in comets (Goesmann et al., 2015), asteroids (Naraoka et al., 2023), the surface of Pluto (Cruikshank et al., 2019), Martian craters (Eigenbrode et al., 2018), Jovian and Saturnian moons (McCord et al., 1997; Postberg et al., 2018; Lorenz et al., 2008), and interplanetary dust (Keller et al., 2004). In the galaxy, carbon takes on many forms (e.g. ionized, atomic, molecular, residing in dust grains), and it is processed in the general cycle of matter where stars are born from gravitational collapse, and later expel their material (enriched by nucleosynthesis) into the

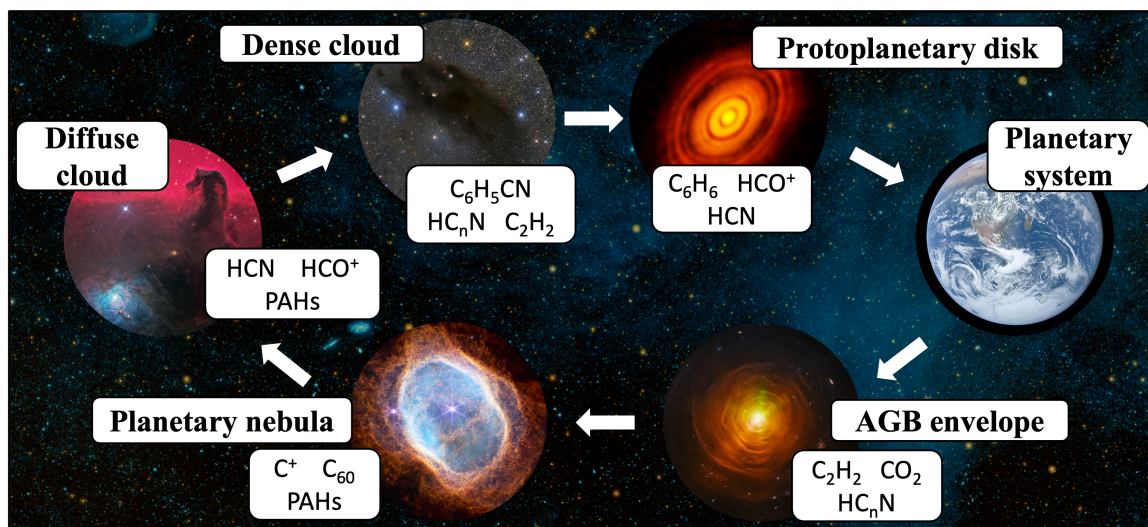


Figure 1.1: Schematic describing the general cycle of carbon in the interstellar and circumstellar medium. At each stage, some examples of known C-bearing species in that environment are listed.

interstellar medium (ISM). The major stages of this cycle, along with some commonly observed carbon-bearing species at each phase, are summarized in Figure 1.1.

From the perspective of organic inheritance, stellar death can be regarded as the beginning of the recycling of cosmic carbon. This can either occur in the gradual mass-loss of low-to-intermediate mass stars ( $1-8 M_{\odot}$ ) as they evolve toward becoming planetary nebulae (PNe), or in much more energetic core collapse supernovae. After carbonaceous gas and dust are released by stellar systems, they are subjected to the harsh environment of the diffuse ISM ( $A_V = 0-5$ ,  $n_H = 1 - 10^3 \text{ cm}^{-3}$ ), where they are chemically processed by large amounts of ionizing radiation and energetic interstellar shocks (Smith, 2011). Further chemical evolution occurs in the ISM as dense molecular clouds form and collapse. In these environments, chemistry is very efficient both in the gas phase and on the icy surfaces of dust grains, and complex molecules with  $> 10$  atoms have been observed in star forming regions and prestellar cores (e.g. Zhou et al., 2020; Belloche et al., 2009). Among all of these unique astrochemical laborato-

ries, over 180 different carbon-bearing molecules have been observed, demonstrating the versatility of C-rich chemistry in space (McGuire, 2022).

### 1.1.1 The Major Carriers of Interstellar Carbon

Interstellar matter is constantly evolving throughout its path prior to star formation; however, some chemical structures have been identified as key carriers of carbon throughout the many phases of the ISM. Chief among these are polycyclic aromatic hydrocarbons (PAHs): large organic compounds comprising numerous fused six- or five-member carbon rings (Gatchell et al., 2021). PAHs were first discovered from a set of unidentified infrared (UIR) emission bands observed in the mid-infrared spectra of the PN NGC 7027, which are consistent with characteristic bending and stretching modes of aromatic C-C and C-H bonds (Russell et al., 1977; Duley & Williams, 1981). Now, they are thought to be an abundant constituent of the ISM, with numerous detections in planetary nebulae, photodissociation regions, as well as external galaxies (Tielens, 2008). It is currently estimated that  $\sim 10\%$  of interstellar carbon resides in aromatic species (Chiar et al., 2013).

Though they are ubiquitous in the ISM, the UIR signatures of PAHs offer no information on their actual composition, which limits our ability to constrain their formation and evolution. The fundamental building block of PAHs, benzene ( $C_6H_6$ ), has been found in the pre-planetary nebula (PPN) CRL 618 (Cernicharo et al., 2001) and more recently in a protoplanetary disk using JWST (Tabone et al., 2023). In the cold prestellar core of the Taurus Molecular Cloud (TMC-1), ring-bearing species have been discovered from rotational lines, including benzonitrile ( $C_6H_5CN$ ), and the first individual PAHs 1- and 2-cyanonaphthalene ( $C_{10}H_7CN$ ) and indene ( $C_9H_8$ ) (McGuire et al., 2018, 2021; Burkhardt et al., 2021b).

These discoveries have added much needed context to the composition of interstel-

lar PAHs; however, the exact formation mechanisms of aromatics and their progression between different states of the ISM remain unconstrained, with current chemical models unable to reproduce abundances observed in prestellar clouds (McGuire et al., 2021). In the ejecta of evolved stars, PAHs are expected to grow through Hydrogen Abstraction and Carbon/Acetylene Addition (HACA), where hydrogen atoms are removed from pure PAHs by reactions with gas phase H, creating radical sites where linear carbon chains can attach and cyclize to form additional rings (Tielens, 2022). However, attempts at modeling this sooting mechanism in stellar outflows have had difficulty at producing a significant abundance of large aromatics, as the window where H abstraction is energetically favored is very small (900–1100 K) (Cherchneff, 2012). One proposed method of alleviating this bottleneck is through photochemistry, as UV photons, if present, could provide an alternative route to removing H and therefore initiating the growth process (Andrews et al., 2016).

In addition to PAHs, a significant fraction (30–60%; Draine, 2016) of interstellar carbon is refractory in nature; that is, locked up in micron-to-millimeter sized dust grains. Dust formation occurs in a variety of stellar environments including supernovae, Luminous Blue Variables, Red Supergiants (RSGs), and Asymptotic Giant Branch (AGB) stars, as these are locations where precursor molecules (e.g.  $\text{Al}_2\text{O}_3$ ,  $\text{C}_2\text{H}_2$ ,  $\text{SiC}_2$ ) exist in the gas phase and are allowed to cool to temperatures where they condense into solid state nuclei (Decin, 2021). The composition of dust is thus entirely dependent on the chemistry (specifically, the C/O ratio) of the environment where it is produced, with carbon-rich sources yielding amorphous carbon, hydrogenated amorphous carbon, graphite, and SiC clusters (Tielens, 2022). Carbon dust and aromatics are closely related, as they are produced in similar high temperature environments, and the break down of the amorphous hydrogenated grains through radiation and shocks has been proposed as an additional source of PAHs later on in

the ISM (Mascali et al., 2022).

### 1.1.2 A Holistic View of Organic Recycling

While the energetic physics of star and planet formation often leads to the destruction and reprocessing of carbon-bearing aggregates, there is a wealth of evidence showing that the chemical composition of our solar system is impacted by all previous stages of interstellar and circumstellar evolution. Isotopic ratios of carbonaceous chondritic meteorites suggest an ISM origin for the insoluble organic carbon macromolecules found in them (Busemann et al., 2006). Similarly, a recent study of organic samples in the Ryugu asteroid found that three-ring PAHs are likely inherited from evolved stars, while other aromatics (naphthalene, pyrene) were formed from the solar nebula or cold interstellar environments (Zeichner et al., 2023). Finally, analyses of presolar dust grains have shown that a significant fraction of minerals in the solar system (e.g. spinel, olivine, carborundum, graphite) were formed in the ejecta of evolved stars (Zinner, 1998).

Together, these results highlight the importance of pursuing a holistic view of cosmic carbon. Because the seeds of biological compounds cannot be attributed to any one astronomical environment, it is imperative that we trace the budget and composition of carbon through all the stages outlined in Fig. 1.1. Given the prevalence of large structured compounds in the ISM and in organic solar system samples, specifically studying the growth of hydrocarbons and the photochemical processing of acetylenic chains is critical in this effort.

## 1.2 The Mass-loss and Chemistry of Evolved Stars

Many of the studies in this thesis are focused on the outflows of evolved stars, as they play a vital role as factories of carbon-rich dust grains and PAHs in the ISM.

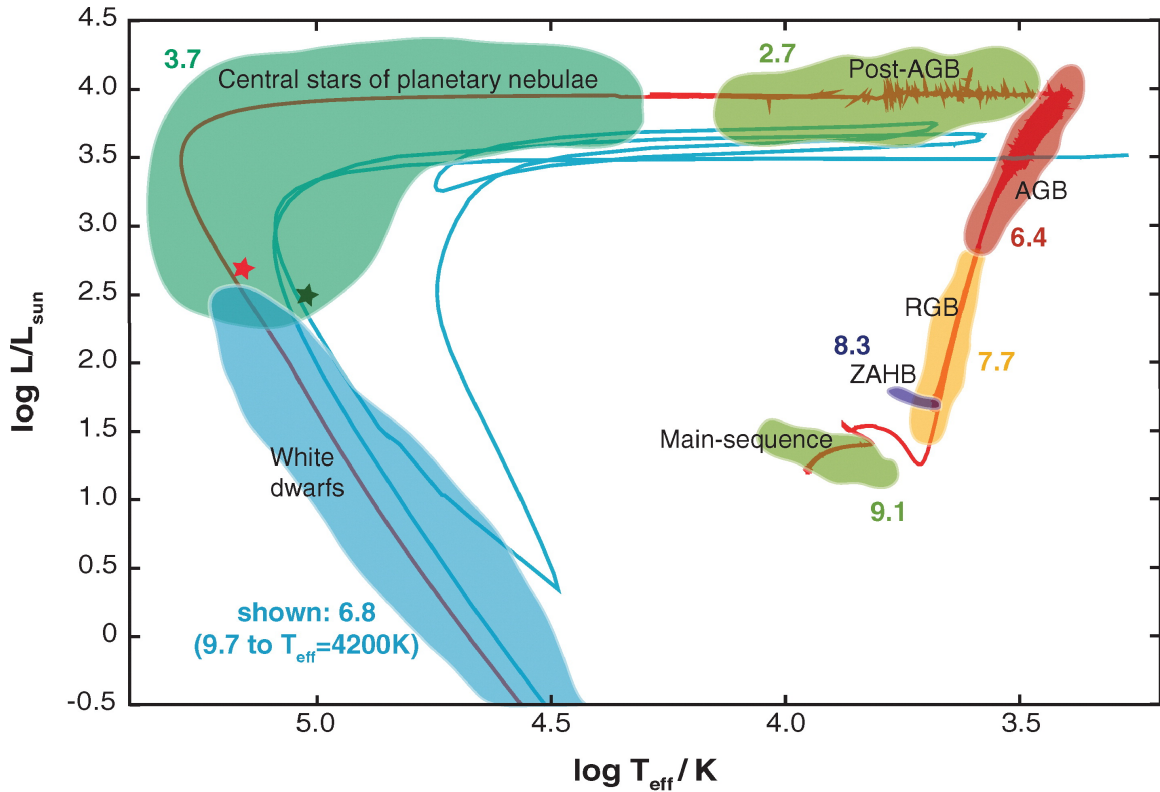


Figure 1.2: Post-main sequence evolution of a  $2M_{\odot}$  star on the Hertzsprung-Russell diagram. Numbers next to each stage denote the approximate duration (in log-years). Adapted from Herwig (2005).

To understand how this yield is produced, I will review concepts of stellar evolution and mass loss of stars on the AGB.

### 1.2.1 The Asymptotic Giant Branch

The post-main sequence evolution of low-to-intermediate mass stars ( $1-8M_{\odot}$ ) is marked by a series of dramatic changes in their physical and nucleosynthetic structure. After periods of time spent H-shell burning and He-core burning on the red giant and horizontal branches (Figure 1.2), these stars eventually reach AGB, where they are powered by the fusion of He and H in two separate shells surrounding an inert carbon/oxygen core, and enveloped by a convective H region (Herwig, 2005). In the very extended atmospheres of AGB stars, pulsations transport molecules to cool

regions ( $2\text{--}10 R_\star$ ) where they condense and form the seeds of dust grains (Cherchneff, 2012), at which point radiation pressure accelerates them (and the coupled gas) above the local escape velocity. The result is a large dusty circumstellar envelope (CSE) expanding into the ISM with a velocity of  $5\text{--}20 \text{ km s}^{-1}$ . A schematic demonstrating the 1D structure of these envelopes is shown in Figure 1.3, and examples of multi-wavelength images of CSEs are shown in the top row of Figure 1.4. These objects represent the beginning of the deaths of stars like the Sun, as they will cumulatively lose about half their total mass ( $\sim 1 M_\odot$ ) in these winds over the  $10^6$  yr duration of this stage. The measured mass-loss rates during this stage range from  $4 \times 10^{-8}$  to  $8 \times 10^{-5} M_\odot \text{ yr}^{-1}$  (De Beck et al., 2010).

The assumption of a 1D stationary wind model is a useful starting point for understanding the conditions in AGB winds broadly (I will discuss more specific cases in later chapters when studying more complex sources). In this model, the envelope is spherically symmetric and has constant expansion velocity, so the mass density beyond the dust condensation region can be obtained from conservation of mass:

$$\frac{dM}{dt} = \dot{M} = 4\pi r^2 \rho(r) v_{\text{exp}} \quad (1.1)$$

where  $\dot{M}$  is the mass-loss rate of the AGB star, and  $v_{\text{exp}}$  is the expansion velocity. The gas-to-dust mass ratios in these winds are typically quite high, between  $10^2$  and  $10^3$  (Groenewegen et al., 2002), so Eq. 1.1 can be inverted to obtain the gas number density as a function of radius and  $\langle m_g \rangle$ , the average mass of gas particles:

$$n(r) = \frac{\dot{M}}{4\pi r^2 v_{\text{exp}} \langle m_g \rangle} \quad (1.2)$$

Gas density is a key parameter in the efficiency of chemical reactions and dust-gas

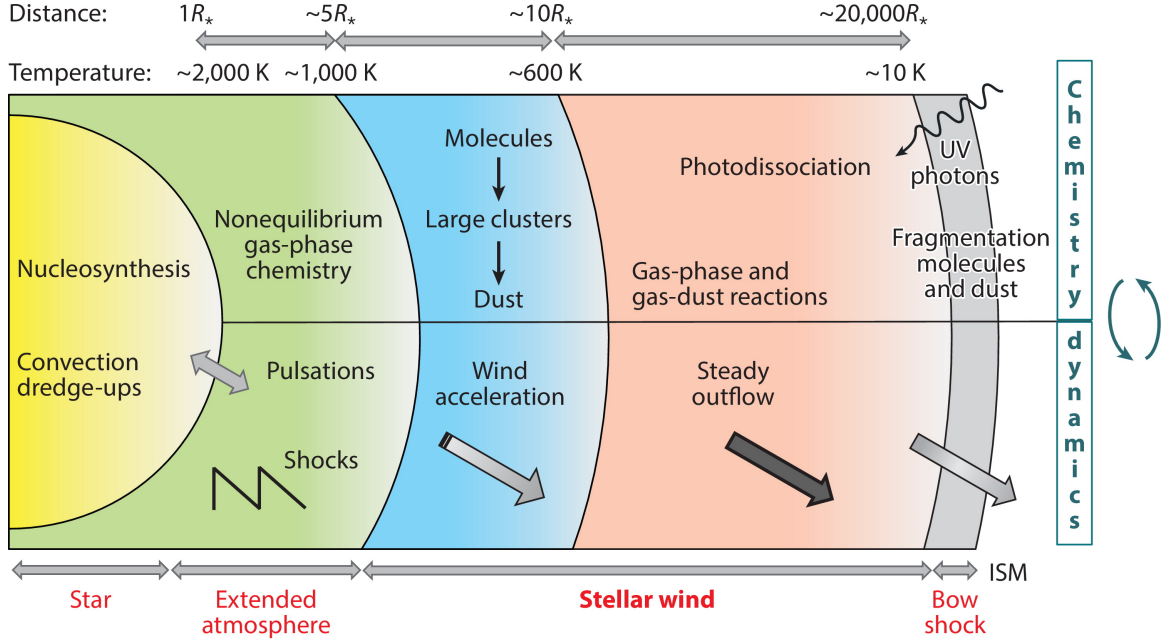


Figure 1.3: Circumstellar structure in the one-dimensional, steady-wind model of an AGB outflow. Major physical and chemical processes are listed on the top and bottom halves, respectively. Adapted from Decin (2021).

interactions, so the quantity  $\dot{M}/v_{\text{exp}}$  is useful for comparing the composition of different sources (Massalkhi et al., 2019). The other important factor is the temperature in the wind, which is mediated by radiative and adiabatic cooling processes (De Beck et al., 2010), and typically described by a power law with radius:

$$T(r) = T_{\star} \left( \frac{R_{\star}}{r} \right)^{\epsilon(r)} \quad (1.3)$$

where  $T_{\star}$  is the effective temperature of the star (2000–3000 K) and  $\epsilon$  ranges from  $\sim 0.5$ – $1.5$  depending on whether rotational line or adiabatic cooling dominate (Agúndez et al., 2012). Given that AGB envelopes are quite extended ( $r_{\text{max}} \sim 10^5$  au, Fig. 1.3), equations 1.2 and 1.3 demonstrate the incredibly wide range of densities ( $> 10^{10}$ – $10^3$  cm $^{-3}$ ) and temperatures (2000–10 K) sampled throughout these objects.

In the later stages of the AGB, recurring thermal pulses alter the outflows and sur-

face chemistry of evolved stars. In this process, the previously exhausted thin shell of helium is reignited, causing a drastic but very brief ( $10^2$  yr) increase in the luminosity and mass-loss rate. During a thermal pulse, the intermediate region between the He and H shells becomes convective, allowing for nuclear products from the degenerate core to be transported to the stellar surface in a process known as third dredge-up (Herwig, 2005). After many cycles of this, dredge-up can raise the C/O ratio in the outer regions of the star from the solar value (0.5) to above unity (Weiss & Ferguson, 2009).

The C/O ratio is the most important parameter in determining the chemistry of the outflow, so AGB stars are classified as either M-type Miras (C/O<1), S-type (C/O~1), or C-type “carbon stars” (C/O>1). Because the available dust precursors in the extended atmospheres of these stars are dependent on the C/O ratio, O-rich Miras expel primarily silicate dust grains, while carbon star envelopes comprise amorphous C, SiC dust, and aromatic soot (Ferrarotti & Gail, 2006). It is important to note that higher-mass stars do not experience third dredge up due to a process known as hot bottom burning, where at the base of the outer convective envelope carbon is destroyed through proton-capture nucleosynthesis (Sackmann & Boothroyd, 1992). This means that only low mass stars ( $<4 M_{\odot}$ ) can become carbon stars, and intermediate-to-high mass AGBs remain O-rich for the entirety of their evolution.

### 1.2.2 Circumstellar Chemistry

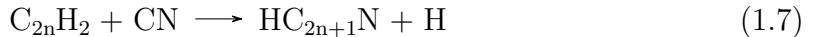
AGB envelopes are responsible for an estimated 80% of interstellar gas and 70% of newly formed dust grains in the Galaxy (Tielens et al., 2005; Zhukovska & Henning, 2013). And while it is difficult to estimate their exact yield with current measurements, carbon stars are thought to be important sources of aromatics in the ISM (Cherchneff et al., 1992; Zeichner et al., 2023). The cool temperatures, and high de-

gree of shielding from UV radiation mean that gas in CSEs is primarily molecular in form.

In the traditional model of AGB chemistry, molecular processes can be broken into two main stages. First, in the dense extended atmosphere of the star, gas phase species are formed from high temperature reactions which are rapid enough to reach thermochemical equilibrium (TE) (Agúndez et al., 2020). Among the small, stable “parent” molecules that form in this environment, CO is the most abundant, and therefore locks up all of the available carbon or oxygen depending on the C/O ratio. In C stars, carbon is therefore free to form additional C-bearing parent molecules like acetylene ( $C_2H_2$ ), HCN, and  $SiC_2$ . Though TE models have been successful at reproducing many abundances measured in AGB winds, observations of departures from TE have provided evidence that non-equilibrium processes, including dust formation/accretion and shock chemistry driven by stellar pulsations are also important (Massalkhi et al., 2018a; Decin et al., 2010).

After parent molecules and dust grains are accelerated further into the envelope, the density and extinction ( $A_V$ ) decrease, and material is increasingly exposed to the interstellar radiation field (ISRF, Fig. 1.3). With this change, the chemistry is dominated by kinetics, as photon (and cosmic ray) ionization and destruction of parent species drive the formation of “daughter” molecules (Millar, 2016). In C-rich environments, this is exemplified by the consecutive production of linear polyynes and cyanopolyynes carbon chains from neutral-radical reactions initiated by the photodissociation of acetylene and HCN:





where  $n = 1, 2, 3, 4, \dots$  (Agúndez et al., 2017). Pathways like these build up complex daughter species and allow for an incredibly rich molecular inventory in the outer regions of CSEs, including very long unsaturated carbon chains (up to  $\text{HC}_9\text{N}$ ; Pardo et al., 2020), partially saturated molecules (e.g.  $\text{CH}_2\text{CHCN}$ ; Agúndez et al., 2008), and metal-bearing species (e.g.  $\text{NaNc}$ ,  $\text{MgCCH}$ ,  $\text{AlF}$ ; Ziurys et al., 2007). In the envelope of CW Leo (IRC+10216, top-right panels of Fig. 1.4), the most well-studied carbon star and the prototype for this chemistry, over 100 different molecules have been identified—many for the first time in any astronomical source (McGuire, 2022). Observing the transition from parent to daughter species in objects like this is thus ideal for testing kinetic chemical theory under a wide range of physical conditions and constraining how C-rich stellar material is processed and transformed in these envelopes.

### 1.2.3 Post-AGB Evolution and Red Supergiant Stars

The mass-loss of stars on the AGB is a relatively slow method of recycling. Once an AGB star has lost nearly all the mass in its convective envelope, it is considered a post-AGB star and its evolution becomes much more dramatic. During this very brief phase ( $<10^4$  yr) the star (previously, the C/O core of the AGB star) contracts, raising its effective temperature and rapidly moving leftward on the HR-diagram (Fig. 1.2) while a pre-planetary nebula (PPN) forms from the circumstellar medium (Miller Bertolami, 2016). Some of the main characteristics of PPNe (in contrast to their progenitor CSEs) are fast ( $>100 \text{ km s}^{-1}$ ) winds and a high degree of asphericity; with bipolar/multipolar lobes, equatorial disks, collimated jets, and irregular structures

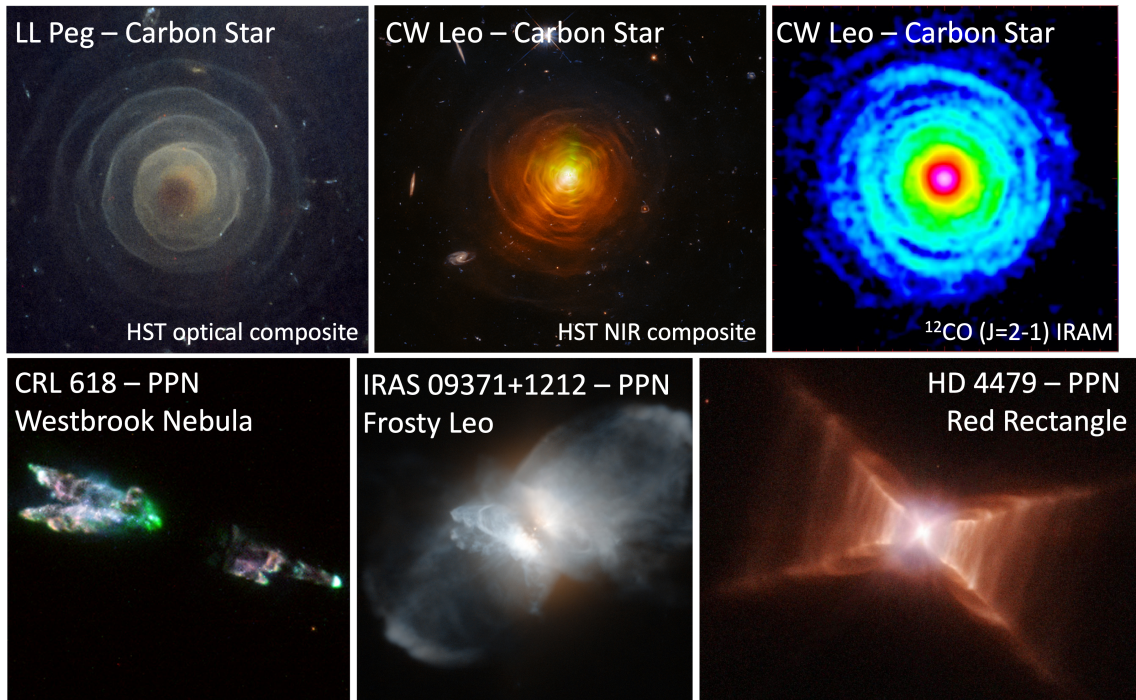


Figure 1.4: Gallery of observed wind structures surrounding AGB-related stars. *Top row*: C-rich AGB stars imaged at optical and infrared wavelengths, as well as molecular gas from Cernicharo et al. (2015). *Bottom row*: Post-AGB nebulae, image credits NASA/ESA.

being very common (bottom row of Figure 1.4) (Sahai et al., 2007). As these sources are quite rare, the physical mechanisms behind the shaping and evolution of PPNe are still not fully understood. However, observational and theoretical works often invoke binary interactions like accretion onto companions and common envelope events to drive the energetic kinematics during this phase (Soker & Kashi, 2012; De Marco, 2009).

The stark changes in the physics of post-AGB stars are met with a similar transformation in their chemistry. Because the star is still not hot enough to fully ionize its wind and form a planetary nebula, much of the circumstellar medium remains molecular in form; however, the previous picture of equilibrium chemistry dominating at close radii and photochemistry affecting outer regions breaks down now that a

central UV source is present, and the newly formed fast winds can drive shock chemistry, leading to molecules not typically seen in AGBs (Woods et al., 2003; Olofsson et al., 2019). In the C-rich PPN CRL 618 (Fig. 1.4 bottom-left), a central HII region has been identified around which carbon chains grow rapidly (Pardo et al., 2007). In addition, PPNe are also where the observational signs of aromatics become commonplace, as CRL 618 is still the only evolved star where the benzene has been discovered (Cernicharo et al., 2001), and the UIR bands are frequently seen in emission toward C- and (surprisingly) O-rich post-AGBs (Matsuura et al., 2014; Gielen et al., 2011). It is presently unclear whether the appearance of aromatic features at this stage arises from an increase in production of these aggregates, or simply from the more suitable conditions for the UV-excitation of these bands (Boersma et al., 2006).

Finally, separate from AGB and post-AGB outflows, massive stars ( $10\text{--}30 M_{\odot}$ ) also undergo significant mass loss at the ends of their lives. Red supergiant stars like VY CMa can reach tremendous mass-loss rates ( $3 \times 10^{-4} M_{\odot} \text{ yr}^{-1}$ ) through a variety of mechanisms including chromospheric activity and convection (Humphreys & Jones, 2022). These processes give rise to complex, asymmetric, and clumpy winds that are also important sources of dust grains. Despite the energetic stellar physics, the molecular inventories of these winds are quite rich, including a wide array of O- and C-bearing species (Ziurys et al., 2007; Singh et al., 2022).

In all of the systems described here, stellar evolution and circumstellar chemistry are intrinsically coupled processes. While the one-dimensional, steady wind model of molecule formation has been instrumental in explaining observations toward evolved stars for many years (Agúndez et al., 2020), we know that stellar mass loss is, more often than not, a complicated process that is constantly evolving (Decin et al., 2020). My work in the following chapters will focus on expanding the picture of AGB chemistry to these non-traditional dynamics, and understanding the impact

of perturbations like binary interactions on carbon processing in these key sites of recycling.

## 1.3 Radio Observations of Interstellar and Circumstellar Molecules

### 1.3.1 Rotational Spectroscopy

For the last half century, rotational spectroscopy has been an essential tool in studying the chemistry of interstellar and circumstellar environments (Cheung et al., 1968). Radiative transitions between the quantized angular momentum states of molecules produce characteristic emission (or absorption) lines at wavelengths ranging from the far-infrared to the radio, which are readily observable by modern ground- and space-based telescopes. To date, over 250 molecules have been detected in space, predominantly through these observations (McGuire, 2022). An important shortcoming of rotational spectroscopy is that it has no use for symmetric molecules (acetylene— $\text{C}_2\text{H}_2$ , for example), as the strength of a transition scales with the square of a molecule’s dipole moment. Additionally, because rotational motions are not permitted for solid-state compounds, only material in the gas phase is accessible with this method. Nevertheless, the microwave spectra of both interstellar clouds and AGB envelopes are rich with rotational lines, making them a central route to characterizing the dominant chemical processes in the ISM.

Following the formalism of (Gordy & Cook, 1984), the energy of a rotational state with total angular momentum quantum number  $J$  is given, to first order, by:

$$E_J = \frac{h^2}{8\pi^2 I} J(J + 1) \tag{1.8}$$

and the rest the frequency of a transition between these states, obeying the selection rule  $\Delta J = \pm 1$ , is therefore

$$\nu_{J+1 \rightarrow J} = \frac{h}{4\pi^2 I} (J + 1) \quad (1.9)$$

where  $I$  is the moment of inertia of the molecule, given by the product of the reduced mass and the square of the distance between atoms  $I = \mu r^2$ . A consequence of Eq. 1.9 is that molecules with less mass and atomic separation have higher fundamental transitions ( $J = 1 \rightarrow 0$ ), and wider line spacing, while larger molecules appear at lower frequencies. Figure 1.5 demonstrates this dependence for three example species, in addition to how different temperature conditions affect molecular spectra. Rotational levels are often populated in a Boltzmann distribution (section 1.3.2), where the column density of a particular state  $N_u$  with degeneracy  $g_u$ , is determined by a characteristic excitation temperature  $T_{\text{ex}}$ :

$$\frac{N_u}{N_T} = \frac{g_u}{Q} e^{-E_u/kT_{\text{ex}}} \quad (1.10)$$

where  $Q$  is the partition function and  $N_T$  is the total column density of the molecule (Goldsmith & Langer, 1999). The exponential in Eq. 1.10 means that states are only well-populated with  $E_u \lesssim T_{\text{ex}}$ , and therefore at higher temperatures emission is shifted to higher energy transitions, as seen in Fig. 1.5.

Figure 1.5 highlights how observational methods should be adapted to the chemical and physical properties of astrophysical sources. When characterizing large molecules at cold temperatures, radio telescopes operating at centimeter wavelengths are efficient (see Chapter 6). On the other hand, if target species reside in warmer gas or are smaller, millimeter or far-infrared facilities are necessary (e.g. Chapters 2, 4, 5). In some cases, if a molecule is present over a wide range of temperature conditions, like

in CSEs, its transitions at different frequencies can trace completely separate regions of the source (Chapter 3), underscoring the importance of multi-wavelength coverage in chemical studies.

### 1.3.2 Local Thermodynamic Equilibrium

To relate observed rotational lines to the physical and chemical conditions in a given source, local thermodynamic equilibrium (LTE) is a key simplifying principle. Under LTE, the excitation of molecules through collisions (or background radiation) is more efficient than the spontaneous radiative decay of rotational levels, and all states are consequently equilibrated to a Boltzmann distribution with a single excitation temperature (Mangum & Shirley, 2015). In the case of collision-dominated excitation, this is equal to the kinetic temperature of the gas  $T_{\text{kin}}$ .

Because LTE assumes one value for the excitation temperature, once  $N_u$  and  $T_{\text{ex}}$  are known, the total column density of the molecule can be found simply by inverting Eq. 1.10.  $N_u$  is obtained from the observed integrated antenna temperature  $T_a$ , the Einstein  $A_{ij}$  coefficient, and a beam-filling factor  $f_s$  (e.g. Goldsmith & Langer, 1999):

$$N_u = \frac{8\pi k\nu^2 f_s \int T_a dv}{hc^3 A_{ul}} \left( \frac{\tau}{1 - e^{-\tau}} \right) \quad (1.11)$$

Though the optical depth,  $\tau$ , is also a function of  $N_u$ , in the optically thin limit ( $\tau \ll 1$ ) the factor on the right side of Eq. 1.11 disappears, and obtaining  $N_u$  is straightforward if the spectroscopic parameters are known ( $A_{ij}$ ,  $g_u$ ).  $T_{\text{ex}}$  can be calculated from the relative brightnesses of observed lines, where in the two-level system:

$$\frac{N_j}{N_i} = \frac{g_j}{g_i} e^{-(E_j - E_i)/kT_{\text{ex}}} \quad (1.12)$$

In practice, we ideally observe far more than two lines of a molecule, in which case

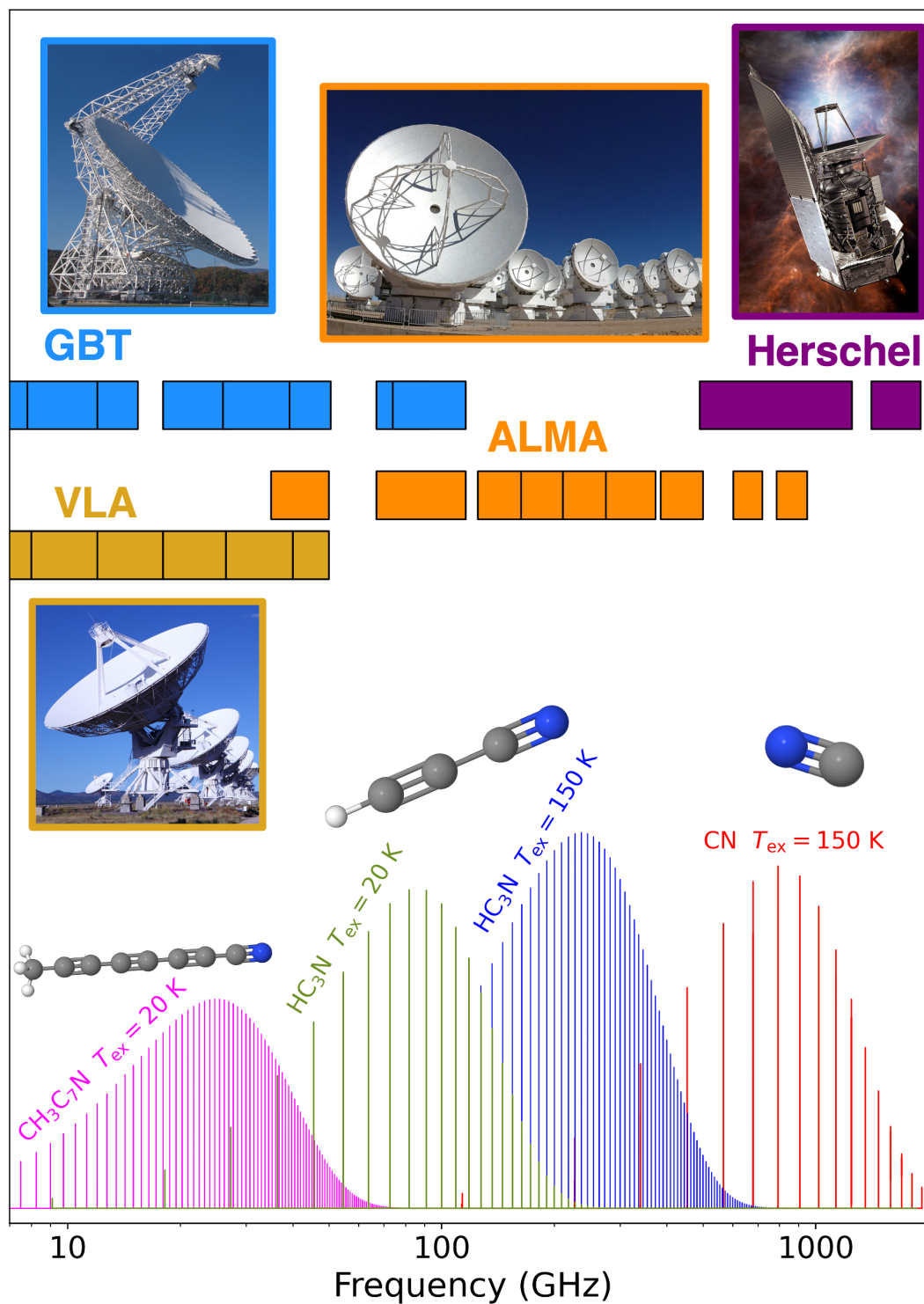


Figure 1.5: LTE simulations of rotational spectra for three molecules ( $\text{CH}_3\text{C}_7\text{N}$ ,  $\text{HC}_3\text{N}$ ,  $\text{CN}$ ). Spectral coverage of example radio/far-infrared observatories are included, with band edges indicated for their respective instruments. Intensity units are arbitrary. Image credits: NRAO, ESO, GBO

the excitation temperature can be derived from a fit to several transitions using a simulation of LTE brightnesses (e.g. Fig. 1.5, Chapters 5 and 6), or the population diagram method (Goldsmith & Langer, 1999, Chapter 4).

### 1.3.3 Non-Thermal Excitation

While LTE is an important and often necessary starting place for analyzing radio/submillimeter spectra, the reality of molecular excitation is often much more complex. For LTE to hold, the density of colliding gas particles must be above a given threshold such that thermal exchange of energy outpaces the radiative decay of rotational states. This is achieved above the “critical density” of a particular transition ( $j \rightarrow k$ ), defined in Shirley (2015) as the density where the sum of all collisional transition rates into the upper rotational level equals the rate of spontaneous emission

$A_{jk}$ :

$$n > n_{\text{crit}} = \frac{A_{jk}}{\sum_{i \neq j} \gamma_{ji}} \quad (1.13)$$

where  $\gamma_{ji}$  is the collisional rate (measured in  $\text{cm}^3 \text{s}^{-1}$ ) into state  $j$  from another state  $i$ . For lines with high  $A_{ij}$  values or in low density gas, the condition in Eq. 1.13 may not be met, in which case the transition will be “subthermally” populated, with  $T_{\text{ex}}$  (as defined in Eq. 1.12) smaller than  $T_{\text{kin}}$ . In this case, a full population analysis, taking into account the collisional rates and physical conditions, is needed to retrieve molecular column densities and abundances from observational data. These non-LTE simulations are typically performed with radiative transfer software (e.g. RADEX; van der Tak et al., 2007). Additionally, because  $A_{jk}$  goes as  $\nu^3$ ,  $n_{\text{crit}}$  increases with larger  $J$  values, and subthermal effects for a given molecule therefore become more important at higher frequencies (Decin et al., 2018).

Another important non-thermal mechanism of rotational excitation is pumping

through vibrational states. In addition to rotational levels, molecular bonds have bending and stretching modes which lie primarily in the infrared, and are therefore excited in environments with high IR flux. Radiative transitions between the ground and excited vibrational states also can exhibit a simultaneous change in rotational energy  $\Delta J = \pm 1$ , so if the rate of IR absorption is fast enough, higher rotational levels in the ground state can be efficiently populated through cycles of vibrational excitation and decay (Carroll & Goldsmith, 1981). To determine the importance of this effect for a given state, a similar condition to Eq. 1.13 can be derived for a molecule irradiated by a blackbody with temperature  $T_{\text{bb}}$ , radius  $R_{\text{bb}}$  at a distance  $r$  (Agúndez et al., 2008):

$$\frac{R_{lu}}{C_{lu}} = \frac{4\pi B_{\nu_1 \rightarrow \nu_0} B_\nu(\nu_{\text{IR}}, T_{\text{bb}}) (R_{\text{bb}}/r)^2}{\gamma_{lu} n(\text{H}_2)} \quad (1.14)$$

where  $B_{\nu_1 \rightarrow \nu_0}$  is the Einstein coefficient for emission, and  $\nu_{\text{IR}}$  is the characteristic frequency of the vibrational state, and  $B_\nu$  is the Planck function. When this ratio is larger than one (i.e. when  $\gamma_{lu}$  and the density are low), the excitation of a transition is faster through IR absorption to the vibrational state  $\nu_1$  than it is through ground state collisions. This pushes the excitation temperature of rotational levels toward  $T_{\text{bb}}$  (Goldsmith et al., 1983), which can appear as superthermal excitation in analysis of molecular lines ( $T_{\text{ex}} > T_{\text{kin}}$ ). IR pumping is particularly important in the case of circumstellar environments, where the presence of warm dust grains and a very red central star produce large amounts of IR photons (Agúndez et al., 2012; Massalkhi et al., 2019).

To summarize, the major sources of rotational excitation (for the studies included in this thesis) are collisions, background radiation, and ambient IR photons. Collisions push populations into a thermal distribution with  $T_{\text{ex}} = T_{\text{kin}}$ , background photons

produce  $T_{\text{ex}} = T_{\text{bg}}$ , and IR pumping causes  $T_{\text{ex}} = T_{\text{bb}}$ . The relative importance of these mechanisms and their efficiency relative to radiative decay vary with temperature, gas density, ambient infrared flux, and the spectroscopic characteristics of a particular molecular *line*. Though non-LTE simulations taking all these effects into account are preferred for observational comparisons, they impose a significant burden both computationally, and with regard to molecular and physical parameters needed *a priori* (e.g. collisional rates, vibrational transition strengths, IR flux model). In the works included here, I will model these effects when possible (Chapter 3), and discuss the necessary simplifications to the problem when some of these prerequisite data are unavailable.

### 1.3.4 Mapping Molecular Lines with Interferometric Observations

The observational foundations of astrochemistry are primarily built from single dish instruments such as the Green Bank Telescope, the IRAM 30-meter Telescope, and the NRAO 140-foot Telescope (McGuire, 2022). While facilities like these represent key means in characterizing the rotational spectra of molecules in the ISM and CSEs, interferometry provides a pathway toward characterizing chemistry at spatial scales unattainable by single dish telescopes. This is most evident by the results from the Atacama Large Millimeter/submillimeter Array (ALMA; Fig. 1.5), which has provided an unprecedented view of the microwave sky since its first light in 2011 (Díaz Trigo et al., 2023).

An interferometer like ALMA works by combining the simultaneous measurements of numerous single dish receivers. Each pair of antennas creates a baseline whose correlated signal measures a particular spatial frequency on the sky, with small baselines characterizing large-scale structures and long baselines observing smaller struc-

tures. In other words, each baseline samples a point in the complex visibility function  $V(u, v)$ , which is the Fourier transform of the sky brightness distribution (Thompson et al., 2001). Obtaining enough antennas thus allows one to describe the observed portion of visibility function, and reconstruct a model of the spatial distribution of incoming flux. In the case of rotational lines, this allows us to map molecular emission in a source, as demonstrated in Figure 1.6.

The benefit of interferometry is clear, as the spatial scales measured by a baseline with separation  $B$  go as  $\lambda/B$ , meaning the full telescope functions with the same resolving power as a single dish with a diameter as large the array (up to several kilometers in size). The trade-off; however, is that because we have a finite number of antennas, there will be some minimum baseline below which visibilities are not sampled, and consequently there is a maximum angular scale above which flux will not be detected. This requires care to be taken in planning observations to ensure that the largest spatial scales of an object are not lost, and often combining executions with multiple array configurations (or auxiliary telescopes, like the Atacama Compact Array; ACA) is necessary to recover all of the emission.

Interferometric imaging is particularly useful in the case of evolved stars, which have a radial stratification in their chemistry due to the changing physical properties of the wind as it travels outward (Section 1.2.2. This structure is readily observable due to the characteristic velocity profile of a spherically-expanding envelope. Figure 1.6 shows images from ALMA observations of the  $J = 8 - 7$  transition  $^{29}\text{SiO}$  in the envelope of IRC+10216, and demonstrates how they map onto the line profile and AGB wind geometry. In the line-wings, the blue- and red-shifted emission represents a column of material traveling toward and away from the observer at the expansion velocity (a.); however, in the central velocity channels, maps provide a cross-section of emission in the envelope (c.). The reduced optical depth and lack of projection

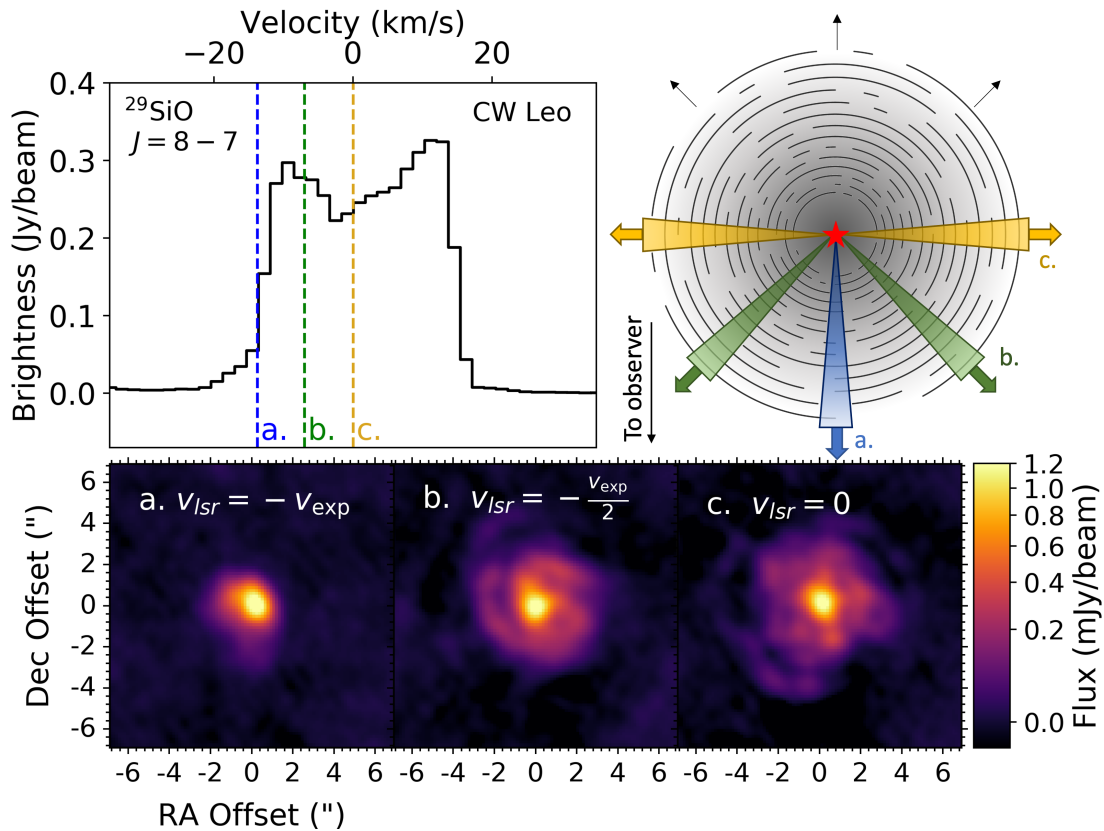


Figure 1.6: *Bottom panels:* ALMA channel maps of the  $J = 8 - 7$  transition of  $^{29}\text{SiO}$  measured toward CW Leo (IRC+10216) at the envelope expansion velocity ( $v_{\text{exp}}$ ),  $v_{\text{exp}}/2$ , and the line center. *Top left:* ALMA spectrum associated with the images, obtained with a  $5'' \times 5''$  diameter circular aperture centered on the position of CW Leo. *Top right:* Schematic of a spherical expanding AGB outflow, indicating the regions sampled by the three imaged velocity channels. In this example, the systemic velocity of CW Leo ( $v_{\text{sys}} = -26.5 \text{ km s}^{-1}$ ) is subtracted from the spectrum and channel maps.

effects in the latter case make these maps particularly powerful for studying how the abundances of molecules change in different regions of an outflow (e.g. Agúndez et al., 2017; Quintana-Lacaci et al., 2017; Unnikrishnan et al., 2023).

One of the most important things to consider when examining images of molecular lines is that the spatial distribution of a particular molecular transition does not

necessarily represent the abundance of that species. As shown in previous sections, the emerging brightness of a line is a function of many parameters governing the populations of rotational states, meaning a transition may not be excited even in a line-of-sight where the molecule is abundant, or a transition can be brightest in a location where its column density is relatively low. This again emphasizes the importance of observing as many transitions as possible, and understanding the physical conditions (temperature and gas density) throughout a source. In Chapters 3 and 4, I will use archival ALMA 12m Array and ACA data to characterize the molecular structure of AGB stars, and will pay particular attention to how these excitation effects impact our interpretations of synthesized maps.

---

Using the observational tools discussed in this section, it is possible to directly characterize the abundances and physics of molecular carbon in a wide variety of astronomical environments. In this thesis, I will use these methods to provide new insights into the chemical processes affecting carbon at two critical stages: the envelopes of dying stars, and cold prestellar clouds. In the former, I will characterize non-equilibrium chemical pathways at play as stellar material is reintroduced into the ISM, and in particular determine how the complications of late-type stellar evolution (binarity, envelope asymmetries, post-AGB onset) can affect our picture of circumstellar chemistry. In the latter, I will investigate the build-up of large carbon chains at low temperatures, and use their excitation properties to gain clues into their formation mechanisms. With these case studies, I aim to develop more nuanced understanding of carbon recycling in our Galaxy that can be built upon by future large-scale observational and theoretical efforts.

## CHAPTER 2

# Small Hydrides in Circumstellar Envelopes

An outstanding question in the chemistry of AGB stars is how hydrides like phosphine ( $\text{PH}_3$ ) and silane ( $\text{SiH}_4$ ) are synthesized in circumstellar envelopes in large amounts. The text in Chapter 2, which appeared in the *Astrophysical Journal* (Siebert et al., 2020) as “A Search for Light Hydrides in the Envelopes of Evolved Stars.”, details a submillimeter spectroscopic study aiming to characterize the diatomic precursors of these molecules.

## 2.1 Introduction

The circumstellar material of a star in its final stages of evolution is well-known for its unique and complex chemical inventory. These objects form around Asymptotic Giant Branch (AGB) and Red Supergiant (RSG) stars when interior thermal pulses eject loosely bound surface material in the form of stellar winds (Ziurys, 2006). These steady winds form large-scale spherical structures of gas and dust known as circumstellar envelopes (CSEs). Due to their large range of temperatures and densities, as

well as an increased abundance of elements produced through nucleosynthesis, CSEs exhibit incredibly diverse chemistry. Of the 204 unique molecules detected in space, more than 60 were first discovered in these objects (McGuire, 2018).

Because the physical conditions near the photospheres of these stars are favorable for the formation of silicate and carbonaceous condensates, AGB and RSG stars are well-known for their efficient production of dust grains. Gehrz (1989) showed that more than 90% of interstellar dust in the galaxy is produced in the envelopes of evolved stars. After they form, dust grains can be studied in great detail through infrared and X-ray spectroscopy, as well as direct analysis of interplanetary material. Through these methods, it has been shown that grains are composed of both crystalline and amorphous magnesium-rich silicates (e.g. olivine, pyroxene, etc.) as well as carbonaceous structures like graphite and amorphous silicon carbide (SiC) and titanium carbide (TiC) clusters. (Campins & Ryan, 1989; Rogantini et al., 2019; Waters et al., 1998; Amari et al., 1990; Bernatowicz et al., 1991).

Though the evolution and interactions of micron-sized dust grains are largely understood in the ISM, the gas-phase chemical pathways leading to their formation are not well-constrained by the present body of observational work. Thus, characterizing the reservoir of molecules in the dust production zones of evolved stellar envelopes (5–20 stellar radii) is crucial to understanding the structure of interstellar grains (Ziurys, 2006).

One class of molecules that is expected to form in these hot, dense environments are diatomic hydrides (XH). These species have been intensely studied since the discovery of CH - the first detected interstellar molecule - in 1937 (Swings & Rosenfeld, 1937). Since then, discoveries of OH, HCl, NH, HF, SH, and (tentatively) SiH in the interstellar medium have added to our understanding of hydrides in space (Adams, 1941; Blake et al., 1985; Meyer & Roth, 1991; Neufeld et al., 1997, 2012). Thermo-

chemical equilibrium models predict a wide variety of these hydride species abundant in the inner winds of evolved stars (Agúndez et al., 2020). However, only three (OH, HCl, and HF) have been detected in these environments to date (Agúndez et al., 2011; Cernicharo et al., 2010). Thus, searching for other monohydrides in CSEs presents a useful opportunity to better understand the inner regions of these important astronomical sources.

Previous theoretical and observational studies of these objects suggest that the ideal candidates for such a search include silicon monohydride (SiH), phosphinidene (PH), and iron hydride (FeH). All these species are predicted to form in the hot inner regions of CSEs through gas-phase reactions of atomic Si, P, and Fe with neutral hydrogen (Agúndez et al., 2020; Cherchneff, 2012), and therefore could exist further out in the envelope as well. Furthermore, Carroll & McCormack (1972) simultaneously reported both the laboratory and solar identification of FeH through observation of its spectrum in the region between 2360 – 8900 Å. This detection was later confirmed by Carroll et al. (1976). Around the same time, the Wing-Ford band at 9900 Å was also identified as arising from FeH (Wing & Ford, 1969; Nordh et al., 1977; Wing et al., 1977; Mould & Wyckoff, 1978b). It is now known that FeH can form in the atmospheres of stars of spectral types M, S, and K (Mould & Wyckoff, 1978a), but despite this, it has not yet been detected in the molecular winds of evolved stars.

Though neither SiH nor PH has been detected in such a CSE to date, their heavier counterparts, silane (SiH<sub>4</sub>) and phosphine (PH<sub>3</sub>), have both been observed in CSEs, and most proposed formation mechanisms for these molecules involve SiH and PH as an intermediate step (Monnier et al., 2000; Agúndez et al., 2014). Therefore, constraining the abundances of the molecules targeted in this work could not only provide a more complete understanding of the dust formation zones in these objects, but it could also shed light on the chemical processes that lead to the formation of

more complex hydrides in CSEs.

Because these are very light molecules, most of their rotational transitions fall in the THz to far-infrared regions of the electromagnetic spectrum. This makes them ideal targets for the German Receiver for Astronomy at Terahertz Frequencies (GREAT) aboard the Stratospheric Observatory for Infrared Astronomy (SOFIA), which operates from 0.5–4.8 THz at an altitude of 12 km, largely eliminating atmospheric absorption due to water vapor. We used this instrument to conduct a search for SiH, PH, and FeH toward two well-studied CSEs.

We observed the carbon star IRC+10216 to search for these hydrides in a circumstellar environment dominated by carbon chemistry. This source has been the subject of numerous single-dish and interferometric spectral line surveys (Avery et al., 1992; Zhang et al., 2017; Cernicharo et al., 2013), revealing a rich gas-phase chemical inventory. Currently, the only diatomic hydrides observed toward IRC+10216 are the halide bearing molecules HCl and HF Agúndez et al. (2011).

To represent an oxygen-rich envelope, we observed the RSG VY Canis Majoris (VY CMa). In contrast to IRC+10216, whose initial stellar mass is  $3 - 5 M_{\odot}$  (Matthews et al., 2015), VY CMa has a mass of  $17 M_{\odot}$ , and is ejecting material at a higher rate of about  $6 \times 10^{-4} M_{\odot} \text{ yr}^{-1}$  (Shenoy et al., 2016). Due to this dramatic mass loss, the envelope of VY CMa is highly asymmetric, consisting of various dusty knots and outflows with non-uniform velocity structure (Smith et al., 2001). Because most of the carbon in this envelope resides in CO, VY CMa does not show the same diversity of C-bearing species seen in carbon-rich sources like IRC+10216. It instead exhibits oxygen-driven chemical structure most notably marked by various metal and non-metal oxides, as well as strong OH maser emission (Ziurys et al., 2007, 2018).

In this paper, we report our search for SiH, PH, and FeH toward these evolved

stars. In Section 2.2, we summarize our observational strategies and specifications. In Section 2.3, we state our findings and numerically constrain the abundances of these molecules by adopting excitation temperatures and source sizes characteristic of molecules formed in the inner regions of CSEs. Finally, in Section 2.4 we discuss how our results relate to the current theoretical framework for chemical processes in these circumstellar environments, and outline prospects for future related works.

## 2.2 Observations

Observations of IRC+10216 and VY Canis Majoris were taken with the SOFIA telescope using the GREAT receiver in its 4GREAT configuration, which simultaneously collects spectra from four co-aligned pixels operating between 490–635 GHz, 890–1100 GHz, 1200–1500 GHz, and 2490–2590 GHz, respectively. The spectral windows relevant for this work are shown in Table 2.1. PH was only targeted during observations of IRC+10216, whereas the SiH and FeH windows were utilized for both sources.

Observations were taken on 14 and 20 December, 2018. The pointing positions for the observations of IRC+10216 and VY CMa were  $\alpha_{J2000} = 9^{\text{h}}47^{\text{m}}57.406^{\text{s}}$ ,  $\delta_{J2000} = +13^{\circ}16'43.56''$  and  $\alpha_{J2000} = 7^{\text{h}}22^{\text{m}}58.329^{\text{s}}$ ,  $\delta_{J2000} = -25^{\circ}46'03.24''$  respectively. We used the single point chopping method for background subtraction, in which the pointing is symmetrically switched between the ON (centered source) and OFF (90" offset in RA) positions at a rate of 2.5 Hz. Spectra were adjusted to systemic velocities of  $v_{\text{lsr}} = -26.0 \text{ km s}^{-1}$  and  $v_{\text{lsr}} = 19.5 \text{ km s}^{-1}$  for IRC+10216 and VY CMa, respectively (Gong et al., 2015; Sahai & Wannier, 1992). The SOFIA GREAT instrument is a heterodyne receiver that gathers data as a dual-sideband spectrum. Therefore, every frequency in the rest band has a corresponding image frequency that can contaminate observed spectral features. While this type of blending does affect some of

Table 2.1: Frequency bands observed with SOFIA GREAT

Targeted Molecule	Rest Band (MHz)	Image Band (MHz)	Channel Width (km s <sup>-1</sup> )	RMS Noise (mK)
SiH (3/2 – 1/2)	622220 – 626220	634220 – 638220	1.051	30.0
SiH (5/2 – 3/2)	1041620 – 1045620	1053620 – 1057620	1.051	80.1
FeH	1322373 – 1324996	1325190 – 1327825	0.995	32.0
PH	1505500 – 1508130	1508340 – 1510970	1.019	96.7

NOTE — RMS noise levels are measured from IRC+10216 observations. Integration time on VY CMa was about half that for IRC+10216, so RMS noise is ~1.4 times those listed here. PH was only targeted during observations of IRC+10216.

the molecular emission seen in our spectra, we selected IFs for each spectral window that ensured no bright lines of known molecules in the image band would overlap with the targeted transitions.

Using the setup described above, we searched for the  $J = 3/2 - 1/2$  and  $J = 5/2 - 3/2$  transitions of SiH, the  $J = 4 - 3$  ( $N = 3 - 2$ ) transition of PH. Table 2.2 includes the spectroscopic parameters for these transitions. The two  $J$  transitions of SiH are split into triplets which we would not expect to resolve given the known expansion velocities of IRC+10216 and VY CMa. The transitions of PH also exhibit hyperfine splitting, and there are  $\sim 10$  distinct emission features from this molecule centered at 1,507,640 MHz. Both molecules have small dipole moments, 0.087 and 0.396 Debye for SiH and PH, respectively (Müller et al., 2005), making detection difficult even with high sensitivity. The dipole moment of PH is based on an unpublished *ab initio* calculation by H. S. P. Müller.<sup>1</sup>

Although the rotational spectrum of FeH is challenging both to observe and to assign in the laboratory, a number of lines have been measured and reported by Brown et al. (2006). The  $\Omega = 5/2$ ;  $J = 5/2 \rightarrow 7/2$  transition of FeH of the  $X^4\Delta$  state was selected because it is the most readily observable transition of the molecule with a frequency and intensity observable by the SOFIA telescope. This transition is split into a pair of  $\Lambda$ -doubled lines at 1316.8387 GHz and 1324.7719 GHz that are predicted to be of similar intensities. While observing with the SOFIA telescope, we decided to focus only on the higher frequency feature so that integration time at that frequency would be maximized.

Spectral data were reduced using the CLASS program as part of the GILDAS software package.<sup>2</sup> Reduction consisted of removing a first-order baseline, calibrating to

---

<sup>1</sup>[cdms.astro.uni-koeln.de](mailto:cdms.astro.uni-koeln.de)

<sup>2</sup><http://www.iram.fr/IRAMFR/GILDAS/>

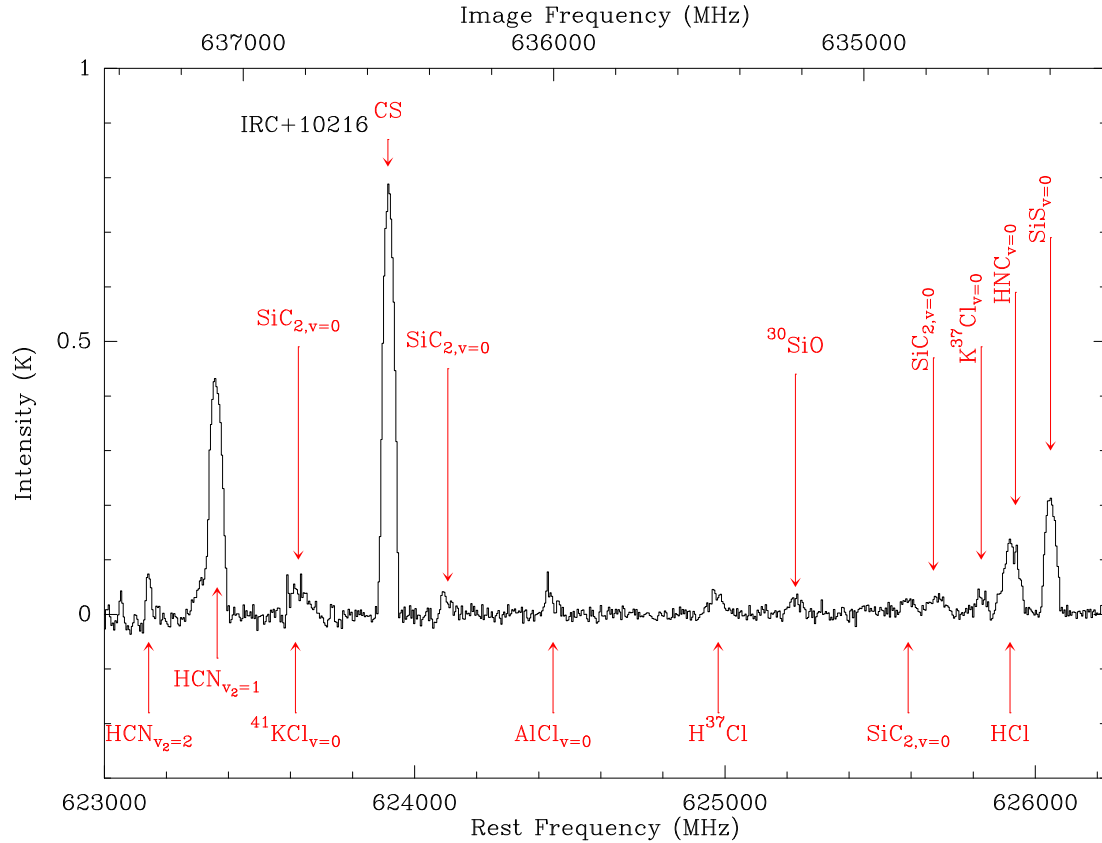


Figure 2.1: Continuum subtracted SOFIA GREAT spectrum of IRC+10216 around targeted 624925 MHz transition of SiH. Emission lines contributed from the rest frequency band are written near the lower x-axis, and those contributed from the image band are written near the upper x-axis.

main beam temperature scale, and smoothing spectra to a resolution of  $1.0 \text{ km s}^{-1}$ .

## 2.3 Results & Analysis

### 2.3.1 IRC+10216

In our search for these hydrides, we detected a total of 26 transitions which we assign to 11 different species toward IRC+10216. Figures 2.1 and 2.2 show the full calibrated and baseline-subtracted spectra for our 624 and 1048 GHz windows. At these frequencies, emission from vibrationally excited HCN dominates most of the

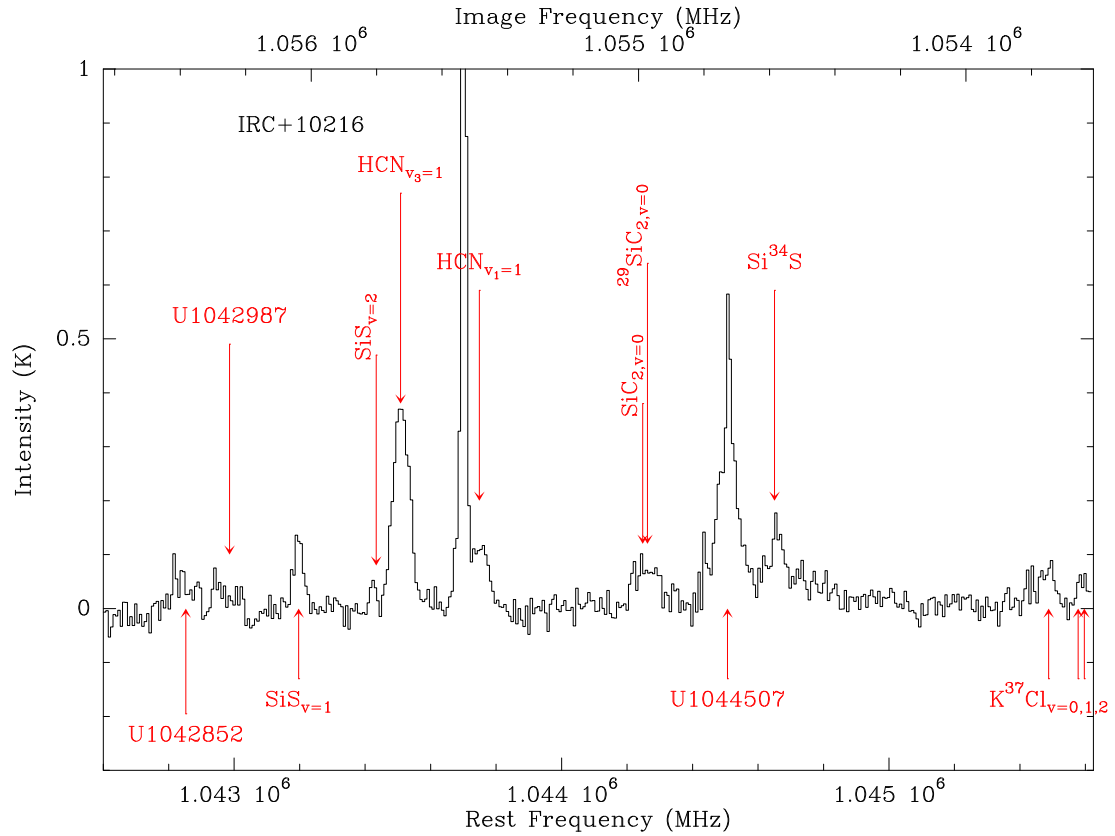


Figure 2.2: Continuum subtracted SOFIA GREAT spectrum of IRC+10216 around targeted 1043918 MHz transition of SiH. Emission lines contributed from the rest frequency band are written near the lower x-axis, and those contributed from the image band are written near the upper x-axis. Unidentified lines are labeled with their observed frequency in the rest band even though they could be contributed from the image band. Corresponding image frequencies for each U line are shown in Table 2.2.

observed bands and accounts for over a quarter of the observed transitions. All other molecules have been previously observed in IRC+10216, with the notable exception of three unidentified features in our 1.04 THz spectral window (labeled in Fig. 2.2). A list of detected transitions is shown in Table 2.2. Each spectral line that was not severely affected by blending was fit with a Gaussian profile in CLASS. Resulting profile widths and integrated line temperatures are included in 2.2 along with their fitting errors.

We compute column densities and abundances for the observed rotational transitions following the formalism of Hollis et al. (2004) for molecular emission described by a single excitation temperature (Eq. 2.1).  $T_{ex}$  is the excitation temperature (K);  $T_{bg}$  is the background continuum temperature and assumed to be 2.7 K;  $k$  is Boltzmann’s constant ( $\text{J K}^{-1}$ );  $h$  is Planck’s constant ( $\text{J s}$ );  $Q$  is the rotational partition function at  $T_{ex}$ ;  $E_u$  is the upper state energy of the transition (K);  $\int TdV$  is the velocity-integrated line area ( $\text{K} \cdot \text{km s}^{-1}$ ) which can be expressed as the product of the peak antenna temperature and the line full width at half maximum;  $S_{ij}\mu^2$  is the transition line strength ( $\text{Debye}^2$ );  $B$  is the beam filling factor; and  $\eta_B$  is the beam efficiency.

$$N_T = \frac{1}{2} \frac{3k}{8\pi^3} \sqrt{\frac{\pi}{\ln 2}} \frac{Q e^{\frac{E_u}{T_{ex}}} \int TdV}{B\nu S_{ij}\mu^2 \eta_B} \frac{1}{1 - \frac{e^{\frac{h\nu}{kT_{ex}} - 1}}{e^{\frac{h\nu}{kT_{bg}} - 1}}} \quad (2.1)$$

For most molecules, including SiH and PH, spectroscopic constants  $Q$  and  $S_{ij}\mu^2$  were obtained from the CDMS and JPL<sup>3</sup> molecular databases (Müller et al., 2005). The only exception to this was FeH, whose partition function was calculated and published by Barklem & Collet (2016). All partition functions were interpolated to our assumed rotational temperatures using a quartic fit on the measured  $Q$  values.

---

<sup>3</sup><https://spec.jpl.nasa.gov>

Unfortunately, there is a lack of spectroscopic data concerning the line strengths of FeH transitions in the  $X^4\Delta$  state. Because of this, we approximate the  $S_{ij}$  value for this molecule as the  $2_1-1_1$  transition of a symmetric top (Gordy & Cook, 1984), yielding a value of  $\sim 0.67$ . The dipole moment was calculated to be 4.1 Debye using Gaussian 09 (Frisch et al., 2009) at the CCSD(T)/aug-cc-pVQZ level of theory and basis set. From this, we obtain a total  $S_{ij}\mu^2$  value of 11.3 Debye<sup>2</sup> (Tables 2.2,2.3). We note that while the above approximation may be a simplified treatment of this molecule, it is still a sufficient choice given the intent of our search, and the current body of spectroscopic data for FeH and similar molecules. We are confident that this value yields column densities and abundances of FeH to within an order of magnitude.

To derive fractional abundances (relative to H<sub>2</sub>) for species detected toward IRC+10216, we employ the formula from Gong et al. (2015) that gives us the average H<sub>2</sub> column density over a radius  $R$  in a spherically expanding wind with velocity  $V_{exp}$ , mass-loss rate  $\dot{M}$ , and mean molecular weight  $\mu$ :

$$N_{H_2} = \frac{\dot{M}}{\pi R V_{exp} \mu m_H} \quad (2.2)$$

For IRC+10216, we take  $\mu = 2.3$  amu,  $V_{exp} = 14.5$  km s<sup>-1</sup>, and  $\dot{M} = 2.0 \times 10^{-5}$  M<sub>⊙</sub>yr<sup>-1</sup> from Massalkhi et al. (2018b).

For every molecule, we assume an emission size characteristic of the inner envelope (denoted by the angular radius  $\theta_{em}$ ), and use this to calculate the beam filling factor and radius  $R$  to compare with the average H<sub>2</sub> column density.

Using this method, we obtain abundances relative to H<sub>2</sub> for some well-characterized molecules in these sources that show emission in our frequency bands. In IRC+10216, for CS we calculate  $f = 5 \times 10^{-7}$  (assuming  $T_{rot} = 175$  K and  $\theta_{em} = 1''$ ); for H<sup>35</sup>Cl:  $f = 1 \times 10^{-7}$  ( $T_{rot} = 150$  K and  $\theta_{em} = 2''$ ); for SiC<sub>2</sub>:  $f = 2 \times 10^{-7}$  ( $T_{rot} = 150$  K and

Table 2.2: List of all detected and targeted rotational transitions toward IRC+10216.

Molecule	Transition	Frequency (MHz)	$\int TdV$ (K · km s <sup>-1</sup> )	$\Delta V$ (km s <sup>-1</sup> )	$E_{up}$ (K)	$S_{ij}\mu^2$ (D <sup>2</sup> )	$\theta_B$ (arcsec)	Comments
<sup>†</sup> CS	$J = 13 - 12$	636 531.5 ± 0.13	16.0 ± 0.1	18.1 ± 0.1	213.9	49.68	42.2	
<sup>†</sup> SiS <sub><math>\nu=0</math></sub>	$J = 35 - 34$	634 398.7 ± 0.33	4.27 ± 0.08	17.8 ± 0.4	548.5	105.4	42.3	
<sup>†</sup> SiS <sub><math>\nu=1</math></sub>	$J = 58 - 57$	1043 196.3 ± 13	1.40 ± 1.0	9.92 ± 8.7	2551	173.6	25.8	
<sup>†</sup> SiS <sub><math>\nu=2</math></sub>	$J = 59 - 58$	1055 811.2 ± 25	0.297 ± 0.67	5.07 ± 13	3659	177.8	25.4	
<sup>†</sup> Si <sup>34</sup> S <sub><math>\nu=0</math></sub>	$J = 60 - 59$	1054 579.5 ± 9.9	2.66 ± 1.3	18.0 ± 6.6	1547	180.7	25.5	
<sup>†</sup> <sup>30</sup> SiO <sub><math>\nu=0</math></sub>	$J = 15 - 14$	635 221.2 ± 8.6	0.615 ± 0.24	20.5 ± 8.2	244.0	144.0	42.3	
<sup>†</sup> SiH	$J = 3/2 - 1/2$	624 924.7 <sup>b</sup>	< 0.172	–	29.99	0.0102 <sup>a</sup>	43.0	
<sup>†</sup> SiH	$J = 5/2 - 3/2$	1043 917.9 <sup>b</sup>	< 0.313	–	80.09	0.0234 <sup>a</sup>	25.7	
<sup>†</sup> PH	$N = 3 - 2, J = 4 - 3$	1507 639.6 <sup>b</sup>	< 1.410	–	144.2	2.346 <sup>a</sup>	17.8	
FeH	$\Omega = 5/2, J = 5/2 - 7/2$	1324 771.4 <sup>b</sup>	< 0.449	–	297.0	11.3	20.4	
<sup>†</sup> HNC <sub><math>\nu=0</math></sub>	$J = 7 - 6$	634 510.8 <sup>b</sup>	?	?	121.8	65.12	42.3	(1)

Table 2.2 continued

Table 2.2: List of all detected and targeted rotational transitions toward IRC+10216. (continued)

Molecule	Transition	Frequency (MHz)	$\int TdV$ (K · km s <sup>-1</sup> )	$\Delta V$ (km s <sup>-1</sup> )	$E_{up}$ (K)	$S_{ij}\mu^2$ (D <sup>2</sup> )	$\theta_B$ (arcsec)	Comments
<sup>†</sup> HCN <sub><math>\nu_2=2</math></sub>	$J = 7 - 6, l = 2f$	623 142.9 ± 0.90	0.612 ± 0.07	7.04 ± 0.8	2172	162.1	43.1	
<sup>†</sup> HCN <sub><math>\nu_2=2</math></sub>	$J = 7 - 6, l = 2e$	623 306.4 <sup>b</sup>	?	?	2172	162.1	43.1	(2)
<sup>†</sup> HCN <sub><math>\nu_2=2</math></sub>	$J = 7 - 6, l = 0$	623 336.6 <sup>b</sup>	?	?	2150	176.4	43.1	(2)
<sup>†</sup> HCN <sub><math>\nu_2=1</math></sub>	$J = 7 - 6, l = 1f$	623 359.2 ± 0.33	10.3 ± 0.1	21.4 ± 0.3	1144	178.1	43.1	(2)
<sup>†</sup> HCN <sub><math>\nu_3=1</math></sub>	$J = 12 - 11$	1055 724.5 ± 5.4	6.66 ± 1.2	16.5 ± 3.6	3346	319.8	25.4	
<sup>†</sup> HCN <sub><math>\nu_1=1</math></sub>	$J = 12 - 11$	1055 501.8 ± 11	3.31 ± 0.81	25.4 ± 5.3	5094	327.7	25.4	
<sup>†</sup> HCN <sub><math>\nu_2=2</math></sub>	$J = 17 - 16, l = 0$	1510 521.2 ± 2.7	21.1 ± 1.4	15.9 ± 1.1	2684	428.4	17.8	
<sup>†</sup> HCN <sub><math>\nu_2=3</math></sub>	$J = 17 - 16, l = 1e$	1507 906.9 ± 3.4	3.62 ± 0.49	9.43 ± 1.4	2684	414.5	17.8	
<sup>†</sup> SiC <sub>2</sub>	$J_{K_a, K_c} = 26_{6,20} - 25_{6,19}$	625 589.0 ± 3.9	0.664 ± 0.12	23.5 ± 5.3	470.6	141.0	42.9	
<sup>†</sup> SiC <sub>2</sub>	$J_{K_a, K_c} = 27_{4,24} - 26_{4,23}$	634 764.8 ± 4.3	0.940 ± 0.14	28.0 ± 4.8	461.7	150.5	42.3	
<sup>†</sup> SiC <sub>2</sub>	$J_{K_a, K_c} = 30_{0,30} - 29_{0,29}$	636 350.9 ± 3.6	0.503 ± 0.12	12.1 ± 4.0	480.8	171.1	42.2	
<sup>†</sup> SiC <sub>2</sub>	$J_{K_a, K_c} = 29_{2,28} - 28_{2,27}$	636 820.3 <sup>b</sup>	?	?	478.1	164.1	42.2	(3)
<sup>†</sup> SiC <sub>2</sub>	$J_{K_a, K_c} = 43_{8,35} - 42_{8,32}$	1054 995.3 <sup>b</sup>	?	?	1208	238.1	25.5	(4)
<sup>†29</sup> SiC <sub>2</sub>	$J_{K_a, K_c} = 44_{6,38} - 43_{6,37}$	1054 973.3 <sup>b</sup>	?	?	1208	245.8	25.5	(4)

Table 2.2 continued

Table 2.2: List of all detected and targeted rotational transitions toward IRC+10216. (continued)

Molecule	Transition	Frequency (MHz)	$\int TdV$ (K · km s <sup>-1</sup> )	$\Delta V$ (km s <sup>-1</sup> )	$E_{up}$ (K)	$S_{ij}\mu_c^2$ (D <sup>2</sup> )	$\theta_B$ (arcsec)	Comments
<sup>35</sup> HCl	$J = 1 - 0$	625 922.7 ± 0.76	3.67 ± 0.10	26.2 ± 0.83	30.04	2.458	42.9	(1)
<sup>37</sup> HCl	$J = 1 - 0$	624 972.4 ± 7.3	0.932 ± 0.29	23.3 ± 8.3	29.99	2.458	43.0	
<sup>37</sup> KCl <sub><math>\nu=0</math></sub>	$J = 86 - 85$	634 623.9 ± 2.7	0.663 ± 0.08	18.1 ± 2.7	1333	9069	42.3	
<sup>37</sup> KCl <sub><math>\nu=0</math></sub>	$J = 145 - 144$	1045 482.5 ± 20	1.35 ± 1.31	18.0 ± 13	3729	15297	25.7	
<sup>37</sup> KCl <sub><math>\nu=1</math></sub>	$J = 146 - 145$	1045 577.8 <sup>b</sup>	?	?	4150	15581	25.7	(5)
<sup>37</sup> KCl <sub><math>\nu=2</math></sub>	$J = 147 - 146$	1045 596.7 <sup>b</sup>	?	?	4567	15871	25.7	(5)
<sup>41</sup> KCl	$J = 84 - 83$	623 616.1 <sup>b</sup>	?	?	1279	8858	43.1	(3)
<sup>1</sup> AlCl	$J = 43 - 42$	624 431.2 ± 3.4	0.630 ± 0.19	10.8 ± 4.2	660.5	45.96*	43.0	
U1042852	-	1056 383 <sup>c</sup>	-	-	-	-	25.8/25.4	(6)
U1042987	-	1056 248 <sup>c</sup>	-	-	-	-	25.8/25.4	(6)

U1044507

1054 728<sup>c</sup>

—

—

—

—

25.7/25.5

(6)

NOTE — (1)  $\text{H}^{35}\text{Cl } J = 1 - 0$  is blended with  $\text{HNC } J = 7 - 6$  from the image band (see Fig. 2.1). Degree of contamination is unclear, but agreement with Agúndez et al. (2014) suggests  $\text{H}^{35}\text{Cl}$  is the dominant contributor of the feature. (2) Three transitions of vibrationally excited  $\text{HCN}$  blend around 623350 MHz;  $\text{HCN } \nu_2 = 1$  is the brightest component due to its lower energy, therefore our Gaussian fit was attributed to it. (3)  $^{41}\text{KCl}$  blended with  $\text{SiC}_2$  29<sub>2,28</sub> - 28<sub>2,27</sub> from the image band. (4)  $\text{SiC}_2$  and its isotopologue  $^{29}\text{SiC}_2$  blend around 1055000 MHz. (5) Vibrationally excited  $\text{K}^{37}\text{Cl}$  transitions are seen at the edge of our 1 THz band. Their emission is blended and difficult to analyze due to the frequency cutoff. (6) Unidentified lines can be seen in Figure 2.2; we do not report line areas or widths for these features as they either had too low S/N to obtain a reliable fit, or exhibit an anomalous line profile that is not well-modeled by a Gaussian.

<sup>a</sup>Sum of unresolved hyperfine components

<sup>b</sup>No fit performed, literature frequency listed

<sup>c</sup>Unclear whether feature is present in rest or image band; therefore, we report the rest frequency as part of the molecule name, and list the corresponding image frequency in the third column.

<sup>†</sup>Spectroscopic data taken from the CDMS catalogue (Müller et al., 2005)

<sup>††</sup>Spectroscopic data taken from the JPL catalogue: <https://spec.jpl.nasa.gov>.

$\theta_{em} = 2''$ ). These results are in agreement with previous studies of IRC+10216 to within a factor of  $\sim 2$ – $3$  (Massalkhi et al., 2018b, 2019; Agúndez et al., 2011). Thus, we are confident that this treatment may be used to obtain accurate constraints on the hydrides targeted in this work.

Neither SiH, PH, nor FeH were detected in the C-rich envelope of IRC+10216 (see Fig. 2.3). Upper limits on the integrated line fluxes, obtained assuming a width of  $14.5 \text{ km s}^{-1}$  and a peak antenna temperature equal to the  $1\sigma$  rms noise level of the observations, are shown in Table 2.2.

The  $J = 4 - 3$  transition of PH has a similar Einstein  $A_{ij}$  coefficient to the  $1 - 0$  transition of HCl. Assuming these molecules have similar collisional excitation rates, we expect PH to thermalize at a similar critical density to HCl given by Agúndez et al. (2011) ( $\sim 10^7 \text{ cm}^{-3}$ ). In IRC+10216, gas densities are below this beyond radii of  $1.3 \times 10^{15} \text{ cm}$  ( $0.7''$ ). Because of this, we assume all PH emission is confined to a  $2''$  source size, and has an effective excitation temperature of 250 K in this region, similar to those measured by Patel et al. (2011) for SiC<sub>2</sub> and HC<sub>3</sub>N. We derive an upper limit column density of  $N_{\text{PH}} < 7 \times 10^{14} \text{ cm}^{-2}$ , corresponding to a fractional abundance relative to H<sub>2</sub> of  $f_{\text{PH}} < 4 \times 10^{-8}$ .

The  $A_{ij}$  values of SiH transitions are much lower than PH, so we expect the excitation of this molecule to be described by LTE conditions out to larger radii than PH and HCl. In this case, we assume a  $5''$  maximum radius of emission and an excitation temperature of 150 K. Given these constraints, the higher temperature  $J = 5/2 - 3/2$  transition is expected to produce a stronger signal than the one at 625 GHz. Using the spectroscopic and observational parameters for this line in the calculation described above, we derive an upper limit column density of  $N_{\text{SiH}} < 2 \times 10^{15} \text{ cm}^{-2}$ , and a fractional abundance relative to H<sub>2</sub> of  $f_{\text{SiH}} < 3 \times 10^{-7}$ .

Finally, for FeH, we assume conditions similar to those of PH, adopting an average

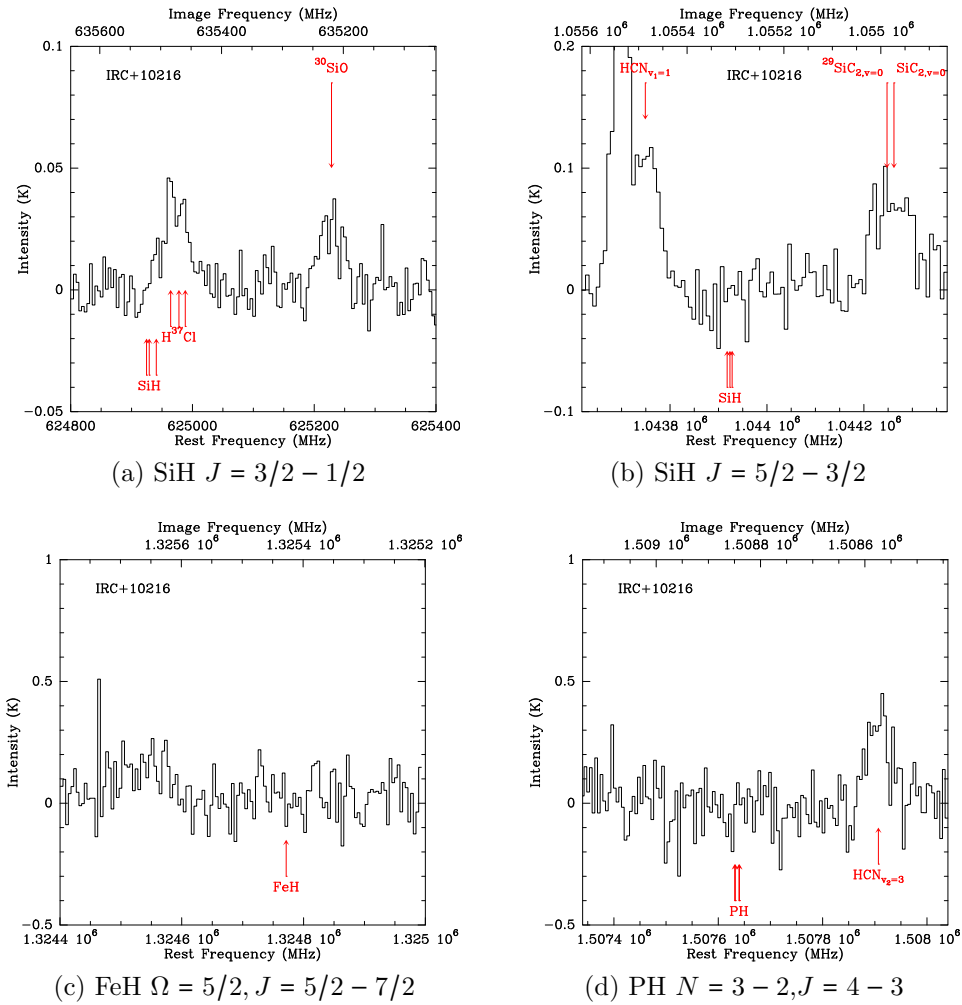


Figure 2.3: SOFIA GREAT spectra of IRC+10216 showing targeted emission lines of SiH  $J = 3/2 - 1/2$  (top left), SiH  $J = 5/2 - 3/2$  (top right), FeH  $\Omega = 5/2, J = 5/2 - 7/2$  (bottom left), and PH  $J = 4 - 3$  (bottom right).

value of  $T_{rot} = 250$  K and  $\theta_{em} = 2''$ . From this, we derive  $N_{\text{FeH}} < 9 \times 10^{13} \text{ cm}^{-2}$  and  $f_{\text{FeH}} < 2 \times 10^{-7}$ .

### 2.3.2 VY CMa

Similar to the case of IRC+10216, we saw no emission from SiH nor FeH in the O-rich envelope of VY CMa (Fig. 2.4). Toward this source, we only detect emission from  $^{30}\text{SiO}$  and SiS. Table 2.3 shows the observational and spectroscopic parameters of these transitions in addition to the targeted lines of SiH and FeH. Much like with IRC+10216, we expect most ro-vibrational emission to come from regions very close to the stellar photosphere (implying compact emission  $\sim 1''$  in radius). This assumption is supported by the fact that all observed molecules exhibit narrow ( $< 40 \text{ km s}^{-1}$ ) emission lines characteristic of regions of the CSE where radiation pressure accelerates ejected material.

As noted before, the CSE of VY CMa is much less isotropic than that of IRC+10216. Ziurys et al. (2007) demonstrate that three separate velocity structures dictate molecular emission profiles in this envelope: a spherically expanding wind centered at the systemic velocity, a tightly collimated blue flow at  $v_{lsr} = -4 \text{ km s}^{-1}$ , and a redshifted expansion at  $v_{lsr} = 48 \text{ km s}^{-1}$ . Some molecules (e.g. SO, SO<sub>2</sub>, HNC, CO, and OH masers) exhibit double- or triple-peaked lines arising from the strong emission in the bipolar outflow (Ziurys et al., 2007; Tenenbaum et al., 2010). However, in a *Herschel* HIFI spectral line survey of VY CMa, Alcolea et al. (2013) note that typical emission profiles above 600 GHz are dominated by the steady wind component. This has been shown to be especially true for all observed transitions of refractory metal-bearing molecules like NaCl, AlCl, AlO, and TiO (Kamiński et al., 2013; Kamiński et al., 2013a). Because of this, we assume that SiH and FeH are only present in the spher-

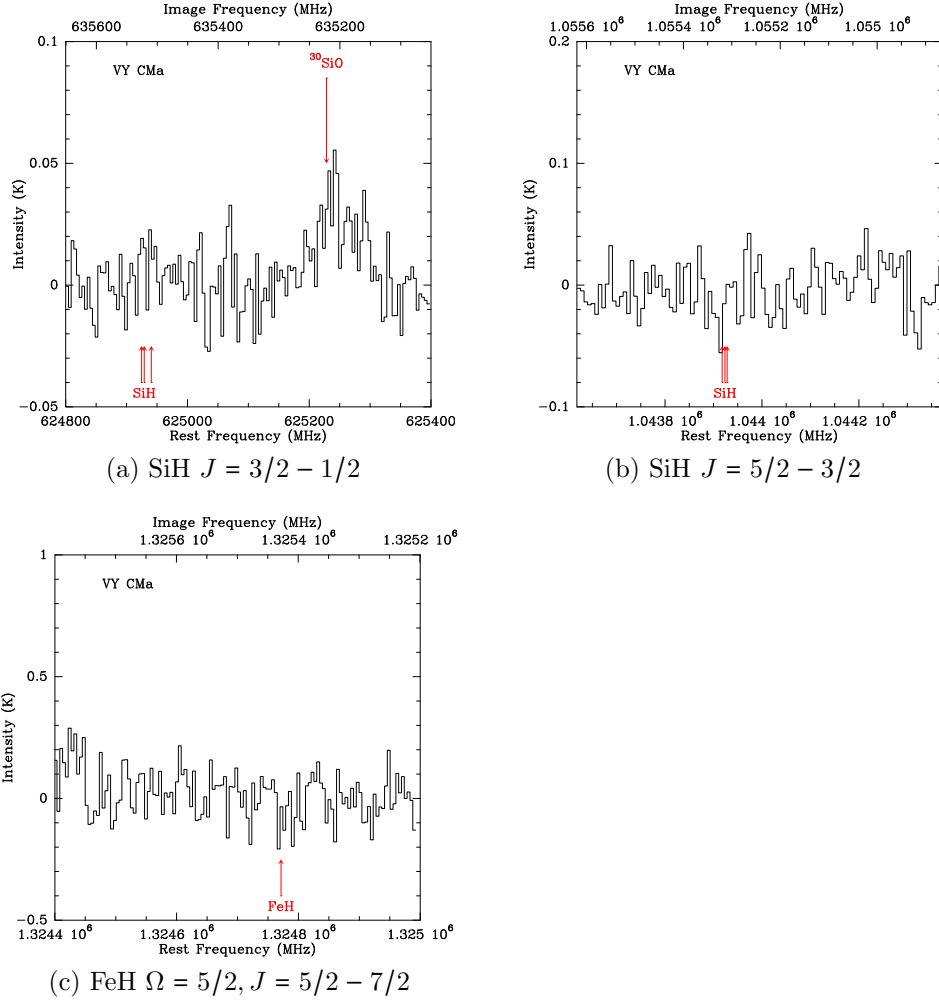


Figure 2.4: SOFIA GREAT spectra of VY CMa showing targeted emission lines of SiH  $J = 3/2 - 1/2$  (top row), SiH  $J = 5/2 - 3/2$  (middle row), and FeH  $\Omega = 5/2, J = 5/2 - 7/2$  (bottom row).

ical wind to calculate their upper limit abundances. This allows us to employ the same quantitative analysis as we did with IRC+10216, by using equations 2.1 and 2.2.

We adopt a mass-loss rate of  $1 \times 10^{-4} M_{\odot} \text{ yr}^{-1}$ , a terminal expansion velocity of  $40 \text{ km s}^{-1}$ , and a mean molecular weight of 2.3 (Ziurys et al., 2007; Kamiński et al., 2013b). We assume SiH and FeH emission come from within a radius of  $1''$ ,

which is typical of molecules in this source (Kamiński et al., 2013a). We adopt line widths equal to the terminal expansion velocity of  $v_{exp} = 40 \text{ km s}^{-1}$ , and rotational excitation temperatures of 250 K for both SiH and FeH. Given these constraints, we derive an upper limit column density  $N_{\text{SiH}} < 2 \times 10^{17} \text{ cm}^{-2}$  and fractional abundance relative to  $\text{H}_2$ ,  $f_{\text{SiH}} < 3 \times 10^{-5}$  in the envelope of VY CMa. And for FeH we derive  $N_{\text{FeH}} < 2 \times 10^{14} \text{ cm}^{-2}$  and  $f_{\text{FeH}} < 3 \times 10^{-8}$ .

It is important to note that we cannot rule out the possibility of these hydrides being present in the bipolar outflow of VY CMa; especially in the case of SiH, as the targeted transitions of this molecule involve lower rotational energy states relative to those of FeH and the species observed in Alcolea et al. (2013). However, given our aim of investigating the potential formation and roles in dust grain chemistry of hydrides in CSEs, we find it important to calculate abundances that can be compared with other species known to exist in the *interior* regions of this source (where grain production takes place and the red- and blue-shifted flows are not yet present). In any case, the upper limit abundances w.r.t.  $\text{H}_2$  reported here are accurate descriptions of the chemical inventory in the spherical component of VY CMa, since an increase of emission in the bipolar flow would imply a lower abundance in the stellar wind.

## 2.4 Discussion

The non detections reported here could be simply due to the weak permanent dipoles of the targeted species, as well as effects related to beam dilution. Nevertheless, additional factors related to the underlying reactivity of these species cannot be ruled out. In this section, we discuss how these non-detections are similarly consistent with previous findings related to SiH, PH, FeH and related molecules and may, in fact, help shed light on the chemistry of CSEs.

Table 2.3: List of all detected and targeted rotational transitions toward VY CMa.

Molecule	Transition	Frequency (MHz)	$\int TdV$ (K · km s <sup>-1</sup> )	$\Delta V$ (km s <sup>-1</sup> )	$E_{up}$ (K)	$S_{ij}\mu_e^2$ (D <sup>2</sup> )	$\theta_B$ (arcsec)	Comments
<sup>†</sup> SiS <sub><math>\nu=0</math></sub>	$J = 35 - 34$	634 377.6 ± 9.6	0.613 ± 0.19	26.0 ± 7.7	548.5	105.4	42.3	
<sup>†</sup> <sup>30</sup> SiO <sub><math>\nu=0</math></sub>	$J = 15 - 14$	635 201.4 ± 7.6	1.32 ± 0.24	38.2 ± 7.6	244.0	144.0	42.3	
<sup>†</sup> SiH	$J = 3/2 - 1/2$	624 924.7 <sup>b</sup>	< 0.413	–	29.99	0.0102 <sup>a</sup>	43.0	
<sup>†</sup> SiH	$J = 5/2 - 3/2$	1043 917.9 <sup>b</sup>	< 0.903	–	80.09	0.0234 <sup>a</sup>	25.7	
FeH	$\Omega = 5/2, J = 5/2 - 7/2$	1316 838.7 <sup>b</sup>	< 0.960	–	297.0	11.3	20.4	

NOTE — <sup>a</sup>Sum of unresolved hyperfine components

<sup>b</sup>No fit performed, literature frequency listed

<sup>†</sup>Spectroscopic data taken from the CDMS catalogue (Müller et al., 2005).

### 2.4.1 Iron Chemistry in CSEs

Due to its refractory nature, a significant fraction of the iron in circumstellar winds is likely incorporated into dust grains (Sofia et al., 1994). After condensing in the inner regions of the envelope, it can be reintroduced into the gas via non-thermal energetic mechanisms like shocks, which drive grain erosion via mechanisms such as sputtering (Tielens et al., 1994; Jones et al., 1996; Schilke et al., 1997; Jones et al., 1994; Caselli et al., 1997; Codella et al., 2010). Nevertheless, Mauron & Huggins (2010) observed absorption from many refractory atomic elements (e.g. Fe, Cr, Ca) in the gas phase toward a background star near IRC+10216, so one cannot safely assume that depletion of Fe onto grains is the sole underlying cause of the non-detection reported here.

Whether sputtered from grains or by some other mechanisms, once in the gas, iron atoms (or  $\text{Fe}^+$ ) can react to form FeH or FeCN. The detection of the latter species in IRC+10216 is significant, since it remains the only iron-bearing molecule definitively identified in interstellar or circumstellar environments to date (Zack et al., 2011) (although Walmsley et al. (2002) have reported a tentative detection of FeO). As an initial guess, it might be assumed that this gas-phase iron chemistry could lead to FeH via one or more of the following reactions:





Cherchneff (2012) included reaction (2.3) (with an estimated activation energy of 30000 K) in her investigation of pulsation-driven shock chemistry in the inner ( $< 5R_*$ ) winds of IRC+10216, as well as the formation of several other diatomic hydrides by this mechanism. Though barriers on the order of  $10^4$  K are prohibitively large in typical interstellar environments, the hot inner regions of CSEs represent one region where such processes may occur with anything other than negligible rates. They found that while this formation route of FeH is more efficient when considering shocks over a pure thermochemical equilibrium model, the derived abundances are still very low (less than the upper limits derived in this work) and fall off exponentially over the dust formation region of this CSE. Interestingly, experiments by Chertihin & Andrews (1995) demonstrated that the photoexcitation of Fe on surfaces could drive reaction (2.3) at low temperatures, and an analogous process might occur on dust grains in the ISM, though not efficiently enough to produce observable quantities of FeH in this source.

Our results likewise suggest that reactions (2.4) - (2.6) are similarly inefficient. For example, gas-phase radiative associations such as reaction (2.4) can be astrochemically important (Herbst, 1976; Vasyunin & Herbst, 2013; Balucani et al., 2015), though as a general rule, emission of a photon is a much slower process than dissociation in the gas, particularly for small molecules like FeH - thereby likely rendering this pathway negligible. Of the above reactions, (2.6) stands out as perhaps the most promising mechanism in the outer envelope, since such ion-neutral reactions are often barrierless, and it is in these regions that photoionization of atomic Fe could be efficient enough to drive this process (Cordiner & Millar, 2009). However, previous

studies suggest that FeH is not a major product of either, yielding instead  $\text{Fe}^+ + \text{H} + \text{H}_2$  or  $\text{FeH}^+ + \text{H}$ , for (2.5) and (2.6), respectively (Harada et al., 2010; Irikura et al., 1990) - conclusions which our results here support.

### 2.4.2 Si and P Hydrides in CSEs

Though larger hydrides are generally regarded as daughter species of smaller molecules like the ones targeted in this work, Mackay (1995) proposed that in the hot cores of star forming regions, SiH could form through  $\text{SiH}_4$  desorbing off dust grains and undergoing hydrogen abstraction reactions.  $\text{SiH}_4$  is known to be abundant in both IRC+10216 and VY CMa (Monnier et al., 2000), so if this process is occurring at a significant rate in either source, we would expect to see cold SiH emission coming from the intermediate CSEs.

Such a formation mechanism for SiH would have to be quite efficient for us to have been able to detect this species in the targeted sources. This is because silicon monohydride reacts readily not only with atoms such as O, N, and C (Wakelam et al., 2015), as well as  $\text{SiH}_4$  itself (Nemoto et al., 1989) - but even with  $\text{H}_2$  (Walch & Dateo, 2001). In their theoretical investigation of the  $\text{SiH} + \text{H}_2$  reaction, Walch & Dateo (2001) found that it occurs with a temperature-dependent 2<sup>nd</sup> order rate coefficient given by  $k(T) = 4.45 \times 10^{-11} e^{-3774/T} \text{ cm}^3 \text{ s}^{-1}$ . Using the temperature profiles derived by (Fonfría et al., 2008), we obtain rate coefficients of  $k(900K) = 7 \times 10^{-13} \text{ cm}^3 \text{ s}^{-1}$  and  $k(475K) = 2 \times 10^{-14} \text{ cm}^3 \text{ s}^{-1}$  for distances of 5 and 15  $R_*$ , respectively. Though these rate coefficients are fairly low, given the large abundance of  $\text{H}_2$ , the overall reaction would be quite efficient. This fact is illustrated by expressing the 2<sup>nd</sup> order rate coefficient in pseudo-1<sup>st</sup> order form, assuming an  $\text{H}_2$  abundance of  $n = 10^7 \text{ cm}^{-3}$ , as  $k'(T) = 4.45 \times 10^{-4} e^{-3774/T} \text{ s}^{-1}$ , which results in values of  $k'(900K) = 7 \times 10^{-6} \text{ s}^{-1}$  and  $k'(475K) = 2 \times 10^{-7} \text{ s}^{-1}$ , again, for distances of 5 and 15  $R_*$ , respectively.

Thus, the gas-phase abundance of SiH in this region of the CSE of both IRC+10216 and VY CMa should be quite low, unless there exists some more efficient method of forming it, which is not what our results suggest.

As for the production of phosphorous hydrides in CSEs, Agúndez et al. (2014) found that  $\text{PH}_3$  accounts for about 2% of the phosphorous content in IRC+10216, making it the second-most abundant gas-phase P-bearing molecule in the envelope (behind HCP). Interestingly, they noted that this species might be formed efficiently on the dust grains that are so characteristic of CSEs. If that is the case then one of the logical precursors of  $\text{PH}_3$  would be PH. Of course, given the fairly large upper limits we have derived from our observational data, all we can say with confidence is that gas-phase PH does not appear to be a major reservoir of phosphorus in the sources targeted in this study.

Nevertheless, if H-addition on grains is indeed an efficient process in the inner regions of CSEs (ca.  $5 < R_* < 20$ ), then our findings are still consistent with there being an possible underlying chemical connection between the non-detection of PH described here, and the previous detection of  $\text{PH}_3$  via the grain surface process



Though PH was not targeted in this work towards VY CMa, the same possible connection might likewise be relevant, though the higher O abundance than in IRC+10216 would make that source an even less hospitable environment for PH, given the efficiency of the reaction



which has been estimated to proceed at approximately the collisional rate (Wakelam

et al., 2015).

Further comparisons with previous findings show that the upper limit abundances derived in this work are larger than the predicted abundances of Agúndez et al. (2020) by one and two orders of magnitude for SiH and PH, respectively. Therefore, we cannot confidently conclude that our non-detections are indicative of these species exhibiting non-equilibrium chemistry in IRC+10216. This observed agreement with inner wind models is interesting given that previous works have shown heavier Si- and P-bearing hydrides, namely silane ( $\text{SiH}_4$ ) and phosphine ( $\text{PH}_3$ ), are observed in stark *overabundance* ( $> 6$  dex) relative to predictions of thermochemical equilibrium (Keady & Ridgway, 1993; Agúndez et al., 2014, 2020). So while our results do not necessarily imply a preferred chemical pathway for the production of SiH and PH in CSEs, they are consistent with the notion that subsequent hydrogenation of such species occurs much more efficiently than a pure gas-phase equilibrium chemistry predicts.

## 2.5 Conclusions

We conducted a search for rotational transitions of SiH, PH, and FeH toward the CSEs of IRC+10216 and VY CMa using the GREAT spectrometer aboard the SOFIA observatory. We detected many high- $J$  transitions from a variety of molecules that have previously been studied in these sources; however, we saw no emission from any of our target species. We derive upper limit column densities and abundances for the targeted molecules in each source using the limiting sensitivities of our measurements along with known physical conditions of both envelopes. Though observational factors like beam dilution undoubtedly play a role in these non-detections, our upper limits reflect the inefficiency of predicted formation routes, and tendency for these hydrides to either be incorporated into dust grains or react with other gas-phase species

abundant in these environments. Our findings also underscore the dichotomy between the observed abundances of diatomic hydrides relative to their heavier counterparts in CSEs, particularly in the cases of SiH and PH.

The presence and build-up mechanisms of hydrides in the inner regions of circumstellar material remain largely unconstrained by the present body of observational work. In order to better understand this process, there is a need for both high-sensitivity FIR measurements targeting new light hydrides like those in this work, in addition to high angular resolution sub-mm interferometric studies of known hydrides in CSEs like  $\text{PH}_3$ ,  $\text{H}_2\text{O}$ , and  $\text{NH}_3$ .

## CHAPTER 3

# Photochemistry in the Inner Layers of IRC+10216

Photochemistry is one of the key processes affecting molecular carbon as it is released into the ISM by AGB stars, but recent observations have shown peculiar departures from predictions of photochemical models in the inner regions of these objects. The text in Chapter 3, which appeared in the *Astrophysical Journal* (Siebert et al., 2022a) as “Investigating Anomalous Photochemistry in the Inner Wind of IRC+10216 Through Interferometric Observations of HC<sub>3</sub>N.”, explores this behavior using archival ALMA observations of cyanoacetylene toward the prototypical carbon star CW Leo, and proposes a novel explanation for its high abundance.

## 3.1 Introduction

IRC+10216, also known as CW Leo, is a well-studied nearby ( $d \sim 130$  pc, Men’shchikov et al., 2001) Asymptotic Giant Branch (AGB) star with a chemically rich expanding circumstellar envelope (CSE). The CSE is the result of dust-driven mass loss at a rate of  $\sim 2 \times 10^{-5} M_{\odot} \text{ yr}^{-1}$  (De Beck et al., 2012), and represents one of the final stages

of evolution for 1–8  $M_{\odot}$  stars immediately preceding the transition between the AGB and the formation of a planetary nebula (PN). During this stage, depending on how much carbon has been convectively dredged up from the star’s core relative to oxygen (Weiss & Ferguson, 2009), AGB stars can either be M-type ( $C/O < 1$ ), C-type ( $C/O > 1$ ), or S-type ( $C/O \sim 1$ ). IRC+10216 has a C/O ratio of 1.4 (Winters et al., 1994), which allows for a complex system of carbonaceous gas phase and dust grain chemistry to occur throughout its extended envelope. To date, more than 95 unique molecules have been identified toward IRC+10216 (McGuire, 2022). Due to its close proximity and history as a molecular line object, IRC+10216 forms the basis of our understanding on how carbon-rich stellar material is processed and returned to the interstellar medium by low-to-intermediate mass stars.

An important aspect of AGB evolution that has become clear with the advent of ALMA is the prevalence of binary companion stars influencing mass loss and shaping circumstellar winds (Decin, 2021). Companions are difficult to detect directly in these systems, due to the intrinsic luminosity of the AGB star, and the high attenuation of visible light by their dusty envelopes. However, several recent studies of gas and dust kinematics have shown the perturbative effects binary companions can have on many AGB and proto-planetary nebula (PPNe) systems. Both small-scale asymmetries, such as density-enhanced clumps (e.g. Khouri et al., 2016; Agúndez et al., 2017; Leão et al., 2006), and large-scale structures, such as spirals (e.g. Mauron & Huggins, 2006; Maercker et al., 2016; Decin et al., 2015; Ramstedt et al., 2017), disk geometries (e.g. Kervella et al., 2014; Homan et al., 2018; Sahai et al., 2022; Homan et al., 2020), and bipolar outflows (e.g. Kim et al., 2015b; Sahai et al., 2017; Lagadec et al., 2011) have been detected. In particular, the ALMA Large Program ATOMIUM (2018.1.000659.L, PI: Decin) has shown the widespread nature of these structures through a survey of numerous AGB outflows (Decin et al., 2020). It is now

thought that influence from stellar and planetary companions is closely related to the stark morphological changes in circumstellar material during the transition between the AGB and PN stages of evolution (Sahai et al., 2007). IRC+10216 shows signs of binary influence, based on the interspaced shells in its extended envelope (Cernicharo et al., 2015; Guélin et al., 2018), spiral structure in its inner layers (Decin et al., 2015), as well as the detection of a tentative compact source  $0.5''$  from the star via archival HST monitoring by Kim et al. (2015a, 2021).

While their physical effects have been studied in detail, the chemical impact of companion stars embedded in CSEs and PPNe has not yet been observationally tested. The typical framework for how gas phase chemistry proceeds in circumstellar envelopes assumes precursor molecules (e.g. CO, HCN, SiO) form out of a combination of equilibrium and shock-induced chemistry in the high temperature regions near the stellar photosphere (Agúndez et al., 2020; Cherchneff, 2012). Once they reach the outer regions of the envelope where the density of attenuating dust grains is lower, UV photons from the interstellar radiation field (ISRF) initiate a kinetically-driven photochemistry to form a variety of exotic product molecules (e.g. HC<sub>7</sub>N, SiN, MgNC) (Ziurys, 2006; Li et al., 2016; Millar, 2020). While this scheme is consistent with the measured abundances of many molecules, recent studies of IRC+10216 have revealed that this picture may be much more complicated than previously thought. Agúndez et al. (2015) and Quintana-Lacaci et al. (2017) discovered that CH<sub>3</sub>CN and NaCN are present in the inner envelope ( $< 5''$ ). This was an unexpected result as the proposed formation routes of both these molecules require photochemistry, which typically takes hold further out ( $10''$ – $25''$ ) in the CSE (Dinh-V-Trung & Lim, 2008). Similar results were also found for the product molecules water (H<sub>2</sub>O) and diacetylene (C<sub>4</sub>H<sub>2</sub>) (Agúndez et al., 2010; Fonfría et al., 2018)

One molecule that is central to photochemistry in CSE environments is cyanoacety-

lene ( $\text{HC}_3\text{N}$ ). In the gas phase, this species is formed primarily through the reaction between acetylene ( $\text{C}_2\text{H}_2$ ) and the cyanide radical ( $\text{CN}$ ), the latter of which is only available as a reactant when the flux of UV photons is large enough to efficiently dissociate the precursor molecule  $\text{HCN}$  (Agúndez et al., 2017). Because  $\text{C}_2\text{H}_2$  is an abundant precursor molecule and one of the main carriers of carbon in C-rich CSEs (Santoro et al., 2020),  $\text{HC}_3\text{N}$  is one of the first product molecules to form out of UV-driven chemistry, making it useful in probing the photoprocessing of gas phase material in these objects.

$\text{HC}_3\text{N}$  and longer cyanopolyynes in the envelope of IRC+10216 were studied with the VLA by Dinh-V-Trung & Lim (2008) and subsequently with ALMA by Agúndez et al. (2017), where it was seen between  $10''$ – $20''$  (1300–2600 AU). This is where the  $\text{HC}_3\text{N}$  abundance is expected to peak based on photochemical models of this CSE; however, these observations targeted low-lying rotational transitions (including states up to  $J = 12$  and  $E_{\text{up}} = 34$  K) which naturally trace lower temperature regions. In order to gain a more complete view of this molecule in the envelope of IRC+10216, and to better understand the onset of photochemistry in these environments, it is important to spatially constrain higher energy transitions of  $\text{HC}_3\text{N}$  that could be discernable in the warmer regions where  $\text{CH}_3\text{CN}$  and  $\text{NaCN}$  were observed.

To this end, we present an archival study of IRC+10216 with the goal of characterizing  $\text{HC}_3\text{N}$  in the inner (arcsecond scale) layers of its envelope. We utilize observations from three separate ALMA projects to analyze the spectra and spatial distributions of the  $J = 28 - 27$ ,  $J = 30 - 29$ , and  $J = 38 - 37$  lines of  $\text{HC}_3\text{N}$  toward IRC+10216. Using maps of these lines at the systemic velocity combined with radiative transfer models, we quantify the abundance of cyanoacetylene in the inner regions of IRC+10216 and discuss how they affect our understanding of photochemical processing in this CSE. In Section 3.2 we describe the observations and reduction

procedure, in Section 3.3.2 we present emission maps, in Section 3.3.3 we use non-LTE radiative transfer models to derive the abundance profile of  $\text{HC}_3\text{N}$ , and in Section 3.4 we utilize a specialized photochemistry model to compare our observations with kinetic theory and test the hypothesis that molecules surrounding IRC+10216 are affected by a binary stellar companion embedded in the inner envelope.

## 3.2 Observations and reduction

We utilize observations from three publicly available archival ALMA projects to map warm  $\text{HC}_3\text{N}$  emission toward IRC+10216. Fig. 3.1 demonstrates the different antenna configurations and coverage of the  $uv$ -plane for the data sets, while Table 3.1 summarizes these different observations and the target  $\text{HC}_3\text{N}$  transitions for this work. Project 2019.1.00507.S provides several spectral scans of IRC+10216 at Band 6 between 250 and 270 GHz using both the main 12m array and the 7m Atacama Compact Array (ACA). These observations were used by He et al. (2019) to study the time-variability of millimeter lines toward IRC+10216, and cover the  $J = 28 - 27$  transition of  $\text{HC}_3\text{N}$ . In order to recover flux from as many spatial scales as possible, we combined visibility measurements from four separate array configurations included in this project, including two 12m executions with baseline lengths ranging from 15 m to 1230 m and two ACA measurements covering baselines between 9 and 50 m (see Fig. 3.1). Data combination was performed with antenna-specific weighting, and the resulting images have a maximum recoverable scale of  $30''$ . Project 2011.0.00229.S provides a Cycle 0 spectral line survey of IRC+10216 covering most of Band 6 using the 12m array, allowing emission from the  $J = 30 - 29$  transition to be mapped as well; however, only 18 antennas were available at this time, as opposed to the 42 that were used for the later data sets. These data cover baselines ranging from 27 m to 402 m with a maximum recoverable scale of  $\sim 1''$ .

Table 3.1: Summary and characteristics of the ALMA data utilized in this work.

ALMA Project Code	Obs. Date(s)	Array(s)	Synthesized beam ( $\theta_{\text{maj}} \times \theta_{\text{min}}$ )	HC <sub>3</sub> N line ( $J' \rightarrow J''$ )	Rest Frequency (MHz)	$E_{\text{up}}$ (K)	Image RMS (mJy/beam)
2019.1.00507.S	Nov. 2019 – Mar. 2020	12m+7m	0.480" $\times$ 0.449"	28 $\rightarrow$ 27	254 699.5	177	1.8
2011.0.00229.S	Apr. 2012	12m	0.725" $\times$ 0.520"	30 $\rightarrow$ 29	272 884.7	203	7.2
2016.1.00251.S	May 2018	12m	0.848" $\times$ 0.761"	38 $\rightarrow$ 37	345 609.0	324	1.9

NOTE — Observations from ALMA Project 2019.1.00507.S include two 12m configurations and two from the 7m ACA. Transition frequencies and upper state energies were obtained from Cologne Database of Molecular Spectroscopy (CDMS) (Müller et al., 2005). Reported RMS values were measured from an emission-free channel of the final reconstructed image cube.

Project 2016.1.00251.S provides a Band 7 observation between 330 and 346 GHz using the 12m array. This ALMA configuration includes baselines between 15 m and 314 m, and offers a maximum recoverable scale of  $8''$ . These data were used to map the  $J = 38 - 37$  line of  $\text{HC}_3\text{N}$  in addition to the  $J = 3 - 2$  line of  $^{13}\text{CO}$  at  $\nu_{\text{rest}} = 330\,588.0$  MHz. The  $^{13}\text{CO}$  observations are useful in qualitatively characterizing the overall envelope density structure.

As Figure 3.1 demonstrates, the ALMA Projects we utilize have very different antenna setups, and consequently disparate spatial frequencies sampled. Due to these differences between instrument configurations and the non-uniqueness of the image reconstruction process, care must be taken when directly comparing brightness distributions between data sets. All observations were pointed near the continuum peak of IRC+10216 at  $\alpha_{\text{J2000}} = 09^{\text{h}}47^{\text{m}}57.458^{\text{s}}$ ,  $\delta_{\text{J2000}} = +13^{\circ}16'43.90''$ , despite having slightly different phase centers between projects. Errors in pointing are estimated to be 30 mas for the  $J = 28 - 27$  observations, and 40 mas for the  $J = 30 - 29$  and  $J = 38 - 37$  observations<sup>1</sup>.

All data were calibrated using the standard calibration pipeline of the Common Astronomy Software Application (CASA) (McMullin et al., 2007). Visibilities from the Band 6 data sets were resampled to a spectral resolution of  $1.7 \text{ km s}^{-1}$  to match the correlator configuration in the Band 7 project. Continuum subtraction was done in visibility space using line free channels present in each spectral window containing  $\text{HC}_3\text{N}$ . Then, imaging was performed with the TCLEAN casatask, using Briggs weighting with a 0.5 robust parameter for the  $J = 28 - 27$  and  $J = 38 - 37$  lines, and natural weighting for the  $J = 30 - 29$  line due to its lower signal-to-noise. Iterative masking was done with user-defined regions to optimize the deconvolution process. In the case of the  $J = 28 - 27$  line, multi-scale cleaning was applied

---

<sup>1</sup>Referencing Section 10.5.2 of the ALMA Technical Handbook (Cortes et al., 2020)

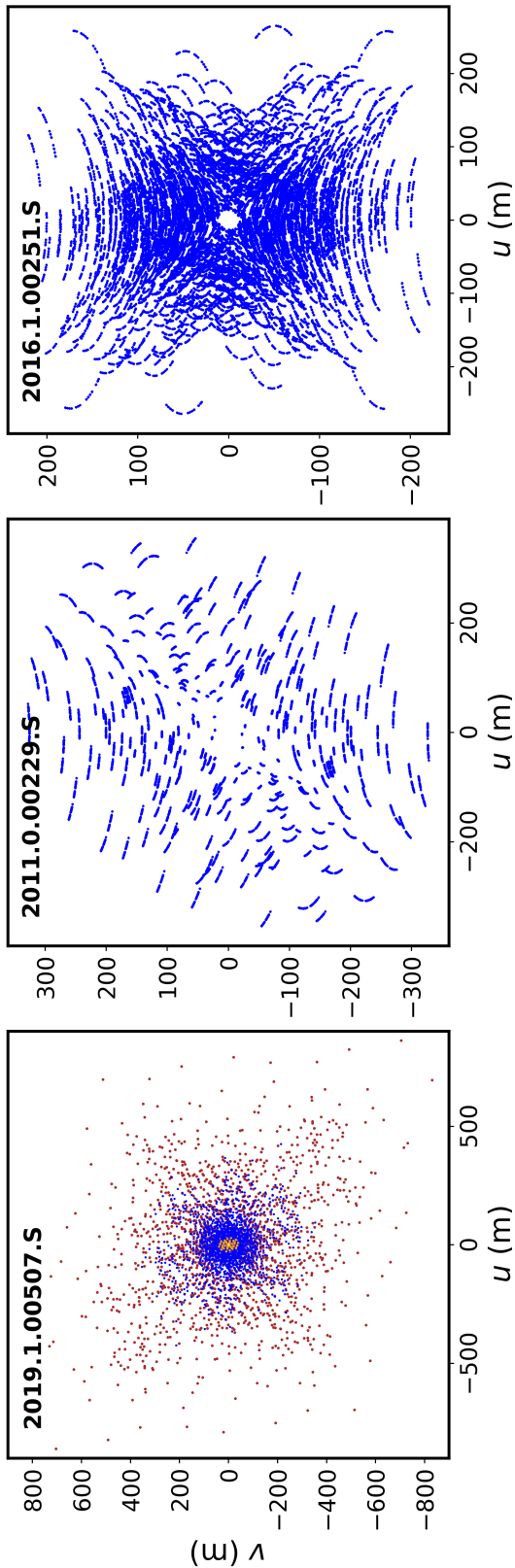


Figure 3.1: Coverage of the  $uv$ -plane offered by the three ALMA projects utilized in this work. Baselines from compact 12m configurations are shown in blue, those from extended 12m configurations are shown in brown, and 7m ACA baselines are shown in orange. Observations from left to right were used to image the  $J = 28 - 27$ ,  $J = 30 - 29$ , and  $J = 38 - 37$  transitions of  $\text{HC}_3\text{N}$ , respectively.

to account for the multiple combined array configurations (Cornwell, 2008). All rest frequencies were obtained from Cologne Database of Molecular Spectroscopy (CDMS) (Müller et al., 2005), and shifted to the systemic velocity of IRC+10216,  $V_{sys} = -26.5 \text{ km s}^{-1}$  (Cernicharo et al., 2000).

## 3.3 Results

### 3.3.1 Spectra, interloping lines, and flux recovery

Integrated spectra from each synthesized image cube were obtained using a  $30''$  circular aperture centered on IRC+10216. These spectra are shown in Figures 3.2a-c. In these, we see emission in the characteristic “double-horned” line profile centered on the systemic velocity of  $-26.5 \text{ km s}^{-1}$ , as well as some contributions from interloping lines. For the  $J = 28 - 27$  line of  $\text{HC}_3\text{N}$ , a very close blend is seen with the  $J(K_a, K_c) = 4(0, 4) - 3(0, 3)$  transition of methanimine ( $\text{CH}_2\text{NH}$ ) at  $\nu_{\text{rest}} = 254\,685.1 \text{ MHz}$ . This line appears  $14 \text{ MHz}$  ( $17 \text{ km s}^{-1}$ ) from the central frequency of  $\text{HC}_3\text{N}$ . In the spectrum (Fig. 3.2a.), a double horn profile of  $\text{CH}_2\text{NH}$  can be seen with the blue-shifted peak falling very close to the central channel of  $\text{HC}_3\text{N}$ . This blend was also detected by Tenenbaum et al. (2010). Since the aim of this study is to characterize the radial abundance using channel maps made at the systemic velocity, we must take care to make sure we do not attribute blue-shifted  $\text{CH}_2\text{NH}$  emission to  $\text{HC}_3\text{N}$ . However, considering the geometry of spherical outflows and empirical evidence from previous ALMA studies of AGB stars (e.g. channel maps in Decin et al. (2018) and Brunner et al. (2018)), we expect that the contamination from the highest velocity emission is limited only to the smallest spatial scales and appears very close to the position of IRC+10216.

In the case of the  $J = 38 - 37$  line of  $\text{HC}_3\text{N}$  (Fig. 3.2c.), there is a slight blend with

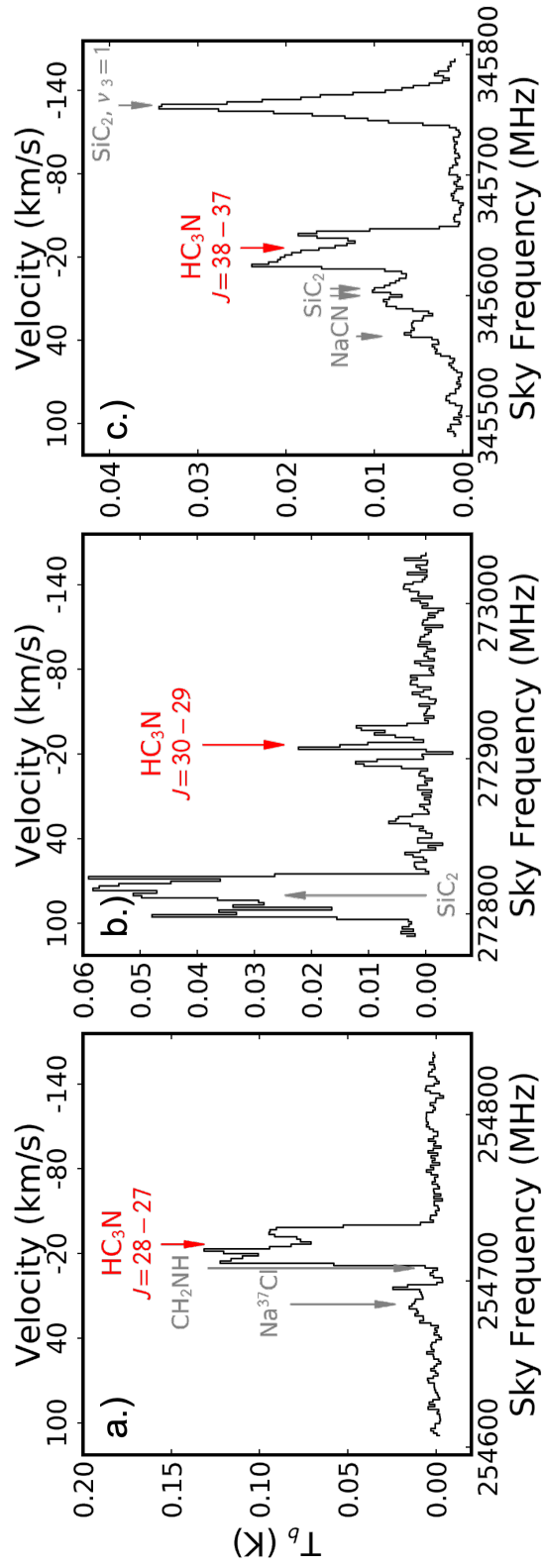


Figure 3.2: Spectra demonstrating the three  $\text{HC}_3\text{N}$  lines studied in this work (red), in addition to nearby and interloping molecular lines (gray). Spectra were created from image cubes using a  $30''$  aperture centered on the position of IRC+10216. The lower x-axes denote sky frequencies, while the upper axis shows velocity using the rest frequency of the respective  $\text{HC}_3\text{N}$  transition. All transitions are from the ground vibrational state unless indicated otherwise.

the  $J(K_a, K_c) = 15(14, 1) - 15(14, 0)$  transition of  $\text{SiC}_2$  at  $\nu_{\text{rest}} = 345\,575.2$  MHz. This lies 34 MHz ( $29 \text{ km s}^{-1}$ ) away from the central frequency of our target  $\text{HC}_3\text{N}$  line, so with a half line width of  $14.5 \text{ km s}^{-1}$ , only the most red-shifted channels of the image cube are contaminated by emission from  $\text{SiC}_2$ .

The  $J = 28 - 27$  and  $J = 30 - 29$  lines of  $\text{HC}_3\text{N}$  were also observed in the single dish line surveys of He et al. (2008) and Tenenbaum et al. (2010), both using the Arizona Radio Observatory 10 m Submillimeter Telescope (SMT). These works provide useful data points that allow us to characterize the amount of spatial filtering in our interferometric measurements of the same lines. Both He et al. (2008) and Tenenbaum et al. (2010) detected the  $J = 28 - 27$  line of  $\text{HC}_3\text{N}$  with a peak brightness temperature  $T_R = 130$  mK. Considering that the SMT has a HPBW of  $30''$  at 254.7 GHz, we can compare this directly with the spectrum in Fig. 3.2a., which peaks at 120 mK. In contrast, the  $J = 30 - 29$  line shown in Fig. 3.2b. was detected in Tenenbaum et al. (2010) with a peak temperature of  $T_R = 90$  mK, while we instead obtain a value of 10 mK. It is clear that the observations from Project 2019.1.00507.S, which comprise both ACA and multiple 12m executions spanning a large range of baselines, are able to recover more than 90% of the  $\text{HC}_3\text{N}$  ( $J = 28 - 27$ ) emission. However the Cycle 0 observations of the  $J = 30 - 29$  line exhibit a large amount of spatial filtering due to the fewer number of antennas and poorer  $uv$ -coverage. Unfortunately, there exist no published single-dish measurements for the  $J = 38 - 37$  transition of  $\text{HC}_3\text{N}$  toward IRC+10216, but we still take steps to account for the flux loss of these measurements described in Section 3.3.3.

### 3.3.2 Emission Maps

Reconstructed maps of the three studied  $\text{HC}_3\text{N}$  lines are shown in Figure 3.3. All images were made at the systemic velocity of IRC+10216 ( $V_{\text{sys}} = -26.5 \text{ km s}^{-1}$ ).

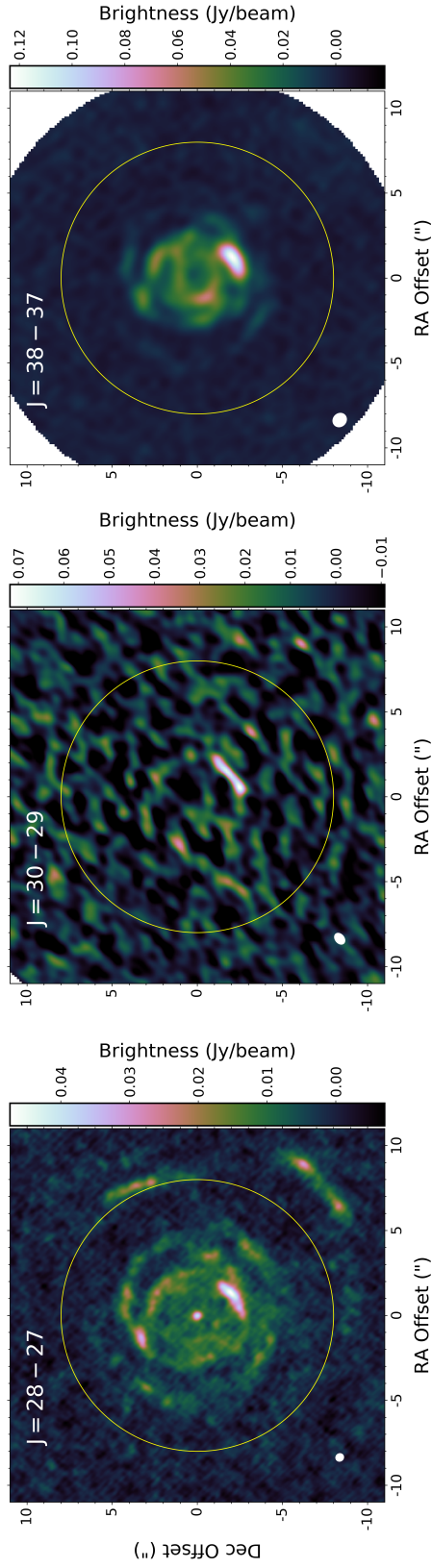


Figure 3.3: ALMA emission maps of three  $\text{HC}_3\text{N}$  lines toward IRC+10216. Images were created at the systemic velocity of  $-26.5 \text{ km s}^{-1}$  with a channel width of  $1.69 \text{ km s}^{-1}$ . IRC+10216 is located at the center of the maps at  $\alpha_{J2000} = 09^{\text{h}}47^{\text{m}}57.458^{\text{s}}$ ,  $\delta_{J2000} = +13^{\circ}16'43.90''$ , and a reference circle with diameter  $15''$  is shown in yellow. Because data from separate observation sets are used, the beam sizes and absolute brightness scales are different for each panel. The shapes of the synthesized beams are shown in the bottom left corner, with sizes  $0.48'' \times 0.45''$ ,  $0.73'' \times 0.52''$ , and  $0.85'' \times 0.76''$  from left to right.

These maps show morphologies centered on the position of the AGB star with emission primarily within a radius of  $5''$ . The distribution of the  $J = 28 - 27$  line includes an extended component out to  $3''$  surrounded by several asymmetric arcs and clumps (Fig. 3.3a.). Due to the higher temperatures probed by this transition, the majority of its emission traces regions entirely separated from that observed in the lower excitation lines mapped by Agúndez et al. (2017) and Dinh-V-Trung & Lim (2008) ( $J = 10 - 9$  and  $J = 5 - 4$ ; which peak at radius  $14''$ ), with the notable exception of a region to the SW at a radius of  $10''$ . In the central component (within  $3''$ ), the average brightness of the  $J = 28 - 27$  line is  $10 \text{ mJy beam}^{-1}$ , with notable bright clumps to the N and SW. Although a central point source is seen at the position of the carbon star, we expect that this is contributed from the most blue-shifted channel of the weak interloping line of  $\text{CH}_2\text{NH}$  (see Section 3.3.1 and Fig. 3.2), since this peak is notably absent from the unblended image in Fig. 3.3c.

The  $J = 38 - 37$  line (Fig. 3.3c.) also shows bright, spatially resolved emission that is entirely distinct from the maps of  $\text{HC}_3\text{N}$  in Agúndez et al. (2017). In contrast to  $J = 28 - 27$ , the distribution of this line is entirely concentrated within a radius of  $4''$  and shows no central peak on the position of IRC+10216, since there is no contaminating emission present in this channel. The imaged line is again not azimuthally symmetric, and traces the same bright clumps and arcs seen in the  $J = 28 - 27$  line. It reaches a peak brightness of  $122 \pm 1.9 \text{ mJy beam}^{-1}$  in the SW clump at  $2''$ . The more compact morphology can be qualitatively explained by the higher upper state energy (323 K) and larger (by a factor of 3) Einstein  $A_{ij}$  coefficient of this transition relative to the  $J = 28 - 27$  line.

Finally, the Fig. 3.3b. shows the  $J = 30 - 29$  line, which also appears toward the same bright clump  $\sim 2''$  to the SW. However due to the sensitivity of these data, very little additional emission is seen from this transition. If this line has a similar

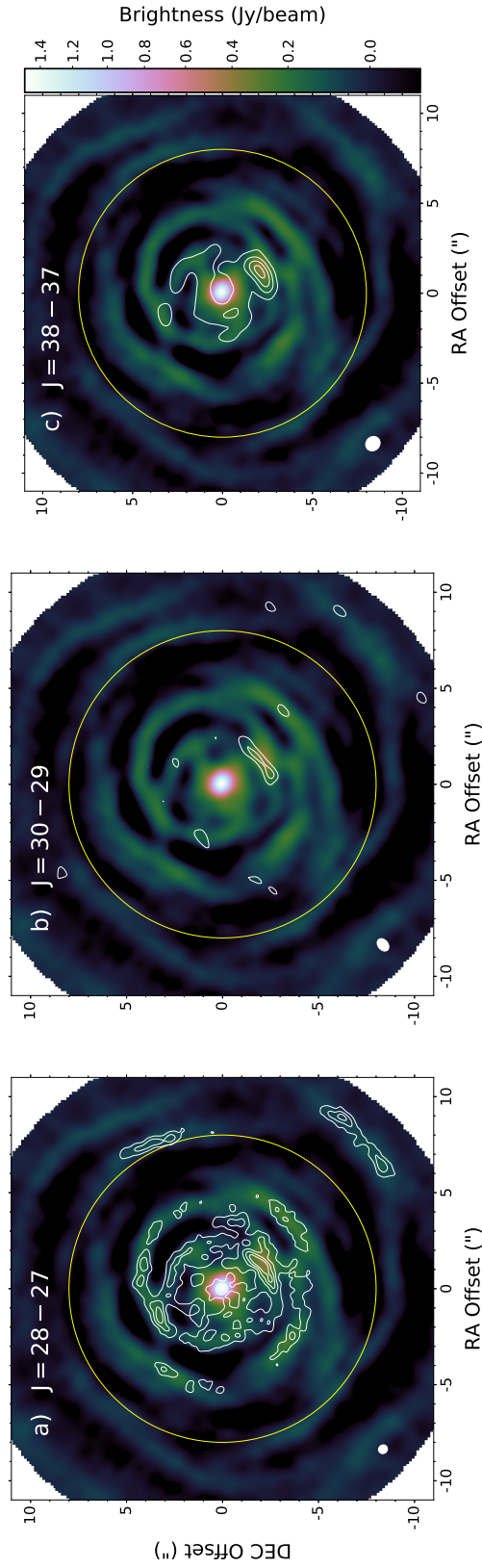


Figure 3.4: Contour maps of  $\text{HC}_3\text{N}$   $J = 28 - 27$ ,  $J = 30 - 29$ , and  $J = 38 - 37$  (white) overlaid on the image of  $^{13}\text{CO}$   $J = 3 - 2$  toward IRC+10216. All components are again taken at the systemic velocity and centered at the position of IRC+10216  $\alpha_{J2000} = 09^{\text{h}}47^{\text{m}}57.458^{\text{s}}$ ,  $\delta_{J2000} = +13^{\circ}16'43.90''$ , and the yellow circle denotes a radius of  $7.5''$ . Contour levels for each line are shown at 3, 6, 9, and 12 times the rms.

extended component as seen in  $J = 28 - 27$ , we would expect most of this flux to be resolved out by the interferometer given its maximum recoverable scale. However, if the  $J = 30 - 29$  line had a compact, point-like, component at the position of IRC+10216 with a similar peak brightness to the SW clump (as is the case with  $J = 28 - 27$ ), we would expect to detect that even at the limited sensitivity of these data. Due to the similar excitation conditions of the  $J = 30 - 29$  and  $J = 28 - 27$  lines, we take this as further evidence of the central peak in Fig. 3.3a) being contributed by  $\text{CH}_2\text{NH}$ , and not  $\text{HC}_3\text{N}$ . Nevertheless, because of the observational limitations of this ALMA project (2011.0.00229.S), we do not include this line in our radiative transfer analysis.

Figure 3.4 shows the observed  $\text{HC}_3\text{N}$  lines as contours overlaid on the image of  $^{13}\text{CO } J = 3 - 2$  at  $\nu_{\text{rest}} = 330\,587.97\text{ MHz}$  created from the Band 7 ALMA observations. Using a CO abundance of  $6 \times 10^{-4}$  (De Beck et al., 2012; Agúndez et al., 2012) and a  $^{12}\text{C}/^{13}\text{C}$  ratio of 48 (Knapp & Chang, 1985), we adopt a constant  $^{13}\text{CO}$  abundance of  $1.3 \times 10^{-5}$  with respect to  $\text{H}_2$  throughout the regions of IRC+10216 we are investigating. Therefore, it is a useful indicator of the density structure. Keeping in mind the spatial filtering effects due to the lack of very short antenna spacings in these data, we see that the structures traced by  $\text{HC}_3\text{N}$  are spatially coincident with density enhancements resulting from non-isotropic mass-loss. The clump SW of IRC+10216 which is seen in all three observed  $\text{HC}_3\text{N}$  lines is also apparent here as the brightest area of  $^{13}\text{CO}$  emission away from the central point source (see Fig. 3.4). Between the bright arcs we see several areas of negative flux, which are image artifacts resulting from resolved out emission and not indicative of actual absorption. When compared with images in Agúndez et al. (2015), we find that both  $\text{HC}_3\text{N}$  and  $^{13}\text{CO}$  trace similar compact structures to  $\text{CH}_3\text{CN } (J_K = 14_3 - 13_3)$ , including the SW clump.

### 3.3.3 Radiative Transfer Modeling

In order to draw conclusions regarding the abundance of  $\text{HC}_3\text{N}$ , we must first consider the excitation physics of this molecule in the inner envelope of IRC+10216. In many cases, Local Thermodynamic Equilibrium (LTE) is a good approximation for chemical studies of CSEs due to their high central densities. However, the rotational transitions observed here have comparatively large Einstein  $A_{ij}$  coefficients ( $10^{-2.9} - 10^{-2.5} \text{ s}^{-1}$ ), so it is possible that they are sub-thermally excited even at arcsecond scales. In Figure 3.5, we show the predicted excitation temperatures of the three  $\text{HC}_3\text{N}$  transitions as a function of gas density for two different kinetic temperatures, generated using the RADEX radiative transfer software (van der Tak et al., 2007). Using the 1D density law from (Eq. 3.1 in Agúndez et al. 2012) along with a mass-loss rate of  $2.7 \times 10^{-5} M_{\odot} \text{ yr}^{-1}$  (Guélin et al., 2018), we also show the expected average gas densities at the radii where most of the emission is seen (between  $1''$  and  $5''$ ). From this, it is clear that LTE could only be assumed if densities were higher than  $10^8 \text{ cm}^{-3}$ , and the observed gas density is below the critical densities of all three  $\text{HC}_3\text{N}$  transitions in the mapped regions. Furthermore, pumping to vibrational states via thermal infrared (IR) photons from dust grains has been shown to be an important excitation mechanism in the envelope of IRC+10216 (Deguchi & Uyemura, 1984; Cernicharo et al., 2014; Agúndez et al., 2017; Keady & Ridgway, 1993; Fonfría et al., 2008), so non-LTE calculations are necessary to take all of these factors into account.

Therefore, we adopt a forward modeling approach in predicting the expected brightness distributions and determining the abundance of  $\text{HC}_3\text{N}$  needed to reproduce the maps in Fig. 3.3. We utilize the LIne Modeling Engine (LIME) to simulate the level populations of  $\text{HC}_3\text{N}$ , solve the radiative transfer equation, and produce

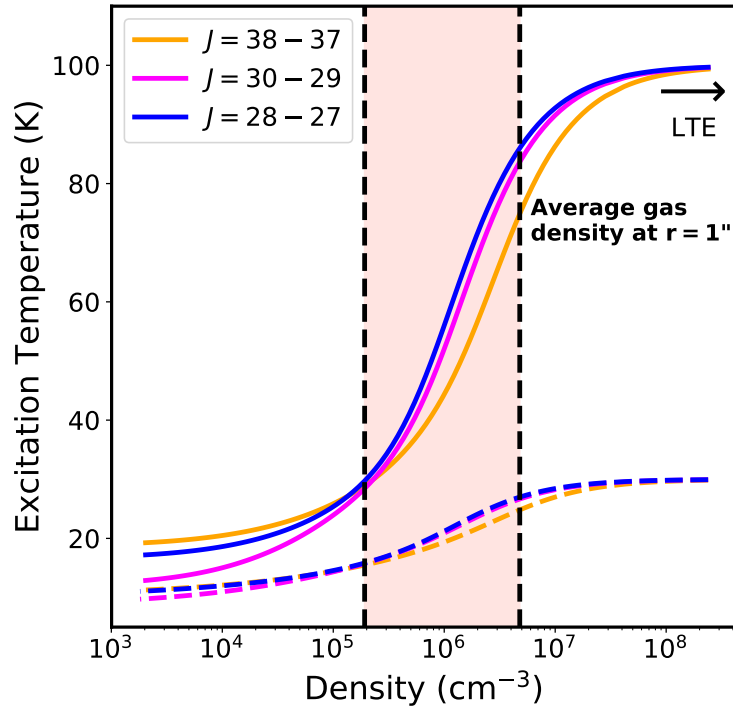


Figure 3.5: RADEX models of the three observed transitions of  $\text{HC}_3\text{N}$  run with a range of densities at  $T_k = 30$  K (dashed lines) and  $T_k = 100$  K (solid lines). The shaded region denotes the average gas densities at radii where we observe these lines toward IRC+10216 (between  $1''$  and  $5''$ ).

synthetic image cubes (Brinch & Hogerheijde, 2010). LIME uses density-weighted grid points distributed in a computational space using Delaunay triangulation. Populations are solved based on the local conditions of the corresponding Voronoi cells, as well as the incident radiation from adjacent cells. For all our calculations, we use 50 000 grid points in a computational volume with radius 130 000 AU ( $1000''$ ). Though LIME performs these calculations in 3D space, we use a 1D approximation for the physical structure of IRC+10216, since the 3D asymmetries apparent in Figures 3.3 and 3.4 are not presently constrained in their local physical conditions and require hydrodynamical simulations that are outside the scope of this work. In general, we

adopt the same model for the CSE of IRC+10216 as Agúndez et al. (2012). This includes the stellar parameters, velocity structure, gas and dust temperature profiles, and density gradient. The only difference in our physical model is the use of a slightly larger mass-loss rate of  $2.7 \times 10^{-5} M_{\odot} \text{ yr}^{-1}$ , as this value was measured by Guélin et al. (2018) specifically using CO emission at radii within  $15''$ , meaning it is better suited for this study of warm  $\text{HC}_3\text{N}$  emission. The gas density in the extended envelope is given by

$$n(r) = \frac{\dot{M}}{4\pi r^2 v_{\infty} m_g} \quad (3.1)$$

where  $\dot{M}$  is the mass-loss rate,  $r$  is the radius,  $v_{\infty}$  is the expansion velocity, and  $m_g$  is the average gas particle mass taken as 2.3 amu considering  $\text{H}_2$ , He, and CO (Agúndez et al., 2012). So a change in  $\dot{M}$  has a significant effect on molecular volume densities and corresponding line intensities. This should be kept in mind when comparing our results with previous chemical studies of IRC+10216 that use the more typical value of  $2.0 \times 10^{-5} M_{\odot} \text{ yr}^{-1}$  (Agúndez et al., 2017; Agúndez et al., 2015; Quintana-Lacaci et al., 2017).

For spectroscopic data, the Leiden Atomic and Molecular Database (LAMDA) provides collisional rates of  $^{13}\text{CO}$  and  $\text{HC}_3\text{N}$  with ortho- and para-  $\text{H}_2$  (van der Tak et al., 2020). The ortho/para  $\text{H}_2$  ratio is assumed to be 3 at all locations in the envelope. For  $\text{HC}_3\text{N}$ , the collisional rates measured by Faure et al. (2016) only go up to the  $J = 37$  rotational state, so we extrapolated these to the  $J = 45$  level and use line strengths from CDMS for the added radiative transitions (Müller et al., 2005). The  $J = 45$  level was chosen to account for population in rotational states above  $J = 38$  while keeping the computational load low. We note that the choice of this maximum level had little effect on the predictions, as we found that running the model with maximum  $J = 40$  and  $J = 50$  yielded nearly identical results.

In addition, we included the first excited states of the  $\nu_5$  and  $\nu_6$  vibrational modes at  $663\text{ cm}^{-1}$  and  $499\text{ cm}^{-1}$  (Jolly et al., 2007) using radiative rates from the HITRAN database (Gordon et al., 2022). The effect of including these states is similar to the result of Massalkhi et al. (2019), where emission is shifted to larger radii as cooler molecules could be pumped to higher  $J$  values by first being radiatively excited into these vibrational states then subsequently de-exciting through the P-branch ( $\Delta J = +1$ ) (Costagliola & Aalto, 2010). Collisional transitions within vibrational states were not considered, as the time scales of vibrational de-excitation ( $\sim 10^{-4}$  s) are several orders of magnitude shorter than the expected collisional excitation rates ( $\sim 10^4$  s). To model thermal emission from dust grains, we use the opacity law of Ossenkopf & Henning (1994).

After obtaining ray-traced simulated image cubes from LIME, we test two separate methods of post-processing before comparing with observations. The first involves a simple image plane continuum subtraction followed by convolution of the channel maps with the synthesized beams in Fig. 3.3. For the second method, we utilize the Python module `vis_sample`<sup>2</sup> to simulate the incomplete sampling of sky brightnesses using input  $uv$  grid points directly from the observation sets. The results are simulated visibilities that were then continuum subtracted and imaged in the same manner as their respective observations (described in Section 3.2). The estimated flux error in the simulated image is 5%, based on the converged signal-to-noise of the individual grid points. Because the input model is spherically symmetric, we take the azimuthal average of the LIME-generated channel map at the systemic velocity of IRC+10216 to compare the modeled emission with ALMA images.

The result of both methods when applied to the  $J = 3 - 2$  line of  $^{13}\text{CO}$ , for

---

<sup>2</sup>`vis_sample` is publicly available under the MIT license at [https://github.com/AstroChem/vis\\_sample](https://github.com/AstroChem/vis_sample) and described in further detail in (Loomis et al., 2018b)

which the abundance is known *a priori*, is shown in Fig. 3.6a. The convolved LIME model of this line overpredicts the brightness, especially in the extended layers of IRC+10216. In contrast, the visibility sampled and reconstructed image reproduces the peak brightness to within 5%, and predicts the much lower average brightness of this line due to spatial filtering. From this it is clear that the latter method better accounts for the lack of data from short baselines and the resulting flux loss at large spatial scales, so we employ the visibility sampling routine for the case of HC<sub>3</sub>N as well.

## Results for HC<sub>3</sub>N

We use the above forward-modeling routine to simulate the  $J = 28 - 27$  and  $J = 38 - 37$  lines of HC<sub>3</sub>N, now varying the abundance to reproduce the observed radial brightness distribution. Primarily, we modify it at radii less than  $4''$ , since this is where we see the bulk of emission (shaded regions in Fig. 3.7); however, we also adjust the peak abundance to reflect the observed lack of emission at radii larger than  $8''$ . We start with a function similar to the modeled result in Agúndez et al. (2017), with a peak abundance of  $1 \times 10^{-6}$  at  $r = 3 \times 10^{16}$  cm that steadily decreases inwards, and drops off steeply outwards. We then adjust the magnitude shape to match the distribution and intensity, by eye, of azimuthally averaged emission for both HC<sub>3</sub>N lines.

The resulting simulated intensity profiles are shown in Figures 3.6b. and 3.6c. The corresponding best-fit abundance profile is shown in Fig. 3.7a., and the volume density is shown in Fig. 3.7b. The resulting modeled intensity curves are in good agreement with the observed azimuthal averages at the radii where we see the bulk of HC<sub>3</sub>N emission. There is a slight disagreement in the regions between  $8'' - 14''$  where the average predicted  $J = 28 - 27$  emission increases  $2 \text{ mJy beam}^{-1}$ ; however, this is

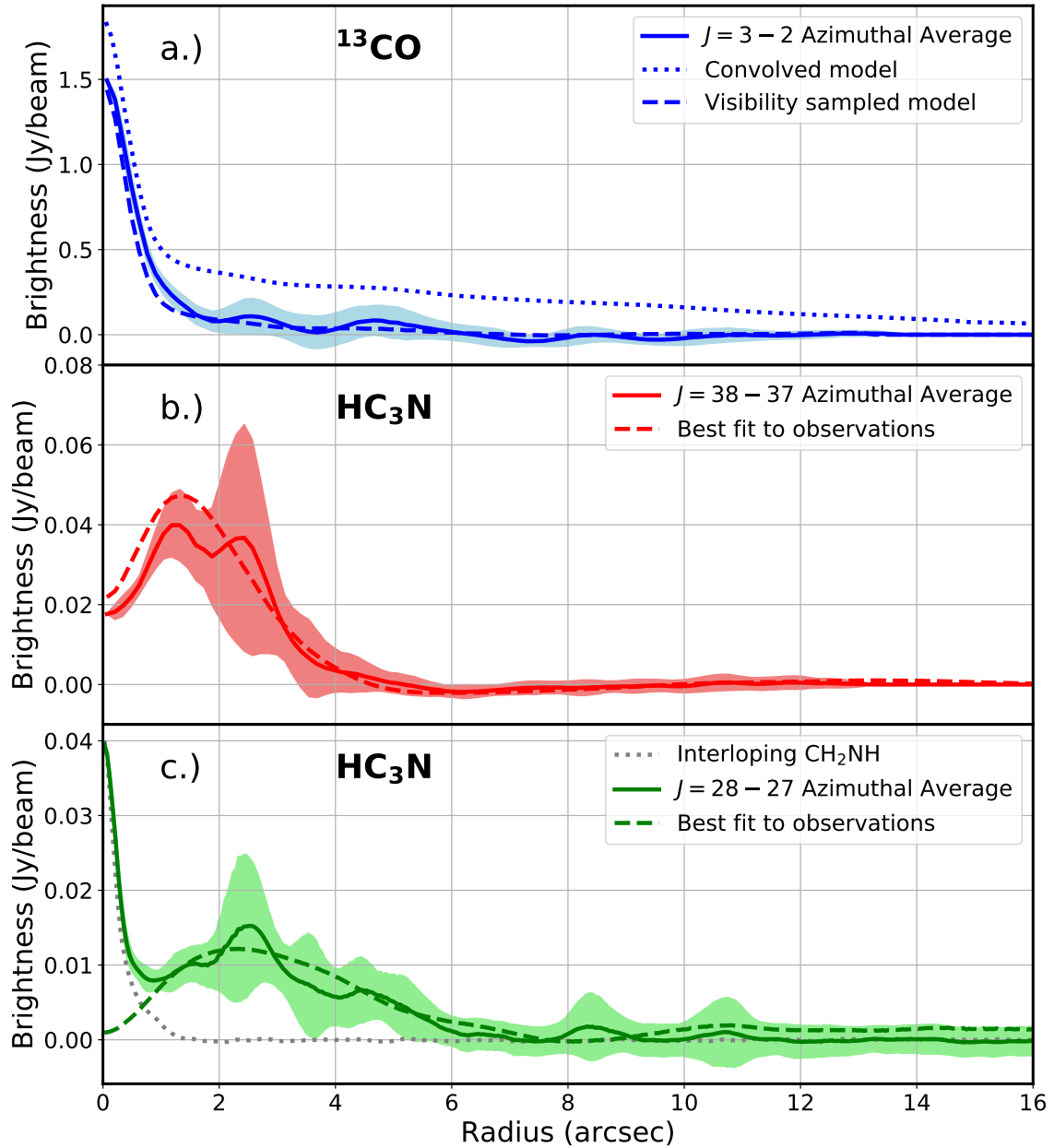


Figure 3.6: Observed (solid lines) and LIME simulated (dashed lines) brightness profiles of  $^{13}\text{CO}$ ,  $\text{HC}_3\text{N}$   $J = 38 - 37$ , and  $\text{HC}_3\text{N}$   $J = 28 - 27$  from top to bottom. Profiles were obtained by taking the azimuthal average of the channel map at the systemic velocity of IRC+10216 centered on the position of the AGB star. Shaded regions denote the standard deviation of the surface brightness in each radial bin. In the top panel, the profile is also shown when a convolution with the synthesized beam of observations is used instead of visibility sampling. In the bottom panel, the expected contaminating emission from  $\text{CH}_2\text{NH}$  is shown as well (dotted line).

very close to the rms of the observations, so it is not expected that we would detect consistent emission at this level. We do detect some clumps with a peak abundance of  $25 \text{ mJy beam}^{-1}$  in these regions, as seen outside the yellow reference circle to the SW and NW in Fig. 3.3a., but no extended component is found.

In the inner layers where the  $\text{HC}_3\text{N}$  emission is primarily seen, an average abundance of  $\sim 10^{-8}$  is needed, and it must be decreasing inward to avoid centrally peaked channel maps. In typical fashion for characterizing the radial abundance distributions of molecules forming in outer regions of CSEs (e.g. Agúndez et al., 2015), we parameterize this with an offset Gaussian in log radius:

$$f(r) = f(r_p) \exp\left(-\left(\frac{\log r - \log r_p}{\Delta \log r}\right)^2\right) \quad (3.2)$$

where  $f$  is the fractional abundance with respect to  $\text{H}_2$ ,  $r_p$  is the peak radius, and  $\Delta \log r$  adjusts the width of the feature. For the retrieved profile, we obtain  $f(r_p) = 2.5 \times 10^{-8}$ ,  $r_p = 2 \times 10^{16} \text{ cm}$ , and  $\Delta \log r = 1.65$ . This is the main function we use to describe the  $\text{HC}_3\text{N}$  abundance in the regions of IRC+10216 probed by our observations, and an additional narrow component peaking at  $r = 3 \times 10^{16} \text{ cm}$  with  $f = 7 \times 10^{-7}$  is included to reflect radii larger than  $10^{16} \text{ cm}$ . This is smaller than the peak derived in Agúndez et al. (2017) by a factor of 1.4, but this inconsistency is expected since a smaller mass-loss rate is used in that work. The retrieved abundance profile is shown in Fig. 3.7a. along with the results of a chemical model for IRC+10216, which is described in Section 3.4.1.

### 3.4 Discussion

When compared with the results of our own chemical model as well as the abundances in Agúndez et al. (2017), the measured  $\text{HC}_3\text{N}$  abundances demonstrated in

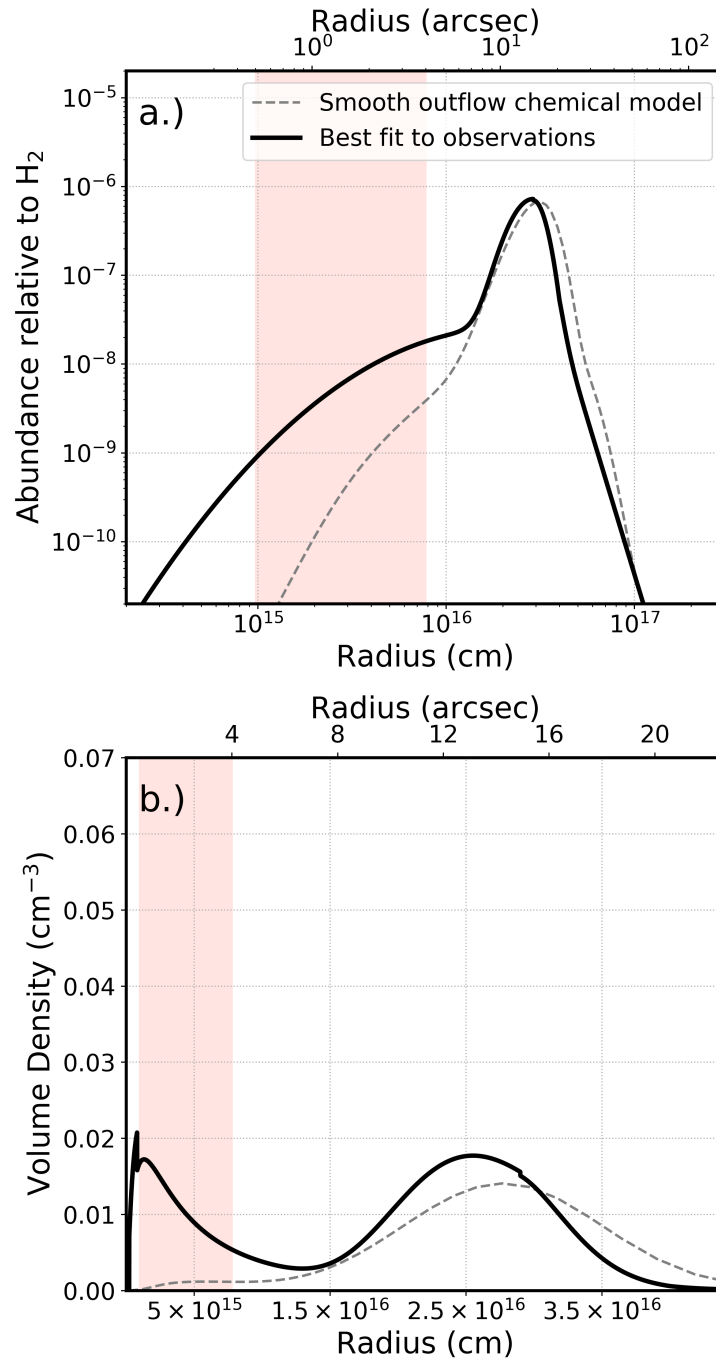


Figure 3.7: Radial abundance with respect to H<sub>2</sub> (top) and volume density (bottom) profiles of HC<sub>3</sub>N in the envelope of IRC+10216. Solid black line represents the best fit profile resulting from the visibility sampled LIME radiative transfer models, while the dashed gray line is the prediction of a simple kinetic chemistry model (described in Section 3.4.1). The shaded red region represents the radii where the HC<sub>3</sub>N abundance is best sampled by the observations.

Fig. 3.7 is about one order of magnitude larger than predictions of kinetic chemistry at radii less than  $10^{16}$  cm. The disparity with Agúndez et al. (2017) is actually greater than that since a lower mass-loss rate was adopted in that work, which will naturally yield higher abundances necessary to reproduce a given observation.

One factor that could potentially affect abundance calculations in the envelope of IRC+10216 is the variability of rotational molecular lines with stellar phase. Pardo et al. (2018) observed periodicity in 3 mm radical, polyynes, and cyanopolyynes species (including  $\text{HC}_3\text{N}$ ) that can be either in or out of phase with the  $\sim 640$  day periodicity of the AGB star as seen in the infrared. He et al. (2017) observed the same behavior in higher frequency lines, including the  $J = 28 - 27$  blend mapped in this work. We do not expect this to have a dramatic effect on our results, mainly because the amplitude of these oscillations are relatively small (ranging from 8%–15% of the average integrated line flux), but also because the combined data we use for the  $J = 28 - 27$  line was taken, and thereby averaged, over the course of five months, almost a quarter of the full period. Nevertheless, if we extrapolate the light curve from He et al. (2017) for the periodicity to the dates of the ALMA observations (Nov. 2019 – Mar. 2020), we find that the map in Fig. 3.3a represents phases near an expected *minimum* of this line. The  $J = 38 - 37$  image was made from a single observation in May 2018, meaning it would instead be expected to near the average brightness if it follows the same function. Once again, however, this is likely a very minor effect on the retrieved abundances since the amplitude of variation is small, especially when taken in comparison to the brightness variation from the asymmetric 3D nature of the outflow (illustrated by the shaded curves in Fig. 3.6), which is the primary source of uncertainty in our analysis.

With this in mind, our results indicate that some process is enhancing the photochemical production of  $\text{HC}_3\text{N}$  in the envelope of IRC+10216. Therefore, our observa-

tions of  $\text{HC}_3\text{N}$  in the inner layers of IRC+10216 follow a pattern of previous results for product molecules in this envelope, namely the studies of  $\text{CH}_3\text{CN}$ ,  $\text{NaCN}$ ,  $\text{H}_2\text{O}$ , and  $\text{C}_4\text{H}_2$  (Agúndez et al., 2015; Quintana-Lacaci et al., 2017; Agúndez et al., 2010; Fonfría et al., 2018). The former is driven by the radiative association of photoionized  $\text{CH}_3^+$  with  $\text{HCN}$ , while  $\text{NaCN}$  is thought to form via a reaction between  $\text{NaCl}$  and  $\text{CN}$  (Agúndez et al., 2008; Petrie, 1996a).  $\text{H}_2\text{O}$  and  $\text{C}_4\text{H}_2$  have formation routes through reactions with the photodissociation products  $\text{C}_2\text{H}$  and neutral  $\text{O}$ .  $\text{HC}_3\text{N}$  formation in the extended CSE is likewise governed by the following reactions:



In common between all these reaction pathways is the need for a source of UV photons to provide the necessary reactants. The anomalous overabundances for all four of these species thus suggest a larger flux of UV radiation than expected in the inner envelope. Agúndez et al. (2015) investigated the possibility that  $\text{CH}_3\text{CN}$  abundances result from the asymmetric clumpiness of the outflow allowing ionizing photons from the ISRF to penetrate farther into the outflow than the smooth spherical case; however, this was also not enough to reproduce their observations. Here, we explore an alternate scenario where the missing UV is provided internally from a binary companion star orbiting IRC+10216 at a close distance.

Evidence of such a companion existing nearby IRC+10216 has grown over recent years, primarily through spatial studies of  $\text{CO}$  and its isotopologues. Cernicharo et al. (2015) and Guélin et al. (1993) note the  $16''$  ( $\sim 700$  yr) spacing of the outermost bright gas shells which is neither consistent with the approximate timescales of thermal

pulses ( $\sim 10^4$  yr) nor the pulsations exhibited by AGB stars ( $\sim 1$  yr). These authors suggest that the shells could instead be explained by a companion on an elliptical orbit periodically affecting the mass-loss rate of IRC+10216 during periastron. Guélin et al. (2018) found that the spacing of these shells decreases moving inwards, indicating mass transfer or additional dynamics occurring. In addition, Decin et al. (2015) detected signatures of spiral arm structure at arcsecond scales which are consistent with a main-sequence  $1M_{\odot}$  companion orbiting at  $\sim 20$  AU with an orbital period of 55 yr. Lastly, Kim et al. (2015a) and Kim et al. (2021) detected a secondary point source of optical light about  $0.5''$  east of IRC+10216 using HST monitoring. Based on its spectral index, they argue that the object could be a binary companion of spectral type M1, but this result has yet to be confirmed. In proposed scenarios of Kim et al. (2015a) and Decin et al. (2015), the binary separation is less than the minimum beam size of our observations, and in the case of Guélin et al. (2018), the proposed separation would be  $\sim 1''$ . So we expect the region of the possible companion to be unresolved, or at most very weakly resolved, from the central AGB star in our observations.

While the exact nature of the orbital system IRC+10216 appears to be a part of is still not well-characterized due to uncertainties in the above works, a binary scenario seems very likely. Although IRC+10216 itself is likely far too red to produce enough UV flux to drive photochemistry in the inner envelope, a companion with a higher surface temperature could accomplish this. To test this scheme in comparison to our measurements of  $\text{HC}_3\text{N}$ , we utilize a detailed chemical model of IRC+10216.

### 3.4.1 Chemical modelling

The chemical kinetics model is that of Van de Sande & Millar (2022), which includes the effect of stellar companion UV photons on the gas-phase chemistry through-

out the outflow. Several assumptions go into the model to reduce the complexity of the problem. The one-dimensional model does not include dust formation and growth, but assumes dust is present from a radius  $R_{\text{dust}}$  onwards. The companion is assumed to be at the center of the outflow and lie within the dust-free region before  $R_{\text{dust}}$ . Considering the scale of the outflow, we consider the effect of misplacing the companion within the dust-free region is negligible. The photon flux of the companion is approximated by blackbody radiation and is set by the stellar radius,  $R_*$  and blackbody temperature,  $T_{\text{comp}}$ . The one-dimensional nature of the model implies that orbital motion cannot be taken into account. Hence, the companion's radiation field is assumed to be always present. This assumption is explored further in Appendix 3.6. The model assumes the companion to be one of three types: a red dwarf at 4000 K, a solar-like star at 6000 K or a white dwarf at 10 000 K.

The effects of a clumpy outflow on the chemistry are taken into account using the porosity formalism, as described by Van de Sande et al. (2018). The formalism divides the outflow in a stochastic two-component medium, consisting of a rarified interclump component and an overdense clumped component, and allows us to include the influence of a clumpy outflow on the penetration of UV photons along with the effect of local overdensities. Dust and gas are assumed to be well-mixed in the interclump and clumped components. The specific locations of the clumps cannot be specified. Rather, the clumpiness of the outflow is determined by three general parameters: the interclump density contrast,  $f_{\text{ic}}$  which describes the distribution of material between the clump and interclump component, the volume filling factor,  $f_{\text{vol}}$  which sets fraction of the total outflow volume occupied by clumps, and the size of the clumps at the stellar surface,  $l_*$ . As volume filling factor is assumed to be constant throughout the outflow and the clumps are assumed to be mass conserving, the clumps expand as they move away from the AGB star.

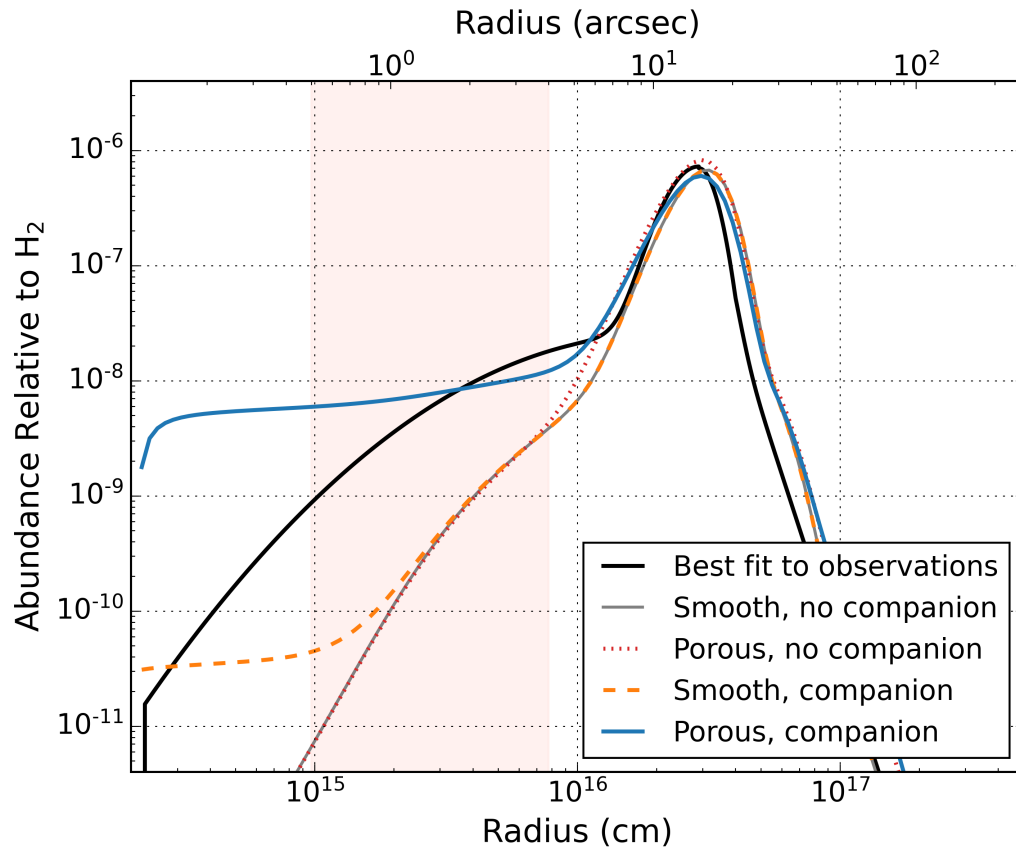


Figure 3.8: The retrieved HC<sub>3</sub>N abundance (black) together with the chemical modelling results. Gray, solid: smooth outflow without a stellar companion. Red, dotted: porous outflow (characterised by  $f_{\text{ic}} = 0.40$ ,  $f_{\text{vol}} = 0.50$ , and  $l_{\star} = 2 \times 10^{13}$  cm) without a stellar companion. Orange, dashed: smooth outflow with a solar-like companion and dust condensation radius  $R_{\text{dust}} = 5 R_{\star}$ . Blue, solid: porous outflow with a solar-like companion and  $R_{\text{dust}} = 5 R_{\star}$ . The shaded red region represents the radii where the HC<sub>3</sub>N abundance is best sampled by the observations.

The values of the three porosity parameters are observationally constrained. The shells and their clumps were resolved in the VLA survey of Keller (2017). At a distance of about  $24''$  from the star, the angular sizes of the clumps were found to range from  $2.0'' \times 3.0''$  up to  $3.0'' \times 7.7''$ . Assuming a distance of 130 pc, this corresponds to an upper limit on the physical sizes of the clumps of  $3.9 - 15.6 \times 10^{15}$  cm at a distance of  $\sim 4.6 \times 10^{16}$  cm from the star. This constrains the value of  $l_*$  to  $2 - 4 \times 10^{13}$  cm. The density contrast between the shell and intershell region was found to lie between 1.5 and 7.6 at a radial distance of  $\sim 15''$  from the star. This is consistent with the shell-intershell brightness contrast of  $\geq 3$  retrieved by Cernicharo et al. (2015). Assuming this density contrast can be applied to the clumped and interclump components, the values of  $f_{ic}$  and  $f_{vol}$  are linked following

$$\frac{\rho_{cl}}{\rho_{ic}} = \frac{1 - (1 - f_{vol})f_{ic}}{f_{vol} f_{ic}}, \quad (3.5)$$

with  $\rho_{cl}$  and  $\rho_{ic}$  the clumped and interclump densities, respectively. Lastly, we assume that dust grains are purely absorbing and therefore neglect the scattering of UV photons. Jones et al. (2013) showed that for small hydrocarbon dust grains, that provide the extinction at UV wavelengths, their albedo is essentially zero at these wavelengths. Such small grains are thought to be present in the inner envelope (Fonfría et al., 2022). Although the Jones et al. models are strictly for interstellar dust, their results are likely to hold for IRC+10216; thus scattering can largely be ignored in the inner regions of the outflow.

The physical parameters adopted for the outflow of IRC+10216, together with those derived for our best-fit chemical model, are listed in Table 3.2. The parent species used are those of Agúndez et al. (2012), but with the initial abundance of  $C_2H_2$  and HCN decreased by a factor two. This was done to ensure agreement with

the results from Fonfría et al. (2008), who observed mid-infrared vibrational lines of these molecules coming from the innermost regions of the envelope. Halving the initial  $\text{C}_2\text{H}_2$  and HCN lies within the error of the abundances they retrieve for the region closest to the star, from the stellar photosphere up to  $5.2 R_*$ , which is where our chemical model starts.

We find that to reproduce the increase in  $\text{HC}_3\text{N}$  in the inner region, both clumpiness and a companion are necessary. The increase is best reproduced assuming a solar-like companion and a dust condensation radius of  $5 R_*$  together with an interclump density contrast  $f_{\text{ic}} = 0.40$ . Figure 3.8 shows the retrieved abundance profile along with chemical model results, for smooth and porous outflows both with and without a solar-like companion. The value of  $R_{\text{dust}}$  corresponds to the results of Fonfría et al. (2022), who found gradual dust growth up to  $5 R_*$ . While the chemical model does not include dust growth, we find that this value of  $R_{\text{dust}}$  best reproduced the retrieved abundance profile. The values of  $f_{\text{vol}}$  and  $l_*$  do not have a large influence on the shape of the abundance profile and are constrained by the observational results of Keller (2017).

Although a mass-loss rate of  $2.7 \times 10^{-5} M_{\odot} \text{ yr}^{-1}$  was used for the radiative transfer model to describe the envelope density within a radius of  $15''$  (Guélin et al., 2018), a lower one is needed for the chemistry model since the entire extended envelope contributes to the extinction of UV photons, and lower average mass-loss rates have been obtained when considering radii out to  $300''$  (Decin et al., 2011; Teyssier et al., 2006; Cernicharo et al., 2015). Therefore, to better fit the attenuation of the extended molecular shell, the mass-loss rate was changed from  $2.7 \times 10^{-5} M_{\odot} \text{ yr}^{-1}$ , as retrieved by Guélin et al. (2018) to  $1.8 \times 10^{-5} M_{\odot} \text{ yr}^{-1}$ .

While the porous model with a solar-like companion shows an increased  $\text{HC}_3\text{N}$  abundance before the molecular shell at  $\sim 15''$ , the gentle increase in the retrieved

Table 3.2: Physical parameters of the chemical model

Parameters adopted from Agúndez et al. (2012)	
Outflow velocity, $v_\infty$	14.5 km s <sup>-1</sup>
Stellar radius, $R_*$	$4 \times 10^{13}$ cm
Stellar temperature, $T_*$	2330 K
Exponent $T(r)$ , $\epsilon$	0.5
Modelling results	
Mass-loss rate, $\dot{M}$	$1.8 \times 10^{-5}$ M <sub>⊙</sub> yr <sup>-1</sup>
Interclump density contrast, $f_{\text{ic}}$	0.50
Clump volume filling factor, $f_{\text{vol}}$	0.25 - 0.80
Companion temperature., $T_{\text{comp}}$ ,	6000 K
Companion radius, $R_{\text{comp}}$ ,	$8.14 \times 10^{10}$ cm
Onset of dust extinction, $R_{\text{dust}}$	$5 R_*$
Start of the model	$1.025 \times R_{\text{dust}}$

abundance cannot be reproduced. This is because the model cannot take the gradual dust growth in the inner wind into account (Fonfría et al., 2022) and starts only after the dust condensation radius, leading to an abrupt start of photochemistry in the inner wind and subsequently a sharp increase in HC<sub>3</sub>N abundance. Additionally, the porosity formalism provides only a one-dimensional approximation of the three-dimensional clumpy substructure seen in IRC+10216’s outflow. Nevertheless, it is once again clear that a classical chemical model of smooth outflow without a stellar companion does not suffice.

### 3.5 Conclusions

We have presented an investigation of warm HC<sub>3</sub>N emission in the inner layers of IRC+10216 utilizing multiple archival ALMA observations. Mapping the  $J = 28 - 27$ ,  $J = 30 - 29$ , and  $J = 38 - 37$  lines of this molecule reveals the most compact distribution ( $r < 10^{16}$  cm) of a cyanopolyne molecule presently detected toward the

outflow of an evolved star, with emission localized to radii where  $\text{CH}_3\text{CN}$ ,  $\text{NaCN}$ ,  $\text{H}_2\text{O}$ , and  $\text{C}_4\text{H}_2$  were previously observed (Quintana-Lacaci et al., 2017; Agúndez et al., 2015, 2010; Fonfría et al., 2018). The emitting region is almost completely distinct from previous works that imaged lower excitation lines of  $\text{HC}_3\text{N}$ , allowing for an in-depth characterization of this molecule throughout the CSE. Using a 1D model of the physical conditions surrounding IRC+10216, we used visibility sampled LIME simulations to derive an average abundance of  $10^{-8}$  with respect to  $\text{H}_2$  for  $\text{HC}_3\text{N}$  at the radii probed by these observations. This is about five to ten times larger than predicted by simple chemical models of IRC+10216, suggesting that photochemistry is occurring more rapidly than expected in these warmer layers.

To explain this result, we investigated the possibility that the enhancement of  $\text{HC}_3\text{N}$  surrounding IRC+10216 is caused by an embedded binary companion emitting UV photons in the inner wind and driving photochemistry. Using known constraints on the physical environment and the abundances of parent molecules, we ran a specialized chemical kinetics network to model the radial  $\text{HC}_3\text{N}$  abundance profile for a variety of different companion scenarios. We find that invoking a solar-like companion and a dust condensation radius of  $5 R_*$  produces a similar abundance feature in the inner wind to that observed, and conclude that this is an strong explanation for the anomalous abundances of product molecules observed at small radii toward IRC+10216.

This result is especially intriguing when considering the newfound prevalence of binary interactions in AGB outflows (e.g. Decin et al., 2020). Since these systems appear to be common among nearby evolved stars, it could be that companions embedded in CSEs have a notable chemical affect on the composition of material returned to the ISM during the AGB and onward. In order to understand the full extent of this effect in IRC+10216, further millimeter and IR studies of photochemistry

products (specifically their higher energy transitions) will be crucial. In addition, rigorous molecular line studies of C- and O-rich evolved stars that show signs of binary shaping could shed important light on this topic.

### 3.6 Appendix: Effect of orbit geometry

The orbital motion of a stellar companion could induce chemical asymmetries in the outflow. Because the chemical model is one-dimensional, orbital motion cannot be taken into account. Moreover, the companion star is assumed to be located at the center of the AGB star, resulting in a continuous irradiation of the outflow by the companion star. Van de Sande & Millar (2022) argue that the limitations of the model are reasonable first-order approximations for a close-by companion with a short orbital period. This assumption should be investigated in more detail for the IRC+10216 system because the tentative orbital solutions presented in Cernicharo et al. (2015) and Decin et al. (2015) of respectively 700 and 55 yr cannot necessarily be considered sufficiently short. For a given point at radius  $r$  in the outflow on the orbital plane of the binary system, assuming a circular orbit, the fraction of the period the companion spends behind the AGB star is given by

$$f \approx \frac{2a \arctan \left[ \frac{r+a}{a} \frac{R_*}{r} \right]}{2\pi a} \quad (3.6)$$

where  $a$  is the semi-major axis and  $R_*$  is the radius of the AGB star, provided  $r \gg R_*$ . Using the empirical values from Cernicharo et al. (2015) ( $a = 42.6 R_*$ ) and Decin et al. (2015) ( $a = 8.2 R_*$ ), we obtain the results shown in Fig. 3.9. In both cases, the perceived occultation time of the companion is less than 10% of the total period at all radii larger than  $R_{\text{dust}}$ . In the outer envelope, this value then drops to 4% and 1% for the long and short period solutions, respectively. From this, we would only expect time-dependent spatial chemistry differences to occur in the innermost regions of the envelope, and these scales are unfortunately not probed by our ALMA observations. Of course, other factors, including the varied dust extinction between

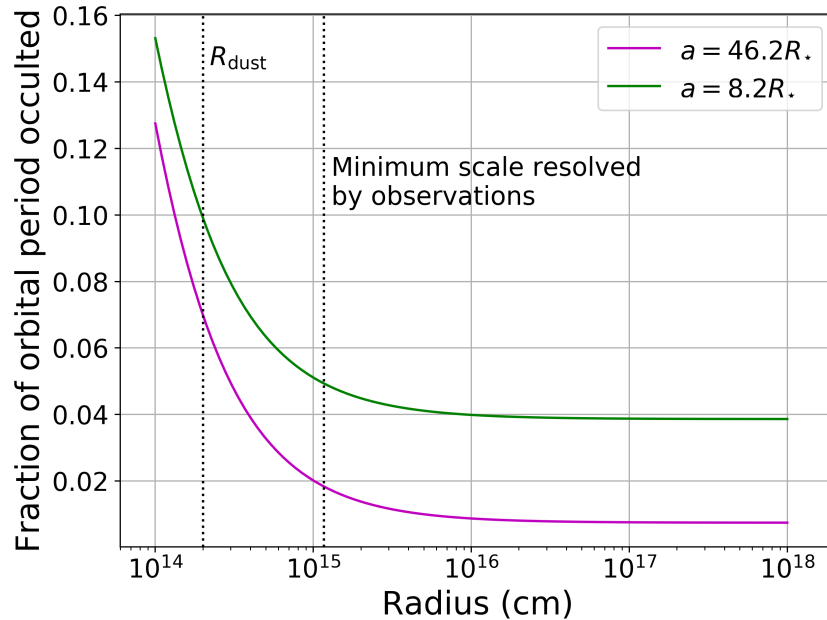


Figure 3.9: Occultation time of a companion star orbiting with IRC+10216 semi-major axis  $a$  as seen by a point on the orbital plane as a function of radius. Magenta and green curves correspond to the semi-major axes proposed in Cernicharo et al. (2015) and Decin et al. (2015), respectively.

the companion and the point as the companion orbits, the eccentricity, the presence of density enhancements, clumps, arcs, etc., do complicate the picture but as a first approximation it is clear that the companion photons are visible for a very large fraction of the orbit even in the long period solution from Cernicharo et al. (2015).

The other important detail here is the inclination of the orbit with respect to the observer. Since we are only mapping the HC<sub>3</sub>N distribution at the systemic velocity, we would only expect chemical asymmetries to arise in regions opposite where the companion crosses the plane of the sky, which is a small fraction even for slight inclinations. Though the exact orbit is uncertain, Decin et al. (2015) proposed that the inclination is larger than 60° based on observed <sup>13</sup>CO PV diagrams. An inclination this high would only cause chemical asymmetries (in the plane of the sky) to be

observable if the envelope was observed during very specific points in the orbit, which is unlikely given the proposed period of 55 – 700 yr (Decin et al., 2015; Cernicharo et al., 2015). Between this and the relatively short fractional occultation period, if a companion is indeed influencing HC<sub>3</sub>N chemistry in the envelope of IRC+10216, we do not expect orbit-induced asymmetries to be prominent or detectable in the ALMA images presented in this work.

## CHAPTER 4

# Molecules in the Circumbinary Disk of V Hya

The previous study revealed a relationship between AGB-companion interactions and the chemical evolution of circumstellar gas, but only for one idealized source. The text in Chapter 4 has been submitted for review in the *Astrophysical Journal* as “Molecular Abundances and Distributions in the Binary-Shaped Outflow of V Hya.”, and details a interferometric line survey of another binary carbon star with a much different outflow morphology.

### 4.1 Introduction

The circumstellar envelopes of Asymptotic Giant Branch (AGB) stars are known for their rich molecular composition and their instrumental role in the chemical enrichment of the interstellar medium (ISM). It is estimated that these evolved stars contribute 80% of recycled interstellar gas, 70% of newly formed dust, in addition to a significant fraction of aromatic molecules (Tielens et al., 2005; Zhukovska & Henning, 2013; Zeichner et al., 2023). The type of enrichment is primarily dependent on the

surface chemistry of the progenitor star, as circumstellar outflows typically exhibit either oxygen-rich ( $C/O < 1$ ) or carbon-rich ( $C/O > 1$ ) chemistry. In the traditional picture of circumstellar chemistry, gas phase molecules in AGB envelopes are produced in two stages, with parent species forming in the extended stellar atmosphere of the star. Then as they travel outward and the density decreases, kinetics and photochemistry dominate, producing a wide variety of daughter molecules (e.g. Höfner & Olofsson, 2018). For C-rich environments, this chemical framework is primarily understood through observations of the nearby prototypical carbon star IRC+10216 and its rich chemistry comprising over 100 uniquely identified molecules (McGuire, 2022); however, the applicability of this model to other sources, especially those with aspherical envelope structure, is presently unclear.

Recently, the prevalence of binary interactions has greatly impacted our understanding of dynamical evolution in AGB and Red Supergiant (RSG) environments. The ATOMIUM<sup>1</sup> survey revealed a vast array of AGB wind morphologies induced by stellar and substellar companions (Decin et al., 2020). These structures can be broadly categorized into two groups, depending on orbital characteristics of the system: spirals structures are associated with high mass-loss rates and wide companions, and can be observed in objects such as CIT 6, AFGL 3068, and R Scl (Kim et al., 2015b; Guerrero et al., 2020; Maercker et al., 2016). In contrast, equatorial density enhancements and disks are more prominent in short period systems, like  $\pi^1$  Gru and R Aqr (Chiu et al., 2006; Liimets et al., 2018).

In addition to the dynamical shaping, stellar companions are believed to have an impact on the chemistry of their surrounding envelope. This was first found theoretically by Van de Sande & Millar (2022), who showed that embedded binaries can provide sufficient visible and UV flux to drive photochemistry at locations

---

<sup>1</sup>ALMA tracing the origins of molecules forming dust in oxygen-rich M-type stars

in the envelope where it is usually inefficient. Siebert et al. (2022a) later invoked a solar-type binary companion to reproduce observed abundances of  $\text{HC}_3\text{N}$  in the inner layers of IRC+10216. Furthermore, Danilovich et al. (2024) recently found evidence of companion-driven chemistry imprinted in the outflow of the highly elliptical system W Aql. The full scope of binary-outflow chemical interactions are still not well-constrained, and given the range of physical structures produced in these environments, unbiased line surveys of objects at different stages of evolution are crucial to building up this picture.

V Hya is a C-rich AGB star with a strongly-interacting, short-period (8–16 yr) stellar companion. Like the other tight binaries discussed above, V Hya harbors a disk undergoing dynamical expansion (DUDE) comprising several concentric toroidal rings, in addition to episodic bipolar bullet-like ejections (Sahai et al., 2016; Scibelli et al., 2019). The observed mass-loss rate among these components is quite high ( $\sim 2 \times 10^{-5} M_{\odot} \text{ yr}^{-1}$ ; Knapp et al., 1997), indicating it is a very evolved source nearing the end of the AGB. The equatorial structure and hints of bipolarity in V Hya suggest the beginnings of the much more dramatic morphologies that are common in protoplanetary nebulae (PPNe) (Olofsson et al., 2019; Sahai et al., 2017). The dense waists of these post-AGB objects have been shown as efficient sites of dust growth during this period of rapid stellar evolution (Sahai et al., 2006), so characterizing molecular processing in their nascent stages is relevant to understanding their overall chemical yields.

V Hya is a unique transitory source that is well-poised to reveal new insights into chemistry in this important type of binary-induced geometry. In this paper, we present an interferometric spectral line study of this source using available ALMA data to constrain its gas phase molecular inventory. Using these observations we aim to characterize the dominant chemical processes throughout this unique source, and

compare it with previous studies of more spherical C-rich AGB targets.

In Section 4.2, we summarize the observations and data reduction. In Section 4.3, we present the spectra and detected molecular lines, as well as spatially resolved maps of key species. Finally, in Section 4.4, we discuss excitation mechanisms, and use multiple methods to derive abundances of chemical species in the disk of V Hya.

## 4.2 Observations and reduction

For this investigation, we utilize data from two archival programs from the Atacama Large Millimeter/submillimeter Array (ALMA). A summary of the frequency coverage, as well as the obtained spectral sensitivity and resolution is shown Table 4.1. Project 2015.1.01271.S (PI: Keller) includes observations of seven carbon stars using the Band 3 receiver (84 – 116 GHz). Two of the sources from this data set were analyzed by Unnikrishnan et al. (2023), who detected and mapped the distributions carbon chemistry products (e.g. HC<sub>3</sub>N, HC<sub>5</sub>N, CN). The observations of V Hya in this data set comprise executions using compact (80th percentile baseline length – 226 m) and extended ( $L_{80\%} \sim 709$  m) configurations of the 12m ALMA Array. This offers an angular resolution of 0".9, and a maximum recoverable scale of 14".7. The receiver setup includes four spectral windows and continuous frequency coverage around 89 and 101 GHz (see Table 4.1), with a total bandwidth of 7.6 GHz.

Project 2018.1.01113.S (PI: Sahai) provides higher frequency observations of V Hya with both the 12 m Array and the 7 m Atacama Compact Array (ACA). These observations were used in the analysis by Sahai et al. (2022), who constrained the physical structure and conditions of the expanding circumstellar disk. While the frequency setups are designed primarily to map <sup>12</sup>CO and <sup>13</sup>CO, the additional spectral windows and bandwidth coverage allow for serendipitous detections of numerous species which we aim to characterize in this work. As shown in Table 4.1, observa-

Table 4.1: Summary and characteristics of the ALMA data utilized in this work.

Project code	Band	Frequency range (GHz)	Obs. date(s)	Array(s)	Synthesized beam ( $\theta_{\text{maj}} \times \theta_{\text{min}}$ )	Spectral res. ( $\text{km s}^{-1}$ )	Image RMS ( $\text{mJy beam}^{-1}$ )
2015.1.01271.S	3	87.2 – 91.0	Mar. – Aug. 2016	12m <sup>a</sup>	1.1'' $\times$ 0.90''	3.2	1.2
	3	99.1 – 102.9	Mar. – Aug. 2016	12m <sup>a</sup>	0.89'' $\times$ 0.74''	2.9	1.1
2018.1.01113.S	6	218.6 – 220.5	Apr. 2020	12m	0.64'' $\times$ 0.54''	0.66	1.1
	6	220.2 – 220.6	Apr. 2020	12m	0.64'' $\times$ 0.54''	0.33	1.8
	7	330.2 – 332.2	Mar. – Apr. 2020	12m+7m	0.51'' $\times$ 0.40''	0.44	1.5
	7	342.3 – 344.2	Mar. – Apr. 2020	12m+7m	0.50'' $\times$ 0.39''	0.43	1.1
	7	345.55 – 346.02	Mar. – Apr. 2020	12m+7m	0.49'' $\times$ 0.39''	0.10	2.8

NOTE — <sup>a</sup>Includes two data sets from the 12m array in short and long baseline configurations

tions from this project were performed at Bands 6 and 7, with spatial resolutions  $0''.6$  and  $0''.5$ , respectively. Accompanying ACA observations are available at Band 7 to increase the maximum recoverable scale of emission; however, none were taken for Band 6. Sahai et al. (2022) discussed the flux recovery in this data set, noting that the 12m  $^{13}\text{CO}$  lines experience up to 25% flux loss, so this effect must be considered when examining Band 6 maps of species with similarly extended distributions.

All observations are located toward  $\alpha_{\text{J2000}} = 10^{\text{h}}51^{\text{m}}37.241^{\text{s}}$ ,  $\delta_{\text{J2000}} = -21^{\circ}15'00.28''$ ; a small deviation in the pointing coordinates of the two ALMA projects was corrected in the imaging process by changing the phase center. Data were newly reduced by these authors using the standard ALMA calibration pipeline, and analysis was performed with the Common Astronomy Software Application (CASA; CASA Team et al., 2022). For observations that were performed with multiple array configurations, and overlapping frequency ranges, data were combined in the uv-plane using antenna-specific weighting. Continuum subtraction was performed on visibilities using a first-order fit to line-free channels in each spectral window. Image cubes were then produced with the TCLEAN task using Briggs weighting and a robust parameter of 0.5. For the full bandwidth products (used to create the spectra in Section 4.3.1), auto-masking was used to identify clean components in the deconvolution process (Kepley et al., 2020). After bright molecular lines were identified and cataloged, their visibilities were re-imaged with an interactive masking procedure to ensure that no artifacts were included in the mask.

Self-calibration was not performed for any of the data sets, as the signal-to-noise of pipeline calibrated data was sufficient for our analysis. The uncertainty in the flux calibration is 5–10%, as is standard for ALMA observations (Cortes et al., 2020).

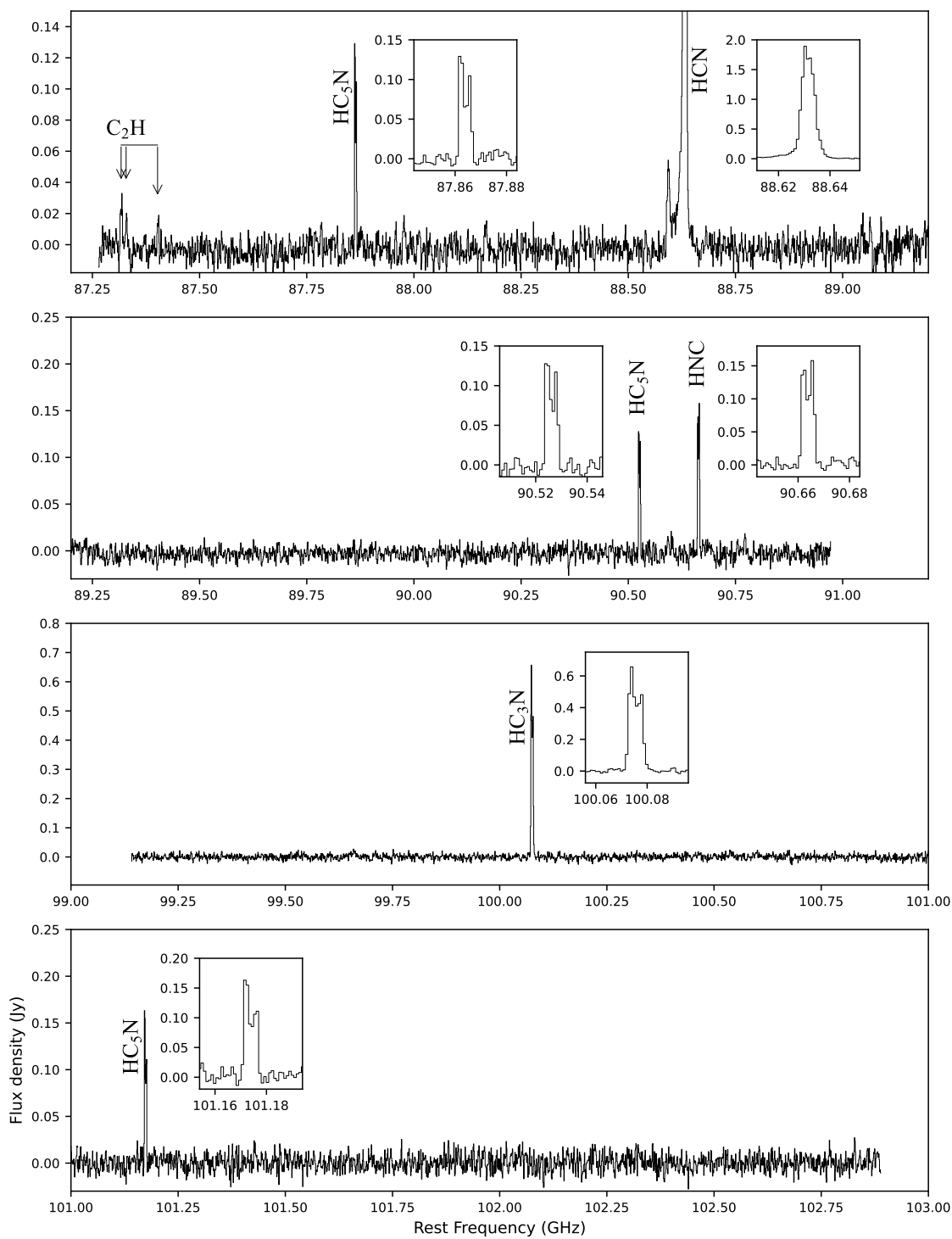


Figure 4.1: Continued.

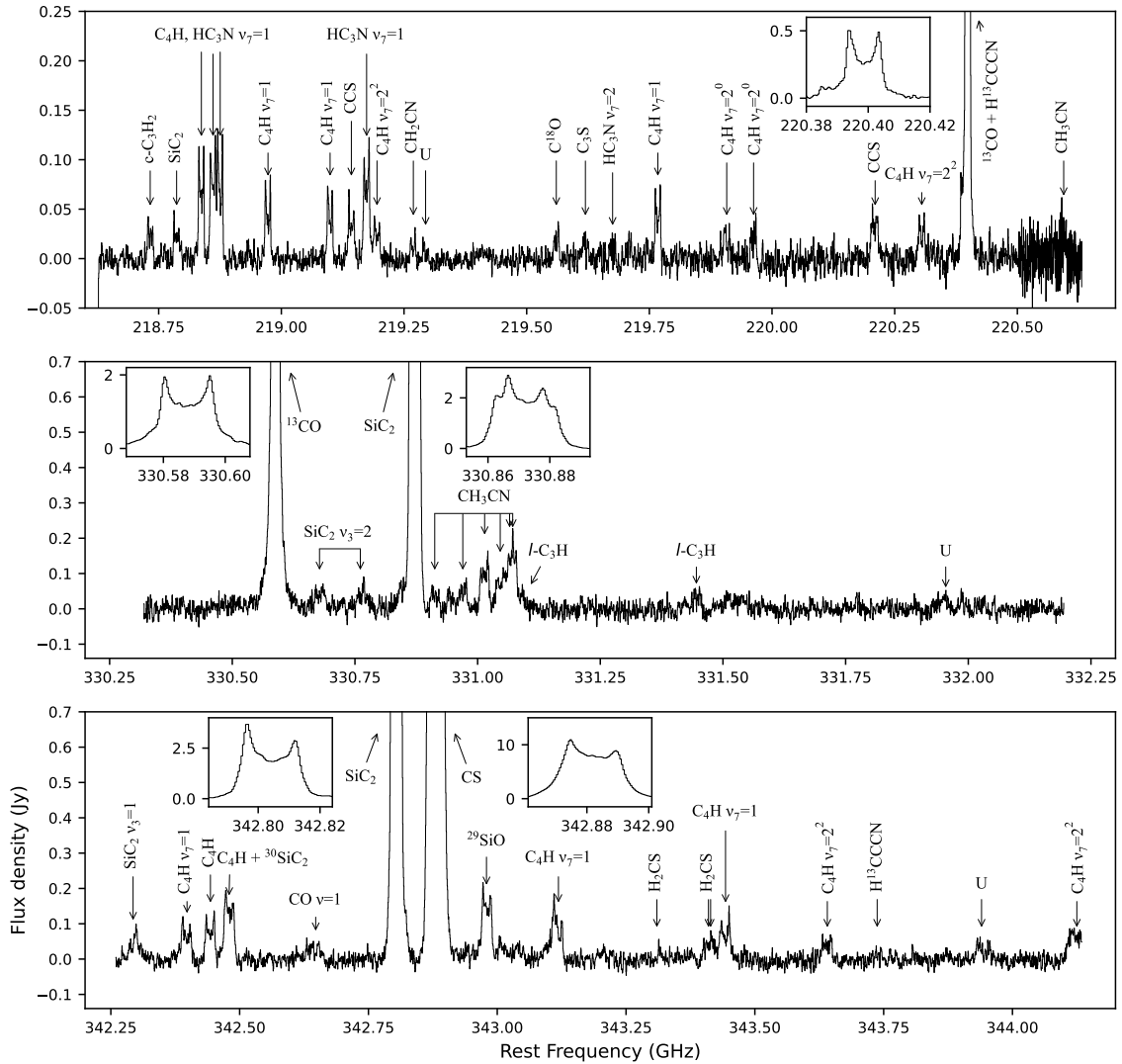


Figure 4.1: Continued. Full spectrum of V Hya obtained from the ALMA observations. Spectra were extracted using a  $4'' \times 6''$  elliptical aperture on the position of V Hya, and shifted to rest frequency using the system velocity  $v_{\text{lsr}} = -17.4 \text{ km s}^{-1}$ . All identified transitions are labeled, and insets are provided for bright lines. Not included here is a separate spectral window covering 345.6–346 GHz, which contains only the <sup>12</sup>CO  $J = 3 - 2$  and HC<sub>3</sub>N  $J = 38 - 37$  lines.

## 4.3 Results

### 4.3.1 Spectra and detected transitions

Spectra were extracted from image cubes using a  $4'' \times 6''$  aperture (aligned with the major axis of the DUDE; position angle  $\sim -5^\circ$ ). While this is smaller than the observed emission of the most extended molecules (see top left panels of Fig. 4.4), we adopt this aperture to increase the sensitivity to weaker lines, which we find are often present in more compact distributions toward V Hya. For the majority of detected molecules, this aperture is large enough to include all of the observed flux. All data were shifted to rest frequency units using the system velocity of V Hya,  $v_{\text{lsr}} = -17.4 \text{ km s}^{-1}$ .

The continuum-subtracted spectra of V Hya are shown in Figure 4.1, including labels for all species contributing emission lines. This includes all spectral ranges in Table 4.1, except for the narrower 345.6–346 GHz window which is dominated only by major transitions of  $^{12}\text{CO}$  and  $\text{HC}_3\text{N}$ . We find that the spectrum of V Hya is relatively line-poor at Band 3, with only seven lines appearing over almost eight GHz of bandwidth. This is in contrast to other C-rich AGB envelopes, which typically show rich spectra at these wavelengths and sensitivities (e.g. see Fig. 4 in Unnikrishnan et al. (2023)). The most notable molecules that are not present in these regions are  $\text{C}_3\text{N}$  and  $\text{SiS}$ , whose transitions in the case of IRC+10216 are equally as bright as  $\text{HC}_5\text{N}$  and  $\text{HNC}$  at Band 3 (Tuo et al., 2024). At Bands 6 and 7 however, the spectrum of V Hya is much richer, as together they account for over 90% of the observed lines.

Table 4.2 lists the identified transitions in Fig. 4.1 with their quantum numbers and spectroscopic constants (upper state energy, line strength). In total, we detect emission from 16 unique molecules, 20 including isotopologues. For four of these

species ( $^{12}\text{CO}$ ,  $\text{HC}_3\text{N}$ ,  $\text{C}_4\text{H}$ , and  $\text{SiC}_2$ ), we see rotational lines from excited vibrational modes, all other transitions are in the ground vibrational state. A full discussion of each molecule, along with its observed spatial distribution and history of study in C-rich AGB outflows is provided in Section 4.4.1.

The line profiles seen in Fig. 4.1 are nearly all double-peaked, as was observed in Sahai et al. (2022). The only exception to this is the  $J = 1-0$  transition of HCN, which shows a central peak and parabolic shape, indicating that this emission is optically thick (Smith et al., 2015). To measure the position and integrated flux of detected lines, we fit them individually with an empirical intensity profile that reproduces the shape of emission. Following the formalism of Wannier et al. (1990), the profile consists of a central parabolic shape that peaks at  $\pm v_{\text{exp}}$ , the radial expansion velocity of the DUDE:

$$S(v) = S_{\text{pk}} \times \left( 1 - \alpha \left[ 1 - \left( \frac{v - v_{\text{l sr}}}{v_{\text{exp}}} \right)^2 \right] \right) \quad (4.1)$$

where  $S_{\text{pk}}$  is the peak flux,  $v_{\text{l sr}}$  is the source velocity, and  $\alpha$  is a shaping parameter ranging from zero (flat-topped profile) to one (intensity minimum of 0 at  $v_{\text{exp}}$ ). Since this function is only applicable for  $|v - v_{\text{l sr}}| < v_{\text{exp}}$ , a gaussian top hat filter is applied to reproduce the line wings (Fig. 4.2). We also must include an asymmetry parameter which allows for the two peaks to have different intensities, as is observed in many transitions (e.g. CS,  $\text{SiC}_2$ ,  $\text{HC}_5\text{N}$ ). This is incorporated by scaling the profile in Eq. 4.1 with a linear function  $\beta$  that can range from  $-1$  (all flux in blue-shifted peak) to zero (symmetric line) to  $+1$  (all red-shifted):

$$S_{\text{asym}}(v) = S(v) \times \left( 1 + \beta \left[ \frac{v - v_{\text{l sr}}}{v_{\text{exp}}} \right] \right) \quad (4.2)$$

In total, we have five variables ( $S_{\text{pk}}$ ,  $v_{\text{l sr}}$ ,  $v_{\text{exp}}$ ,  $\alpha$ ,  $\beta$ ) determining the line shape

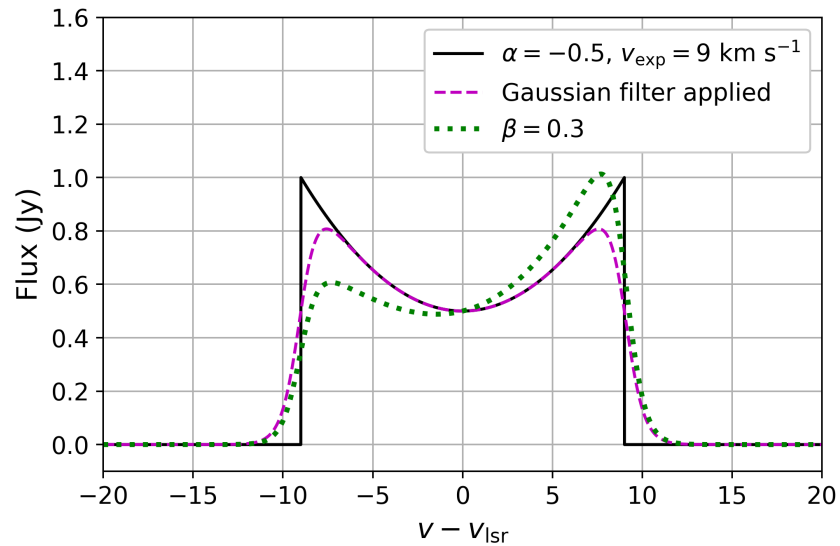


Figure 4.2: Demonstration of the parametric model used to fit individual lines. Solid line depicts the original double-peaked model of Wannier et al. (1990) with  $S_{\text{pk}} = 1$  Jy, the dashed line represents the result of applying a gaussian top hat filter to model line wings, and the dotted line shows the effect of using a positive non-zero value for the asymmetry parameter  $\beta$  (Eq. 4.1).

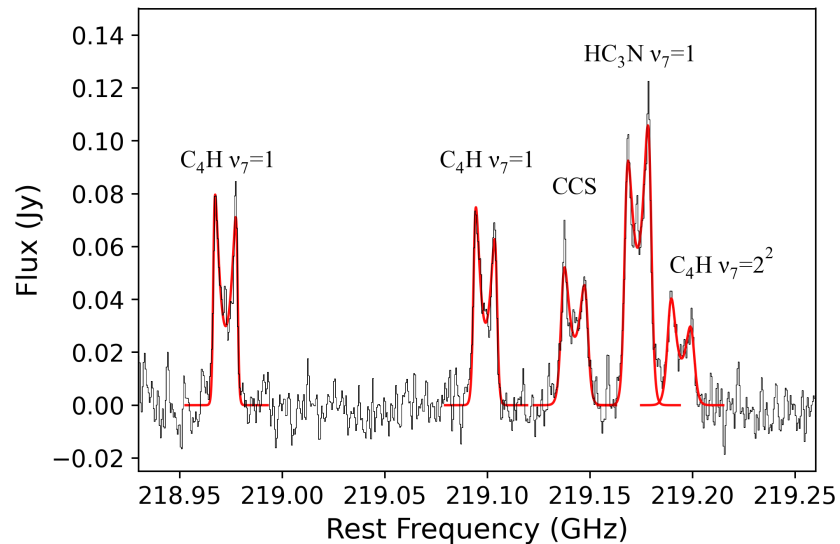


Figure 4.3: Individual line-fitting results for a group of transitions at Band 6. The observed ALMA spectrum of V Hya is shown in black, while the model fits are overlaid in red. The best-fit central frequencies, expansion velocities, and resulting integrated line fluxes are listed in Table 4.2.

which we fit with a least-squares minimization. We apply this to every unblended transition that is detected above  $3\sigma$ , and integrate the emission models to obtain the integrated line fluxes. This value, along with the best-fit central frequency, and expansion velocity are listed in Table 4.2, and a sample of these fits is shown in Fig. 4.3.

We find that almost all transitions are well-fit with an expansion velocity of  $\sim 8 \text{ km s}^{-1}$ , which is consistent with the physical model of the DUDE proposed in Sahai et al. (2022). We also find no evidence of lines that solely arise from the innermost regions of the outflow ( $< 200 \text{ au}$ ), where gas is still being accelerated and thus yields narrower profiles (Decin et al., 2018). This is supported in our spatial analysis of these data (Section 4.3.2), as all molecular emission is found to be at least partially resolved by the ALMA beam.

We report three unidentified lines centered at rest frequencies of 219 294 MHz, 331954 MHz, and 343 940 MHz. Another feature which could be classified as a U line appears very close to the  $J = 1 - 0$  transition of HCN. We instead interpret this as highly redshifted component of HCN, where it would correspond to a velocity of  $+127 \text{ km s}^{-1}$ . Though this is very fast for circumstellar envelopes, it is remarkably close to the redshifted high-velocity bullet observed in  $^{12}\text{CO}$  by Sahai et al. (2022). It also exhibits a small westward offset in position that is associated with this clump. Because of this, we conclude that the emission is contributed by HCN in a dense, high-velocity clump ejected by V Hya, and fit it with a separate profile listed in Table 4.2.

Table 4.2: List of all detected transitions

Rest Frequency	Molecule (MHz)	Transition	$E_{\text{up}}$ (K)	$S_{ij}\mu^2$ ( $D^2$ )	$v_{\text{exp}}$ $\text{km s}^{-1}$	$\int Sdv$ ( $\text{Jy km s}^{-1}$ )	$\sigma^a$ ( $\text{Jy km s}^{-1}$ )
87 316.83(310)	CCH	$N = 1 - 0, J = 3/2 - 1/2, F = 2 - 1$	4.193	1.425	$8.4 \pm 3.0$	0.4548	0.106
87 327.55(75)	CCH	$N = 1 - 0, J = 3/2 - 1/2, F = 1 - 0$	4.193	0.7095	$8.34 \pm 4.0$	0.2532	0.106
87 402.00	CCH	$N = 1 - 0, J = 1/2 - 1/2, F = 1 - 1$	4.193	0.7095	—	—	—
87 863.59(5)	$\text{HC}_5\text{N}$	$J = 33 - 32$	71.69	1856.0	$7.91 \pm 0.2$	1.75	0.116
88 593.39(33) <sup>b</sup>	HCN	$J = 1 - 0$	4.254	26.82	$12.4 \pm 1.0$	1.351	0.116
88 630.96(8)	HCN	$J = 1 - 0$	4.254	26.82	$9.74 \pm 0.3$	38.61 <sup>c</sup>	0.116
90 525.86(61)	$\text{HC}_5\text{N}$	$J = 34 - 33$	76.03	1912.0	$8.04 \pm 1.0$	1.881	0.108
90 663.42(2)	HNC	$J = 1 - 0$	4.351	9.302	$7.68 \pm 0.1$	2.377	0.108
100 076.25(3)	$\text{HC}_3\text{N}$	$J = 11 - 10$	28.82	153.2	$7.84 \pm 0.2$	9.511	0.141
101 174.58(5)	$\text{HC}_5\text{N}$	$J = 38 - 27$	94.69	2138.0	$7.63 \pm 0.2$	2.118	0.137
218 732.70(16)	$\text{c-C}_3\text{H}_2$	$J_{K_a, K_c} = 7_{1,6} - 7_{0,7}, 7_{2,6} - 7_{1,7}$	61.17	44.0	$7.88 \pm 0.3$	0.4571	0.11
218 786.12(16)	$\text{SiC}_2$	$J_{K_a, K_c} = 11_{2,10} - 11_{0,11}$	81.85	1.004	$8.36 \pm 0.3$	0.4518	0.11
218 836.59(6)	$\text{C}_4\text{H}$	$N = 23 - 22, J = 47/2 - 45/2$	126.0	207.1	$8.01 \pm 0.1$	1.293	0.11
218 860.80	$\text{HC}_3\text{N } \nu_7=1$	$J = 24 - 23, l = 1e$	452.1	332.0	—	—	—
218 875.35	$\text{C}_4\text{H}$	$N = 23 - 22, J = 45/2 - 43/2$	126.0	198.2	—	—	—
218 972.30(6)	$\text{C}_4\text{H } \nu_7=1$	$J = 45/2 - 43/2, l = f$	372.8	232.0	$8.01 \pm 0.1$	0.8833	0.11
219 098.98(7)	$\text{C}_4\text{H } \nu_7=1$	$J = 47/2 - 45/2, l = e$	371.4	242.0	$7.54 \pm 0.2$	0.8625	0.11
219 142.49(14)	CCS	$N = 17 - 16, J = 16 - 15$	100.1	132.3	$8.17 \pm 0.4$	0.7707	0.11
219 173.35(10)	$\text{HC}_3\text{N } \nu_7=1$	$J = 24 - 23, l = 1f$	452.3	332.0	$8.35 \pm 0.3$	1.594	0.11
219 194.46(15)	$\text{C}_4\text{H } \nu_7=2^2$	$J = 47/2 - 45/2$	617.1	394.1	$7.76 \pm 0.6$	0.5624	0.11
219 267.89(11)	$\text{CH}_2\text{CN}$	$J = 21/2 - 19/2$	76.35	381.8	$7.09 \pm 0.2$	0.236	0.11

Table 4.2 continued

Table 4.2: List of all detected transitions (continued)

Rest Frequency	Molecule (MHz)	Transition	$E_{\text{up}}$ (K)	$S_{ij}\mu^2$ ( $D^2$ )	$v_{\text{exp}}$ km s $^{-1}$	$\int S dv$ (Jy km s $^{-1}$ )	$\sigma^a$ (Jy km s $^{-1}$ )
219 293.90(19)	U	–	–	–	8.44 ± 0.3	0.1342	0.11
219 560.00(17)	C $^{18}$ O	$J = 2 - 1$	15.81	0.0244	7.39 ± 0.4	0.3421	0.11
219 620.10(30)	C $_3$ S	$J = 38 - 37$	205.6	521.3	7.9	0.2364	0.11
219 675.11	HC $_3$ N $\nu_7=2$	$J = 24 - 23, l = 0$	773.5	331.1	–	–	–
219 766.95(7)	C $_4$ H $\nu_7=1$	$J = 47/2 - 45/2, l = f$	371.8	232.0	8.02 ± 0.1	0.8241	0.11
219 908.65(26)	C $_4$ H $\nu_7=2^0$	$J = 47/2 - 45/2, N = 23 - 22$	662.9	242.7	5.28 ± 2.0	0.4298	0.11
219 961.44(18)	C $_4$ H $\nu_7=2^0$	$J = 45/2 - 43/2, N = 23 - 22$	662.9	232.3	8.54 ± 0.3	0.3844	0.11
220 208.88(24)	CCS	$N = 17 - 16, J = 17 - 16$	103.8	140.5	6.33 ± 2.0	0.8523	0.11
220 304.86(14)	C $_4$ H $\nu_7=2^2$	$J = 45/2 - 43/2$	615.6	410.4	7.42 ± 0.6	0.5849	0.11
220 390.20	H $^{13}$ CCCN	$J = 25 - 24$	137.5	348.1	–	–	–
220 398.68	$^{13}$ CO	$J = 2 - 1$	15.87	0.04869	–	–	–
220 594.32(19)	CH $_3$ CN	$J_K = 12_6 - 11_6$	325.9	381.5	8.83 ± 0.3	0.3082	0.264
330 587.49(15)	$^{13}$ CO	$J = 3 - 2$	31.73	0.07297	7.52 ± 0.4	27.39	0.282
330 677.46(53)	SiC $_2$ $\nu_3=2$	$J_{K_a, K_c} = 13_{2,14} - 12_{2,13}$	645.1	83.94	6.71 ± 2.0	1.032	0.282
330 760.82(35)	SiC $_2$ $\nu_3=2$	$J_{K_a, K_c} = 16_{0,16} - 15_{0,15}$	646.3	90.96	7.9	0.7261	0.282
330 872.01(12)	SiC $_2$	$J_{K_a, K_c} = 14_{6,9} - 13_{6,8}$	189.1	65.47	7.48 ± 0.4	44.45	0.282
330 913.37(37)	CH $_3$ CN	$J_K = 18_5 - 17_5$	329.5	352.1	8.13 ± 0.5	0.6962	0.282
330 969.07(41)	CH $_3$ CN	$J_K = 18_4 - 17_4$	265.2	362.7	7.98 ± 0.7	0.905	0.282
331 013.44(18)	CH $_3$ CN	$J_K = 18_3 - 17_3$	215.2	741.9	8.43 ± 0.3	1.985	0.282
331 046.10	CH $_3$ CN	$J_K = 18_2 - 17_2$	179.5	376.9	–	–	–
331 065.18	CH $_3$ CN	$J_K = 18_1 - 17_1$	158.1	380.4	–	–	–

Table 4.2 continued

Table 4.2: List of all detected transitions (continued)

Rest Frequency	Molecule (MHz)	Transition	$E_{\text{up}}$ (K)	$S_{ij}\mu^2$ ( $D^2$ )	$v_{\text{exp}}$ km s $^{-1}$	$\int S dv$ (Jy km s $^{-1}$ )	$\sigma^a$ (Jy km s $^{-1}$ )
331 071.54	CH <sub>3</sub> CN	$J_K = 18_0 - 17_0$	151.0	381.6	—	—	—
331 084.76	<i>l</i> -C <sub>3</sub> H	$J = 29/2 - 27/2, l = f$	142.7	360.9	—	—	—
331 445.88(17)	<i>l</i> -C <sub>3</sub> H	$J = 29/2 - 27/2, l = e$	142.9	360.9	9.69 ± 0.2	0.622	0.282
331 954.00	U	—	—	—	—	—	0.282
342 292.93(43)	SiC <sub>2</sub> $\nu_3=1$	$J_{K_a, K_c} = 15_{9,6} - 14_{9,5}$	578.2	110.0	7.9	0.8341	0.235
342 396.94(20)	C <sub>4</sub> H $\nu_7=1$	$J = 73/2 - 71/2, l = e$	549.5	376.7	7.87 ± 0.4	1.434	0.235
342 442.95(11)	C <sub>4</sub> H	$N = 36 - 35, J = 73/2 - 71/2$	304.1	317.4	8.1 ± 0.2	1.583	0.235
342 479.35	<sup>30</sup> SiC <sub>2</sub>	$J_{K_a, K_c} = 15_{8,8} - 14_{8,7}$	257.4	61.48	—	—	—
342 481.36	C <sub>4</sub> H	$N = 36 - 35, J = 71/2 - 69/2$	304.2	308.6	—	—	—
342 646.31(32)	CO $\nu=1$	$J = 3 - 2$	3117.0	0.02164	7.9	0.5096	0.235
342 804.47(7)	SiC <sub>2</sub>	$J_{K_a, K_c} = 15_{2,14} - 14_{2,13}$	141.4	83.93	8.26 ± 0.1	44.64	0.235
342 882.22(10)	CS	$J = 7 - 6$	65.83	26.75	7.79 ± 0.3	178.4	0.235
342 980.09(16)	<sup>29</sup> SiO	$J = 8 - 7$	74.08	76.78	7.87 ± 0.4	3.092	0.235
343 118.11(42)	C <sub>4</sub> H $\nu_7=1$	$J = 71/2 - 69/2, l = f$	551.2	366.5	7.88 ± 0.9	2.139	0.235
343 311.83(412)	H <sub>2</sub> CS	$J_{K_a, K_c} = 10_{4,7} - 9_{4,6}$	301.1	22.84	7.9	0.1912	0.235
343 409.17(38)	H <sub>2</sub> CS	$J_{K_a, K_c} = 10_{3,8} - 9_{3,7}$	209.1	74.24	7.9	0.7369	0.235
343 414.15	H <sub>2</sub> CS	$J_{K_a, K_c} = 10_{3,7} - 9_{3,6}$	209.1	74.24	—	—	—
343 442.43(18)	C <sub>4</sub> H $\nu_7=1$	$J = 73/2 - 71/2, l = f$	550.4	376.7	7.95 ± 0.4	1.673	0.235
343 640.05(19)	C <sub>4</sub> H $\nu_7=2^2$	$J = 73/2 - 71/2$	795.7	624.3	8.8 ± 0.2	0.8023	0.235
344 123.63(35)	C <sub>4</sub> H $\nu_7=2^2$	$J = 71/2 - 69/2$	794.7	641.4	7.9	1.133	0.235
343 737.40	H <sup>13</sup> CCCN	$J = 39 - 38$	330.0	543.1	—	—	—

Table 4.2 continued

Table 4.2: List of all detected transitions (continued)

Rest Frequency	Molecule (MHz)	Transition	$E_{\text{up}}$ (K)	$S_{ij}\mu^2$ ( $D^2$ )	$v_{\text{exp}}$ $\text{km s}^{-1}$	$\int Sdv$ ( $\text{Jy km s}^{-1}$ )	$\sigma^a$ ( $\text{Jy km s}^{-1}$ )
343 942.00(74)	U	–	–	–	$10.9 \pm 1.0$	0.6825	0.235
345 608.26(5)	HC <sub>3</sub> N	$J = 38 - 37$	323.5	529.1	$8.4 \pm 0.1$	25.06	0.576
345 795.99	CO	$J = 3 - 2$	33.19	0.03631	–	–	–

NOTE — Spectroscopic data were obtained from Cologne Database of Molecular Spectroscopy (CDMS) (Müller et al., 2005), except in the case of CH<sub>3</sub>CN, for which the Jet Propulsion Laboratory catalog was used (Pickett et al., 1998). For blended lines and those with peak flux under  $3\sigma$ , no fit was performed, and the catalog frequency is shown with no uncertainty. In the case of weak lines that initially failed to converge, the line width was fixed to  $7.9 \text{ km s}^{-1}$  and no error for that parameter is listed. <sup>a</sup>Reported rms is given over  $17 \text{ km s}^{-1}$  line width. <sup>b</sup>Redshifted component of HCN emission, separate fit performed. <sup>c</sup>Gaussian profile used for line fit, listed expansion velocity is half the FWHM.

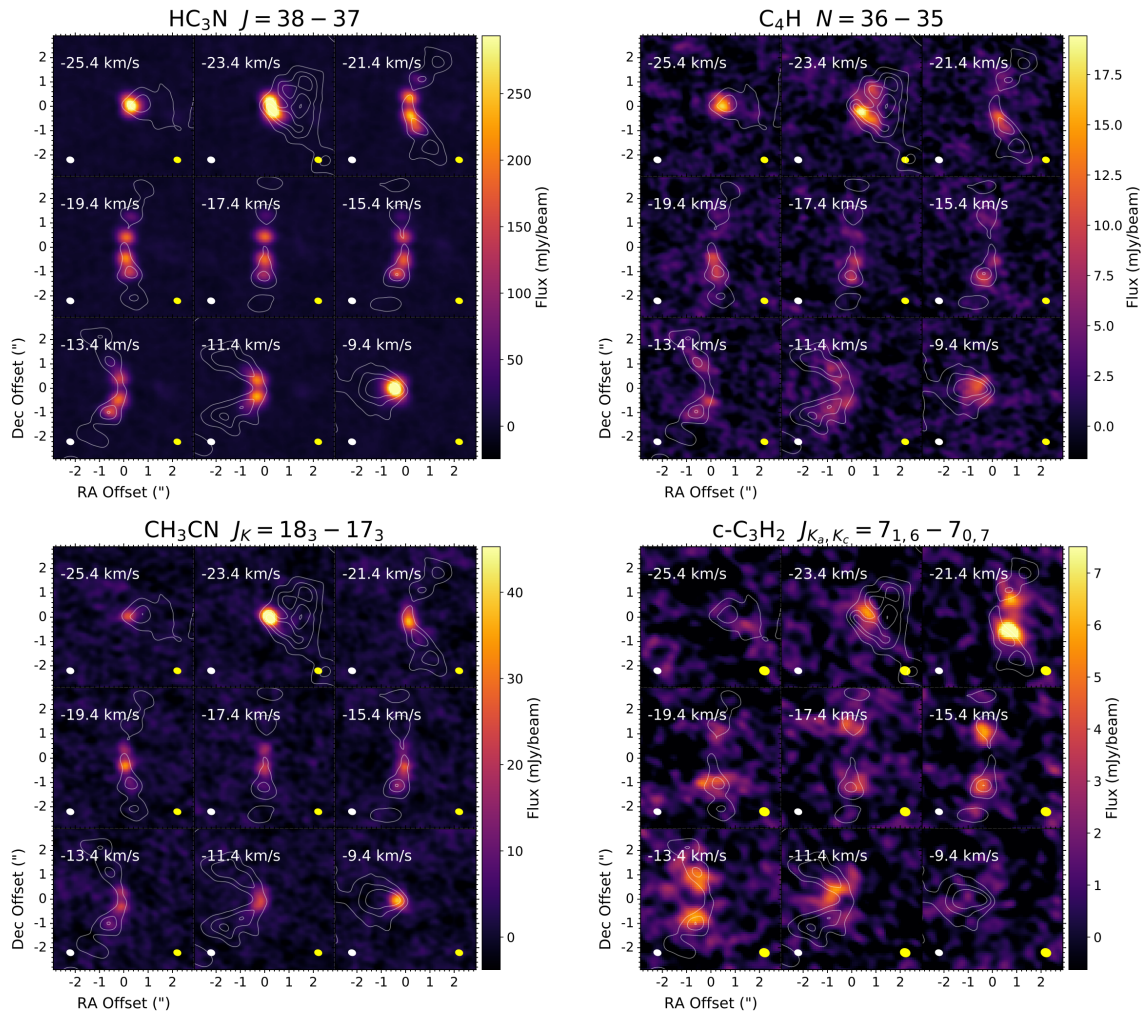


Figure 4.4: Channel maps of selected C-bearing molecular transitions. All images are overlaid with corresponding channel maps from  $^{13}\text{CO } J = 3 - 2$  in white at 20%, 40%, and 60% the peak flux of that image (0.166 Jy). White ellipses denote the synthesized beam for the  $^{13}\text{CO}$  window, while yellow ellipses indicate the shape of the beam for the mapped molecule.

### 4.3.2 Emission maps

To explore the spatial morphologies of chemical products in the DUDE, we first create channel maps for all unblended transitions above a  $5\sigma$  intensity threshold. The channel maps span a range of  $50 \text{ km s}^{-1}$  and are centered on the system velocity of V Hya. A sample of these channel maps, chosen to demonstrate the range of

regions in the disk sampled by hydrocarbon daughter species, is shown in Fig. 4.4. The transitions mapped here ( $\text{HC}_3\text{N}$ ,  $\text{C}_4\text{H}$ ,  $c\text{-C}_3\text{H}_2$ , and  $\text{CH}_3\text{CN}$ ) show the expected velocity pattern of an expanding disk inclined (roughly) along the N-S axis, and mostly appear to be spatially coincident with  $^{13}\text{CO}$ , and thus the density structure of the outflow. In our discussion of these maps, we adopt the nomenclature of Sahai et al. (2022), who labeled the major density rings at 560, and 1040, and 1740 au as R1, R2, and R3, respectively. In the  $-17.4 \text{ km s}^{-1}$  velocity channel seen in Fig. 4.4, the positions of the R1 and R2 structures can be seen as the two peaks in the N-S direction at distances of  $1''$  and  $2.5''$  from the image center.

Sahai et al. (2022) also identified a central “R0” ring from the distribution of the  $\text{HC}_3\text{N } J = 38 - 37$  transition, apparent in Fig. 4.4 as well. They note that this should be considered separately from the other rings in the DUDE, as it is not reproduced in  $^{12}\text{CO}$  or  $^{13}\text{CO}$ , and therefore could result from chemistry in this region of the DUDE. We now see in Fig. 4.4 that this R0 ring is also observed in  $\text{C}_4\text{H}$ , and potentially  $\text{CH}_3\text{CN}$  as well. In our calculation of abundances (Section 4.4), we will discuss whether the R0 structure is actually a region of increased chemistry producing these daughter species, or rather a location where conditions are energetically favorable for the mapped lines to be excited.

After image cubes were created for each transition, we then made velocity-integrated intensity maps (moment zero) to investigate the total distribution of emission for each transition. A selection of these maps is shown in Figure 4.4, including the positions of R0, R1, R2, and R3. Most species show ring-like patterns tracing the general structure of the DUDE, and often exhibit intensity minima at the position of V Hya. The exceptions to this are lines with centrally peaked emission maps including parent molecules  $\text{SiO}$ ,  $\text{CS}$ ,  $\text{HCN}$ ,  $\text{SiC}_2$ , and peculiarly, the more complex species  $\text{CH}_3\text{CN}$ .

The vast majority of flux for even the most extended species comes from within the

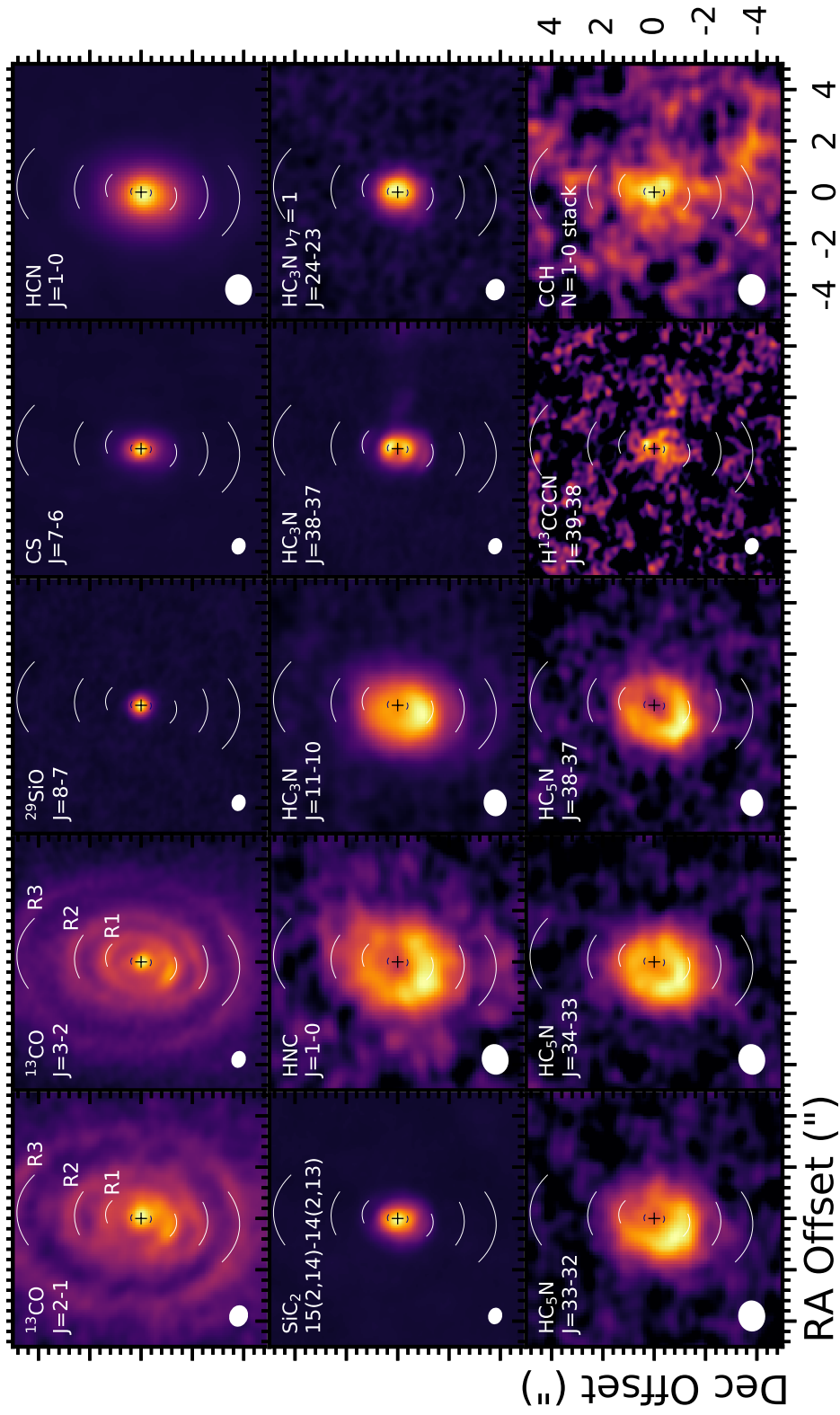


Figure 4.4: Integrated intensity maps of the brightest transitions detected for all species. Ring structures R1, R2, and R3 are denoted by white arcs in each panel, and the synthesized beams are shown in the bottom-left corners. The compact ring R0 at 160 au is shown in black arcs surrounding the position of V Hya (black cross). The color scale in each image is adjusted to best show emission sub-structure. Maps were integrated over a width of  $21 \text{ km s}^{-1}$  centered on the system velocity of V Hya.

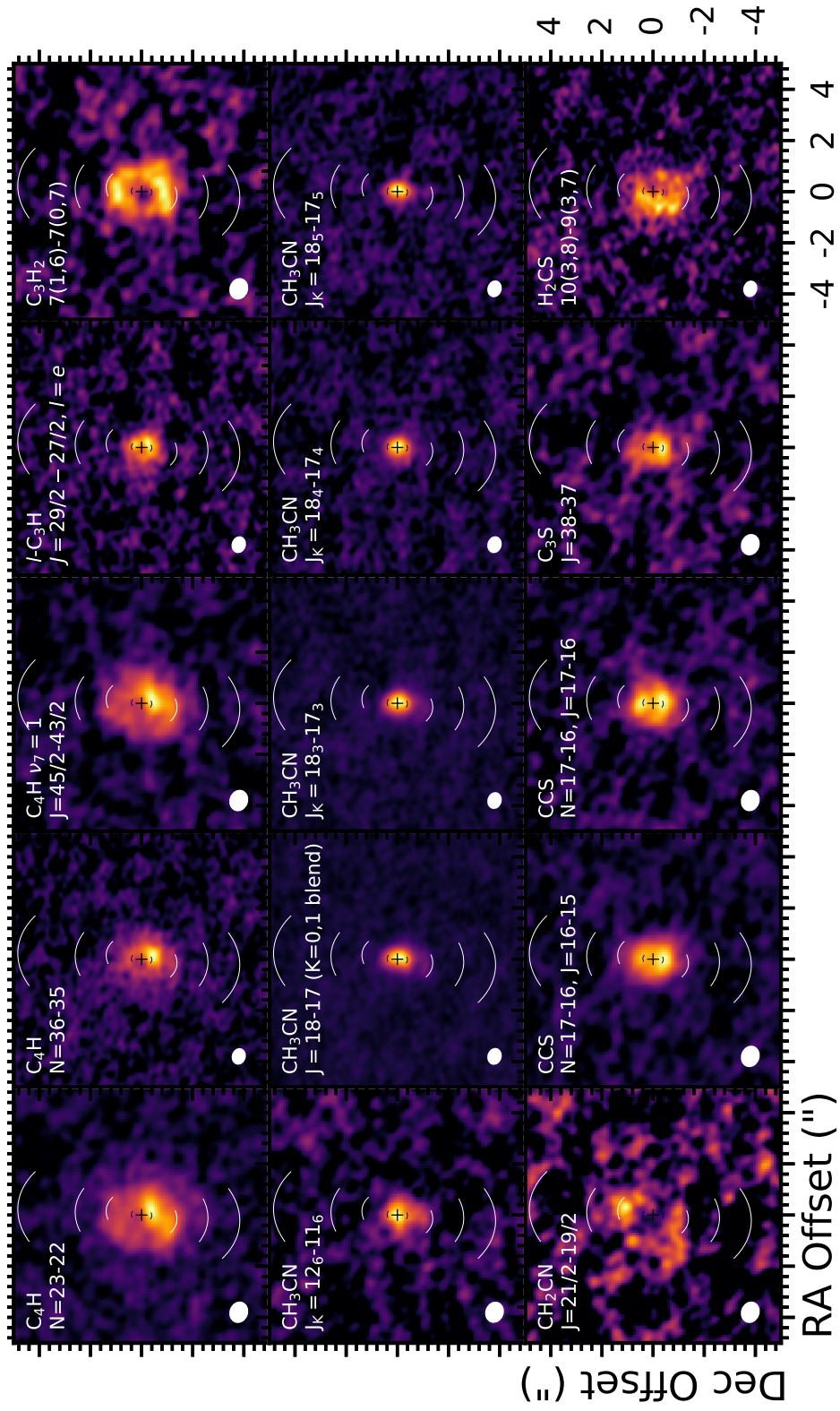


Figure 4.4: Continued.

R2 ring. And for lines detected at Bands 6 and 7, emission is primarily constrained within R1, and often traces the innermost ring R0 at 160 au. In general, the lines observed at Band 3 show a larger area of emission, and a farther radial intensity peak than those at higher frequencies, with HNC  $J = 1 - 0$  and HC<sub>3</sub>N  $J = 11 - 10$  being the only species with emission detected at R3. This is typical for observations of AGB stars, where low-lying rotational states tend to be populated more in cooler regions of the envelope (Agúndez et al., 2017; Siebert et al., 2022a).

Due to the inclination of the source we expect to see a systematic azimuthal brightness asymmetry, i.e., even if the DUDE was a uniform disk, it would appear brighter along the N–S direction than along the E–W direction. Interestingly though, in Fig. 4.4 we also find departures from this expected pattern in the spatial distributions of the most compact molecules. The clearest example of this is C<sub>4</sub>H, which shows brighter emission on the southern side of R0 in every transition we observed (this is also apparent in the channel maps in the top right panel of Fig. 4.4). The same behavior is also observed in C<sub>3</sub>S and to a lesser extent in CCS, and it is notably absent from the  $J = 38 - 37$  line of HC<sub>3</sub>N. This effect is different from the anisotropy noted in the R1 ring by Sahai et al. (2022) (which can also be seen in panels of Fig. 4.4 with emission at R1), as it is not observed in the density tracing <sup>13</sup>CO lines, and it is only specific to these molecules. This points to these brightness enhancements being driven by asymmetric chemistry in the inner regions of the DUDE.

### 4.3.3 Kinematic structure and radial profiles

To further investigate these maps within the context of V Hya’s circumstellar structure, we utilize the publicly available Python module GoFish (Teague, 2019). With these tools, we are able to take advantage of the known geometric and velocity properties of the DUDE to shift the spectra associated with each pixel to a com-

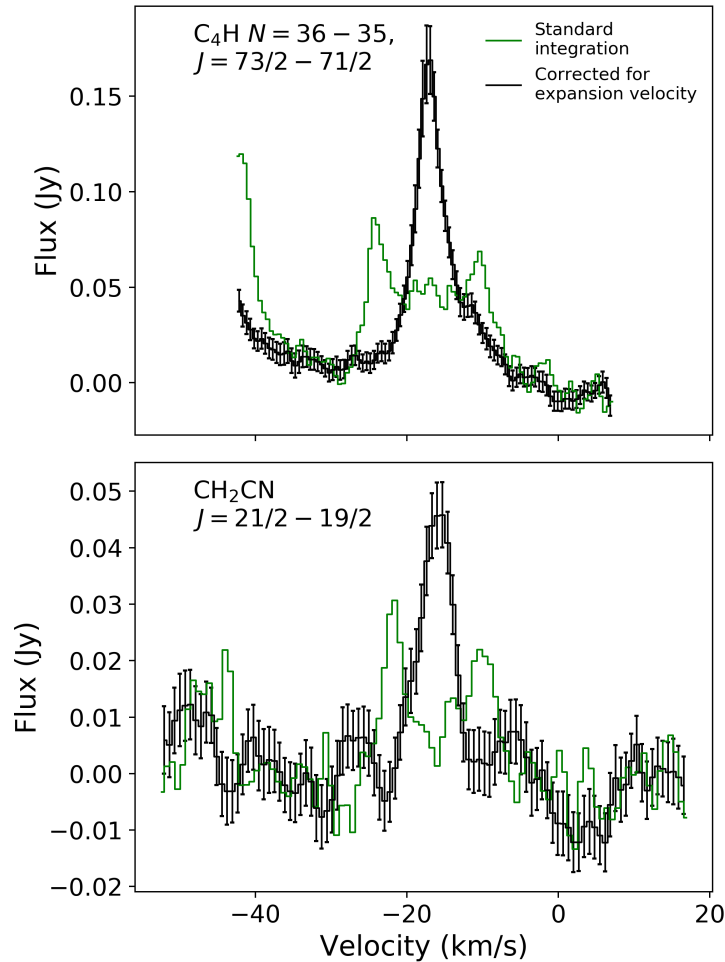


Figure 4.5: Demonstration of line shifting and stacking algorithm for a strong (top) and weak (bottom) rotational line. Error bars in the corrected spectra denote the standard deviation of flux measurements in a particular velocity bin. Spatial integrations were performed over a deprojected radius range of  $0'' - 1.5''$  for  $C_4H$  and  $0'' - 3''$  for  $CH_2CN$ .

mon line center and stack them (Yen et al., 2016), increasing the S/N of detections. Because this software is built for analysis of protoplanetary disks, we modified the Keplerian velocity model it uses to instead account for the expanding nature of V Hya’s torus, using the velocity profile presented in Sahai et al. (2022) and the inclination of the disk ( $46^\circ$ ). To test the utility this kinematic model has in manipulating spectra at different locations in the DUDE, we performed a velocity-corrected stack for the

$N = 36 - 35$  transition of  $C_4H$  and the tentatively-detected the  $J = 21/2 - 19/2$  line of  $CH_2CN$  Fig. 4.5. We find here that when the spectra are averaged with a common central velocity, the line profiles become single-peaked, and the signal-to-noise ratios are boosted by over 100%. This method could thus be a powerful tool in the future for identifying weak molecular signatures in interferometric observations of disk/torus structures surrounding evolved stars, as has proven to be the case for protoplanetary disks (e.g. Matrà et al., 2017). Refer to Appendix 4.6 for additional applications of line stacking in these observations.

In addition to increasing significance of molecular detections, we also use GoFish to measure the radial profile of line intensities in the outflow of V Hya. Using the same physical model of the DUDE, for each transition we compute velocity-integrated line fluxes averaged within annuli at all radii in the disk, and convert to temperature. It is important to note that this method assumes an infinitely thin 2D structure, and therefore does not take into account the height and flared structure of the DUDE. This means that each bin samples a slightly larger range of radii than expected, since line of sight positions can be contaminated with emission from above/below the mid-plane of the disk.

The deprojected and azimuthally averaged radial profiles for each mapped transition toward V Hya are shown in Fig. 4.6. The conversion to brightness temperature was done under the Rayleigh-Jeans approximation, and the physical units shown on the upper axis of each plot were calculated using a distance of 400 pc (eDR3, Gaia Collaboration et al., 2021). We do note that Andriantsaralaza et al. (2022) present statistical corrections to GAIA distances for many AGB stars including V Hya (529 pc) using a Bayesian statistical method based on VLBI measurements of maser sources, as well as new distances calculated using a revised period-luminosity relationship (311 pc). For consistency with Sahai et al. (2022), and we choose to

adopt the uncorrected GAIA distance (400 pc) in this work.

Looking in general at the intensity profiles in Fig. 4.6, we find that most transitions have ring-like distributions with a single maximum, occurring at various positions in the disk. We also see that every transition has a primary maximum at or within the position of R1, and rarely (only in the case of Band 3 lines) do we see any flux outside of R2. The position of R0 can be seen as the maximum for  $\text{HC}_3\text{N } J = 38 - 37$  and all  $\text{C}_4\text{H}$  lines; however, there is also evidence of species that peak in intermediate regions of the inner 500 au, for example, *c*- $\text{C}_3\text{H}_2$  and  $\text{H}_2\text{CS}$  are found slightly inward of R1 but not as compact as R0. In addition to the species with ring-shaped intensity profiles, others show centrally-peaked emission. These transitions can be categorized into two groups: those with flat-topped patterns (e.g.  $\text{CCS}$ ,  $\text{C}_3\text{S}$ ), and those with more “cusped” profiles (e.g.  $\text{CS}$ ,  $\text{HCN}$ ). Interestingly, the distributions of  $\text{CH}_3\text{CN}$  lines appear to modulate from nearly flat-topped to cusped with increasing  $K$  values, indicating an energetic dependence on the spatial extent of this molecule. We will explore this effect further in our discussion of excitation and abundances in Section 4.4.

Fig. 4.6 also shows a comparison between the global intensity average and that obtained over a  $100^\circ$  wedge directed to the south. The latter is included to quantitatively demonstrate spatial asymmetries which tend to occur in this direction. We again see that  $\text{C}_4\text{H}$  shows consistent anisotropy among its transitions, with its southward profiles appearing  $\sim 50\%$  brighter than the average over all angles of the disk. This is the only molecule that shows this degree of angular asymmetry. A similar behavior of southward brightness enhancement can be seen for many lines showing emission at R1 (e.g.  $\text{HNC}$ ,  $\text{CH}_3\text{CN}$ ,  $\text{HC}_3\text{N}$ ), which is due to a density asymmetry in this ring, as it is apparent in  $^{13}\text{CO}$  as well.

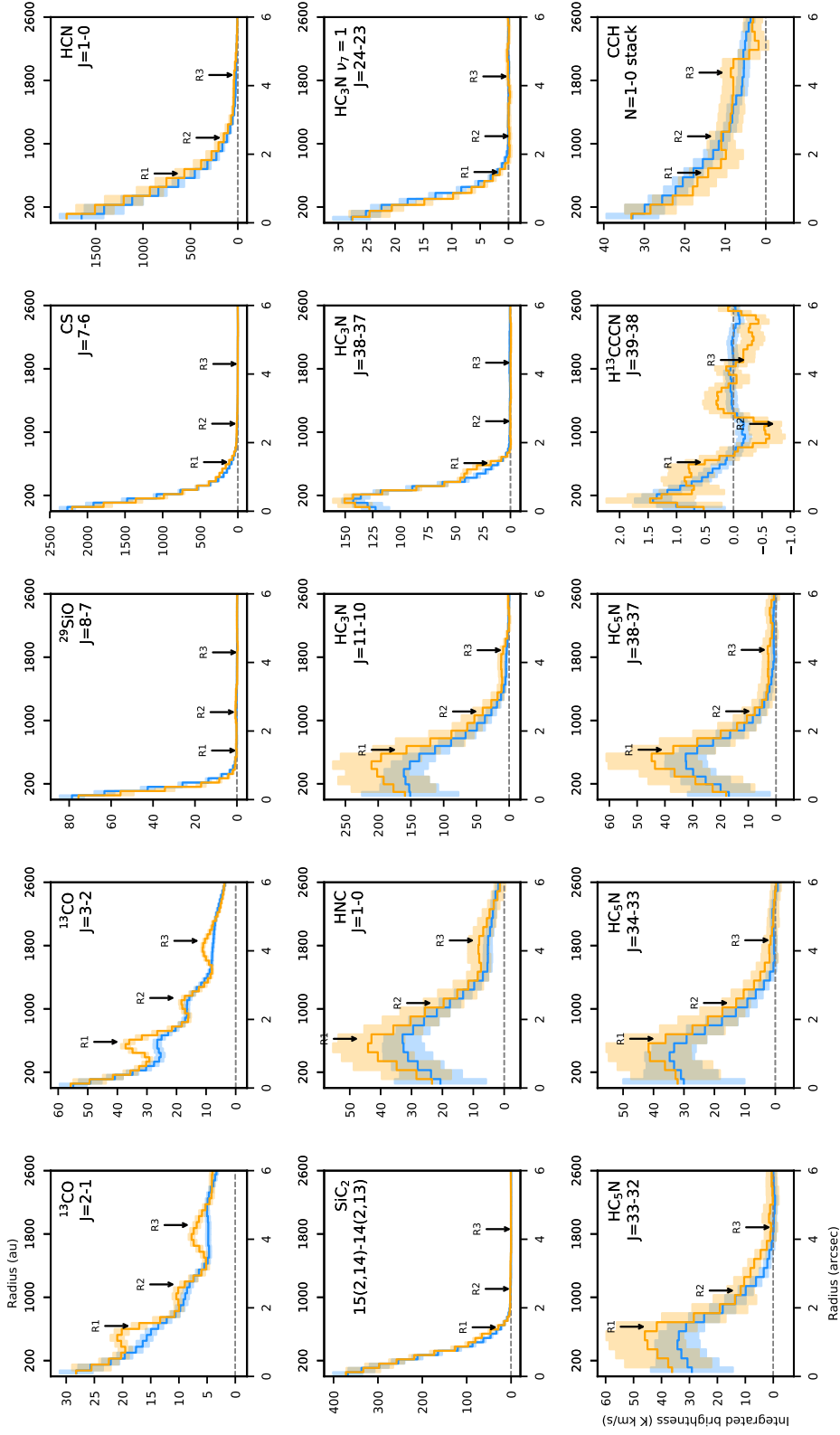


Figure 4.6: Velocity-integrated radial intensity profiles of unblended, mapped transitions toward V Hya. For each line, two profiles are shown; one corresponding to the average over all angles in the disk (blue), the other extracted over a southward-pointing  $100^\circ$  wedge. Shaded regions around both curves denote the standard deviation in each radial bin. Bin sizes are one quarter the major axis of the synthesized beam. Ring structures R1, R2, and R3 are labeled with arrows.

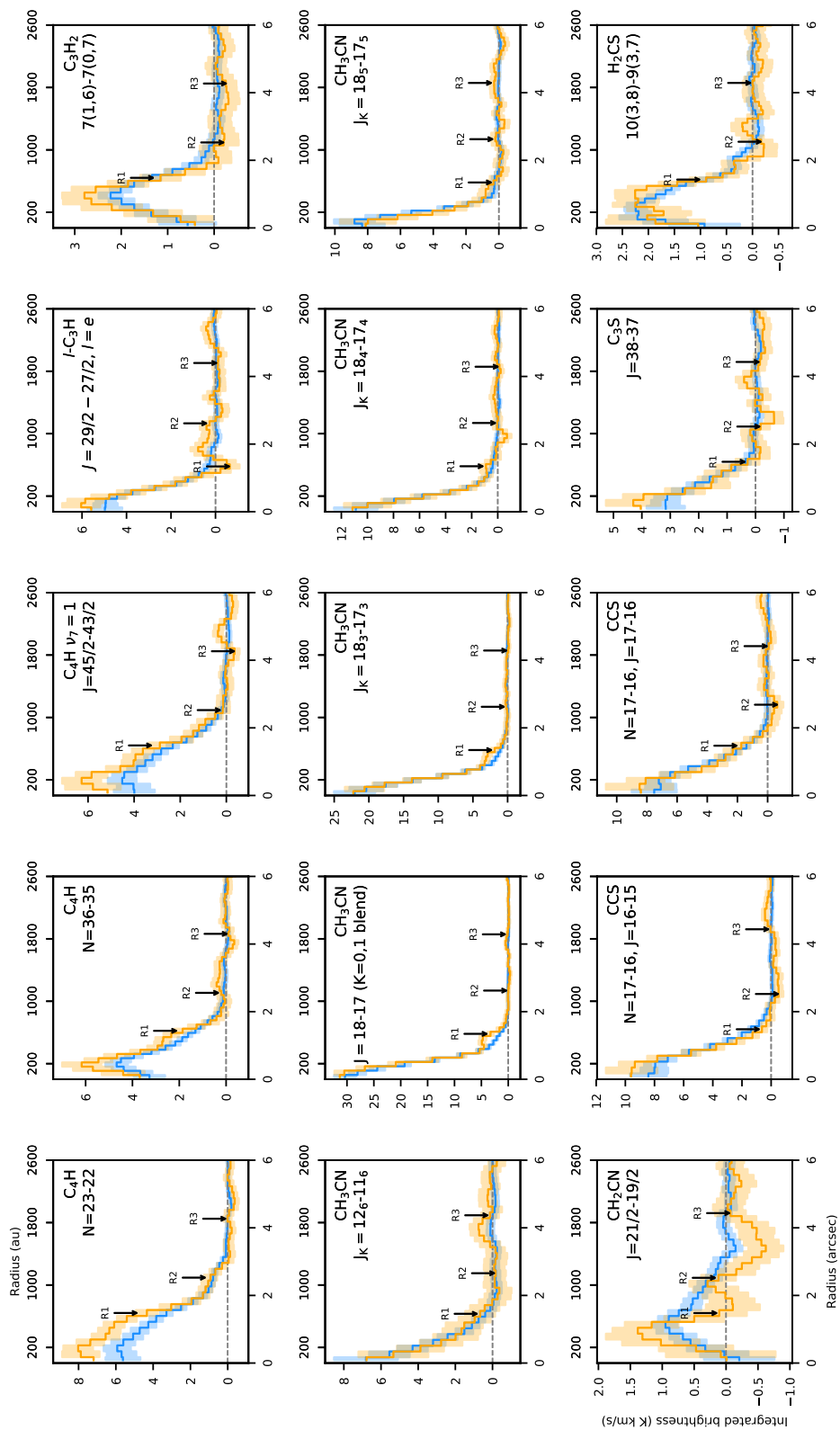


Figure 4.6: Continued.

## 4.4 Discussion

### 4.4.1 Summary of detected species

The species detected and imaged in this work are important pieces in a broad network of chemical processes at work in the circumbinary waist of V Hya. Here, we will examine this molecular inventory in the context of circumstellar chemistry as a whole, and discuss the observed lines and likely formation mechanisms of each species found in this unique source.

#### SiO (silicon monoxide)

An abundant parent molecule known for its maser emission in M-type AGB envelopes (Gray et al., 1999; Chibueze et al., 2016), SiO is the only major carrier of oxygen other than CO in C-rich stellar outflows (Agúndez et al., 2020). Toward V Hya, the  $J = 8 - 7$  transition  $^{29}\text{Si}$  isotopologue is detected with a centrally-peaked distribution that is likely optically thick (Sahai et al., 2022).

#### CS (carbon monosulfide)

CS is the primary gas phase reservoir of sulfur in carbon rich stellar winds, and forms out of thermochemical equilibrium in the extended atmospheres of AGB stars (Agúndez et al., 2020). The emission of this molecule toward V Hya was also discussed in Sahai et al. (2022), where it is found that the  $J = 7 - 6$  transition shown here is optically thick and subthermally excited.

#### SiC<sub>2</sub> (silacyclopropynylidene)

SiC<sub>2</sub> is another important parent molecule in C-rich AGB stars. There is observational evidence that this species is a precursor to SiC grains in the inner regions of stellar envelopes (Massalkhi et al., 2018a), making it important to dust nucleation

models. In these ALMA observations, the  $15(2, 14) - 14(2, 13)$  transition is prominent and centrally peaked (Sahai et al., 2022), and we also find evidence of emission lines from the  $\nu_3 = 1$  vibrational state, which lies at  $196.37 \text{ cm}^{-1}$ . Though these transitions are too weak to map, their profiles suggest that they arise from central regions of the DUDE where the IR flux is high.

### **HCN (hydrogen cyanide)**

Along with  $\text{C}_2\text{H}_2$ , HCN is one of the most abundant parent molecules in carbon star environments (Agúndez et al., 2020). In addition to being a major reservoir of carbon, this molecule is important precursor to more complex species, as its photodissociation into  $\text{H} + \text{CN}$  drives the formation of cyanopolyynes and longer carbon chains (Agúndez et al., 2017). In V Hya, we detect the  $J = 1 - 0$  transition of this species, which is optically thick due to the high abundance and intrinsic line strength. Like CS its average brightness temperature in the central region of the DUDE ( $\sim 60 \text{ K}$ ) implies that it may trace warmer regions near the surface of the disk. We also find HCN in the high velocity spot.

### **HNC (hydrogen isocyanide)**

As a less stable isomer of HCN, HNC requires additional chemical processing to appear in stellar winds. It is formed primarily through the dissociative recombination of  $\text{HCNH}^+$ , which is supplied from cosmic ray and photochemical interactions (Daniel et al., 2012). Because of this, HNC typically shows shell-like distributions in carbon-rich outflows. Toward V Hya, we see emission from the  $J = 1 - 0$  transition in an large ring peaking at R1 and extending past R3.

## HC<sub>3</sub>N (cyanoacetylene)

HC<sub>3</sub>N is a key molecule in kinetic-driven photochemistry surrounding carbon stars. Produced from the reaction between C<sub>2</sub>H<sub>2</sub> and CN, HC<sub>3</sub>N is the first (and most abundant) cyanopolyynes to form, and thus marks the location in an outflow where carbon chain polymerization becomes efficient. We detect HC<sub>3</sub>N at both Band 3 and Band 7, in addition to the  $\nu_7 = 1$  excited state at Band 6. Like in the case of IRC+10216 (Siebert et al., 2022a; Agúndez et al., 2017), the  $J = 38 - 37$  transition shows a more compact emission than the lower energy line  $J = 11 - 10$ ; however, unlike IRC+10216, these lines do overlap in their spatial distributions toward this source. The  $J = 24 - 23$  line of the  $\nu_7 = 1$  state notably shows centrally-peaked emission.

## HC<sub>5</sub>N (cyanodiacetylene)

Similar to HC<sub>3</sub>N, HC<sub>5</sub>N is primarily formed through diacetylene (C<sub>4</sub>H<sub>2</sub>) reacting with CN. Because this process requires available C<sub>4</sub>H<sub>2</sub> from hydrocarbon growth, this higher level of complexity is only reached in regions where UV-driven photochemistry is very active (see Fig. 5 in Agúndez et al., 2017). In the environment of V Hya, we see HC<sub>5</sub>N emission peaking near R1; however, interestingly its flux does not drop to zero at the center of the map as it does in other C-rich sources. Though the beam size of ALMA is larger at the  $\lambda \sim 3$  mm wavelengths where HC<sub>5</sub>N is detected, we do not attribute this behavior to these observational effects, as even in the system velocity channel map where ring emission is at its farthest extent, these transitions are seen at the central position of V Hya.

## **CCH (ethynyl radical)**

CCH is the main photodissociation product of acetylene ( $C_2H_2$ ). Because it is quick to undergo neutral-neutral reactions and thereby extend carbon chains, its abundance typically peaks at larger radii than cyanopolyynes, where the extinction of UV photons is lower (Agúndez et al., 2017). Toward V Hya, we find weak emission from a group of features consistent with the spin-coupling hyperfine components of the  $N = 1 - 0$  transition of this molecule. The stacked emission of the brightest components ( $F = 2 - 1$  and  $F = 1 - 0$ ) reveals a peculiar spatial distribution that is centrally peaked and gradually decreases throughout the DUDE. This is in stark contrast to other AGB envelopes, where CCH is almost always found in a shell pattern (Unnikrishnan et al., 2023).

## ***l*-C<sub>3</sub>H (propynylidyne radical)**

Next in the sequence of hydrocarbon radicals, linear  $C_3H$  was first detected in IRC+10216 (Thaddeus et al., 1985), and has been observed in other C-rich AGBs and post-AGBs as well (Unnikrishnan et al., 2023; Pardo et al., 2007). In our data, we see two lines at Band 7 corresponding to two components of the  $J = 29/2 - 27/2$  transition. The distribution is compact, and peaks near R0 like  $HC_3N$ .

## **C<sub>4</sub>H (butadiynyl radical)**

$C_4H$  has two main formation pathways: the first, analogous to CCH, is through the photodestruction of  $C_4H_2$ ; the second is through the reaction  $CCH + C_2$ . In this sense, this molecule is parallel to  $HC_5N$  in its chain length since it is mainly dependent on the availability of  $C_4H_2$ . Because of this, its abundance typically follows a similar distribution to  $HC_5N$  (Cordiner & Millar, 2009).

As noted previously,  $C_4H$  is one of the most prominent species found in this

study of V Hya, with 16 total transitions detected spanning four different vibrational modes (including the ground state). All observed lines are co-spatial with each other, appearing in a compact ring peaking near R0 (160 au), with a strong preference toward the southern portion of the DUDE.

### **c-C<sub>3</sub>H<sub>2</sub> (cyclopropenylidene)**

c-C<sub>3</sub>H<sub>2</sub> is another important hydrocarbon in C-rich stellar outflows. It is proposed to form in trace amounts as a parent species, but in regions of kinetic-driven chemistry c-C<sub>3</sub>H<sub>2</sub> can be synthesized from barrierless reactions involving CH, CCH, and C<sub>3</sub>H (Van de Sande et al., 2018). This species was shown to be coincident with C<sub>4</sub>H toward the carbon star IRAS 15194-5115 by Unnikrishnan et al. (2023), and its excitation temperature in IRC+10216 also implies a daughter-like distribution (Kawaguchi et al., 1995). Toward V Hya, the emission we observe from the 7(1,6) – 7(0,7) transition shows a hollow distribution with a maximum at ~400 au. This is notably at a larger radius than C<sub>4</sub>H, which may result from the smaller upper state energy of the c-C<sub>3</sub>H<sub>2</sub> transition.

### **CH<sub>3</sub>CN (methyl cyanide)**

Methyl cyanide is one of the more complex species we detect toward V Hya, in addition to being a useful temperature probe due its symmetric top geometry. This molecule is produced mainly through the dissociative recombination of CH<sub>3</sub>CNH<sup>+</sup>, an intermediate formed from the radiative association of CH<sub>3</sub><sup>+</sup> and HCN. Despite this being a process predominantly driven by photochemistry (in addition to cosmic rays), Agúndez et al. (2015) report a very compact (though still hollow) abundance distribution of this molecule in the envelope of IRC+10216 which could not be reproduced by chemical models. We detect the  $J = 18 - 17$  family of lines toward V Hya, in addition to the  $K = 6$  component of  $J = 12 - 11$ . These transitions show centrally-peaked

integrated intensity maps, though inspection of channel maps (Fig. 4.4) shows a ring located at  $r \sim 0.35''$  from V Hya.

### **CH<sub>2</sub>CN (cyanomethyl radical)**

To date, CH<sub>2</sub>CN has only been observed in the envelope of IRC+10216, where its column density is less than CH<sub>3</sub>CN by a factor of three (Agúndez et al., 2008). This species is formed from the same dissociative recombination that is responsible for CH<sub>3</sub>CN, with a comparable branching ratio between the two products (Loison et al., 2014). We initially label CH<sub>2</sub>CN as a tentative detection toward V Hya because only one transition ( $J = 21/2 - 19/2$ ) is observed, and it is quite weak; however, as discussed in Section 5.3.1, applying a pixel-by-pixel velocity correction increases this significance notably. The intensity map and radial profile are consequently low S/N, though emission is seen slightly interior to R1, similar to c-C<sub>3</sub>H<sub>2</sub>.

### **CCS (dicarbon sulfide)**

Analogous to the polyene and cyanopolyene chemistry discussed above, sulfur-terminated carbon chains are also known to form in AGB environments. In the ISM, a common pathway to CCS is through the exothermic reaction between atomic S and CCH (Petrie, 1996b), which is likely dominant in evolved stars due to the availability of acetylene and CCH. CCS is known in IRC+10216, as well as three additional carbon stars studied in Unnikrishnan et al. (2023). Here, we detect two transitions of CCS toward V Hya. The integrated maps show intensity peaks near R0 with a relatively flat profile inward. This distribution is likely very similar to HC<sub>3</sub>N  $J = 38 - 37$ , though appears less ring-like due to the larger beam size at Band 6 where CCS is detected.

## **C<sub>3</sub>S (tricarbon monosulfide)**

C<sub>3</sub>S can be formed through direct C addition onto CCS or through another neutral-radical reaction between CCH and CS (Millar et al., 2001). We report one cleanly detected transition of this molecule toward V Hya at 219 620 MHz, which shows a similar distribution to CCS, though with a slight enhancement to the southern portion of the DUDE.

## **H<sub>2</sub>CS (thioformaldehyde)**

H<sub>2</sub>CS is known toward IRC+10216, and the proto-planetary nebula CRL 2688 (Agúndez et al., 2008; Zhang et al., 2013). The main chemical route to this species involves a neutral–neutral reaction between CH<sub>3</sub> and atomic S (Woods et al., 2003). In V Hya, we detect blended emission from the 10(3, 8)–9(3, 7) and 10(3, 7)–9(3, 6) transitions, as well as a very weak feature that could be attributed to the 10(4, 7)–9(4, 6) line. The stacked intensity map of the former two lines shows flux out to R1, and a peculiar east-west asymmetry that is not seen from any other molecule in V Hya.

### **4.4.2 Excitation analysis of CH<sub>3</sub>CN**

To investigate temperature and excitation conditions in the inner disk of V Hya, we employ a radial population diagram method (similar to that performed in Loomis et al., 2018a) using the integrated intensity profiles of CH<sub>3</sub>CN derived in Section 5.3.1. Following the formalism of (Goldsmith & Langer, 1999), the Boltzmann equation for rotational populations can be arranged in the following way:

$$\ln \frac{N_u}{g_u} = \ln \left( \frac{N_T}{Q(T_{\text{rot}})} \right) - \frac{E_u}{kT_{\text{rot}}} \quad (4.3)$$

Where  $N_u$  is the column density of the upper state,  $g_u$  is the degeneracy of the

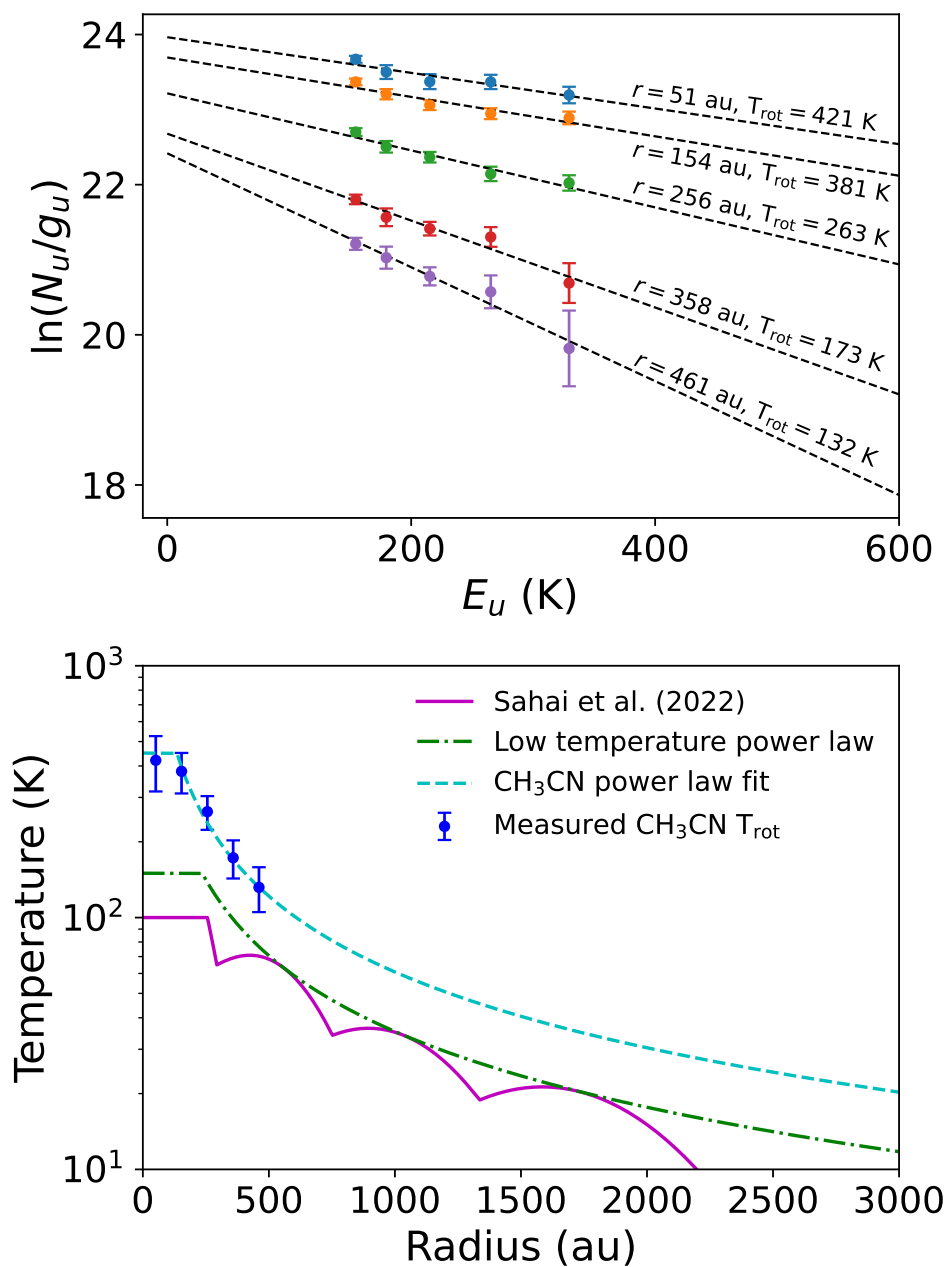


Figure 4.7: Top: Population diagrams constructed using radial brightness distributions of  $\text{CH}_3\text{CN}$  lines detected toward V Hya. Points correspond to  $K$ -states of the  $J = 18 - 17$  transition, from left to right:  $K = 0, 1$  blend,  $K = 2, \dots, K = 5$ . Dashed lines denote linear fits to the temperature. Bottom: Measured excitation temperature compared with the kinetic temperature profile calculated in Sahai et al. (2022).

upper state,  $N_T$  is the total column density,  $Q$  is the partition function,  $E_u$  is the upper state energy, and  $T_{\text{rot}}$  is the rotational excitation temperature. We obtain  $\frac{N_u}{g_u}$  first using the optically-thin intensity approximation:

$$\frac{N_u^{\text{thin}}}{g_u} = \frac{3k \int T dv}{8\pi^3 \nu S_{ij} \mu^2} \quad (4.4)$$

where  $\nu$  is the transition frequency,  $S_{ij} \mu^2$  is the line strength, and  $\int T dv$  is the velocity-integrated intensity. We also apply an optical depth correction factor  $C_\tau$ :

$$N_u = N_u^{\text{thin}} C_\tau \quad (4.5)$$

$$C_\tau = \frac{\tau}{1 - e^{-\tau}} \quad (4.6)$$

where  $\tau$  can be estimated to first-order by substituting Eq. 4.4 into the following:

$$\tau = \frac{8\pi^3 S_{ij} \mu^2}{3h\Delta v} \frac{N_u}{g_u} \left( e^{h\nu/kT_{\text{rot}}} - 1 \right) \quad (4.7)$$

using  $16 \text{ km s}^{-1}$  as the line width ( $\Delta v$ ). This allows us to plot  $\ln \frac{N_u}{g_u}$  as a function of  $E_u$  for the observed transitions of  $\text{CH}_3\text{CN}$  and obtain  $N_T$  and  $T_{\text{rot}}$  from a linear fit to Eq. 4.3. This method is then performed on each radial measurement of  $\int T dv$ , which is re-binned to half the beam size of the maps to reduce the correlation between points. While most of the  $K$ -components of the  $J = 18 - 17$  transition are clearly separated in velocity, the  $K = 0$  and  $K = 1$  lines are blended, so we treat these as a single point in the rotation diagram. To do this, we combine their line strengths and integrate the total intensity over the blend to apply Eq. 4.4, and use the average of  $E_u$ , weighted by the respective  $S_{ij} \mu^2$  values of the two components, for the effective upper state energy. Because the resolution of the  $J_K = 12_6 - 11_6$  line does not match that of the  $J = 18 - 17$  lines, we omit it from this analysis, leaving five points to

constrain the temperature.

The results of these spatial population diagrams are shown in Fig. 4.7. At all radii in the DUDE where  $\text{CH}_3\text{CN}$  is seen, its transition intensities are well fit with a single rotational temperature. We obtain  $T_{\text{rot}} = 421$  K in the innermost regions of the disk, and this value decreases gradually with annuli at larger distances. The calculated  $\tau$  and  $C_\tau$  values are all  $< 0.01$  and  $< 1.005$ , respectively, suggesting that the transitions are optically thin.

If local thermodynamic equilibrium (LTE) is assumed, we find that the kinetic temperatures implied by  $\text{CH}_3\text{CN}$  are considerably larger than those derived in Sahai et al. (2022) through measurements of the brightness temperature of optically thick  $^{12}\text{CO}$  lines (bottom panel of Fig. 4.7). One possible explanation for this discrepancy could be that  $\text{CH}_3\text{CN}$  emission is arising from warmer vertical regions of the DUDE than  $^{12}\text{CO}$ . However, this would imply a temperature gradient that increases toward lower heights in the disk, which is opposite the result suggested from CS emission, as it shows higher brightness temperatures for larger  $\tau$ .

Another more likely scenario is that we are observing an effect of infrared (IR) pumping, where molecules are radiatively excited to higher vibrational states, and subsequently return to the ground state with larger rotational energy. This behavior was first observed for  $\text{CH}_3\text{CN}$  in the Orion molecular cloud by Goldsmith et al. (1983), and Agúndez et al. (2008) note that it can produce superthermal excitation temperatures for certain molecules in the envelope of IRC+10216. Massalkhi et al. (2019) showed that IR-pumping can yield  $T_{\text{ex}}/T_{\text{kin}} > 4$  for transitions of CS, SiO, and SiS in other carbon stars, which is consistent with the discrepancy in temperature laws shown in Fig. 4.7. Though we did not detect any transitions from vibrationally excited states of  $\text{CH}_3\text{CN}$ , the number of these lines we see from other species like  $\text{C}_4\text{H}$  and  $\text{HC}_3\text{N}$  suggests that IR pumping is an important excitation mechanism in

V Hya.

An important distinction between the result here and that observed in Goldsmith et al. (1983) is that the relative line strengths of ground state  $\text{CH}_3\text{CN}$  are well-characterized by a single excitation temperature, as opposed to having  $T_{\text{rot}}$  vary among K-states. This suggests that the rotational populations have still equilibrated to a Boltzmann distribution through a mix of collisional and radiative processes. Therefore, although the excitation temperature may not reflect the kinetic temperature in the DUDE, it can still be used as an estimate to derive the column densities and abundances using Eq. 4.3.

### 4.4.3 Abundance distributions

#### LTE abundance estimates

With new information on molecular excitation and temperature structure in the DUDE, we now aim to place estimates on the abundances of various species detected toward V Hya. Here, we will focus mainly on daughter species, as they are important in constraining circumstellar chemistry, and have more extended distributions resulting in lower optical depths.

As discussed previously, rotational populations in the DUDE are a result of a complex combination of collisional and radiative pumping processes. Unfortunately, a full simulation of these mechanisms for every molecule is not feasible due to a lack of an IR flux model throughout the DUDE, and unknown collisional excitation rates and vibrational band strengths for many of the species of interest. Therefore, in order to calculate abundances, we first employ an LTE approach adopting two different excitation models: the first is a cool model reflecting species thermalized to the kinetic temperature law in Sahai et al. (2022) (“low-temperature” curve in Fig. 4.7), the second is a warmer model representing molecules that have radiatively-

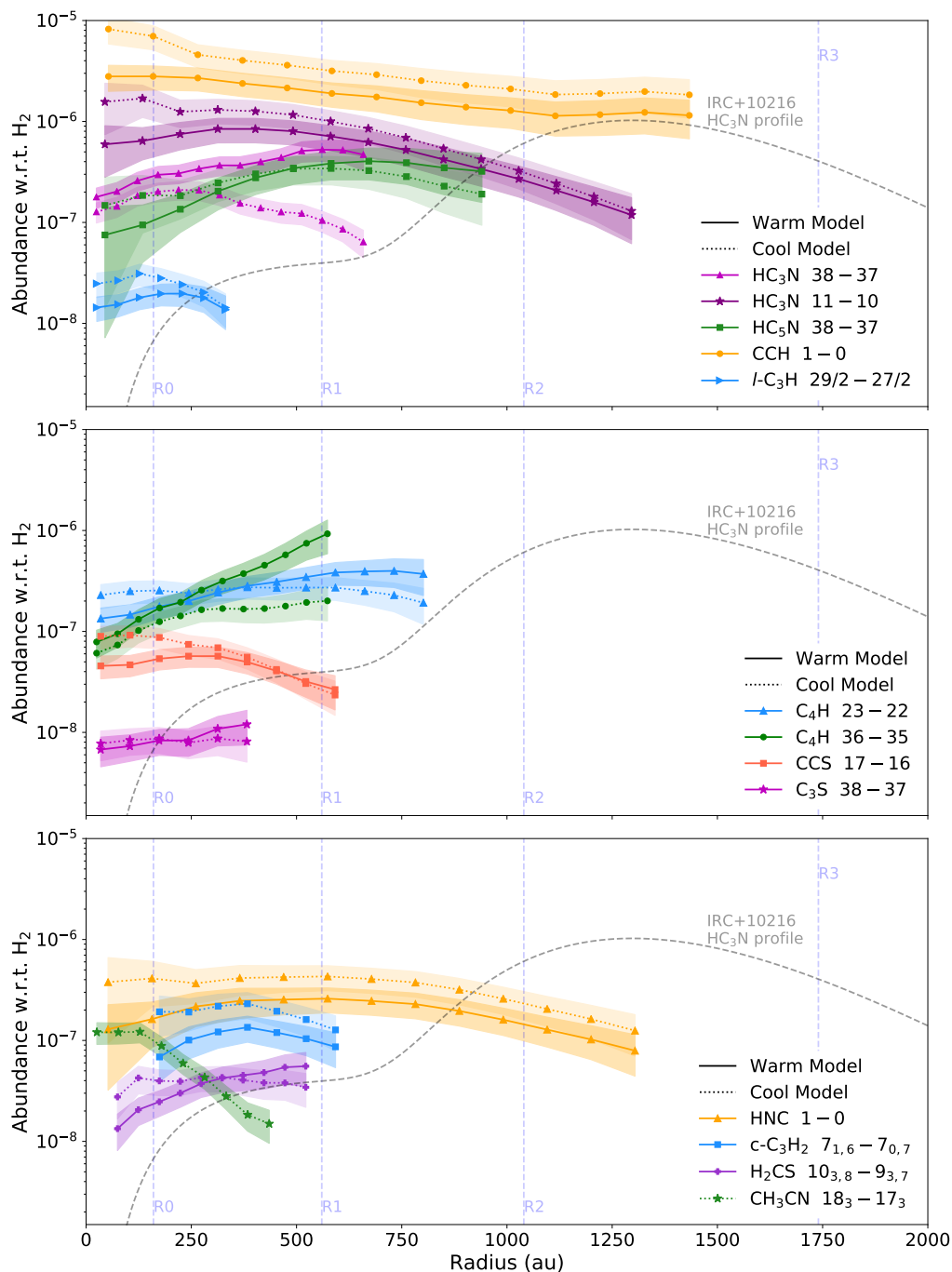


Figure 4.8: LTE-calculated radial abundance profiles of molecules detected toward V Hya. For each transition, two abundances are shown, corresponding to the cool (solid) and warm (dotted) temperature models discussed in Section 4.4.2. The shaded region around each profile denotes the uncertainty, including the standard deviation of flux in the radial bin, the noise level of the integrated image, and the ALMA flux calibration error. Radial spacing of points is one-quarter of the beam size, and values are only shown where the azimuthally averaged line flux is larger than 3 times the rms of the image.

driven excitation like  $\text{CH}_3\text{CN}$ . This casts a wide range in physical conditions, allowing us to still place strict bounds (within an order of magnitude) on abundances despite lacking a detailed excitation model.

To calculate the radial abundance profiles, we first measure the column densities yielded by each line using equations 4.3 and 4.4. We again apply a first-order optical depth correction, use the radial brightness profiles from Fig. 4.6 for values of  $\int T dv$ , and adopt the two temperature profiles discussed above to approximate  $T_{\text{rot}}$ . Then, we do the same calculation to obtain the radial column density of  $^{13}\text{CO}$ , and calculate the molecular abundance relative to  $\text{H}_2$  using the following:

$$f(r) = \frac{N_T(r)}{N_{^{13}\text{CO}}(r)} \times \frac{[^{13}\text{C}]}{[^{12}\text{C}]} \times f_{^{12}\text{CO}} \quad (4.8)$$

using a flat abundance of  $f_{^{12}\text{CO}} = 10^{-3}$  for  $^{12}\text{CO}$  and a  $^{12}\text{C}/^{13}\text{C}$  ratio of 70 (Sahai et al., 2022). To ensure that the numerator and denominator in Eq. 4.8 are sampled on the same spatial scales, we convolve the  $^{13}\text{CO}$   $J = 3 - 2$  map to match the beam size for each respective molecule, and recalculate the  $^{13}\text{CO}$  brightness profile with the new resolution. Abundances are then derived for all radii in the DUDE where the integrated line brightness is larger than 3 times the rms, with radial bin spacings at one-quarter the major axis of the beam.

The results of this analysis are shown in Fig. 4.8. Because the large mass-loss rate of V Hya ( $>10^{-5} M_{\odot} \text{ yr}^{-1}$ ; Knapp et al., 1997) is similar to that of IRC+10216, we also show the measured abundance profile of  $\text{HC}_3\text{N}$  in that source (Siebert et al., 2022a) as a reference for the typical distribution of a daughter molecule in C-rich AGBs. In general, the observed abundance profiles follow nearly log-linear or single-peaked distributions, and the radii where these product molecules are most abundant are all within 500 au. Furthermore, we see no correlation between the trends here

and the locations of the density enhancements R0–R2, meaning the chemistry appears to be independent of these physical structures. In Table 4.3, we provide the average abundances and column densities of each molecule in V Hya under the two temperature assumptions, along with their observed abundances in IRC+10216.

The difference between results obtained from the two adopted temperature profiles is typically less than a factor of two. The exceptions to this occur in cooler regions of the DUDE (around R1) for the high- $J$  transitions of  $\text{HC}_3\text{N}$  and  $\text{C}_4\text{H}$ . These higher energy states have larger transition rates, and are consequently more likely to be affected by non-LTE effects especially in cooler, lower density regions of the DUDE. We further explore these possibilities in Section 4.4.3 to better constrain the abundances of these molecules.

The observed abundances and column densities of the cyanopolyynes are in good agreement with those seen in the prototypical source IRC+10216 and other C-rich AGBs (Unnikrishnan et al., 2023), with the abundance of  $\text{HC}_3\text{N}$  reaching a maximum of  $\sim 10^{-6}$  and  $\text{HC}_5\text{N}$  showing slightly lower density and peaking farther out in the wind. In contrast, the obtained abundance for  $\text{C}_4\text{H}$  is notably smaller in V Hya ( $1\text{--}3 \times 10^{-7}$ ) than in other C-rich AGBs, where it is normally similar to that of  $\text{HC}_3\text{N}$ . A likely explanation for this is that an increased population of  $\text{C}_4\text{H}$  is present in vibrationally excited states, from which we have detected numerous rotational transitions (Table 4.2). If we take the  $J = 45/2 - 43/2$  transition of the  $\nu_7 = 1$  state as an example and apply Eq. 4.4 with an excitation temperature of 150 K (assuming the same  $\text{H}_2$  column density as the ground vibrational state), we find an estimate fractional abundance of  $4 \times 10^{-7}$  for  $\text{C}_4\text{H } \nu_7 = 1$  in V Hya, which is comparable to the values obtained for the ground state. Thus, given that  $\text{C}_4\text{H}$  is present in much warmer regions around V Hya than in spherical AGBs like IRC+10216, IR excitation to its many vibrational states is likely much more efficient in this object, causing the observed underabundance of

ground state  $C_4H$  relative to those sources.

The distribution of  $C_4H$  density shown in Fig. 4.8 is also found to be relatively flat or increases steadily in the regions sampled, unlike  $HC_3N$  and  $HC_5N$  where we have found a clear growth *and* decrease of the abundance. The average abundance of *l*- $C_3H$  is two orders of magnitude less than CCH, consistent with this observed ratio in IRC+10216 (Thaddeus et al., 1985).

The large abundance of CCH ( $2-8 \times 10^{-6}$ ) also matches observations of IRC+10216; however, it shows no evidence of the shell-like distribution it exhibits in other AGB sources (Unnikrishnan et al., 2023; Agúndez et al., 2017). Since our observations do not sample radii less than  $\sim 100$  au, it is possible that the CCH abundance has a steep drop-off within this distance that we are not able to detect. However, from the available information, it appears that this photodissociation product is available immediately in the circumbinary environment of V Hya.

The sulfur-terminated carbon chains show another slight discrepancy from their presence in IRC+10216. The average abundance ratio of  $[C_3S] / [CCS]$  calculated here is  $\sim 0.1$  in V Hya, whereas in IRC+10216 this ratio is closer to unity (Bell et al., 1993). This could be owing to non-LTE effects, as the  $J = 38 - 37$  of  $C_3S$  may be sub-thermally excited resulting in underestimated abundances; however, an exact analysis of this is not presently possible due to a lack of collisional rates for this molecule. Using  $HC_3N$  as a proxy, the critical density of the observed line would be  $5 \times 10^6 \text{ cm}^3$  (Siebert et al., 2022a) scaled by the ratio of Einstein  $A_{ij}$  values of these transitions for  $C_3S$  ( $\log A_{ij} = -3.08$ ) and  $HC_3N$  ( $\log A_{ij} = -2.48$ ), respectively. This gives a value of  $\sim 1 \times 10^6 \text{ cm}^3$ , which is larger than the average gas density within R1 ( $10^5 \text{ cm}^{-3}$ ), meaning the transition could be subthermally excited.

The measured abundance of  $CH_3CN$  ( $\sim 10^{-7} \text{ cm}^{-3}$ ) is consistent with its peak abundance in IRC+10216 (Agúndez et al., 2015), but like CCH we see no evidence of

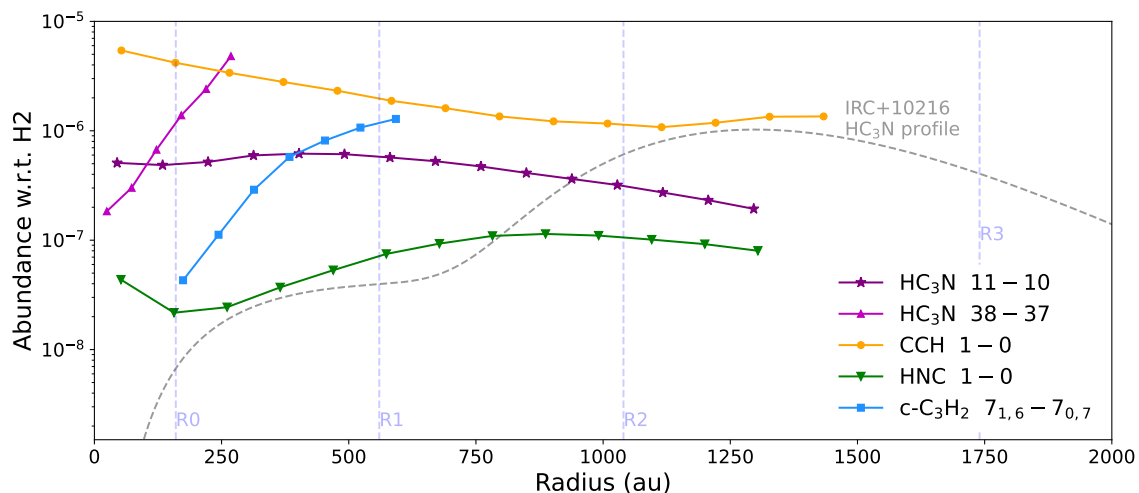


Figure 4.9: Non-LTE-simulated abundances of molecules in V Hya using RADEX, assuming purely collisional excitation (no vibrational pumping). Radial spacing of points is one-quarter of the beam size, and abundances are only calculated where the disk-averaged line flux is larger than 3 times the rms of the image. Since the uncertainty could not be carried through the forward-modeling process, it is assumed to be 30%, matching the typical error in radial integrated line flux.

a decrease in this abundance at the center of the DUDE. The abundance ratio of  $[\text{CH}_3\text{CN}]/[\text{H}_2\text{CS}] \sim 2$  is in agreement with that for IRC+10216 (Agúndez et al., 2008), though  $\text{H}_2\text{CS}$  appears farther out in the wind, between R0 and R1.  $\text{c-C}_3\text{H}_2$  shows a clear ring distribution peaking around  $\sim 400$  au with an abundance matching those found for the carbon stars in studied in Unnikrishnan et al. (2023).

We stress that the results in Fig. 4.8 and Table 4.3 are initial estimates for this source, as they are mostly derived from one or two lines of each molecule, assuming temperature profiles from this work and Sahai et al. (2022). To reduce the uncertainty to within a factor of two and confirm peculiarities we highlight for daughter species in the disk of V Hya, future wideband surveys are necessary as they will offer crucial information on the full ro-vibrational populations of these chemical products.

Table 4.3: Average column densities and abundances of daughter molecules in the disk of V Hya

Molecule	$r_{\min}$ [au]	$r_{\max}$ [au]	$N_1$ [cm <sup>-2</sup> ]	$N_2$ [cm <sup>-2</sup> ]	$f_{\text{LTE1}}$	$f_{\text{LTE2}}$	$f_{\text{RADEX}}$	$f_{\text{IRC+10216}}$	ref
HC <sub>3</sub> N	45	1296	6.4(14)	1.2(15)	5.2(-7)	8.4(-7)	4.5(-7)	1.4(-6)	1
HC <sub>5</sub> N	53	1002	3(14)	4(14)	3(-7)	3.4(-7)	-	2(-7)	1
CCH	53	1433	2.1(15)	4.6(15)	1.8(-6)	3.4(-6)	2.2(-6)	3(-6)	1
<i>l</i> -C <sub>3</sub> H	25	331	4.2(13)	6.3(13)	1.7(-8)	2.4(-8)	-	5(-8)	1
C <sub>4</sub> H	35	801	3.4(14)	3.6(14)	2.8(-7)	2.5(-7)	-	1.1(-6)	2
HNC	52	1304	1.9(14)	3.7(14)	1.9(-7)	3.3(-7)	7.3(-8)	5.8(-8)	3
CCS	35	592	8.2(13)	1.2(14)	4.5(-8)	6.3(-8)	-	3(-8)	1
C <sub>3</sub> S	35	382	1.8(13)	1.7(13)	8.9(-9)	8.3(-9)	-	1.2(-8)	1
<i>c</i> -C <sub>3</sub> H <sub>2</sub>	174	593	1.4(14)	2.7(14)	1.1(-7)	1.9(-7)	6(-7)	5.6(-8)	2
CH <sub>3</sub> CN	26	435	1.1(14)	1.9(14)	-	6.8(-8)	-	2.6(-8)	2
H <sub>2</sub> CS	75	522	5.9(13)	7.1(13)	3.7(-8)	3.9(-8)	-	8.7(-9)	4 <sup>a</sup>

NOTE — Second and third columns denote the range of radii where the molecule is detected above  $3\sigma$ , and also the distances over which abundances and column densities are averaged. Values are written with the exponent in parentheses. For each molecule in V Hya, two column densities and abundances (relative to H<sub>2</sub>) are listed, the first (subscript 1) was calculated assuming LTE and the kinetic temperature profile from Sahai et al. (2022); the other (subscript 2) uses the higher temperature law derived from an excitation analysis of CH<sub>3</sub>CN. For species with available collisional rates, non-LTE calculated abundance using RADEX is provided. Given the uncertainties in line flux, and the spread of abundances obtained over a wide range of temperature assumptions, the estimated error for these single-transition calculations is a factor of five. The last two columns list the observed abundance toward IRC+10216 and the reference for that value. <sup>a</sup>Published column density converted to fractional abundance assuming source size matches that of CH<sub>3</sub>CN [1] Agúndez (2009), [2] Gong et al. (2015) [3] Tuo et al. (2024) [4] Agúndez et al. (2008)

## Radiative transfer calculations

While IR-pumping is often a factor in AGB envelopes, it is also important to consider non-LTE effects for collisionally-dominated transitions as well. The disagreement between the abundances yielded by the  $J = 11 - 10$  and  $J = 38 - 37$  lines of  $\text{HC}_3\text{N}$  shown in Fig. 4.8 implies that the effective excitation temperatures of one or both of these lines is lower than the LTE temperature assumptions.

For species with available collisional excitation rates, we investigate these non-LTE effects in a line-by-line manner using the radiative transfer code RADEX (van der Tak et al., 2007). Similar to our previous analysis, for each radial bin, we fit the integrated line flux to obtain the column density, then perform the same analysis on the  $^{13}\text{CO}$  to convert this to an abundance. The kinetic temperature profiles used in the RADEX calculation are once again those shown in Fig. 4.7, including the cool model derived in Sahai et al. (2022) as well as the warm model we find from  $\text{CH}_3\text{CN}$  population analysis. The gas density profile for V Hya is also adopted from Sahai et al. (2022).

For the collisional excitation rates, we use the available molecular data from the Leiden Atomic and Molecular Database (LAMDA; van der Tak et al., 2020). In the case of  $\text{HC}_3\text{N}$ , the collisional rates are only calculated up to  $J = 37$ , so we extrapolate these up to  $J = 45$  using radiative transitions rates from CDMS (Müller et al., 2005).

The results of this non-LTE analysis are shown in Fig. 4.9, and the ensuing average abundances are included in Table 4.3. The steep increasing abundances of the obtained from the  $J = 38 - 37$  transition of  $\text{HC}_3\text{N}$  can be attributed to the high sensitivity of this line to gas density, as collisional excitation becomes very inefficient moving outward with radius. Because the addition of vibrational pumping would increase the accessibility of higher rotational states, the  $J = 38 - 37$  abundances in

Fig. 4.9 can be considered upper limits. In contrast, when the  $J = 11 - 10$  transition is used to calculate the abundance it appears much closer to the profile we found in the previous section, and the total average abundance is within 20% of the cool-temperature model ( $f_{\text{LTE1}}$ ), meaning LTE is a valid approximation for these lower  $J$  states. While the shapes of the  $J = 38 - 37$  and  $J = 11 - 10$  non-LTE profiles are quite different due to radiative effects, the abundances within R0 (where collisions are expected to be the dominant excitation mechanism for *both* transitions) are consistent, meaning  $\sim 3 - 5 \times 10^{-7}$  is a good estimate for the abundance of  $\text{HC}_3\text{N}$  in these central regions of the DUDE.

Similar to the low-energy line of  $\text{HC}_3\text{N}$ , the calculated abundance of CCH shows only a marginal change when RADEX is used. This is expected, as the transition rate of this line is quite low ( $A_{ij} \sim 10^{-6}$ ), so it is likely thermally populated throughout most of the DUDE. The overall shape of the abundance is also preserved in our RADEX calculations, and we continue to see that CCH is abundant even at very small radii in V Hya.

The derived abundance profiles of HNC and  $\text{c-C}_3\text{H}_2$  show a clear shift to larger radii when LTE is not assumed. This can again be attributed to the reduced effectiveness of collisions at large radii (and consequently lower densities). For  $\text{c-C}_3\text{H}_2$ , the large jump in its peak abundance (from  $\sim 10^{-7}$  to  $10^{-6}$ ) in the non-LTE model indicates that the excitation temperature is much lower than the kinetic temperature. This case is likely similar to  $\text{HC}_3\text{N}$   $J = 38 - 37$ , where the transition rate is so high that collisions alone cannot populate the rotational levels, and an additional mechanism like IR-pumping is needed. For lines like these, the high temperature LTE approximation in the previous section is more accurate. In contrast, for the low-lying  $J$ -states sampled by Band 3 transitions (HNC, CCH, and  $\text{HC}_3\text{N}$   $J = 11 - 10$ ), the non-LTE collisional model shown in Fig. 4.9 is a good representation of the abundance

distribution in V Hya.

## Chemistry in the Circumbinary Disk

The observed molecular inventory of V Hya is not unlike other carbon-rich AGB sources, and the estimated abundances indicate that the established gas phase pathways to daughter species (e.g. polymerization of carbon chains) are not drastically different in this unique morphology. At the same time however, the relatively compact distributions of daughter molecules in the flared disk indicate that photochemical processes are affected in this unique morphology. To maintain the observed abundances of CCH near the center of the outflow, there must be a sufficient amount of dissociating radiation (typically UV) present in these regions. We propose three potential scenarios for the source of this excess radiation in the inner disk of V Hya. The first is an external origin. In the traditional AGB case, interstellar photons at the center of the outflow are attenuated by the entire envelope, resulting in a large degree of extinction and a slow build-up of photochemical products. In the environment of V Hya though, the geometry of the DUDE also allows for ambient interstellar photons to penetrate from less obscured directions above and below the disk, which could reduce the  $A_V$  at small radii significantly. This would also imply that there could be a height stratification of chemical species in the DUDE, similar to what is seen in protoplanetary systems (Öberg et al., 2023).

Another explanation is that the chemistry-driving radiation is produced internally, either from a higher temperature companion, or from the evolved star itself if it is transitioning to the post-AGB phase and thus exposing a hot central star. The latter is the case for the C-rich protoplanetary nebula CRL 618, which harbors a central photon-dominated region (PDR) and initiates a fast-evolving photochemistry (Woods et al., 2003). V Hya shares kinematic similarities with CRL 618 with the presence of

periodic high-velocity, bulleted-ejections; however, CRL 618 is B0-type and is clearly ionizing the inside of its envelope (Fong et al., 2001), whereas V Hya is much more red (C6; Samus' et al., 2017) and shows no spectral evidence of having left the AGB.

The binary-induced chemistry hypothesis was recently found to be important in IRC+10216 (Siebert et al., 2022a) and the S-type AGB W Aql (Danilovich et al., 2024). It is well-known that V Hya has a companion with an orbital period of 8.5 (Sahai et al., 2016) or 17 yr (Knapp et al., 1999), and a large eccentricity, though its mass and spectral type are presently unconstrained. W Aql is also part of a very eccentric binary, and Danilovich et al. (2024) found enhancements of SiN in the location where periastron occurred with an F-type companion. While we do find evidence of some asymmetric abundance distributions in V Hya (i.e. C<sub>4</sub>H), none are as stark as those seen in W Aql. We also note that in general, most daughter species in V Hya do not show any anisotropies in their emission beyond the expected projection effects of an inclined disk.

Without a detailed 3-dimensional radiative and chemical model of this source, it is unclear which of the above scenarios are factors in the observed chemistry of V Hya. Nevertheless, the observational analysis provided in this work provides the initial chemical constraints intended to guide future theoretical and observational efforts for this source and similarly complex evolved star environments.

## 4.5 Conclusions

The environment of V Hya is a prime location to examine C-rich AGB chemistry in a complex, binary-induced circumstellar morphology. To this end, we have presented a spatio-chemical analysis of this object using available ALMA observations with the goal of mapping the gas phase molecular inventory in its expanding disk. We report rotational lines from 20 unique molecules and isotopologues, including parent

molecules, polyne carbon chains, and more saturated species like  $c\text{-C}_3\text{H}_2$ ,  $\text{CH}_3\text{CN}$ , and  $\text{H}_2\text{CS}$ . With a physical model of the DUDE in hand, we compared the spatial distributions of detected transitions of these molecules, and derived excitation conditions and initial estimates on abundances throughout this source. The main results of these analyses are summarized as follows:

1. Emission from all detected molecules is primarily constrained within the first density-enhanced ring of the DUDE (R1; 560 au). Low-energy transitions of HNC, CCH, and  $\text{HC}_3\text{N}$  can extend farther than this.
2. Most lines from daughter species display single-peaked, ring-shaped spatial distributions. The radial positions of the intensity maxima vary among detected transitions. Parent species, and curiously  $\text{CH}_3\text{CN}$  exhibit centrally-peaked distributions.
3. The “R0” ring identified from  $\text{HC}_3\text{N}$  emission by Sahai et al. (2022) at 160 au is detected in some other transitions like those of  $\text{C}_4\text{H}$ . However, the non-ubiquity of this ring among chemical species, as well as its absence from the  $^{13}\text{CO}$  maps suggests that this is not a physical sub-structure in the disk, but a location that is favorable for the excitation of carbon chains.
4. Some molecules show peculiar asymmetries in their emission. This is most commonly seen in the many detected lines of  $\text{C}_4\text{H}$ , which all appear brighter in southern regions of the DUDE at a deprojected distance of  $\sim 200$  au from V Hya. These anisotropies are not apparent in  $^{13}\text{CO}$  nor other molecular lines tracing this region ( $\text{HC}_3\text{N}$ ,  $\text{CH}_3\text{CN}$ ), suggesting they reflect a chemical asymmetry in the disk.
5. Using the known velocity-structure of the outflow, image cubes of V Hya can

be effectively shifted and stacked with a common line center to greatly boost the significance of rotational line detections. Using these methods, we confirm the detection of CH<sub>2</sub>CN in V Hya, and separate emission from *l*-C<sub>3</sub>H from a blended transition of CH<sub>3</sub>CN. This type of spectral cube manipulation could also be useful for other sources with well-constrained kinematics.

6. A spatial population analysis of CH<sub>3</sub>CN yields  $T_{\text{rot}}$  values in the inner 100 au of the DUDE up to ~420 K which decrease outward with radius. These temperatures are far above the previously calculated kinetic temperature model of the disk by Sahai et al. (2022). Further calculations confirm that this is caused by vibrational pumping of rotational states, driven by the high flux of IR photons in the disk. Despite this non-LTE mechanism, the population of CH<sub>3</sub>CN  $K$  states is well-fit by a single excitation temperature at each sampled radius.
7. The single-line estimated average abundances of carbon chain species in the disk are consistent (to within a factor of ~5) with C-rich AGB envelopes of similar mass-loss rate to V Hya.
8. The spatial distributions of molecular abundances are more compact than in comparable carbon star envelopes. Some daughter species (e.g. CCH and CH<sub>3</sub>CN) show no evidence of central minima in their abundance profiles at the resolution of these observations. In both LTE and non-LTE estimates, CCH must have a fractional abundance w.r.t. H<sub>2</sub> larger than  $10^{-6}$  in the inner ~150 au of the DUDE to reproduce the observed lines. For comparison, in IRC+10216 this abundance is only reached at radii larger than 1000 au (Agúndez et al., 2017).

These results highlight both similarities and differences between this unique source and the traditional spherical winds of more well-studied carbon stars. It is presently

unclear what chemical mechanisms are responsible for the close-in production of carbon chain species in the expanding disk of V Hya. To resolve this, further analysis of this source (and similarly-perturbed AGBs) will be key, including large bandwidth surveys covering many transitions of the species investigated in this work, and 3D chemical modeling efforts for these wind structures. In particular, we stress the need to characterize small photodissociation products and carbon-bearing radicals (e.g. CCH, C<sub>4</sub>H, CN) in the innermost regions of stellar winds, as these are crucial to initiating the formation of larger species, and also appear to have some of the most peculiar behavior in V Hya.

Equatorial circumstellar density structures have been increasingly common in the study of AGB stars (Decin et al., 2020), and are well-established in more evolved systems (Sahai et al., 2007; Olofsson et al., 2019). As observational capabilities grow, chemical case studies of rapidly evolving AGB and RSG sources will be key in understanding the full scope of molecular processes in evolved stars, and how they are coupled with complex mass-loss mechanisms. Pursuing this broad characterization of circumstellar chemistry will in turn allow us to place important constraints on the recycling of stellar material, and the budget of complex species which can be inherited by later stages of the ISM.

## 4.6 Appendix: Further applications of line stacking

The spectral stacking method first developed for protostellar sources, and described in Section 4.4, has proven a useful tool for examining weak line signatures and from this evolved star. Here, we explore the results of this method in detail, and investigate additional use cases for it in the context of V Hya, as well as objects with similar morphology. Fig. 4.10 shows the original and expansion velocity-corrected spectra of two example transitions ( $\text{HC}_3\text{N}$  and  $\text{c-C}_3\text{H}_2$ ). We find that the line shapes of the corrected spectra are not Gaussian, but are instead well fit by a Lorentzian profile:

$$S(v) = \frac{S_{\text{pk}}}{1 + \left(\frac{v-v_0}{\gamma}\right)^2} \quad (4.9)$$

This line shape is typically characteristic of pressure broadening; however, we do not expect that this is what is represented by the corrected line width in Fig. 4.10. Instead, we recall that the DUDE has a 3D flared structure and is not the infinitely thin disk assumed by the stacking method. Because the DUDE is rather thick, with an opening angle of  $\sim 39^\circ$ , this effect likely dominates any other sources of line broadening, so the reduction in line-width is not as dramatic as it is in the case of protoplanetary disks (e.g. Fig. 3 in Yen et al., 2016). The additional flux in the line wings could also be contributed by the base of the high-velocity outflow in V Hya, which is not accounted for in the velocity model used for stacking, and therefore could result in a profile that appears Lorentzian in shape.

We also note that in Fig. 4.10, the best-fit lsr velocities are well-constrained at

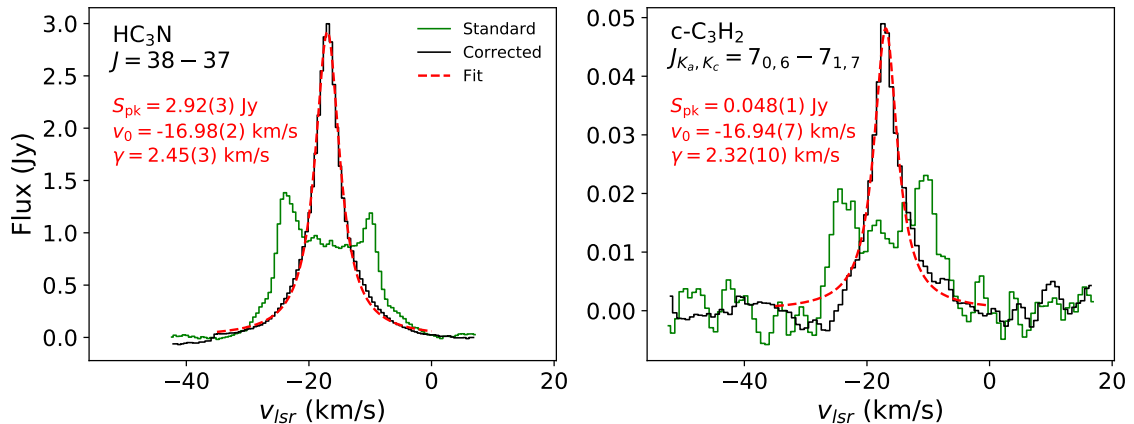


Figure 4.10: Original (solid green) and velocity-stacked (solid black), spatially-integrated line profiles for  $\text{HC}_3\text{N}$  and  $\text{c-C}_3\text{H}_2$  toward V Hya. Dashed red line profile shows a Lorentzian fit to the corrected spectrum. Best fit values for the parameters in Eq. 4.9 are labeled, with last-digit errors shown in parentheses. All spectra were obtained over a deprojected radius range from  $0''$ – $1.5''$  (600 au), and therefore neglect emission outside of R1.

$-16.96$ – $16.98 \text{ km s}^{-1}$ . This is also consistent with the observed peaks of  $\text{C}_4\text{H}$  and  $\text{CH}_2\text{CN}$  in Fig. 4.5. Since the shifting and stacking algorithm only accounts for the motion of gas relative to the disk as a whole, this value can be interpreted as a more accurate value for the system velocity (elsewhere quoted in this work as  $-17.4 \text{ km s}^{-1}$ ), at least for the central regions that we use for these spectra ( $0''$ – $1.5''$ ).

Applying these position-dependent velocity corrections also is a useful way to investigate blended regions of emission lines. This is because the emission can be partially decoupled by moving spectra on either side of the DUDE away from each other in velocity space. The best examples of this are apparent in the  $\text{CH}_3\text{CN}$  and  $\text{H}_2\text{CS}$  groups of blended lines, shown both corrected and uncorrected in Fig. 4.11. For  $\text{CH}_3\text{CN}$ , we can clearly see the peaks of  $K=0$ ,  $K=1$ , and  $K=2$  in the stacked spectrum, which were previously not distinguished in the original spectrum due to the width and complexity of the original line profile. The positions of these peaks agree to within

1% of the catalog rest frequency when shifted using the modified system velocity of  $-16.98 \text{ km s}^{-1}$ . Additionally, this method reveals the detection of the  $J = 21/2 - 19/2$  transition of  $l\text{-C}_3\text{H}$ , which was only marginally seen in the uncorrected spectrum.

The  $\text{H}_2\text{CS}$  lines shown in Fig. 4.11b. are also obvious after stacking. The  $10_{3,8} - 9_{3,7}$ ,  $10_{3,7} - 9_{3,6}$  transitions of this molecule are the nearest components that we separate with this method, only  $3.6 \text{ km s}^{-1}$  (4.2 MHz), less than 25% the original double-peaked profile width. The stacked spectrum also improves the S/N of the much weaker  $10_{4,7} - 9_{4,6}$  and  $10_{2,9} - 9_{2,8}$   $\text{H}_2\text{CS}$  lines, and reveals another feature that was previously buried among the  $\text{H}_2\text{CS}$  and  $\text{C}_4\text{H } \nu_7 = 1$  transitions centered at 343424 MHz. We attribute this to the  $15_{9,7} - 14_{9,6}$  transition of  $\text{Si}^{13}\text{CC}$ .

While stacking is incredibly useful in de-blending molecular signatures, care must be taken when choosing the bandwidth over which this is applied. Because the appropriate velocity shift of each pixel is dependent on the rest frequency of a given line, its accuracy decreases for lines at the edge of a large band. Another caveat is that this method is only applicable to objects where every line of sight in an image can be mapped to a single (central) lsr velocity, which is the case for an inclined, expanding disk as we have approximated V Hya. This means it is unfortunately not possible for a spherical AGB envelope, as each position in the plane of the sky corresponds is still centered on the systemic velocity, and thus there is no valid shift in frequency that can be used to co-add spectra. The analysis is thus restricted to equatorial structures in sources with well-characterized expansion or rotation, and we recommend this approach for future interferometric spectral line analyses of AGB-related sources exhibiting such velocity gradients.

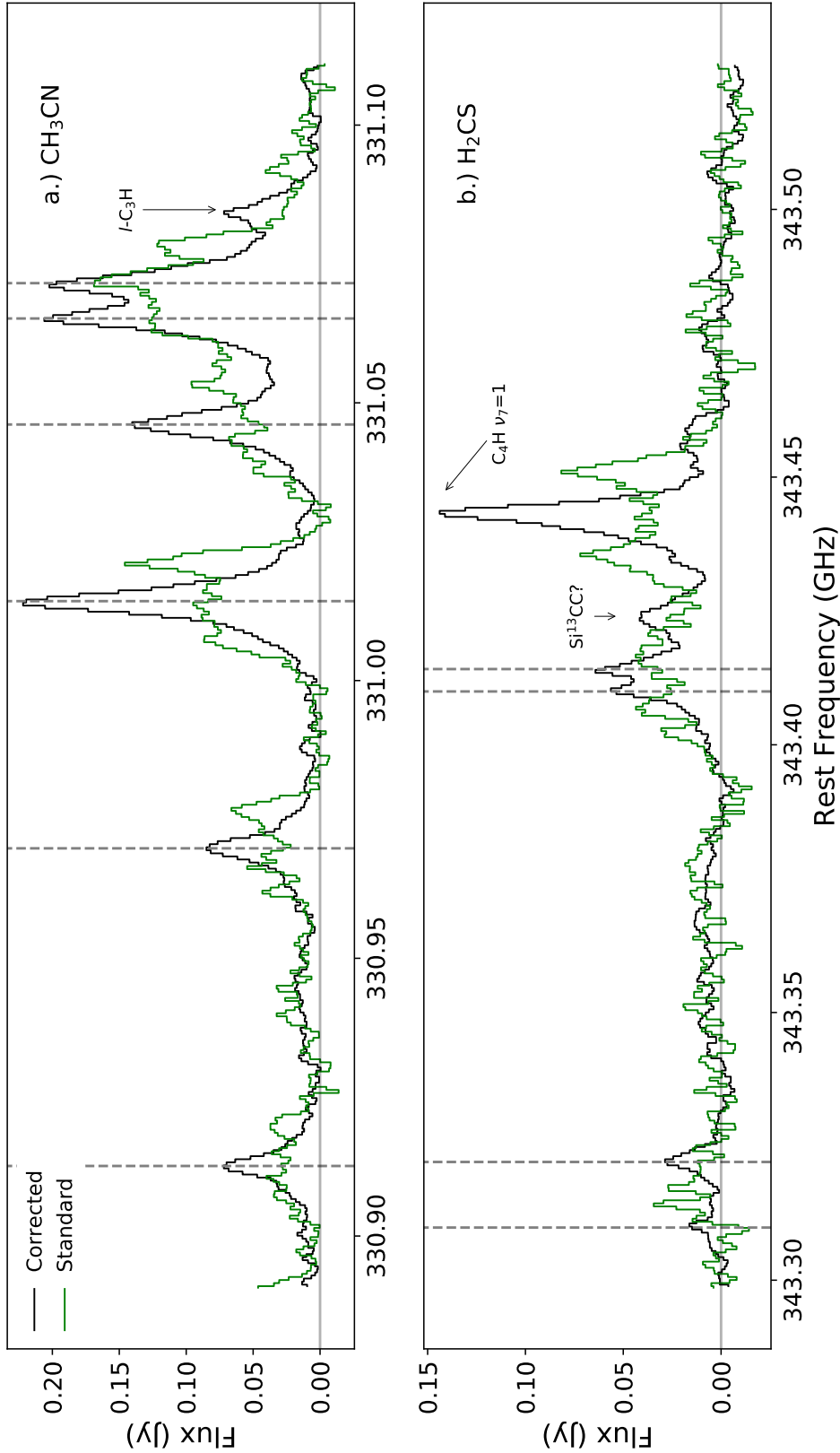


Figure 4.11: Application of line shifting and stacking procedure on larger bandwidths covering groups of CH<sub>3</sub>CN (top) and H<sub>2</sub>CS (bottom) transitions. For these molecules, we indicate the catalog rest frequencies (CDMS; Müller et al., 2005) with vertical dashed lines. From left to right, these represent the  $K = 5, 4, 3, \dots, 0$  components of the  $J = 18 - 17$  transition of CH<sub>3</sub>CN, and the  $J_{K_a, K_c} = 10_{4,7} - 9_{4,6}, 10_{2,9} - 9_{2,8}, 10_{3,8} - 9_{3,7}, 10_{3,7} - 9_{3,6}$  lines of H<sub>2</sub>CS. Additional blended species are labeled with arrows. Both the corrected and uncorrected spectra were converted to rest frequency using a modified systemic velocity of  $v_{lsr} = -16.96 \text{ km s}^{-1}$ , and were extracted from the central region of the DUDE ( $0'' - 1.5''$ ).

## CHAPTER 5

# A Spectral Line Survey of the Exotic Proto-Planetary Nebula V510 Pup

The physical interaction of binary evolved star systems is perhaps most pronounced when stars reach the post-AGB phase, yet chemical studies of these objects are rare due to the fast and therefore elusive nature of this stage. The following Chapter has been accepted for publication in Proceedings of the Astronomical Union as “Clues to PPN Chemical Evolution: The Unique Molecular Environment of V510 Pup”, and describes a pilot survey of a unique binary post-AGB object which shows signs of mixed C- and O-rich chemistry.

## 5.1 Introduction

The nebulae surrounding evolved stars undergoing mass loss represent important sites of recycling for metal-rich gas and dust in our Galaxy. As low–intermediate mass stars leave the Asymptotic Giant Branch (AGB), their circumstellar envelopes

undergo dramatic changes: transitioning from slow, spherical winds to complex bipolar/multipolar outflows seen in planetary nebulae (PNe) (Sahai et al., 2011). These dynamics are often met with a chemical transition as well, with molecules and dust being increasingly affected by conditions including high-velocity shocks, internal UV radiation, and AGB dredge up events (Pardo et al., 2007; Weiss & Ferguson, 2009). The mechanisms for the physical and chemical changes during the transitional pre-planetary nebula (PPN) phase are still not fully understood, but recent work has shown that binary and common envelope interactions are key to this evolution (e.g. Sahai et al., 2018).

One puzzling class of object that is critical to understanding the chemical output of evolved stars are PPNe showing signs of mixed chemistry. Stellar outflows are designated as either carbon- or oxygen-rich depending on the C/O ratio of the central star, which typically determines the molecular and dust grain composition throughout the wind (Höfner & Olofsson, 2018). However, it appears that this dichotomy is not universal, especially as stars evolve off the AGB. Evidence of this includes the widespread IR observations of fullerene and PAH features toward O-rich PNe (Gielen et al., 2011), as well as the existence of “silicate carbon stars” which have C-rich photospheres but are surrounded by O-rich circumstellar dust, and often show OH masers (Ohnaka et al., 2013).

V510 Pup (IRAS 08005-2356) is post-AGB star surrounded by a young high-velocity outflow that shows clear evidence of mixed chemistry. It exhibits OH maser emission typical of O-rich evolved stars (Zijlstra et al., 2001), but also shows optical absorption lines from C<sub>2</sub> and CN (Bakker et al., 1997). The extreme dynamics of V510 Pup were characterized recently by Sahai & Patel (2015), where broad (~200 km/s) line profiles were observed in CO and SiO using the Submillimeter Array (SMA). Analysis of the velocity gradient across the nebula showed that radiation pressure

alone is insufficient to drive the outflow. Optical observations later discovered that V510 Pup is part of a radial-velocity binary, and that its  $H\alpha$  line profile modulates with the seven-year orbital period, confirming that the high-velocity bipolar outflow originates from accretion onto a close binary companion (Manick et al., 2021). This makes it the only extreme PPN whose jet origin is directly observed.

V510 Pup is at a critical point in its evolution to offer new insights into chemical transitions and binary interaction in exotic PPNe, but it lacks key constraints on its gas phase chemical inventory. To address this, a detailed spectroscopic study of this source is needed to determine the molecular abundances and their relationship to kinematic structures within the wind. We used interferometric observations from the Atacama Compact Array (ACA) to perform these measurements, and reveal the unique dynamics of C- and O-rich material in this source.

## 5.2 Observations

We utilize archival data from a Cycle 6 ACA filler program which observed 16 evolved stars transitioning between the AGB and PNe phases (Project code 2018.A.00047.S). These data include spectral line observations of V510 Pup covering the entirety of Bands 3 and 6 (85–115 GHz, and 211–274 GHz) at 1~3 km/s velocity resolution. Calibrated visibilities were produced using the standard pipeline of the Common Astronomy Software Application (CASA; McMullin et al., 2007), and each spectral window was then continuum-subtracted, then imaged and deconvolved using the `tclean` CASA task with `briggs` weighting. The resulting rms sensitivity ranges between 5 and 13 mJy/beam among the 56 spectral windows. Some spectral windows overlap in their frequency coverage, so these data were combined in the visibility plane to improve sensitivity. The ACA beam size is 10.1”–11.5” and 4.3”–5.3” at Bands 3 and 6, respectively. This is notably larger than the ~2” nebular extent of V510 Pup

observed by Sahai & Patel (2015), meaning a spatial analysis was not possible with these data, and our study is purely spectroscopic.

## 5.3 Results & Analysis

### 5.3.1 Detected species and line profiles

We detect emission from a total of 16 molecules and isotopologues toward V510 Pup, 13 of which have not yet been observed in this source. A list of all detected species is shown in Table 5.1, including the number of lines observed of each, and whether they are typically found in C- or O-rich sources, using Ziurys (2006) as reference. All these molecules are common in evolved stars environments, including “parent” molecules originating from the stellar atmosphere (e.g. SO, HCN, CS), as well as species produced through photochemistry like  $\text{HCO}^+$ , HNC,  $\text{HC}_3\text{N}$ , and  $\text{C}_2\text{H}$  (Woods et al., 2003). The remarkable result seen in Table 5.1 is the presence of characteristic O-rich molecules (SO,  $\text{SO}_2$ ) paired with C-rich species (HNC, CN,  $\text{C}_2\text{H}$ , and  $\text{HC}_3\text{N}$ ). This is the first AGB-related source with simultaneous detections of all these molecules, lending support to previous classifications of mixed chemistry.

The peculiar chemistry of V510 Pup can be further explored using the kinematic information provided by molecular line profiles. Figure 5.1 shows a sample of these spectra. The full extent of the extreme outflow can be seen in the broad CO and SiO line profiles which span the range between  $-150$  and  $200$  km/s. Following Sahai & Patel (2015), we decompose this into three main velocity components: a central component (CV) centered on the system velocity ( $V_{\text{sys}} = 48$  km/s), a intermediate component (MV) at  $V_{\text{sys}} \pm 50$  km/s, and high-velocity wings (HV) at  $V_{\text{sys}} \pm 110$  km/s, all shown in Fig. 5.1. With the improved sensitivity on the  $^{13}\text{CO } J = 2 - 1$  line now available, we note that the CV component has a narrow feature (width  $< 10$  km/s)

Table 5.1: Summary of detected molecules and isotopologues

Molecule	No. of transitions	Range in $E_{\text{up}}$ (K) <sup>a</sup>	Velocity Component(s) <sup>b</sup>	Chemistry <sup>c</sup>
$^{12}\text{CO}$	2	10 – 30	CV, MV, HV	Both
$^{13}\text{CO}$	2	10 – 30	CV, MV, HV	Both
SiO	3	6 – 45	CV, MV, HV	Both
$^{29}\text{SiO}$	2	31 – 45	CV, MV, HV	Both
$^{30}\text{SiO}$	2	31 – 45	CV, MV, HV	Both
HCN	1	26	CV, MV	Both
$\text{H}^{13}\text{CN}$	1	25	CV, MV	Both
CS	1	35	CV(?), MV	C-rich
$\text{C}^{34}\text{S}$	1	28	MV	C-rich
$\text{HCO}^+$	1	26	CV, MV	Both
SO	5	44 – 56	CV	O-rich
$\text{SO}_2$	9	24 – 94	CV	O-rich
HNC	1	26	MV	C-rich
CN	1	16	MV	C-rich
$\text{C}_2\text{H}$	1	25	MV	C-rich
$\text{HC}_3\text{N}$	7	131 – 203	MV	C-rich

NOTE — <sup>a</sup>Upper state energies obtained from Cologne Database of Molecular Spectroscopy (CDMS) Müller et al. 2005. <sup>b</sup>LSR velocity ranges of the CV, MV, and HV components are defined in Section 5.3.1 and shown in Fig. 5.1. <sup>c</sup>Denotes whether a particular molecule is typically associated with a carbon- or oxygen-rich surface chemistry in circumstellar envelopes, using the list from Ziurys (2006).

appearing on top of the broad line profile, similar to how this transition appears toward the similar extreme PPN HD 101584 (Olofsson et al., 2019). This narrow CV component is also observed isolated from the MV and HV components in the emission profiles of SO, SO<sub>2</sub>, and HCN. Table 5.1 also lists which velocity components are detected for each molecule. We find that all molecules which are primarily associated with carbon-rich outflows appear solely in the MV component, while oxygen-rich species are located in the narrow CV region. This can be seen in the middle and right panels of Fig. 5.1.

Figure 5.2 shows the measured brightnesses of SO ( $6_5-5_4$ ) and HC<sub>3</sub>N ( $24-23$ ) relative to <sup>13</sup>CO compared with more well-studied PPNe for which these transitions have been observed previously (Olofsson et al., 2019; Pardo et al., 2004). From this, we see that the CV component of V510 Pup is chemically similar to O-rich sources like HD 101584, while the MV component is like the prototypical C-rich PPN CRL 618. Furthermore, this comparison provides evidence that the narrow CV is not depleted in its molecular chemistry as is the case for the Red Rectangle and other “disk-prominent” post-AGBs (Gallardo Cava et al., 2022).

### 5.3.2 LTE modeling

To obtain estimates on the abundances of detected molecules, we model the observed transitions assuming local thermodynamic equilibrium (LTE). This assumption is necessary since we lack spatial data and constraints on the physical conditions of the velocity components to perform a full radiative transfer analysis. To simulate line profiles and fit the transitions, we use the publicly available package `molSim`. For each velocity component, we perform a least-squares minimization of the column density, rotational temperature, and line width of a given molecule. For species where only one transition was available, we fix the rotational temperature to that obtained for

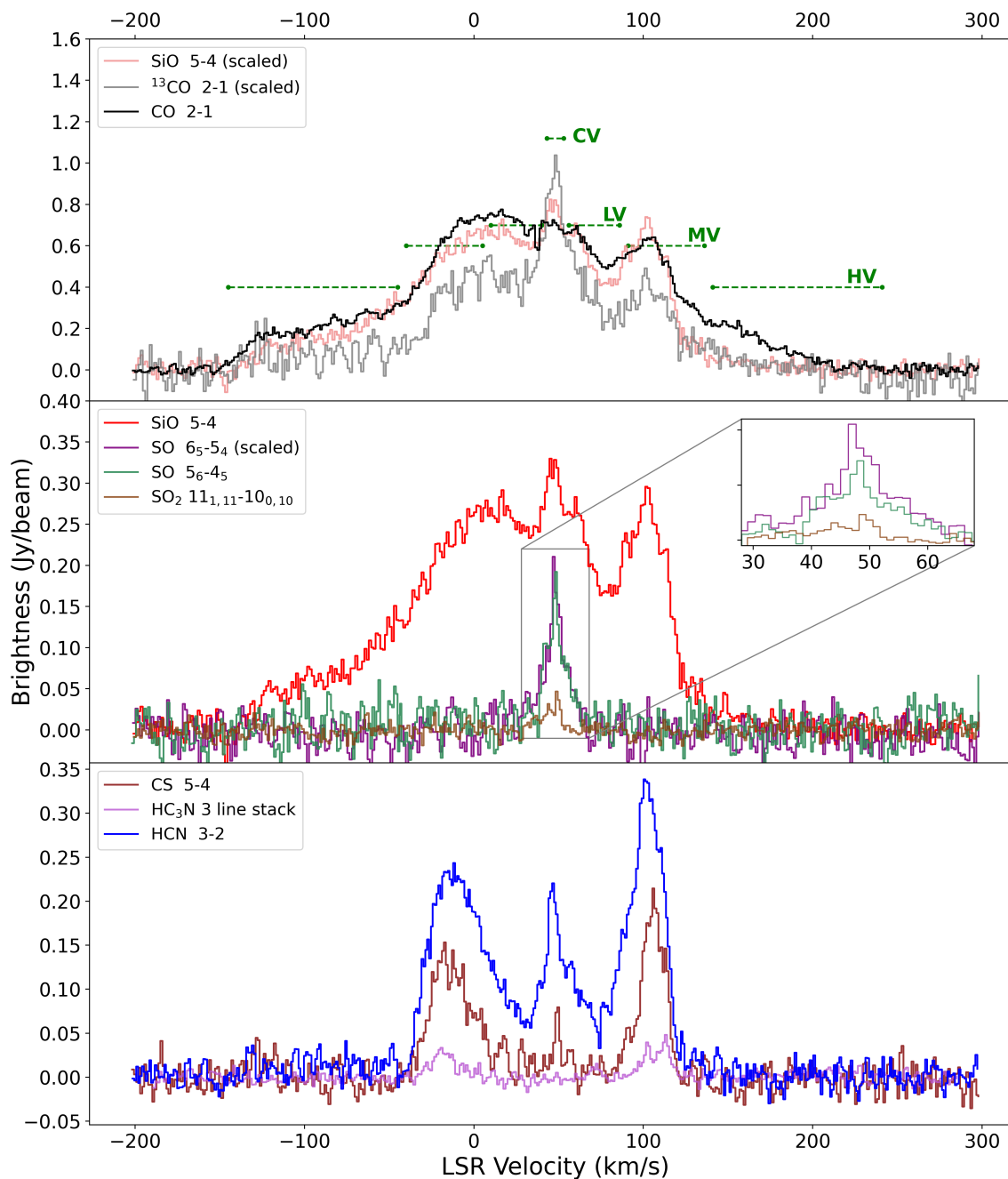


Figure 5.1: Emission line profiles of various molecules measured by the ACA toward V510 Pup. The central velocity (CV), medium-velocity (MV), and high-velocity (HV) components are defined in the left panel. Species that are typically associated with O- and C-rich evolved stellar outflows are shown in the middle and bottom panels, respectively. Spectra were extracted from an aperture with diameter  $10''$  centered on the position of the post-AGB star. Some transitions are scaled for comparison.

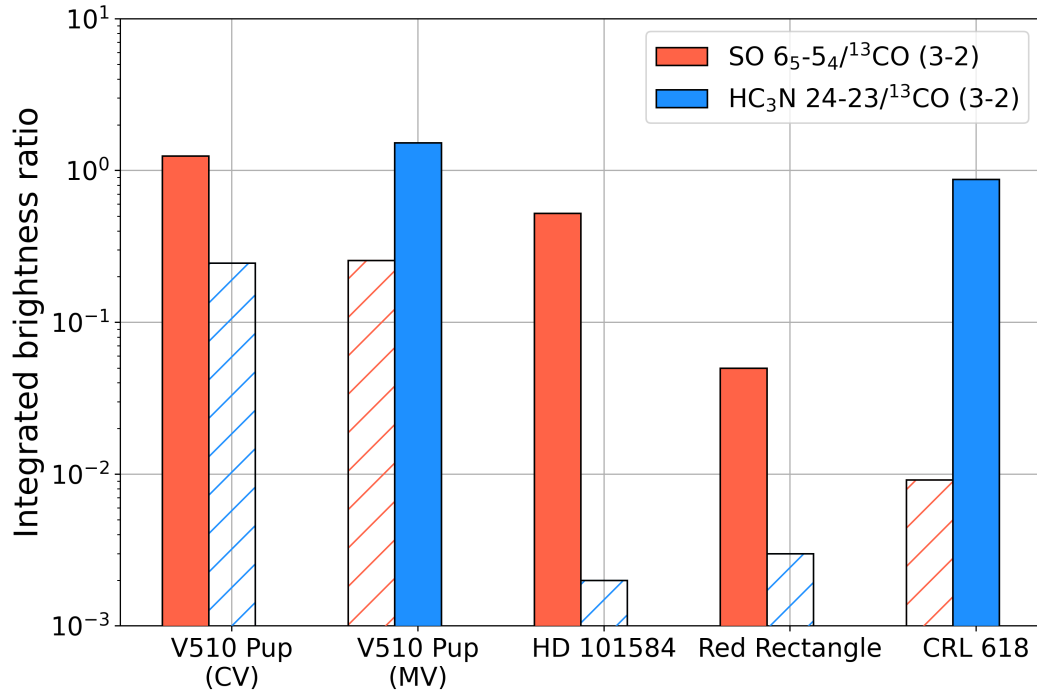


Figure 5.2: Comparison of integrated molecular line brightness (relative to  $^{13}\text{CO}$ ) for SO (red) and  $\text{HC}_3\text{N}$  (blue) among a sample of nearby PPNe. For V510 Pup, the O-rich central and C-rich medium velocity components are labeled CV and MV, respectively. Hatched regions denote upper limits, while solid regions indicate detected transitions. Data for sources other than V510 Pup adapted from Olofsson et al. (2019), Gallardo Cava et al. (2022), and Pardo et al. (2004).

SO (CV) or  $\text{HC}_3\text{N}$  (MV). We employ the same procedure for  $^{13}\text{CO}$ , simultaneously fitting the overlapping CV, MV, and HV components. Then, assuming a  $^{13}\text{CO}/\text{H}_2$  ratio of  $3.9 \times 10^{-5}$  (Sahai & Patel, 2015), we use the relative column densities to calculate final abundances. While this eliminates the need to adopt an explicit angular source size, it does assume that this size is equal to that of  $^{13}\text{CO}$  emission (whether in the CV or MV component).

The results of this analysis are shown in Figure 5.3 and Table 5.2. We find that the CV component exhibits excitation temperatures between 40–60 K, while the MV component (measured by  $\text{HC}_3\text{N}$ ) is about 63 K. These values are in line with the

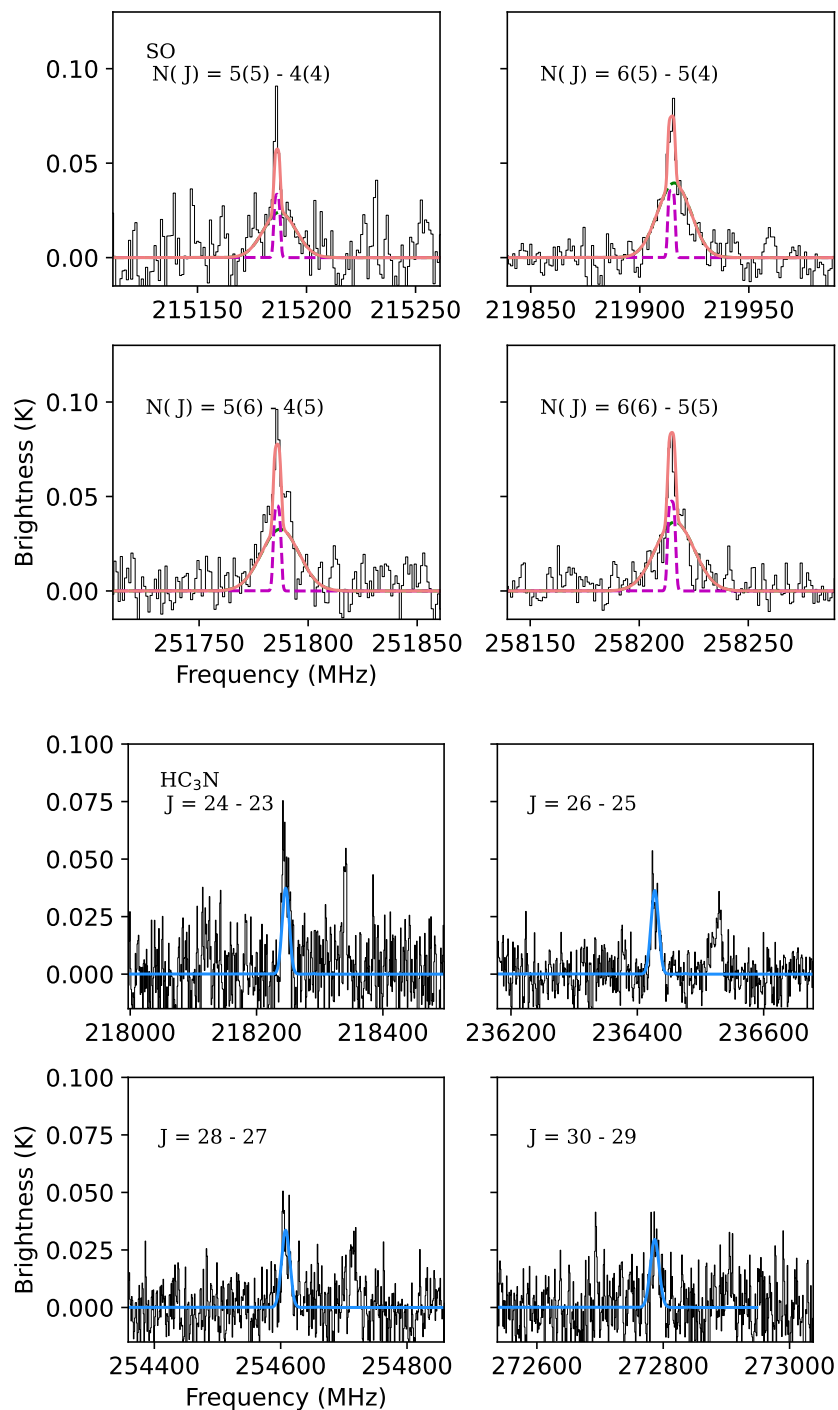


Figure 5.3: Examples of LTE emission line fits for SO (left panels) and HC<sub>3</sub>N (right panels). ACA spectrum shown in black, while colored lines represent fitted `molsim` simulation. For SO, a narrow (magenta dashed) and wide (green dashed) gaussian were needed to reproduce the shape of the CV component. For HC<sub>3</sub>N, one component was used, centered on the red-shifted side of the MV region.

Table 5.2: Measurements of physical parameters of optically thin species in the outflow of V510 Pup

Molecule	Component	$T_{\text{rot}}$ (K)	$f_{\text{H}_2}$ (err.)
SO	CV	$43 \pm 13$	$4.5 \times 10^{-6}$ (1.0)
SO <sub>2</sub>	CV	$57 \pm 18$	$4.8 \times 10^{-6}$ (0.9)
HC <sub>3</sub> N	MV	$63 \pm 16$	$1.6 \times 10^{-6}$ (0.6)
CS	MV	$63^a$	$5.1 \times 10^{-6}$ (0.5)
CN	MV	$63^a$	$1.3 \times 10^{-5}$ (0.1)
C <sub>2</sub> H	MV	$63^a$	$2.8 \times 10^{-6}$ (0.3)

NOTE — <sup>a</sup>Rotational temperature of HC<sub>3</sub>N adopted for abundance calculation.

temperatures found in the slowly expanding equatorial waist and the bipolar outflow of HD 101584 (Olofsson et al., 2019). The abundances of molecules observed in the MV component are close (within a factor of five) to their measured abundances in C-rich AGB stars (Agúndez et al., 2017; Massalkhi et al., 2019), indicating that this component does derive from acetylene-rich stellar material.

## 5.4 Conclusions

Using archival ACA observations, we analyzed the millimeter spectrum of V510 Pup to provide some of the first constraints on its molecular inventory. The new sensitivity and velocity information offered by our spectra indicate that not only does V510 Pup exhibit mixed chemistry in its outflow, but the carbon- and oxygen-rich material is separated into reservoirs of gas that are morphologically unique. The line profiles of the newly characterized CV component appear remarkably similar to the “disk-prominent” subclass of post-AGB stars (Gallardo Cava et al., 2022), as well as the central region of the similar PPN HD 101584 (Olofsson et al., 2019). These equatorial density enhancements (EDEs) are common in PPNe and PNe, and recent

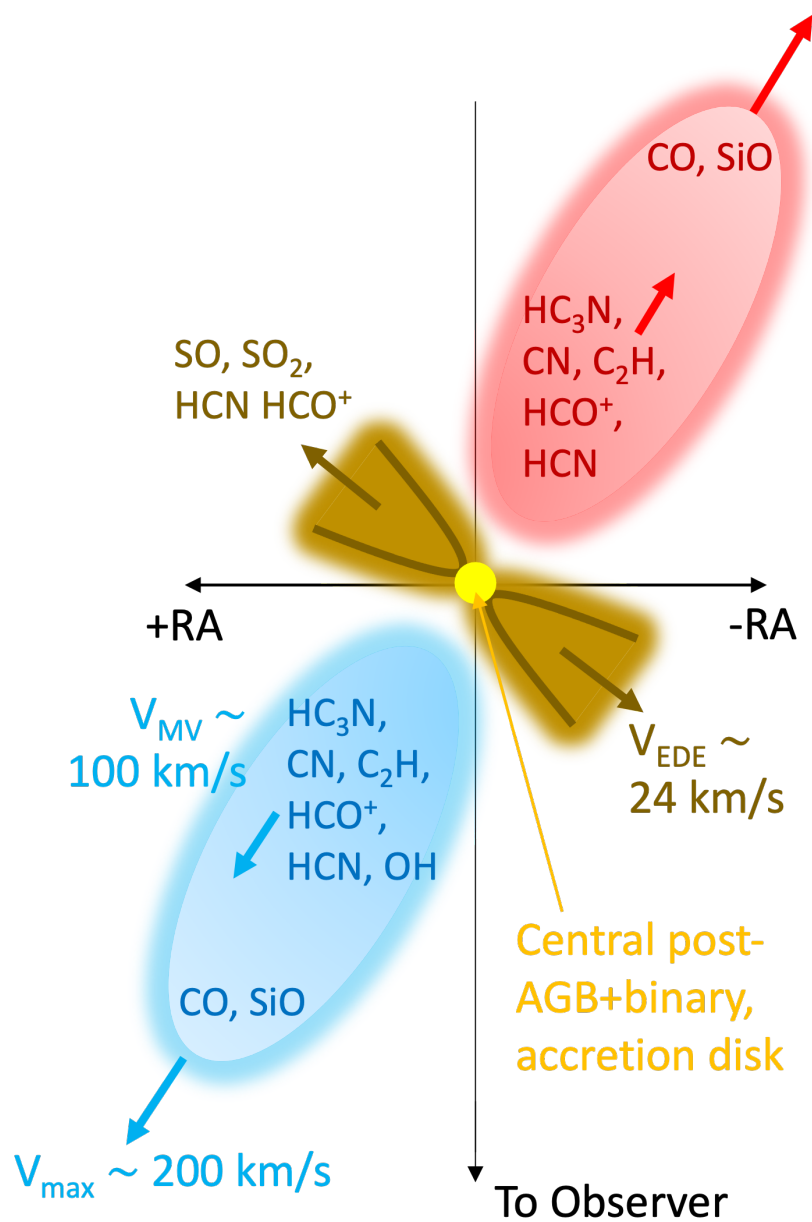


Figure 5.4: Diagram of the circumstellar environment of V510 Pup as suggested by our ACA analysis of its millimeter spectrum. Includes major morphological structures and their velocities, as well as the observed chemistry in each region. Proposed components include a carbon-rich bipolar outflow (red and blue), and a slowly expanding oxygen-rich equatorial waist surrounding the central binary (brown).

works suggest that they can form during the AGB phase through binary-shaping (Sahai et al., 2022; Decin et al., 2020). Thus, one possible explanation for the observed chemistry (summarized in Fig. 5.4) is that V510 Pup harbors a slowly expanding waist from an earlier stage of evolution when its surface chemistry was O-rich, then as its fast bipolar outflow formed it also underwent a transition to ejecting C-rich material. This scenario has been proposed to explain mixed dust features in silicate carbon stars (Ohnaka et al., 2013), but the observations presented here provide some of the first kinematic evidence for it. To confirm this, future observations of V510 Pup at higher resolution will be critical, as spatially resolving the chemically distinct CV, MV, and HV components will allow one to determine their physical conditions and dynamical histories.

## CHAPTER 6

# Methyl-terminated Carbon Chains in the Taurus Molecular Cloud

Moving away from carbon chemistry in the outflows of evolved stars, the following Chapter details a study of carbon chain species in a dark prestellar cloud. The text in this Chapter appeared in the *Astrophysical Journal* (Siebert et al., 2022b) as “CH<sub>3</sub>-Terminated Carbon Chains in the GOTHAM Survey of TMC-1: Evidence of Interstellar CH<sub>3</sub>C<sub>7</sub>N.”

## 6.1 Introduction

One of the most well-studied sites of cold, interstellar carbon chemistry is a prestellar core within the Taurus Molecular Cloud complex commonly referred to as Taurus Molecular Cloud 1 (TMC-1) (Churchwell et al., 1978). The chemistry occurring in TMC-1 produces a suite of exotic molecules (by terrestrial standards) including unsaturated cyanopolyynes (HC<sub>2n+1</sub>N;  $n = 1, 2, 3, \dots$ ) and acetylenic (C<sub>2n</sub>H<sub>2</sub>) linear carbon chains. Among the variations on these abundant molecules are the symmetric top methylpolyynes (MPs) and methylcyanopolyynes (MCPs), which have the form

$\text{CH}_3\text{C}_{2n}\text{H}$  and  $\text{CH}_3\text{C}_{2n-1}\text{N}$ , respectively. These species have been known in the interstellar medium (ISM) since the discovery of methyl cyanide ( $\text{CH}_3\text{CN}$ ) (Solomon et al., 1971) and methyl acetylene ( $\text{CH}_3\text{CCH}$ ) (Irvine et al., 1981). Toward TMC-1, methylpolyynes and methylcyanopolyynes as large as  $\text{CH}_3\text{C}_6\text{H}$  and  $\text{CH}_3\text{C}_5\text{N}$  have been detected and characterized (Matthews & Sears, 1983; Irvine et al., 1981; Broten et al., 1984; Walmsley et al., 1984; MacLeod et al., 1984; Loren et al., 1984; Snyder et al., 2006; Remijan et al., 2006).

Currently, the chemical formation of MPs and MCPs in TMC-1 is unconstrained. While it is possible that simple carbon addition reactions occurring on the surfaces of dust grains may account for the growth of these species toward cold, dark clouds (Turner et al., 2000), it is also plausible that ion-molecule reaction pathways in the gas phase can account for their formation (Quan & Herbst, 2007). Because molecules with  $\text{C}_{3v}$  symmetry have unique excitation properties that do not allow for easy interconversion between  $A$  and  $E$  symmetry states, the relative populations of their  $K$ -ladders can offer additional clues to their formation conditions (see e.g. Minh et al. (1993) Askne et al. (1984), Willacy et al. (1993), (Mendoza et al., 2018)), but to date, analysis of these populations has only been done for the shortest MPs and MCPs. Furthermore, comparing the relative column densities of the similarly structured cyanopolyynes has proven to be a useful tool in testing chemical models and assessing the mechanisms through which carbon chain species grow in the ISM (Loomis et al., 2021; Agúndez et al., 2017; Burkhardt et al., 2018).

Obtaining a more complete understanding of their chemistry and setting constraints on the abundances and excitation conditions of the various methyl-terminated carbon chains requires exploring the extent to which these types of species can grow (i.e. how long of a C-chain can form). Such observations would enable the direct comparison of measured abundances with both grain-surface and gas-phase reaction

pathways, especially when combined with a fully self-consistent excitation analysis of MPs and MCPs in TMC-1. In addition, these studies will set the overall limit to the detectability of longer chain MPs and MCPs based on both an improved understanding of the chemical formation pathway and on a new computational methodology to detect the weak signals coming from the larger C-chain species.

The ongoing GOTHAM survey (GBT Observations of TMC-1: Hunting for Aromatic Molecules) along with a deep Q-band survey being conducted on the Yebes 40 m radio telescope (Cernicharo et al., 2020) have thus far proven to be very useful for rigorous studies of exotic molecules in TMC-1. With many new detections of various carbon-bearing molecules, their isomers, and cyclic/polycyclic species, these projects have effectively expanded our knowledge of the interstellar molecular carbon reservoir before star formation occurs (Xue et al., 2020; Loomis et al., 2021; McGuire et al., 2018; McCarthy et al., 2020; McGuire et al., 2020, 2021; Cabezas et al., 2021; Cernicharo et al., 2021). In this work, we present a detailed analysis of  $\text{CH}_3$ -terminated carbon chains toward TMC-1 as well as the first detection of methylcyanotriacetylene ( $\text{CH}_3\text{C}_7\text{N}$ , Chen et al. (1998)) using the second data release of GOTHAM. We also search for methyltetraacetylene ( $\text{CH}_3\text{C}_8\text{H}$ , Travers et al. (1998)) in our data, but do not find significant emission and thus report upper limits on its abundance.

In Section 6.2, we outline the specifics of our observations and reduction methods. In Section 6.3 we describe our spectroscopic calculations for the targeted molecules and statistical analysis procedures. In Section 6.4 we present our results for all targeted molecules and discuss their relative column densities and excitation physics. Finally, in Section 6.5 we discuss how our results fit in to the current understanding of chemistry in TMC-1, and compare them with predictions of our chemical model.

## 6.2 Observations

Observations obtained in this study were collected as part of the GOTHAM Survey. GOTHAM is a large project on the 100m Green Bank Telescope (GBT) currently carrying out dedicated spectral line observations of TMC-1 covering almost 30 GHz of radio bandwidth at high sensitivity and ultra-fine spectral resolution. This work uses the second data release (DR2) of GOTHAM, which includes over 600 hours of observations targeting the cyanopolyne peak (CP) of TMC-1, centered at  $\alpha_{\text{J2000}} = 04^{\text{h}}41^{\text{m}}42.5^{\text{s}}$ ,  $\delta_{\text{J2000}} = +25^{\circ}41'26.8''$ . A full description of DR2 specifications and our reduction pipeline is described (McGuire et al., 2020), but put briefly, the spectra in this data set cover the entirety of the X-, K-, and Ka-receiver bands with nearly continuous coverage from 8.0 to 11.6 GHz and 18.0 to 33.5 GHz (25.6 GHz of total bandwidth). All spectra have a uniform frequency resolution of 1.4 kHz (0.05–0.01 km/s in velocity) and an RMS noise of  $\sim 2$ –20 mK, with the RMS gradually increasing toward higher frequency because of the lower integration times. Data reduction involved removal of RFI and artifacts, baseline continuum fitting, and flux calibration using complementary VLA observations of the source J0530+1331. Uncertainty from to this flux calibration is estimated at  $\sim 20\%$ , and is factored into our statistical analysis described below (McGuire et al., 2020).

## 6.3 Methods & Analysis

### 6.3.1 Molecular spectroscopy

All the MPs and MCPs are prolate symmetric top molecules with  $C_{3v}$  symmetry, meaning their rotational energy states are defined by the total angular momentum state  $J$  in addition to its projection along the unique axis of rotation, denoted by the

Table 6.1: Spectroscopic properties of stacked  $\text{CH}_3\text{C}_7\text{N}$  lines covered by the GBT X-band receiver

$J' \rightarrow J''$	Transitions $K$	$F' \rightarrow F''$	Symm.	Frequency (MHz)	$E_{up}$ (K)	$S_{ij}\mu^2$ ( $\text{D}^2$ )
11 $\rightarrow$ 10	1	10 $\rightarrow$ 9	<i>E</i>	8243.824	9.92	355.325
		11 $\rightarrow$ 10	<i>E</i>	8243.824	9.92	389.482
		12 $\rightarrow$ 11	<i>E</i>	8243.836	9.92	426.877
	0	10 $\rightarrow$ 9	<i>A</i>	8243.851	2.37	358.286
		11 $\rightarrow$ 10	<i>A</i>	8243.859	2.37	392.727
		12 $\rightarrow$ 11	<i>A</i>	8243.865	2.37	430.435
12 $\rightarrow$ 11	1	11 $\rightarrow$ 10	<i>E</i>	8993.262	10.35	391.696
		12 $\rightarrow$ 11	<i>E</i>	8993.263	10.35	426.021
		13 $\rightarrow$ 12	<i>E</i>	8993.272	10.35	463.320
	0	11 $\rightarrow$ 10	<i>A</i>	8993.293	2.81	394.435
		12 $\rightarrow$ 11	<i>A</i>	8993.299	2.81	429.000
		13 $\rightarrow$ 12	<i>A</i>	8993.304	2.81	466.560
13 $\rightarrow$ 12	1	12 $\rightarrow$ 11	<i>E</i>	9742.699	10.82	428.012
		13 $\rightarrow$ 12	<i>E</i>	9742.700	10.82	462.478
		14 $\rightarrow$ 13	<i>E</i>	9742.708	10.82	499.692
	0	12 $\rightarrow$ 11	<i>A</i>	9742.733	3.27	430.560
		13 $\rightarrow$ 12	<i>A</i>	9742.739	3.27	465.231
		14 $\rightarrow$ 13	<i>A</i>	9742.743	3.27	502.666
14 $\rightarrow$ 13	1	13 $\rightarrow$ 12	<i>E</i>	10492.136	11.33	464.286
		14 $\rightarrow$ 13	<i>E</i>	10492.137	11.33	498.870
		15 $\rightarrow$ 14	<i>E</i>	10492.144	11.33	536.010
	0	13 $\rightarrow$ 12	<i>A</i>	10492.173	3.78	466.667
		14 $\rightarrow$ 13	<i>A</i>	10492.178	3.78	501.429
		15 $\rightarrow$ 14	<i>A</i>	10492.181	3.78	538.758
15 $\rightarrow$ 14	1	14 $\rightarrow$ 13	<i>E</i>	11241.572	11.86	500.524
		15 $\rightarrow$ 14	<i>E</i>	11241.573	11.86	535.211
		16 $\rightarrow$ 15	<i>E</i>	11241.579	11.86	572.284
	0	14 $\rightarrow$ 13	<i>A</i>	11241.612	4.32	502.759
		15 $\rightarrow$ 14	<i>A</i>	11241.616	4.32	537.600
		16 $\rightarrow$ 15	<i>A</i>	11241.619	4.32	574.839

NOTE — Only  $K = 0$  and  $K = 1$  are included here since they contribute the brightest transitions; however we still considered states as high as  $K = 13$  in our MCMC model and stacking procedure. Similarly, lines ranging from  $J' = 27$  to  $J' = 44$  are covered by the GBT K- and Ka-bands and included in our analysis, but not shown here. For the full list of transitions used for  $\text{CH}_3\text{C}_7\text{N}$  and all other methyl carbon chains treated in this work, please refer to the linked Dataverse repository, [10.7910/DVN/K9HRCK]10.7910/DVN/K9HRCK.

quantum number  $K$ . Depending on the value of  $J$  and  $K$ , symmetric top molecules will either exhibit  $A$  or  $E$  symmetry due to the nuclear spin on the methyl group; and since radiative and collisional transitions between these symmetry states are strictly limited, their relative populations can be far from the expected thermal distribution. Because of this, we treat transitions from non-degenerate ( $A_1, A_2$  symmetry) and doubly degenerate ( $E$ ) levels separately by running independent MCMC fits. As such, we can compare the relative abundances of carbon chains in these energy states, similar to the separate treatment of the  $K = 0$  and  $K = 1$  components employed by Snyder et al. (2006) and Remijan et al. (2006).

For molecules with  $C_{3v}$  symmetry, the total statistical weight of rotational energy levels is the product of the typical  $J$ -degeneracy  $g_J = 2J + 1$ , the  $K$ -level degeneracy ( $g_k = 1$  for  $K = 0$  and  $g_k = 2$  for  $K \neq 0$ ), and the nuclear spin degeneracy  $g_I$  (Gordy & Cook, 1984). The reduced statistical weight contributed by nuclear spin statistics of three identical hydrogen nuclei in a methyl group (each with spin  $I = 1/2$ ) can be computed with the following:

$$g_I = \frac{1}{3} \frac{(4I^2 + 4I + 3)}{(2I + 1)^2}, \quad \text{for } K = 0, 3, 6, 9, \dots \quad (6.1)$$

$$g_I = \frac{1}{3} \frac{(4I^2 + 4I)}{(2I + 1)^2}, \quad \text{for } K \neq 0, 3, 6, 9, \dots \quad (6.2)$$

After combining all degeneracies, the states with  $A$  symmetry are weighted 2:1 relative to those with  $E$  symmetry, except in the case of  $K = 0$  which is weighted equally because of the lower factor of  $g_k$ . The rotational constants for the largest MCPs and MPs were measured by Chen et al. (1998) and Travers et al. (1998). To generate the spectroscopic data used for this work from these measurements, we used PGopher (Western, 2017; Western & Billingham, 2019), which is able to account for

the necessary symmetry and statistical considerations. The input files and line lists for all six species are available on the Harvard DataVerse[10.7910/DVN/K9HRCK].

As an example, Table 6.1 summarizes the spectroscopic properties of the rotational transitions of  $\text{CH}_3\text{C}_7\text{N}$  in X-band that were a part of this investigation. The transition quantum numbers, calculated rest frequencies (MHz), upper state energy level ( $K$ ), transition line strengths  $S(J, K)$  are presented. In the case of the MCPs, the nuclear spin on the nitrogen nucleus contributes hyperfine splitting to each rotational energy level.

Methyl acetylene ( $\text{CH}_3\text{CCH}$ ) was not included in our analysis as it does not have any transitions covered by the GOTHAM survey. Similarly, although the fundamental transition of methyl cyanide ( $\text{CH}_3\text{CN}$ ) is included in our spectra, a lack of additional lines prevents us from performing a full characterization of this molecule. For both  $\text{CH}_3\text{CN}$  and  $\text{CH}_3\text{CCH}$ , we refer to previous works studying these molecules in TMC-1 (e.g. Askne et al. (1984); Minh et al. (1993)), and instead base our analysis on the longer species.

### 6.3.2 MCMC modeling

In order to derive physical characteristics for the  $\text{CH}_3$ - polyynes and cyanopolyynes species in TMC-1, we use the same Markov-Chain Monte Carlo (MCMC) model employed in previous publications from the GOTHAM collaboration McGuire et al. (2020); Xue et al. (2020); McCarthy et al. (2020). This procedure is discussed at length in Loomis et al. (2021), but we will summarize it here as well. In short, the MCMC model calculates probability distributions and covariances for parameters describing the physical and excitation conditions of a molecule in TMC-1. Based on recent observations performed with the 45 m telescope at Nobeyama Radio Observatory (Dobashi et al., 2018, 2019), as well as our data (Loomis et al., 2021), emission

from molecules in TMC-1 toward the cyanopolyne peak display at least four individual velocity components. In our current model, we make the assumption that the emission from each velocity component is cospatial, similar to the approach adopted in Loomis et al. (2021) for the cyanopolyynes. To summarize, the model describing a given methyl chain comprises a source size, four radial velocities, eight column densities and two excitation temperatures describing A/E components, and a linewidth parameter, giving a total of 16 parameters.

Line profile simulations were performed using MOLSIM (Lee & McGuire, 2020). The MCMC simulations used wrapper functions in MOLSIM to ARVIZ (Kumar et al., 2019) and EMCEE (Foreman-Mackey et al., 2013); the former for analyzing the results of sampling, and the latter implements an affine-invariant MCMC sampler. As prior parameters, we used the marginalized posteriors from the corresponding cyanopolyne chain (e.g. HC<sub>3</sub>N and CH<sub>3</sub>C<sub>3</sub>N). The prior distributions are approximated as normally distributed (i.e.  $p(\theta) \sim N(\mu_\theta, \sigma_\theta)$  for parameter  $\theta$ ) with modifications to the variance  $\sigma_\theta$  as to avoid overly constrictive/influential priors. Convergence of the MCMC was confirmed using standard diagnostics such as the Gelman & Rubin (1992)  $\hat{R}$  statistic, and by visually inspecting the posterior traces. With each of the six species studied in this work, we compute separate MCMC model fits for the *A* and *E* symmetry states so their relative populations could be derived directly through comparison of the posterior distributions.

### 6.3.3 Spectral line stacking and matched filter

Following the formalism of Loomis et al. (2018); Loomis et al. (2021), we perform a combined velocity stack and matched filter analysis in order to verify that the results of the MCMC model are consistent with the data, and determine the statistical significance of molecular detections. The first step involves a noise-weighted sum in

velocity space of all expected transitions in our spectra, excluding any interloping transitions from known molecules in TMC-1; however, this was not necessary for any of the transitions in this analysis as there were no such interlopers. Next, the resulting composite spectrum is passed through a matched filter, using the best-fit parameters of the MCMC to create a model stacked spectrum. The impulse response of the matched filter, measured in signal-to-noise ratio  $\sigma$ , is a representation of how well the MCMC model reproduces GOTHAM spectra. Generally, we adopt a lower limit of  $5\sigma$  as a threshold for confirmation of a molecule in TMC-1.

## 6.4 Results & Discussion

### 6.4.1 Column densities and physical characteristics

Figure 6.1 shows the stacked data, the stacked MCMC model, as well as the matched filter response of all the methyl carbon chains considered in this work. We clearly detect  $\text{CH}_3\text{C}_3\text{N}$ ,  $\text{CH}_3\text{C}_5\text{N}$ ,  $\text{CH}_3\text{C}_4\text{H}$ , and  $\text{CH}_3\text{C}_6\text{H}$  at high significance, and the model is able to fit all components (both velocity and hyperfine) of these molecules. In the case of  $\text{CH}_3\text{C}_7\text{N}$ , though no individual lines are present above the current noise level of the survey, the stacked emission in the top right of Figure 6.1 exhibits noteworthy signal. Furthermore, its matched filter has a central peak at  $4.6\sigma$ , indicating evidence that this molecule is present in our data, and that the MCMC model converged to a set of parameters that reproduce its emission. The matched filter response is weaker than previous molecules that were found using this same method (Loomis et al., 2021; Lee et al., 2021; McGuire et al., 2021) and falls just below our desired  $5.0\sigma$  threshold for a definitive discovery, but it is sufficient to consider a tentative detection and adopt the parameters of its fit in our analysis. For more information on this detection as it is indicated in the Bayesian fit to the spectra (prior to any

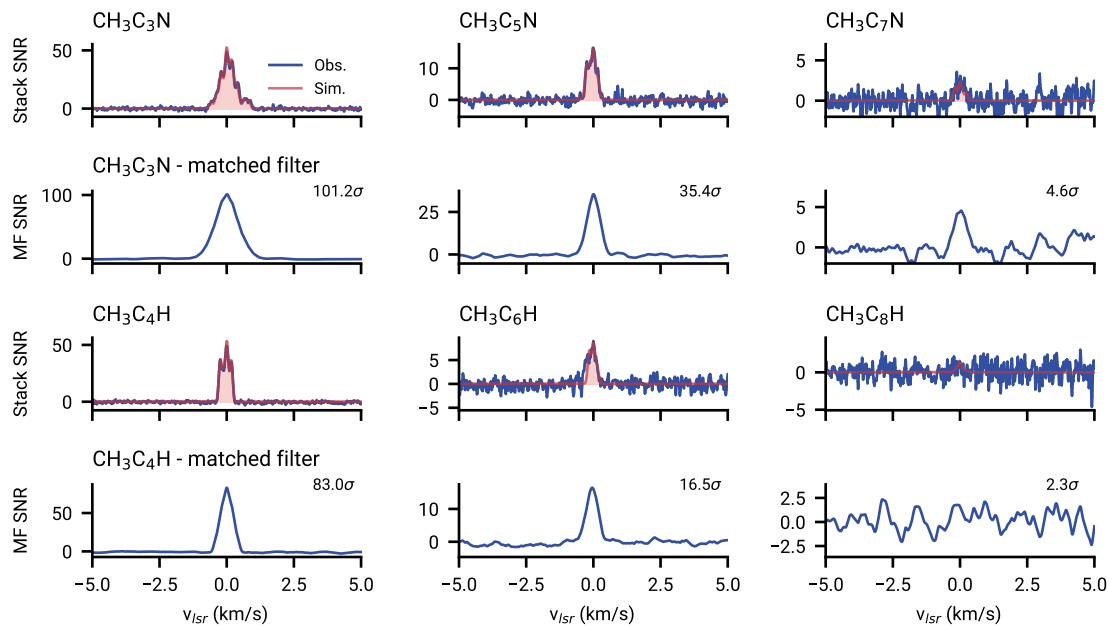


Figure 6.1: (*First and third rows*) Velocity stacks of the observational (blue) and MCMC simulated (red) spectra. The cross-correlation of the two velocity stacks for each molecule corresponds to the matched filter (MF) spectrum (*second and fourth rows*), which are shown in the second and fourth rows. Though the transitions belonging to *A* and *E* symmetry states were treated with separate MCMC fits, their results are combined here. The peak impulse response are annotated on the MF spectra.

stacking of emission lines), in Appendix 6.7, we present corner plots illustrating the full results of the MCMC model for both  $\text{CH}_3\text{C}_7\text{N}$  and  $\text{CH}_3\text{C}_8\text{H}$ , and discuss the posterior distributions and covariances in the parameter spaces for each. In contrast to  $\text{CH}_3\text{C}_7\text{N}$ ,  $\text{CH}_3\text{C}_8\text{H}$  shows a much higher degree of uncertainty in its fit, in addition to no signal in the stack nor its matched filter response (bottom-right panels of Fig. 6.1), so we therefore place upper limits on its column density.

A summary of parameters derived from the posterior distributions is provided in Table 6.2. Here, we note that the excitation temperatures of MPs (4.3 – 7.2 K) are systematically higher than those of the MCPs (3.4 – 3.9 K), which is in agreement

with previous studies of these species in TMC-1 (Brotten et al., 1984; Askne et al., 1984; Snyder et al., 2006). However, one exception to this is seen for the  $E$  state of  $\text{CH}_3\text{C}_3\text{N}$ , which has  $T_{ex} \sim 5.7$  K. At all derived excitation temperatures, we find that less than 4% of the total integrated line flux is contributed by transitions with  $K > 1$ . Furthermore, the population of the  $K = 2$  state at these low temperatures is less than 1% for all detected chains, which is well within the uncertainty of our measured column densities. In that sense, although states up to  $K = 13$  were considered, the column densities of the  $A$  and  $E$  components reported in Table 6.2 can be treated as equivalent to the column densities of the  $K = 0$  and  $K = 1$  components, respectively.

The total column densities (combining both  $A$  and  $E$  symmetries) decrease with increasing carbon chain length, much like the similar linear cyanopolyynes (Loomis et al., 2021). This is shown pictorially in Figure 6.2, with a comparison to the column densities found by Remijan et al. (2006). There is small but notable disagreement (less than a factor of four) between the column densities we find and those derived in Remijan et al. (2006). We attribute this discrepancy to the intrinsic line strengths ( $S_{ij}$ ) adopted from our numerical treatment of these molecules (see Section 6.3.1) as they are factors of 2–3 larger than the analytic values employed in Remijan et al. (2006) and Snyder et al. (2006). Another important factor is that the column densities we derive take into account decreasing source sizes, whereas previous studies of TMC-1 assume no effects due to beam dilution.

$\text{CH}_3\text{C}_7\text{N}$  has a total best-fit column density of  $8.60 \pm 1.9 \times 10^{10} \text{ cm}^{-2}$ , which matches well with the log-linear slope set by  $\text{CH}_3\text{C}_3\text{N}$  and  $\text{CH}_3\text{C}_5\text{N}$  (Fig. 6.2). Furthermore, this slope is very similar to that observed for the cyanopolyynes, and would imply the next chain ( $\text{CH}_3\text{C}_9\text{N}$ ) to have a column density of about  $3 \times 10^{10} \text{ cm}^{-2}$ . To detect stacked emission from this molecule at such an abundance, the RMS noise of the survey would need to be reduced by at least factor of five. This would require several

Table 6.2: MCMC model results for all observed CH<sub>3</sub>-terminated carbon chains. Uncertainties are listed as the 95% confidence level.

Molecule	$N_T$ ( $10^{11}$ cm <sup>-2</sup> )	$N_A$ ( $10^{11}$ cm <sup>-2</sup> )	$N_E$ ( $10^{11}$ cm <sup>-2</sup> )	$T_{ex}$ (A sym.) (K)	$T_{ex}$ (E sym.) (K)	Source Size <sup>b</sup>	A/E Ratio
-	-	-	-	-	-	-	-
CH <sub>3</sub> C <sub>3</sub> N	8.66 (.46)	5.00 (.40)	3.66 (.24)	3.36 (.40)	5.70 (.26)	481.0 (8.7) <sup>a</sup>	1.37 (.15)
CH <sub>3</sub> C <sub>5</sub> N	2.86 (.30)	2.01 (.29)	0.85 (.07)	3.48 (.34)	3.97 (.48)	128.7 (4.9) <sup>b</sup>	2.40 (.40)
CH <sub>3</sub> C <sub>7</sub> N	0.86 (.19)	0.69 (.18)	0.17 (.06)	3.82 (.25)	3.90 (.44)	53.9 (1.0) <sup>c</sup>	4.20 (1.8)
CH <sub>3</sub> C <sub>4</sub> H	100.8 (5.7)	60.0 (5.0)	40.8 (2.8)	4.31 (.84)	5.50 (.37)	481.0 (8.6) <sup>a</sup>	1.46 (.15)
CH <sub>3</sub> C <sub>6</sub> H	10.4 (.72)	6.10 (.60)	4.30 (.40)	7.19 (1.2)	6.41 (1.1)	128.3 (4.8) <sup>b</sup>	1.41 (.20)
CH <sub>3</sub> C <sub>8</sub> H	< 0.98	< 0.8	< 0.18	-	-	-	-

NOTE — <sup>a</sup>HC<sub>3</sub>N source size adopted as prior. See Loomis et al. (2021) for more details. <sup>b</sup>HC<sub>5</sub>N source size adopted as prior.  
<sup>c</sup>HC<sub>7</sub>N source size adopted as prior.

hundred more hours of integration time, primarily at lower frequencies (e.g. the GBT X-band receiver) because the brightest transitions of this molecule are simulated to be present in the 8–10 GHz range.

In contrast to the cyanopolyynes and MCPs, the MPs decrease in abundance at a much faster rate than the other carbon chains in TMC-1 (about 1 dex for each subsequent species). Furthermore, the upper limit we place on  $\text{CH}_3\text{C}_8\text{H}$  appears to break the trend seen in the shorter methylpolyynes. A linear extrapolation on the column densities of  $\text{CH}_3\text{C}_4\text{H}$  and  $\text{CH}_3\text{C}_6\text{H}$  (the blue points in Fig. 6.2) would imply the next chain length has a column density  $\sim 2 \times 10^{11} \text{ cm}^{-2}$ , but in this case we would have detected emission from  $\text{CH}_3\text{C}_8\text{H}$  at the sensitivity of our survey. Instead, it appears that the methylpolyynes experience a sharp drop-off in column density after  $\text{CH}_3\text{C}_6\text{H}$ , which indicates that the production of these carbon chains is severely hindered for these longer species.

A comparison to analogous linear species in TMC-1 is more difficult for the MPs, because the acetylene chains  $\text{H}_2\text{C}_{2n}$  have no dipole moment, and thus no rotational transition lines with which we could apply a similar analysis. However, the hydrocarbon radicals ( $\text{C}_{2n}\text{H}$ ) do exhibit transitions in the radio/sub-mm and have been characterized in TMC-1 up to a chain length of eight by Brünken et al. (2007) (green points in Fig. 6.2). Here, it is apparent that those species also exhibit a non-linear decrease in column density after a carbon chain length of six. In other words, a similar ratio of  $\frac{[\text{CH}_3\text{C}_8\text{H}]}{[\text{CH}_3\text{C}_6\text{H}]}$  to what is observed for  $\frac{[\text{C}_8\text{H}]}{[\text{C}_6\text{H}]}$  would be in agreement with the upper limits we set in this work. This may suggest that similar chemical routes govern the abundances of both the MPs and the hydrocarbon radicals. However, since our upper limit on  $\text{CH}_3\text{C}_8\text{H}$  is still very close to the log-linear extrapolated column density, it will be imperative to continue studying this molecule with future more sensitive data releases from GOTHAM survey to identify how steep this drop-off is, and how similar

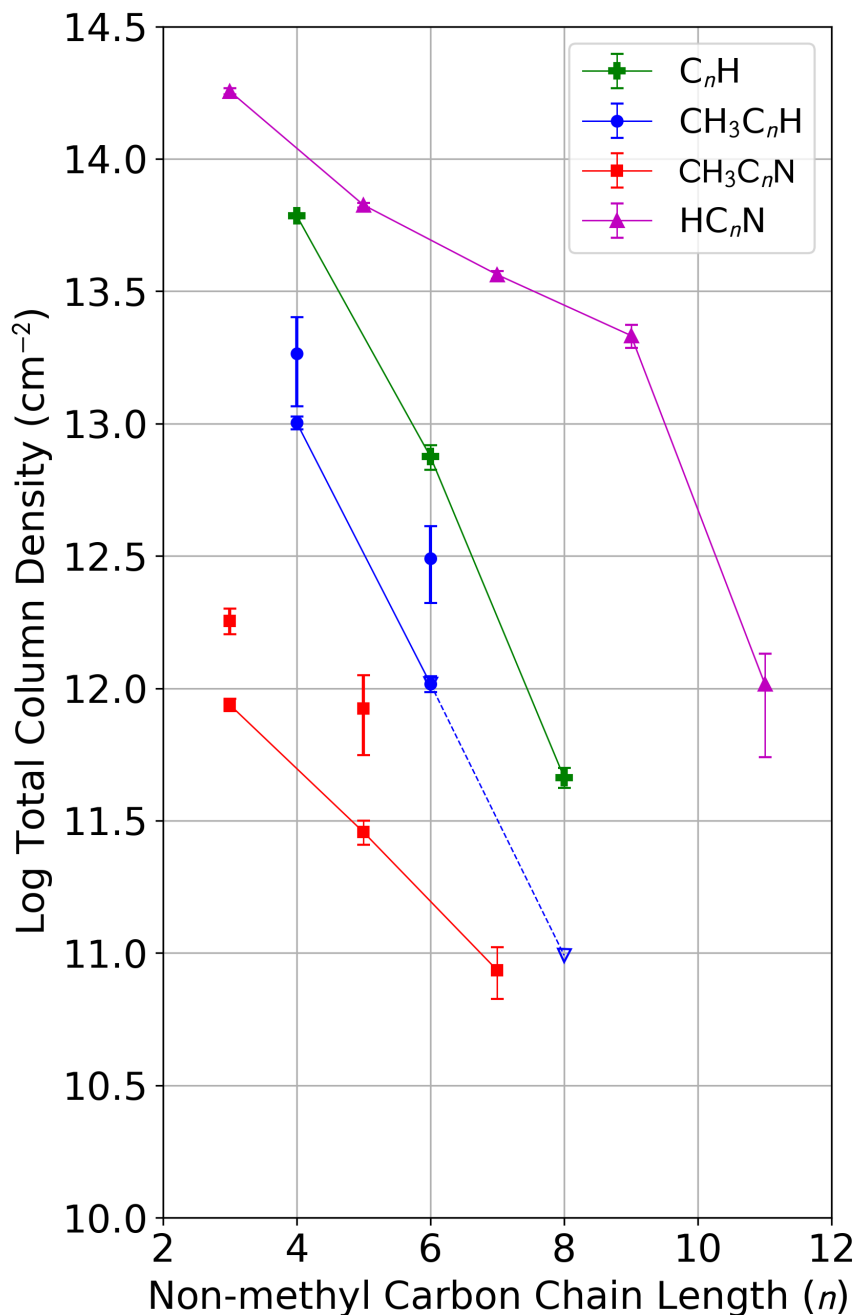


Figure 6.2: Derived total column densities of methyl-terminated carbon chains in TMC-1 as a function of chain length. Methylcyanopolyynes are shown in red while methylpolyynes are shown in blue. Contributions from the A and E symmetries of each species are summed, with their errors added in quadrature.  $CH_3C_8H$  is denoted with a triangle as it is an upper limit. Results from Remijan et al. (2006) are overplotted in their respective colors with no connecting line. Additionally, column densities of the linear cyanopolyynes and hydrocarbons radicals published in Loomis et al. (2021) and Brünken et al. (2007) are shown in pink and green, respectively.

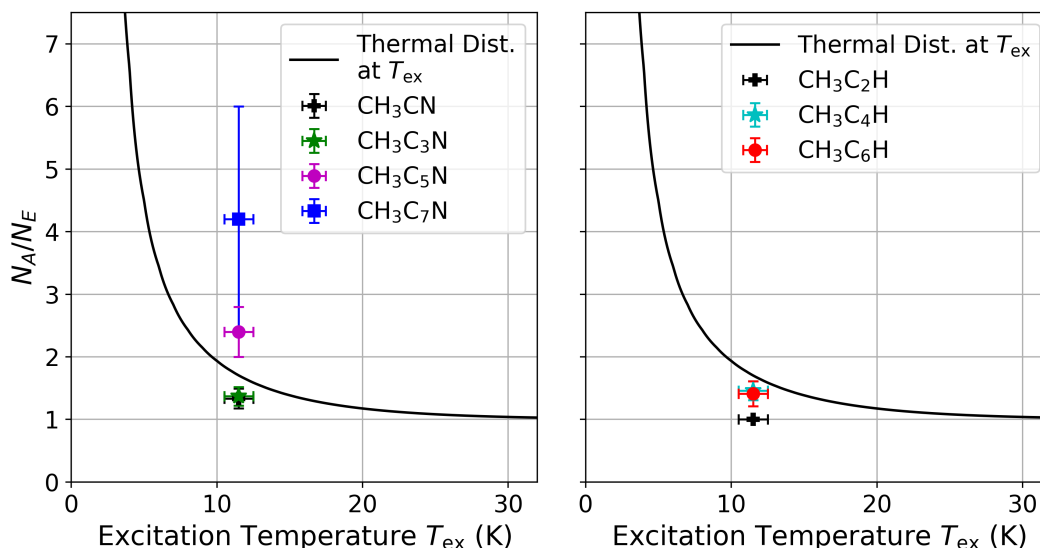


Figure 6.3: Column density ratios toward TMC-1 of  $A$  and  $E$  symmetry states for each of the chains studied in this work (colored points), as well as those derived for methyl cyanide and methyl acetylene by Minh et al. (1993) and Askne et al. (1984), respectively (black points). Also plotted in black is the expected ratio of these two populations if the molecules are thermalized to a Boltzmann distribution at a range of kinetic temperatures. The vertical error on the points represents the 95% confidence level from our MCMC modeling results, and the horizontal error bars denote the range of kinetic temperatures observed for gas phase molecules toward the CP region TMC-1 (Fehér et al., 2016).

it is to the relative column density of  $\text{C}_3\text{H}$ .

#### 6.4.2 $A/E$ symmetry state populations

Askne et al. (1984) found that in TMC-1, methyl acetylene ( $\text{CH}_3\text{CCH}$ ) has about equal abundances of  $A$  and  $E$  symmetry states, which is not expected under LTE conditions and could indicate this molecule formed at a higher temperature. A similar result was found for  $\text{CH}_3\text{C}_4\text{H}$  by Walmsley et al. (1984). In contrast, Minh et al. (1993) found that for  $\text{CH}_3\text{CN}$  in TMC-1,  $N_E/N_A = 0.76 \pm 0.09$ , which suggests that these states are equilibrated to the kinetic temperature. With the sensitivity and bandwidth of GOTHAM DR2, we are able to revisit some of these population studies

with a larger data set and expand them to the longer molecules  $\text{CH}_3\text{C}_6\text{H}$ ,  $\text{CH}_3\text{C}_3\text{N}$ ,  $\text{CH}_3\text{C}_5\text{N}$ , and  $\text{CH}_3\text{C}_7\text{N}$ . Because we performed separate MCMC analyses for the  $A$  and  $E$  states of each symmetric top carbon chain, their ratios can be computed directly and are shown in the last column of Table 6.2.

Figure 6.3 shows a comparison of all  $A/E$  ratios derived in this work plotted alongside the expected ratio in a thermalized distribution for a range of excitation temperatures. The gas phase kinetic temperature at the CP of TMC-1 has recently been placed at  $11 \pm 1.0$  K by Fehér et al. (2016), so methyl chains with  $A/E \approx 1.75$  can be considered as having equilibrated to this temperature.

For the MCPs (left plot in Fig. 6.3), we note that the  $A/E$  ratio increases for longer chain lengths, starting at a superthermal value of 1.33 for  $\text{CH}_3\text{CN}$  (as measured by Minh et al. (1993)) and reaching  $4.2 \pm 1.8$  for  $\text{CH}_3\text{C}_7\text{N}$  which corresponds to an excitation temperature of  $6.1 \pm 2$  K, which is much lower than the kinetic temperature in TMC-1. In contrast, the MPs (right plot in Fig. 6.3) have nearly constant  $A/E$  ratios between 1.4 and 1.5. While this is only slightly smaller than the equilibrium value of 1.75, it is indicative that all MPs studied here have slightly larger  $E$  symmetry populations than what is expected given the physical conditions in TMC-1.

As noted in Section 6.3.1, both radiative and collisional interconversion between the  $A$  and  $E$  symmetry states are forbidden for both the MCPs and MPs (unless proton exchange collisions are non-negligible). Willacy et al. (1993) investigated the possibility that  $E \rightarrow A$  conversion of  $\text{CH}_3\text{CN}$  occurs through  $E$ -state species adsorbing to and subsequently desorbing from grain surfaces in TMC-1. They found that this is an efficient process so long as the desorption rate is high enough. This may suggest that an important distinction may be happening in TMC-1. Highly exothermic reactions in the gas phase (e.g. dissociative recombination) may drive the formation of the MPs, forcing them into superthermal  $A/E$  distributions, where

as the largest MCPs may preferentially form on (or stick to) the surfaces of dust grains. The non-thermal desorption of large complex molecules like the MCPs in TMC-1 has been a topic of numerous recent computation efforts (Garrod et al., 2007; Herbst & Cuppen, 2006; Hoang & Tung, 2019; Minissale et al., 2016; Shingledecker et al., 2021), but it is still difficult to say exactly how efficient this process is for the species explored here. The investigation of the potential bifurcation of the formation pathways between the MPs and the MCPs using astrochemical models might shed further light on this intriguing situation.

## 6.5 Chemical modeling of methyl chains

To further explore the chemistry of methyl-terminated carbon chains in TMC-1, we utilized the adapted three-phase gas-grain chemical network model `nautilus v1.1` code (Ruaud et al., 2016) discussed in previous analysis of GOTHAM data, which has previously been used to successfully study the formation of carbon-chain molecules (Xue et al., 2020; McGuire et al., 2020; Shingledecker et al., 2021). The physical conditions of the model are equal to what has been previously used with this network ( $T_{\text{gas}} = T_{\text{grain}} = 10$  K,  $n_{\text{H}_2} = 2 \times 10^4 \text{ cm}^{-3}$ ,  $A_V = 10$ , and  $\zeta_{\text{CR}} = 1.3 \times 10^{-17} \text{ s}^{-1}$ ; Hincelin et al. (2011)) as are the elemental abundances (Loomis et al., 2021). Based originally off of the KIDA network, the network already contained the formation of MCPs up to  $n = 7$  and MPs up to  $n = 6$ . Here, we expanded on this to include the formation of  $\text{CH}_3\text{C}_8\text{H}$ , as well as additional reaction to better constrain the formation of the smaller members of this family.

To simulate the formation and destruction of  $\text{CH}_3\text{C}_8\text{H}$ , we utilized the analogous pathways for the existing network of  $\text{CH}_3\text{C}_6\text{H}$ , whose primary formation routes are from the dissociate recombination of  $\text{C}_7\text{H}_5^+$ . As such, we expanded out the formation of  $\text{C}_9\text{H}_5^+$  from ion-neutral reactions with semi-saturated carbon chains, whose rates

were estimated using the Langevin formula (Woon & Herbst, 2009). It should be noted that the rates for  $C_7H_5^+$  and  $CH_3C_6H$  are calculated using the Modified Arrhenius formula, which may result in some potential discrepancies between this and  $CH_3C_8H$ . As a source of destruction of  $C_9H_5^+$ , we adapted existing dissociate recombination of similar cations. The rates and branching ratios  $C_9H_5^+$  and  $C_7H_5^+$  were estimated and updated, respectively, based on the dissociate recombination of  $C_5H_5^+$  whose rates are taken from Herbst & Leung (1989) and branching ratios are discussed in detail on the KIDA website<sup>1</sup>. In addition to dissociative recombination,  $C_nH_5^+$  ions present in KIDA were also destroyed by reactions with anions. As such, the rates of the anion destruction of  $C_9H_5^+$  were based off analogous rates estimated for  $C_7H_5^+$  by Harada & Herbst (2008). Due to a lack of robust isomerization for large molecules within existing chemical networks, we only consider the  $C_7H_5^+$  and  $C_9H_5^+$  isomers with KIDA entries (i.e.  $CH_3C_nCH_2^+$ )

The analogous destruction of  $CH_3C_6H$  was also adapted for  $CH_3C_8H$ . This included 1) dissociation due to photons and cosmic rays 2) ion-neutral reactions with abundant ions (i.e.  $H^+$ ,  $H_3^+$ ,  $C^+$ ,  $HCO^+$ , and  $He^+$ ) which were estimated with Langevin formula and 3) reaction with elemental carbon to form  $C_{10}H_2$  and  $H_2$ . To properly study  $C_9H_5^+$ , we also added in several neutral-neutral reactions to better account for the formation of  $C_5H_3$ , a  $C_9H_5^+$ -precursor, which were obtained originally from Hébrard et al. (2009). Finally, we included an additional formation pathway for the MPs by reactions of the  $C_{2n}H$  family with methane based on work by Quan & Herbst (2007) and formation of  $CH_3C_4H$  from  $CH_3CHCH_2$  by Berteloite et al. (2010).

For the MCPs, no additional reactions or rates were added from the KIDA network beyond the related adaptations from other recent molecular detections (e.g. the expanded semi-saturated carbon-chain networks for  $HC_4NC$  (Xue et al., 2020),

---

<sup>1</sup>[http://kida.astrophy.u-bordeaux.fr/datasheet/datasheet\\_2761\\_C5H5++e-\\_V1.pdf](http://kida.astrophy.u-bordeaux.fr/datasheet/datasheet_2761_C5H5++e-_V1.pdf)

$C_6H_5CN$  (Burkhardt et al., 2021a),  $H_2CCCHC_3N$  (Shingledecker et al., 2021), and indene (Burkhardt et al., 2021b)).

The results of this model can be seen in Figure 6.4 at a time of  $2.5 \times 10^5$  yrs, assuming a TMC-1 hydrogen column density of  $N_{H_2} = 10^{22} \text{ cm}^{-2}$ . At this time in the model, the simulated abundances of all studied species are within an order of magnitude of their observed values. For the MCPs (solid red line in Fig. 6.4), the abundance of  $CH_3C_3N$  is higher than the observed value, while the remainder of the family are somewhat below their observed value. As such, the log-linear trend is less well constrained here. The relative trend line was also fairly independent of time, with a slight increase of the longer chains at later times, as seen in Fig. 6.7. This is expected as longer chains typically have their peak abundance several  $10^5$  years after similar smaller chains, as seen by the cyanopolyynes (Loomis et al., 2021). The dominant formation pathways for the MCPs are the dissociative recombination of the  $C_{n+1}H_4N^+$  ion family, which are in turn primarily produced by reactions between the cyanopolyynes and  $CH_3^+$ , with minor contributions from  $C_{n+1}H_3N^+$  and  $N + C_{n+1}H_5^+$  after several  $10^5$  years. In particular,  $CH_3C_3N$  has an additional production from  $H_3C_4N^+ + H_2$  that may account for its deviation from the trendline of the rest of the MCP family. The MCPs are primarily destroyed by ion-neutral reactions with abundant ions (i.e.  $H^+$ ,  $H_3^+$ ,  $C^+$ ,  $HCO^+$ , and  $He^+$ ). The dependence on the cyanopolyynes (solid pink line in Fig. 6.4) is consistent with the similar observed abundance trends seen in Figure 6.2.

For the MPs (solid blue line in Fig. 6.4), the relative abundance trends of both the simulated and observed values are in good agreement at this time. This slope of this trend is also very consistent with the simulated abundance trend of the  $C_nH$  family (solid green line in Fig. 6.4). Within the general uncertainties of the source age of TMC-1 ( $\sim 2\text{-}5 \times 10^5$  years), the abundance of  $CH_3C_4H$  was found to be consis-

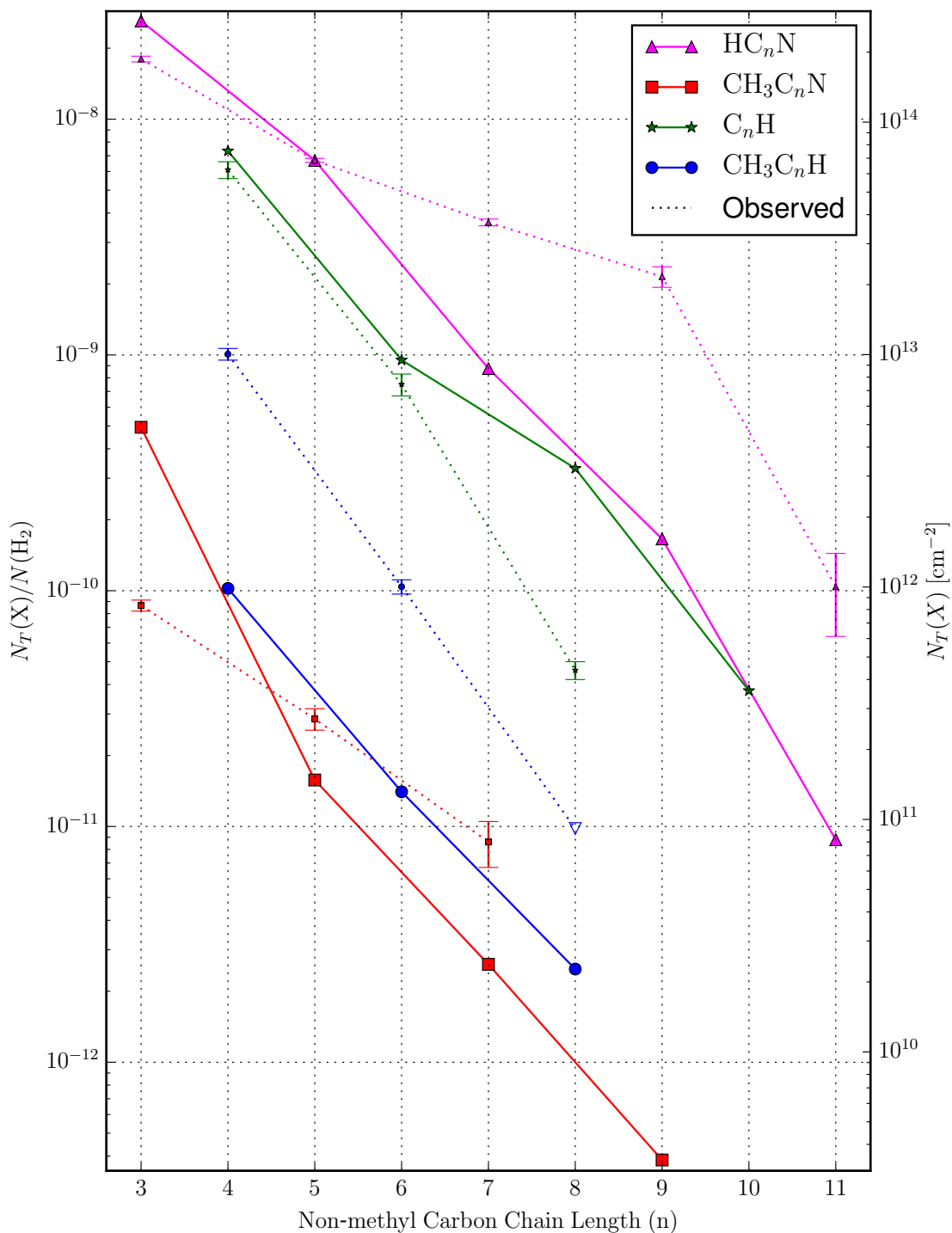


Figure 6.4: Simulated abundances and column densities of the four carbon chain families studied here at a model time of  $2.5 \times 10^5$  years, with the same colors and markers as Figure 6.2. Observed values are shown as dotted lines and the  $CH_3C_8H$  upper limit is denoted as an unfilled triangle.

tently in worst agreement with the observed values but improving at later times by a ~60% abundance increase, while the longer chains increased up to nearly an order of magnitude (See Fig. 6.7). As a result, the trend line was in less consistently in agreement with the observed trend at later times, while reproducing the observed abundances better. Due to the overall depletion of  $\text{CH}_3\text{C}_4\text{H}$ , we have chosen this as a representative time as the simulated abundances are still within typical uncertainties for kinetic chemical models and we suspect the trend at this model time would remain consistent if a more efficient production is found either through new proposed pathways or improved reaction rate measurement/calculations. More generally, this strong dependence on the source age contrasts with other carbon chain families such as the cyanopolyynes and MCPs, whose observed trends are fairly consistent across the possible source ages of TMC-1.

The dominant formation route for the MPs are from the dissociative recombination of the  $\text{C}_{n+1}\text{H}_5^+$  family, with a significant contribution from  $\text{C}_n\text{H}$  reactions with methane after  $\sim 10^5$  years. The  $\text{C}_{n+1}\text{H}_5^+$  family are produced by various ion-neutral reactions, notably  $\text{C}_n\text{H}_2^+$  with methane and  $\text{C}_{n+1}\text{H}_2$  with  $\text{C}_2\text{H}_4^+$  ( $< 10^5$  years). These dominant pathways provide strength for the observed relation between the MPs and  $\text{C}_n\text{H}$  families. There is also an increased importance after  $10^5$  years of  $\text{C}_4\text{H}_3^+$  + methane for  $\text{CH}_3\text{C}_4\text{H}$  and  $\text{C}_3\text{H}_3 + \text{C}_4\text{H}_2$  for  $\text{CH}_3\text{C}_6\text{H}$ . MPs are mostly destroyed by ion-neutral reactions and reactions with carbon atoms.

Overall, the predictions of these chemical models are within an order of magnitude of agreement with the observed values of TMC-1, indicating that carbon chain chemistry can be fairly well understood. In addition, the observed MP trend line can be reproduced well and is also analogous to what is observed for  $\text{C}_n\text{H}$ . The estimated branching ratios and reaction rates still remain a major source of uncertainties in the models, which provide a strong motivation for further laboratory and theoretic-

cal studies. As discussed in Burkhardt et al. (2021b), detailed study of increasing larger molecules (e.g. molecules with 7+ heavy atoms and/or aromatic rings) will likely require a rigorous study of the formation of semi-saturated carbon chains that have historically been performed piecewise. The recent expanded inventory of known carbon chains in TMC-1 will provide key constraints in this study.

## 6.6 Conclusions

We performed a rigorous, self-consistent study of methylpolyynes and methylcyanopolyynes in TMC-1 using the second data release of GOTHAM. Through MCMC modeling and matched filter analysis of stacked of emission lines, we derived column densities, excitation temperatures, and  $A/E$  symmetry ratios for all previously found species, and discovered evidence for a new interstellar symmetric top, methylcyanotriacetylene ( $\text{CH}_3\text{C}_7\text{N}$ ), at a confidence level of  $4.6\sigma$ . We also searched for methyltetraacetylene ( $\text{CH}_3\text{C}_8\text{H}$ ) in our spectra and place upper limits on its column density in TMC-1.

In our analysis, we found two important divisions between the different families of molecules explored in this work:

1. The column densities of methylcyanopolyynes decrease in a log-linear manner with increasing carbon chain length, and the slope of this trend is similar to the cyanopolyynes. In contrast, the methylpolyynes experience a drop-off in column density for species larger than  $\text{CH}_3\text{C}_6\text{H}$  that is not consistent with the trend set by the smaller species.
2. The  $A/E$  ratios of methylcyanopolyynes increase with carbon chain length, and are subthermal for the larger species. The detected methylpolyynes have systematically smaller  $A/E$  ratios which are not equilibrated to the kinetic

temperature in TMC-1.

Given the structural similarity of the two classes of molecules, these dichotomies are striking and point to separate formation and carbon chain growth mechanisms in TMC-1. Whether these differences exist between the analogous cyanopolyynes ( $\text{HC}_{2n+1}\text{N}$ ) and the pure hydrocarbon polyynes ( $\text{H}_2\text{C}_{2n}$ ) is unclear, as the latter have no dipole moment. To understand this, future infrared observations of vibrational bands from these molecules toward TMC-1 would be instrumental in constraining their abundances and understanding their formation chemistry.

Finally, utilizing a gas-grain chemical network, we modeled the formation and destruction of  $\text{CH}_3$ -terminated carbon chains in TMC-1. The model is able to reproduce our observed column densities to within an order of magnitude, and we see very similar trends in the exponentially decreasing abundances with carbon chain length. However, we are not able to predict the observed drop-off in column density for  $\text{CH}_3\text{C}_8\text{H}$  or  $\text{C}_8\text{H}$  using this model.

The results of this analysis offer important insights into the formation of carbon chain molecules in cold pre-stellar conditions, but it is important to note that many other families of unsaturated carbon chain species are known to form in TMC-1 (e.g.  $\text{C}_n\text{O}$ ,  $\text{C}_n\text{S}$ ,  $\text{HC}_n\text{O}$ ). Similar in-depth analyses of these groups of molecules would be instrumental in improving our understanding the extent and efficiency of carbon chemistry in TMC-1.

## 6.7 Appendix: MCMC posterior distributions

Figure 6.5 and 6.6 shows the MCMC posterior distributions for  $\text{CH}_3\text{C}_7\text{N}$  and  $\text{CH}_3\text{C}_8\text{H}$  respectively. Based on the off-diagonal heatmaps, we see that the majority of modeling parameters do not demonstrate significant covariance; those that do typically pertain to radial velocities and column densities of each velocity component, often those adjacent to one another in velocity and within the same symmetry group (i.e.  $E$  state column densities in neighboring velocity components). We do not expect significant covariance between the  $A/E$  states for both species, as they are by in large spectroscopically separate.

Regarding the treatment of source sizes, we observe quite different posteriors in comparison to the earlier work done by Loomis et al. (2021), which highlighted significant covariance between source sizes and column densities. We do not observe this for  $\text{CH}_3\text{C}_7\text{N}$  most likely due to an overly constrained prior placed on the source size, and we likely underestimate its uncertainty and covariance. In the case of  $\text{CH}_3\text{C}_8\text{H}$ , we fixed the mean value of  $\text{HC}_7\text{N}$  Loomis et al. (2021), as we were interested in estimating upper limits to the column densities, and thus not shown in Figure 6.6.

Comparison of the posterior distributions for the column densities between  $\text{CH}_3\text{C}_7\text{N}$  and  $\text{CH}_3\text{C}_8\text{H}$  provides a margin for detection and non-detection cases. In the former, where the matched filtering shown in Figure 6.1 indicates a  $4.6\sigma$  likelihood for  $\text{CH}_3\text{C}_7\text{N}$ , corroborating with smaller uncertainties in the column densities in comparison to  $\text{CH}_3\text{C}_8\text{H}$ , particularly for the first velocity component. We interpret this as a smaller range of column density values provide evidential support for the tentative detection of  $\text{CH}_3\text{C}_7\text{N}$ : even with the absence of individual lines, the likelihood-based sampling is able to place relatively large constraints on the possible values.

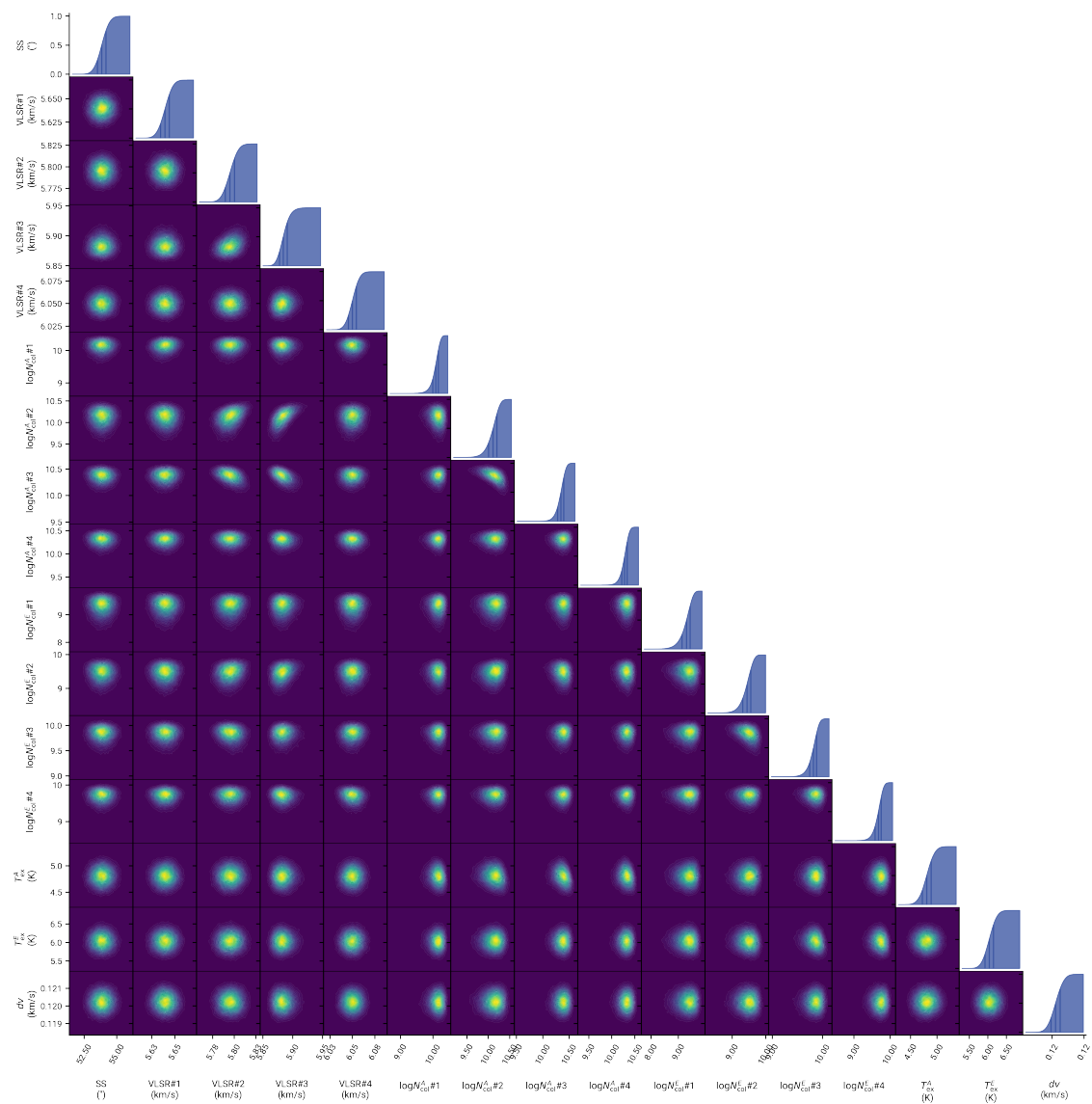


Figure 6.5: Corner plot for CH<sub>3</sub>C<sub>7</sub>N. The diagonal traces correspond to the marginalized, cumulative posterior distributions for each parameter, and off-diagonal heatmaps represent parameter covariances. Vertical lines in the cumulative distribution plots represent the first, second, and third quantiles.

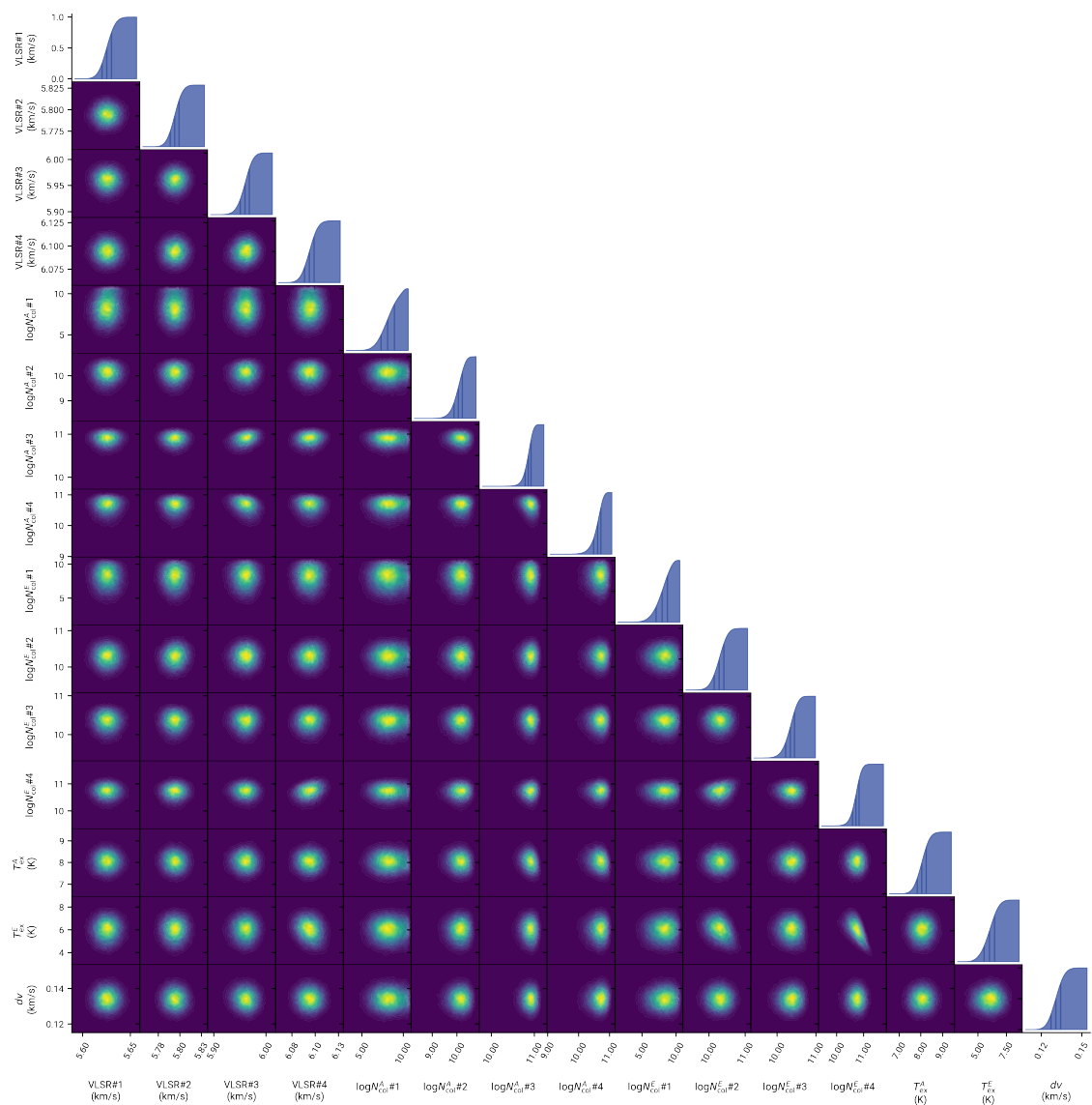


Figure 6.6: Corner plot for CH<sub>3</sub>C<sub>8</sub>H. The diagonal traces correspond to the marginalized, cumulative posterior distributions for each parameter, and off-diagonal heatmaps represent parameter covariances. Vertical lines in the cumulative distribution plots represent the first, second, and third quantiles.

## 6.8 Appendix: Chemical Model Time Dependence

Figure 6.7 shows the time-dependence of the simulated abundances within the *nautilus* chemical models in relation to the observed values. As it can be seen, the relative trend lines of these species can be quite time dependent, the time of peak abundance is strongly dependent on carbon chain length.

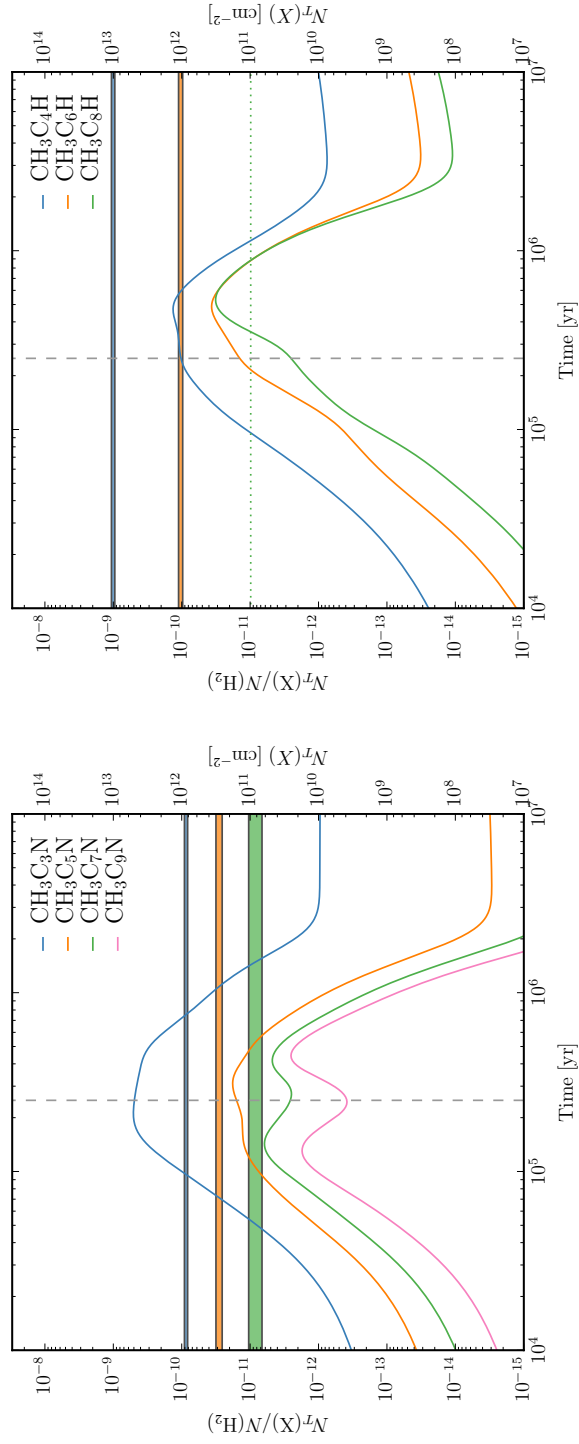


Figure 6.7: Simulated gas-phase abundance and column densities of the  $\text{CH}_3\text{C}_n\text{N}$  (*left*) and  $\text{CH}_3\text{C}_n\text{H}$  (*right*) families from nautilus chemical models in comparison to the observed values with uncertainties as a horizontal bars. The upper limit of the  $\text{CH}_3\text{C}_8\text{H}$  is shown as green dotted line. The time used in Figure 6.4 is shown as a vertical dashed gray line.

## CHAPTER 7

# Conclusions

In this thesis, I have undertaken multiple observational studies of carbon-rich chemistry in the outflows of dying stars, as well as the quiescent molecular cloud TMC-1. Characterizing how carbonaceous molecules are formed and processed in these objects is fundamental to understanding the chemical evolution of astronomical environments as well as the origin of organic material in the Solar System.

In Chapter 2, I reported a submillimeter search for the diatomic hydrides SiH, PH, and FeH along the line of sight toward the carbon- and oxygen- rich circumstellar envelopes of IRC+10216 and VY Canis Majoris. These molecules are thought to form in high temperature regions near the photospheres of these dying stars, and may then further react via gas-phase and dust-grain interactions leading to more complex species, but they had yet to be constrained by observations. We used the GREAT spectrometer on SOFIA to search for rotational emission lines of these molecules in four spectral windows ranging from 600 GHz to 1500 GHz. Though none of the targeted species were detected in our investigation, we calculated their upper limit abundances in each source and discussed how they influence the current understanding of hydride chemistry in dense C-rich circumstellar media. From these results, it is

clear that fully hydrogenated molecules such as  $\text{SiH}_4$ ,  $\text{PH}_3$ , and likely  $\text{CH}_4$  must be synthesized rapidly, with minimal intermediate steps that would be expected if they were formed under equilibrium conditions.

In Chapter 3, I explored photochemistry in the warm regions of circumstellar envelopes, and presented archival ALMA observations which we used to map rotational lines involving high energy levels of cyanoacetylene ( $\text{HC}_3\text{N}$ ) toward the inner envelope (radius  $< 8''/1000 \text{ AU}$ ) of the carbon star IRC+10216. The observed lines included the  $J = 28 - 27$ ,  $J = 30 - 29$ , and  $J = 38 - 37$ , transitions of  $\text{HC}_3\text{N}$  in its ground vibrational state. In contrast to previous observations of linear carbon chains toward this AGB star which show extended, hollow emission at  $15'' - 20''$  radii (e.g.  $\text{C}_4\text{H}$ ,  $\text{C}_6\text{H}$ ,  $\text{HC}_5\text{N}$ ), our maps of the  $\text{HC}_3\text{N}$  lines showed compact morphologies comprising various arcs and density enhancements, with significant emission from gas clumps at an angular distance of  $\sim 3''$  (350 au) from the central AGB star. We compared visibility sampled non-LTE radiative transfer models with the observed brightness distributions, and calculated a fractional abundance with respect to  $\text{H}_2$  of  $10^{-8}$  for  $\text{HC}_3\text{N}$  at the radii probed by these lines. These results are consistent with enhanced photochemistry occurring in warm ( $\sim 200 \text{ K}$ ) regions of the circumstellar envelope. After application of a specialized chemical model for IRC+10216, we found evidence that the enhanced  $\text{HC}_3\text{N}$  abundances in the inner wind are most likely due to a solar-type binary companion initiating photochemistry in this region.

In Chapter 4, I further investigated the connection between binaries and circumstellar chemistry by presenting a detailed spectroscopic case study of the binary C-rich AGB star V Hya. Using spatially resolved ALMA observations at Bands 3, 6 and 7, we characterized the rotational emission lines and distributions of molecules in its surrounding disk undergoing dynamical expansion. We found emission from over 15 molecules and isotopologues toward this source, and produced resolved maps for the

brightest tracers of carbonaceous chemistry (e.g. CCH, C<sub>4</sub>H, HC<sub>5</sub>N, HNC, CH<sub>3</sub>CN). Employing LTE and non-LTE models of emission from the DUDE, we estimated the abundance distributions for optically thin species, and compare them with prototypical carbon-rich AGB envelopes. We saw that the detected species and their average abundances are not far off from sources with similar mass-loss rates; however, the distribution of daughter species in V Hya is much more compact, with carbon chain radicals appearing with large abundances ( $>10^{-7}$ ) in the inner 200 au of the disk. We proposed that this behavior is the result of an excess of dissociating radiation driving photochemistry at close radii in this source, potentially caused by the unique binary-induced geometry of the outflow.

In Chapter 5, I moved to the more evolved source, V510 Pup: a binary post-AGB system with a fast molecular outflow that has been noted for its puzzling mixture of carbon- and oxygen-rich features in the optical and infrared. To explore this chemical dichotomy and relate it to the kinematics of the source, I presented an ACA spectral line survey detailing fourteen newly detected molecules in this pre-planetary nebula. The simultaneous presence of CN/C<sub>2</sub>H/HC<sub>3</sub>N and SO/SO<sub>2</sub> supported the previous conclusion of mixed chemistry, and their line profiles indicated that the C- and O-rich material trace distinct velocity structures in the outflow. This evidence suggests that V510 Pup could harbor a dense O-rich central waist from an earlier stage of evolution, which persisted after a fast bipolar C-rich molecular outflow formed.

Finally, in Chapter 6, I provided a systematic study of all known methyl carbon chains toward the dark cloud TMC-1 using the second data release of the GOTHAM survey, as well as a search for larger species. Using Markov-Chain Monte Carlo simulations and spectral line stacking of over 30 rotational transitions, we reported statistically significant emission from methylcyanotriacetylene (CH<sub>3</sub>C<sub>7</sub>N) at a confidence level of  $4.6\sigma$ , and used it to derive a column density of  $\sim 10^{11}$  cm<sup>-2</sup>. We also searched

for the related species, methyltetraacetylene ( $\text{CH}_3\text{C}_8\text{H}$ ), and place upper limits on the column density of this molecule. By carrying out the above statistical analyses for all other previously detected methyl-terminated carbon chains that have emission lines in our survey, we assessed the abundances, excitation conditions, and formation chemistry of methylpolyynes ( $\text{CH}_3\text{C}_{2n}\text{H}$ ) and methylcyanopolyynes ( $\text{CH}_3\text{C}_{2n-1}\text{N}$ ) in TMC-1, and compared those with predictions from a chemical model. Based on the observed trends in column density and relative populations of the *A* and *E* nuclear spin isomers, we found that the methylpolyyne and methylcyanopolyyne families exhibit stark differences from one another, pointing to separate interstellar formation pathways, which was confirmed by a gas-grain chemical network.

## 7.1 Future Work

The work included in this thesis provides a few exciting examples of how carbon chemistry is inherently coupled to the physics of evolved star outflows. The case studies of IRC+10216, V Hya, and V510 Pup exist as key evidence that complex stellar evolution breeds complex circumstellar chemistry; however, these three sources only represent snapshots of a dynamic and varied process that takes place over  $\sim 10^6$  yr. To capture the breadth of these asymmetric effects, and their impact on the organic yield of these systems as a whole, upcoming observational surveys should emphasize expanding the chemical sample size of evolved stars to as many stages of stellar and binary evolution as possible. A crucial piece of this analysis, as exemplified by the chapters in this thesis, should be obtaining as much spectral coverage as possible and high spatial resolving power, as they allow us to better constrain molecular abundances and excitation conditions in the complicated morphologies of such objects. Fortunately, this will be enabled better-than-ever by the upcoming ALMA Wideband Sensitivity Upgrade (Carpenter et al., 2023).

Additionally, while the studies here are meant to characterize the relevant chemical steps (e.g. photochemistry, shocks) in complex stellar environments, how these impact the primary recycling products of AGB stars, like dust and aromatics, is presently unclear. And although chemical models of prestellar clouds can reproduce the observed abundances of linear and symmetric-top carbon chains like the ones I studied in Chapter 6, they are not nearly as successful for the cyclic and polycyclic species that are now being discovered at an incredible pace (McGuire et al., 2021; Burkhardt et al., 2021b). Because it is already known that a significant fraction of aromatics in the solar system are inherited from hot stellar environments (Zeichner et al., 2023), observing ring-bearing molecules in evolved stars is paramount to placing these discoveries in the broader context of the evolution and inheritance of organics in the ISM. This could be accomplished by JWST, which can observe vibrational transitions of benzene (Tabone et al., 2023), or with ultra-deep radio spectroscopic surveys similar to those performed for TMC-1.

# Bibliography

- Adams, W. S. 1941, *The Astrophysical Journal*, 93, 11
- Agúndez, M. 2009, PhD thesis, Center for Astrobiology, Madrid
- Agúndez, M., Cernicharo, J., Decin, L., Encrenaz, P., & Teyssier, D. 2014, *ApJ*, 790, L27, doi: 10.1088/2041-8205/790/2/L27
- Agúndez, M., Cernicharo, J., & Guélin, M. 2010, *Astrophysical Journal, Letters*, 724, L133, doi: 10.1088/2041-8205/724/2/L133
- Agúndez, M., Cernicharo, J., Quintana-Lacaci, G., et al. 2015, *Astrophysical Journal*, 814, 143, doi: 10.1088/0004-637X/814/2/143
- Agúndez, M., Cernicharo, J., Waters, L. B. F. M., et al. 2011, *Astronomy and Astrophysics*, 533, L6, doi: 10.1051/0004-6361/201117578
- Agúndez, M., Fonfría, J. P., Cernicharo, J., et al. 2012, *Astronomy and Astrophysics*, 543, A48, doi: 10.1051/0004-6361/201218963
- Agúndez, M., Fonfría, J. P., Cernicharo, J., Pardo, J. R., & Guélin, M. 2008, *Astronomy and Astrophysics*, 479, 493, doi: 10.1051/0004-6361:20078956
- Agúndez, M., Martínez, J. I., de Andres, P. L., Cernicharo, J., & Martín-Gago, J. A. 2020, *Astronomy and Astrophysics*, 637, A59, doi: 10.1051/0004-6361/202037496
- Agúndez, M., Cernicharo, J., Quintana-Lacaci, G., et al. 2017, *A&A*, 601, A4, doi: 10.1051/0004-6361/201630274

- Agúndez, M., Cernicharo, J., Quintana-Lacaci, G., et al. 2017, *Astronomy and Astrophysics*, 601, A4, doi: 10.1051/0004-6361/201630274
- Alcolea, J., Bujarrabal, V., Planesas, P., et al. 2013, *Astronomy and Astrophysics*, 559, A93, doi: 10.1051/0004-6361/201321683
- Amari, S., Anders, A., Virag, A., & Zinner, E. 1990, *Nature*, 345, 238, doi: 10.1038/345238a0
- Andrews, H., Candian, A., & Tielens, A. G. G. M. 2016, *Astronomy and Astrophysics*, 595, A23, doi: 10.1051/0004-6361/201628819
- Andriantsaralaza, M., Ramstedt, S., Vlemmings, W. H. T., & De Beck, E. 2022, *Astronomy and Astrophysics*, 667, A74, doi: 10.1051/0004-6361/202243670
- Askne, J., Hoglund, B., Hjalmarson, A., & Irvine, W. M. 1984, *Astronomy and Astrophysics*, 130, 311
- Avery, L. W., Amano, T., Bell, M. B., et al. 1992, *Astrophysical Journal, Supplement*, 83, 363, doi: 10.1086/191742
- Bakker, E. J., van Dishoeck, E. F., Waters, L. B. F. M., & Schoenmaker, T. 1997, *Astronomy and Astrophysics*, 323, 469, doi: 10.48550/arXiv.astro-ph/9610063
- Balucani, N., Ceccarelli, C., & Taquet, V. 2015, *Monthly Notices of the Royal Astronomical Society*, 449, L16, doi: 10.1093/mnrasl/slv009
- Barklem, P. S., & Collet, R. 2016, *Astronomy and Astrophysics*, 588, A96, doi: 10.1051/0004-6361/201526961
- Bell, M. B., Avery, L. W., & Feldman, P. A. 1993, *Astrophysical Journal, Letters*, 417, L37, doi: 10.1086/187088
- Belloche, A., Garrod, R. T., Müller, H. S. P., et al. 2009, *Astronomy and Astrophysics*, 499, 215, doi: 10.1051/0004-6361/200811550
- Bernatowicz, T. J., Amari, S., Zinner, E. K., & Lewis, R. S. 1991, *Astrophysical Journal, Letters*, 373, L73, doi: 10.1086/186054

- Berteloite, C., Le Picard, S. D., Balucani, N., Canosa, A., & Sims, I. R. 2010, *Physical Chemistry Chemical Physics*, 12, 3666
- Blake, G. A., Keene, J., & Phillips, T. G. 1985, *Astrophysical Journal*, 295, 501, doi: 10.1086/163394
- Boersma, C., Hony, S., & Tielens, A. G. G. M. 2006, *Astronomy and Astrophysics*, 447, 213, doi: 10.1051/0004-6361:20053904
- Brinch, C., & Hogerheijde, M. R. 2010, *Astronomy and Astrophysics*, 523, A25, doi: 10.1051/0004-6361/201015333
- Brotten, N. W., MacLeod, J. M., Avery, L. W., et al. 1984, *Astrophysical Journal, Letters*, 276, L25, doi: 10.1086/184181
- Brown, J. M., Körsgen, H., Beaton, S. P., & Evenson, K. M. 2006, *The Journal of Chemical Physics*, 124, 234309
- Brünken, S., Gupta, H., Gottlieb, C. A., McCarthy, M. C., & Thaddeus, P. 2007, *Astrophysical Journal, Letters*, 664, L43, doi: 10.1086/520703
- Brunner, M., Danilovich, T., Ramstedt, S., et al. 2018, *Astronomy and Astrophysics*, 617, A23, doi: 10.1051/0004-6361/201832724
- Burkhardt, A. M., Herbst, E., Kalenskii, S. V., et al. 2018, *Monthly Notices of the Royal Astronomical Society*, 474, 5068, doi: 10.1093/mnras/stx2972
- Burkhardt, A. M., Loomis, R. A., Shingledecker, C. N., et al. 2021a, *Nature Astronomy*, 5, 181, doi: 10.1038/s41550-020-01253-4
- Burkhardt, A. M., Long Kelvin Lee, K., Bryan Changala, P., et al. 2021b, *The Astrophysical Journal*, 913, L18, doi: 10.3847/2041-8213/abfd3a
- Busemann, H., Young, A. F., O'D. Alexander, C. M., et al. 2006, *Science*, 312, 727, doi: 10.1126/science.1123878
- Cabezas, C., Tercero, B., Agúndez, M., et al. 2021, *Astronomy and Astrophysics*, 650, L9, doi: 10.1051/0004-6361/202141274

- Campins, H., & Ryan, E. V. 1989, *Astrophysical Journal*, 341, 1059, doi: 10.1086/167563
- Carpenter, J., Brogan, C., Iono, D., & Mroczkowski, T. 2023, in *Physics and Chemistry of Star Formation: The Dynamical ISM Across Time and Spatial Scales*, ed. V. Ossenkopf-Okada, R. Schaaf, I. Breloy, & J. Stutzki, 304, doi: 10.48550/arXiv.2211.00195
- Carroll, P. K., & McCormack, P. 1972, *The Astrophysical Journal Letters*, 177, L33, doi: 10.1086/181047
- Carroll, P. K., McCormack, P., & Oconnor, S. 1976, *The Astrophysical Journal*, 208, 903, doi: 10.1086/154679
- Carroll, T. J., & Goldsmith, P. F. 1981, *Astrophysical Journal*, 245, 891, doi: 10.1086/158865
- CASA Team, Bean, B., Bhatnagar, S., et al. 2022, *Publications of the ASP*, 134, 114501, doi: 10.1088/1538-3873/ac9642
- Caselli, P., Hartquist, T. W., & Havnes, O. 1997, *Astronomy and Astrophysics*, 322, 296
- Cernicharo, J., Agúndez, M., Cabezas, C., et al. 2021, *Astronomy and Astrophysics*, 649, L15, doi: 10.1051/0004-6361/202141156
- Cernicharo, J., Daniel, F., Castro-Carrizo, A., et al. 2013, *Astrophysical Journal Letters*, 778, L25, doi: 10.1088/2041-8205/778/2/L25
- Cernicharo, J., Guélin, M., & Kahane, C. 2000, *Astronomy and Astrophysics, Supplement*, 142, 181, doi: 10.1051/aas:2000147
- Cernicharo, J., Heras, A. M., Tielens, A. G. G. M., et al. 2001, *Astrophysical Journal Letters*, 546, L123, doi: 10.1086/318871
- Cernicharo, J., Marcelino, N., Agúndez, M., et al. 2020, *Astronomy and Astrophysics*, 642, L17, doi: 10.1051/0004-6361/202039351
- Cernicharo, J., Marcelino, N., Agúndez, M., & Guélin, M. 2015, *Astronomy and Astrophysics*, 575, A91, doi: 10.1051/0004-6361/201424565

- Cernicharo, J., Decin, L., Barlow, M. J., et al. 2010, *Astronomy & Astrophysics*, 518, L136
- Cernicharo, J., Teyssier, D., Quintana-Lacaci, G., et al. 2014, *Astrophysical Journal Letters*, 796, L21, doi: 10.1088/2041-8205/796/1/L21
- Chen, W., Grabow, J.-U., Travers, M., et al. 1998, *Journal of Molecular Spectroscopy*, 192, 1, doi: <https://doi.org/10.1006/jmsp.1998.7665>
- Chen, W., Grabow, J. U., Travers, M. J., et al. 1998, *Journal of Molecular Spectroscopy*, 192, 1, doi: 10.1006/jmsp.1998.7665
- Cherchneff, I. 2012, *Astronomy and Astrophysics*, 545, A12, doi: 10.1051/0004-6361/201118542
- Cherchneff, I. 2012, *Astronomy & Astrophysics*, 545, A12
- Cherchneff, I., Barker, J. R., & Tielens, A. G. G. M. 1992, *Astrophysical Journal*, 401, 269, doi: 10.1086/172059
- Chertihin, G. V., & Andrews, L. 1995, *The Journal of Physical Chemistry*, 99, 12131, doi: 10.1021/j100032a013
- Cheung, A. C., Rank, D. M., Townes, C. H., Thornton, D. D., & Welch, W. J. 1968, *Physical Review Letters*, 21, 1701, doi: 10.1103/PhysRevLett.21.1701
- Chiar, J. E., Tielens, A. G. G. M., Adamson, A. J., & Ricca, A. 2013, *Astrophysical Journal*, 770, 78, doi: 10.1088/0004-637X/770/1/78
- Chibueze, J. O., Miyahara, T., Omodaka, T., et al. 2016, *Astrophysical Journal*, 817, 115, doi: 10.3847/0004-637X/817/2/115
- Chiu, P.-J., Hoang, C.-T., Dinh-V-Trung, et al. 2006, *Astrophysical Journal*, 645, 605, doi: 10.1086/504309
- Churchwell, E., Winnewisser, G., & Walmsley, C. M. 1978, *Astronomy and Astrophysics*, 67, 139
- Codella, C., Lefloch, B., Ceccarelli, C., et al. 2010, *Astronomy and Astrophysics*, 518, L112, doi: 10.1051/0004-6361/201014582

- Cordiner, M. A., & Millar, T. J. 2009, *Astrophysical Journal*, 697, 68, doi: 10.1088/0004-637X/697/1/68
- Cornwell, T. J. 2008, *IEEE Journal of Selected Topics in Signal Processing*, 2, 793, doi: 10.1109/JSTSP.2008.2006388
- Cortes, P. C., Remijan, A., Biggs, A., et al. 2020, *ALMA Technical Handbook*, <https://almascience.eso.org/documents-and-tools/cycle8/alma-technical-handbook>
- Costagliola, F., & Aalto, S. 2010, *Astronomy and Astrophysics*, 515, A71, doi: 10.1051/0004-6361/200913370
- Cruikshank, D. P., Materese, C. K., Pendleton, Y. J., et al. 2019, *Astrobiology*, 19, 831, doi: 10.1089/ast.2018.1927
- Daniel, F., Agúndez, M., Cernicharo, J., et al. 2012, *Astronomy and Astrophysics*, 542, A37, doi: 10.1051/0004-6361/201118449
- Danilovich, T., Malfait, J., Van de Sande, M., et al. 2024, *Nature Astronomy*, doi: 10.1038/s41550-023-02154-y
- De Beck, E., Decin, L., de Koter, A., et al. 2010, *Astronomy and Astrophysics*, 523, A18, doi: 10.1051/0004-6361/200913771
- De Beck, E., Lombaert, R., Agúndez, M., et al. 2012, *Astronomy and Astrophysics*, 539, A108, doi: 10.1051/0004-6361/201117635
- De Marco, O. 2009, *Publications of the ASP*, 121, 316, doi: 10.1086/597765
- Decin, L. 2021, *Annual Review of Astron and Astrophys*, 59, 337, doi: 10.1146/annurev-astro-090120-033712
- Decin, L., Richards, A. M. S., Danilovich, T., Homan, W., & Nuth, J. A. 2018, *Astronomy and Astrophysics*, 615, A28, doi: 10.1051/0004-6361/201732216
- Decin, L., Richards, A. M. S., Neufeld, D., et al. 2015, *Astronomy and Astrophysics*, 574, A5, doi: 10.1051/0004-6361/201424593

- Decin, L., Agúndez, M., Barlow, M. J., et al. 2010, *Nature*, 467, 64, doi: 10.1038/nature09344
- Decin, L., Royer, P., Cox, N. L. J., et al. 2011, *Astronomy and Astrophysics*, 534, A1, doi: 10.1051/0004-6361/201117360
- Decin, L., Montargès, M., Richards, A. M. S., et al. 2020, *Science*, 369, 1497, doi: 10.1126/science.abb1229
- Deguchi, S., & Uyemura, M. 1984, *Astrophysical Journal*, 285, 153, doi: 10.1086/162486
- Díaz Trigo, M., De Breuck, C., Hatziminaoglou, E., et al. 2023, *The Messenger*, 191, 6, doi: 10.18727/0722-6691/5334
- Dinh-V-Trung, & Lim, J. 2008, *Astrophysical Journal*, 678, 303, doi: 10.1086/527669
- Dobashi, K., Shimoikura, T., Nakamura, F., et al. 2018, *The Astrophysical Journal*, 864, 82, doi: 10.3847/1538-4357/aad62f
- Dobashi, K., Shimoikura, T., Ochiai, T., et al. 2019, *The Astrophysical Journal*, 879, 88, doi: 10.3847/1538-4357/ab25f0
- Draine, B. T. 2016, *Astrophysical Journal*, 831, 109, doi: 10.3847/0004-637X/831/1/109
- Duley, W. W., & Williams, D. A. 1981, *Monthly Notices of the RAS*, 196, 269, doi: 10.1093/mnras/196.2.269
- Eigenbrode, J. L., Summons, R. E., Steele, A., et al. 2018, *Science*, 360, 1096, doi: 10.1126/science.aas9185
- Faure, A., Lique, F., & Wiesenfeld, L. 2016, *Monthly Notices of the RAS*, 460, 2103, doi: 10.1093/mnras/stw1156
- Fehér, O., Tóth, L. V., Ward-Thompson, D., et al. 2016, *Astronomy and Astrophysics*, 590, A75, doi: 10.1051/0004-6361/201424385
- Ferrarotti, A. S., & Gail, H. P. 2006, *Astronomy and Astrophysics*, 447, 553, doi: 10.1051/0004-6361:20041198

- Fonfría, J. P., Agúndez, M., Cernicharo, J., Richter, M. J., & Lacy, J. H. 2018, *Astrophysical Journal*, 852, 80, doi: 10.3847/1538-4357/aa9ee0
- Fonfría, J. P., Cernicharo, J., Richter, M. J., & Lacy, J. H. 2008, *Astrophysical Journal*, 673, 445, doi: 10.1086/523882
- Fonfría, J. P., DeWitt, C. N., Montiel, E. J., Cernicharo, J., & Richter, M. J. 2022, *Astrophysical Journal, Letters*, 927, L33, doi: 10.3847/2041-8213/ac5a58
- Fonfría, J. P., Cernicharo, J., Richter, M. J., & Lacy, J. H. 2008, *The Astrophysical Journal*, 673, 445, doi: 10.1086/523882
- Fong, D., Meixner, M., Castro-Carrizo, A., et al. 2001, *Astronomy and Astrophysics*, 367, 652, doi: 10.1051/0004-6361:20000434
- Foreman-Mackey, D., Hogg, D. W., Lang, D., & Goodman, J. 2013, *Publications of the Astronomical Society of the Pacific*, 125, 306, doi: 10.1086/670067
- Frisch, M. J., Trucks, G. W., Schlegel, H. B., et al. 2009, *Gaussian 09, Revision B.01*, Gaussian, Inc., Wallingford CT
- Gaia Collaboration, Brown, A. G. A., Vallenari, A., et al. 2021, *Astronomy and Astrophysics*, 649, A1, doi: 10.1051/0004-6361/202039657
- Gallardo Cava, I., Bujarrabal, V., Alcolea, J., Gómez-Garrido, M., & Santander-García, M. 2022, *Astronomy and Astrophysics*, 659, A134, doi: 10.1051/0004-6361/202142339
- Garrod, R. T., Wakelam, V., & Herbst, E. 2007, *Astronomy and Astrophysics*, 467, 1103, doi: 10.1051/0004-6361:20066704
- Gatchell, M., Ameixa, J., Ji, M., et al. 2021, *Nature Communications*, 12, 6646, doi: 10.1038/s41467-021-26899-0
- Gehrz, R. 1989, in *IAU Symposium, Vol. 135, Interstellar Dust*, ed. L. J. Allamandola & A. G. G. M. Tielens, 445
- Gelman, A., & Rubin, D. B. 1992, in *Bayesian Statistics (Oxford University Press)*, 625 – 631

- Gielen, C., Cami, J., Bouwman, J., Peeters, E., & Min, M. 2011, *Astronomy and Astrophysics*, 536, A54, doi: 10.1051/0004-6361/201117961
- Goesmann, F., Rosenbauer, H., Bredehöft, J. H., et al. 2015, *Science*, 349, 2.689, doi: 10.1126/science.aab0689
- Goldsmith, P. F., Krotkov, R., Snell, R. L., Brown, R. D., & Godfrey, P. 1983, *Astrophysical Journal*, 274, 184, doi: 10.1086/161436
- Goldsmith, P. F., & Langer, W. D. 1999, *Astrophysical Journal*, 517, 209, doi: 10.1086/307195
- Goldsmith, P. F., & Langer, W. D. 1999, *Astrophys. J.*, 517, 209
- Gong, Y., Henkel, C., Spezzano, S., et al. 2015, *Astronomy & Astrophysics*, 574, A56
- Gong, Y., Henkel, C., Spezzano, S., et al. 2015, *Astronomy and Astrophysics*, 574, A56, doi: 10.1051/0004-6361/201424819
- Gordon, I. E., Rothman, L. S., Hargreaves, R. J., et al. 2022, *Journal of Quantitative Spectroscopy and Radiative Transfer*, 277, 107949, doi: 10.1016/j.jqsrt.2021.107949
- Gordy, W., & Cook, R. 1984, *Microwave Molecular Spectra* (John Wiley & Sons)
- Gray, M. D., Humphreys, E. M. L., & Yates, J. A. 1999, *Monthly Notices of the RAS*, 304, 906, doi: 10.1046/j.1365-8711.1999.02372.x
- Groenewegen, M. A. T., Sevenster, M., Spoon, H. W. W., & Pérez, I. 2002, *Astronomy and Astrophysics*, 390, 511, doi: 10.1051/0004-6361:20020728
- Guelin, M., Lucas, R., & Cernicharo, J. 1993, *Astronomy and Astrophysics*, 280, L19
- Guélin, M., Patel, N. A., Bremer, M., et al. 2018, *Astronomy and Astrophysics*, 610, A4, doi: 10.1051/0004-6361/201731619
- Guerrero, M. A., Ramos-Larios, G., Toalá, J. A., Balick, B., & Sabin, L. 2020, *Monthly Notices of the RAS*, 495, 2234, doi: 10.1093/mnras/staa1225
- Harada, N., & Herbst, E. 2008, *The Astrophysical Journal*, 685, 272, doi: 10.1086/590468

- Harada, N., Herbst, E., & Wakelam, V. 2010, *The Astrophysical Journal*, 721, 1570, doi: 10.1088/0004-637X/721/2/1570
- He, J. H., Dinh-V-Trung, & Hasegawa, T. I. 2017, *Astrophysical Journal*, 845, 38, doi: 10.3847/1538-4357/aa7e76
- He, J. H., Dinh-V-Trung, Kwok, S., et al. 2008, *Astrophysical Journal*, Supplement, 177, 275, doi: 10.1086/587142
- He, J. H., Kamiński, T., Mennickent, R. E., et al. 2019, *Astrophysical Journal*, 883, 165, doi: 10.3847/1538-4357/ab3d37
- Hébrard, E., Dobrijevic, M., Pernot, P., et al. 2009, *Journal of Physical Chemistry A*, 113, 11227, doi: 10.1021/jp905524e
- Herbst, E. 1976, *Astrophysical Journal*, 205, 94, doi: 10.1086/154253
- Herbst, E., & Cuppen, H. M. 2006, *Proceedings of the National Academy of Science*, 103, 12257, doi: 10.1073/pnas.0601556103
- Herbst, E., & Leung, C. M. 1989, *The Astrophysical Journal Supplement Series*, 69, 271, doi: 10.1086/191314
- Herwig, F. 2005, *Annual Review of Astron and Astrophys*, 43, 435, doi: 10.1146/annurev.astro.43.072103.150600
- Hincelin, U., Wakelam, V., Hersant, F., et al. 2011, *Astronomy & Astrophysics*, 530, A61, doi: 10.1051/0004-6361/201016328
- Hoang, T., & Tung, N.-D. 2019, *Astrophysical Journal*, 885, 125, doi: 10.3847/1538-4357/ab4810
- Höfner, S., & Olofsson, H. 2018, *Astronomy and Astrophysics Reviews*, 26, 1, doi: 10.1007/s00159-017-0106-5
- Hollis, J. M., Jewell, P. R., Lovas, F. J., & Remijan, A. 2004, *The Astrophysical Journal*, 613, L45
- Homan, W., Danilovich, T., Decin, L., et al. 2018, *Astronomy and Astrophysics*, 614, A113, doi: 10.1051/0004-6361/201732246

- Homan, W., Montargès, M., Pimpanuwat, B., et al. 2020, *Astronomy and Astrophysics*, 644, A61, doi: 10.1051/0004-6361/202039185
- Humphreys, R. M., & Jones, T. J. 2022, *Astronomical Journal*, 163, 103, doi: 10.3847/1538-3881/ac46ff
- Irikura, K., Goddard, W., & Beuchamp, J. 1990, *International Journal of Mass Spectrometry and Ion Processes*, 99, 213
- Irvine, W. M., Høglund, B., Friberg, P., Askne, J., & Ellder, J. 1981, *Astrophysical Journal, Letters*, 248, L113, doi: 10.1086/183637
- Jolly, A., Benilan, Y., & Fayt, A. 2007, *Journal of Molecular Spectroscopy*, 242, 46, doi: 10.1016/j.jms.2007.01.008
- Jones, A. P., Fanciullo, L., Köhler, M., et al. 2013, *Astronomy and Astrophysics*, 558, A62, doi: 10.1051/0004-6361/201321686
- Jones, A. P., Tielens, A. G. G. M., & Hollenbach, D. J. 1996, *Astrophysical Journal*, 469, 740, doi: 10.1086/177823
- Jones, A. P., Tielens, A. G. G. M., Hollenbach, D. J., & McKee, C. F. 1994, *Astrophysical Journal*, 433, 797, doi: 10.1086/174689
- Kamiński, T., Gottlieb, C. A., Young, K. H., Menten, K. M., & Patel, N. A. 2013a, *Astrophysical Journal, Supplement*, 209, 38, doi: 10.1088/0067-0049/209/2/38
- Kamiński, T., Schmidt, M. R., & Menten, K. M. 2013b, *Astronomy and Astrophysics*, 549, A6, doi: 10.1051/0004-6361/201220650
- Kamiński, T., Gottlieb, C. A., Menten, K. M., et al. 2013, *Astronomy & Astrophysics*, 551, 113
- Kawaguchi, K., Kasai, Y., Ishikawa, S.-I., & Kaifu, N. 1995, *Publications of the ASJ*, 47, 853
- Keady, J. J., & Ridgway, S. T. 1993, *Astrophysical Journal*, 406, 199, doi: 10.1086/172431

- Keller, D. 2017, PhD thesis, Max Planck Institute for Radio Astronomy, Bonn, Germany
- Keller, L. P., Messenger, S., Flynn, G. J., et al. 2004, *Geochimica Cosmochimica Acta*, 68, 2577, doi: 10.1016/j.gca.2003.10.044
- Kepley, A. A., Tsutsumi, T., Brogan, C. L., et al. 2020, *Publications of the ASP*, 132, 024505, doi: 10.1088/1538-3873/ab5e14
- Kervella, P., Montargès, M., Ridgway, S. T., et al. 2014, *Astronomy and Astrophysics*, 564, A88, doi: 10.1051/0004-6361/201323273
- Khouri, T., Vlemmings, W. H. T., Ramstedt, S., et al. 2016, *Monthly Notices of the RAS*, 463, L74, doi: 10.1093/mnrasl/slw161
- Kim, H., Lee, H.-G., Maunon, N., & Chu, Y.-H. 2015a, *Astrophysical Journal, Letters*, 804, L10, doi: 10.1088/2041-8205/804/1/L10
- Kim, H., Lee, H.-G., Ohyama, Y., et al. 2021, *Astrophysical Journal*, 914, 35, doi: 10.3847/1538-4357/abf6cc
- Kim, H., Liu, S.-Y., Hirano, N., et al. 2015b, *Astrophysical Journal*, 814, 61, doi: 10.1088/0004-637X/814/1/61
- Knapp, G. R., & Chang, K. M. 1985, *Astrophysical Journal*, 293, 281, doi: 10.1086/163235
- Knapp, G. R., Dobrovolsky, S. I., Ivezić, Z., et al. 1999, *Astronomy and Astrophysics*, 351, 97, doi: 10.48550/arXiv.astro-ph/9907234
- Knapp, G. R., Jorissen, A., & Young, K. 1997, *Astronomy and Astrophysics*, 326, 318
- Kumar, R., Carroll, C., Hartikainen, A., & Martin, O. 2019, *Journal of Open Source Software*, 4, 1143, doi: 10.21105/joss.01143
- Lagadec, E., Verhoelst, T., Mékarnia, D., et al. 2011, *Monthly Notices of the RAS*, 417, 32, doi: 10.1111/j.1365-2966.2011.18557.x

- Leão, I. C., de Laverny, P., Mékarnia, D., de Medeiros, J. R., & Vandame, B. 2006, *Astronomy and Astrophysics*, 455, 187, doi: 10.1051/0004-6361:20054577
- Lee, K. L. K., & McGuire, B. A. 2020, molsim, Zenodo. <https://zenodo.org/record/4122749>
- Lee, K. L. K., Loomis, R. A., Burkhardt, A. M., et al. 2021, *Astrophysical Journal, Letters*, 908, L11, doi: 10.3847/2041-8213/abdbb9
- Li, X., Millar, T. J., Heays, A. N., et al. 2016, *Astronomy and Astrophysics*, 588, A4, doi: 10.1051/0004-6361/201525739
- Liimets, T., Corradi, R. L. M., Jones, D., et al. 2018, *Astronomy and Astrophysics*, 612, A118, doi: 10.1051/0004-6361/201732073
- Loison, J.-C., Wakelam, V., & Hickson, K. M. 2014, *Monthly Notices of the RAS*, 443, 398, doi: 10.1093/mnras/stu1089
- Loomis, R. A., Cleeves, L. I., Öberg, K. I., et al. 2018a, *Astrophysical Journal*, 859, 131, doi: 10.3847/1538-4357/aac169
- Loomis, R. A., Öberg, K. I., Andrews, S. M., et al. 2018b, *Astronomical Journal*, 155, 182, doi: 10.3847/1538-3881/aab604
- Loomis, R. A., Burkhardt, A. M., Shingledecker, C. N., et al. 2021, *Nature Astronomy*, 5, 188, doi: 10.1038/s41550-020-01261-4
- Loomis, R. A., Öberg, K. I., Andrews, S. M., et al. 2018, *The Astronomical Journal*, 155, 182, doi: 10.3847/1538-3881/aab604
- Loren, R. B., Wootten, A., & Mundy, L. G. 1984, *Astrophysical Journal, Letters*, 286, L23, doi: 10.1086/184377
- Lorenz, R. D., Mitchell, K. L., Kirk, R. L., et al. 2008, *Geophysics Research Letters*, 35, L02206, doi: 10.1029/2007GL032118
- Mackay, D. D. S. 1995, *MNRAS*, 274, 694, doi: 10.1093/mnras/274.3.694
- MacLeod, J. M., Avery, L. W., & Broten, N. W. 1984, *Astrophysical Journal, Letters*, 282, L89, doi: 10.1086/184312

- Maercker, M., Vlemmings, W. H. T., Brunner, M., et al. 2016, *Astronomy and Astrophysics*, 586, A5, doi: 10.1051/0004-6361/201527128
- Mangum, J. G., & Shirley, Y. L. 2015, *Publications of the Astronomical Society of the Pacific*, 127, 266
- Manick, R., Miszalski, B., Kamath, D., et al. 2021, *Monthly Notices of the RAS*, 508, 2226, doi: 10.1093/mnras/stab2428
- Mascali, D., Santonocito, D., de Angelis, G., et al. 2022, *Frontiers in Astronomy and Space Sciences*, 9, 1087543, doi: 10.3389/fspas.2022.1087543
- Massalkhi, S., Agúndez, M., & Cernicharo, J. 2019, *Astronomy and Astrophysics*, 628, A62, doi: 10.1051/0004-6361/201935069
- Massalkhi, S., Agúndez, M., Cernicharo, J., Fonfría, J. P., & Santander-García, M. 2018a, *IAU Symposium*, 332, 261, doi: 10.1017/S1743921317007566
- Massalkhi, S., Agúndez, M., Cernicharo, J., et al. 2018b, *Astronomy and Astrophysics*, 611, A29, doi: 10.1051/0004-6361/201732038
- Matrà, L., MacGregor, M. A., Kalas, P., et al. 2017, *Astrophysical Journal*, 842, 9, doi: 10.3847/1538-4357/aa71b4
- Matsuura, M., Bernard-Salas, J., Lloyd Evans, T., et al. 2014, *Monthly Notices of the RAS*, 439, 1472, doi: 10.1093/mnras/stt2495
- Matthews, H. E., & Sears, T. J. 1983, *The Astrophysical Journal*, 272, 149, doi: 10.1086/161271
- Matthews, L. D., Gérard, E., & Le Bertre, T. 2015, *Monthly Notices of the RAS*, 449, 220, doi: 10.1093/mnras/stv263
- Mauron, N., & Huggins, P. J. 2006, *Astronomy and Astrophysics*, 452, 257, doi: 10.1051/0004-6361:20054739
- Mauron, N., & Huggins, P. J. 2010, *A&A*, 513, A31
- McCarthy, M. C., Lee, K. L. K., Loomis, R. A., et al. 2020, *Nature Astronomy*, 1, doi: 10.1038/s41550-020-01213-y

- McCord, T. B., Carlson, R., Smythe, W., et al. 1997, *Science*, 278, 271, doi: 10.1126/science.278.5336.271
- McGuire, B. A. 2018, *Astrophysical Journal, Supplement*, 239, 17, doi: 10.3847/1538-4365/aae5d2
- . 2022, *Astrophysical Journal, Supplement*, 259, 30, doi: 10.3847/1538-4365/ac2a48
- McGuire, B. A., Burkhardt, A. M., Kalenskii, S., et al. 2018, *Science*, 359, 202, doi: 10.1126/science.aao4890
- McGuire, B. A., Burkhardt, A. M., Kalenskii, S., et al. 2018, *Science*, 359, 202, doi: 10.1126/science.aao4890
- McGuire, B. A., Burkhardt, A. M., Loomis, R. A., et al. 2020, *Astrophysical Journal, Letters*, 900, L10, doi: 10.3847/2041-8213/aba632
- McGuire, B. A., Loomis, R. A., Burkhardt, A. M., et al. 2021, *Science*, 371, 1265, doi: 10.1126/science.abb7535
- McMullin, J. P., Waters, B., Schiebel, D., Young, W., & Golap, K. 2007, in *Astronomical Society of the Pacific Conference Series*, Vol. 376, *Astronomical Data Analysis Software and Systems XVI*, ed. R. A. Shaw, F. Hill, & D. J. Bell, 127
- Mendoza, E., Bronfman, L., Duronea, N. U., et al. 2018, *Astrophysical Journal*, 853, 152, doi: 10.3847/1538-4357/aaa1ec
- Men'shchikov, A. B., Balega, Y., Blöcker, T., Osterbart, R., & Weigelt, G. 2001, *Astronomy and Astrophysics*, 368, 497, doi: 10.1051/0004-6361:20000554
- Meyer, D. M., & Roth, K. C. 1991, *Astrophysical Journal, Letters*, 376, L49, doi: 10.1086/186100
- Millar, T. J. 2016, in *Journal of Physics Conference Series*, Vol. 728, *Journal of Physics Conference Series*, 052001, doi: 10.1088/1742-6596/728/5/052001
- Millar, T. J. 2020, *Chinese Journal of Chemical Physics*, 33, 668, doi: 10.1063/1674-0068/cjcp2008145

- Millar, T. J., Flores, J. R., & Markwick, A. J. 2001, *Monthly Notices of the RAS*, 327, 1173, doi: 10.1046/j.1365-8711.2001.04823.x
- Miller Bertolami, M. M. 2016, *Astronomy and Astrophysics*, 588, A25, doi: 10.1051/0004-6361/201526577
- Minh, Y. C., Irvine, W. M., Ohishi, M., et al. 1993, *Astronomy and Astrophysics*, 267, 229
- Minissale, M., Dulieu, F., Cazaux, S., & Hocuk, S. 2016, *Astronomy and Astrophysics*, 585, A24, doi: 10.1051/0004-6361/201525981
- Monnier, J. D., Danchi, W. C., Hale, D. S., Tuthill, P. G., & Townes, C. H. 2000, *Astrophysical Journal*, 543, 868, doi: 10.1086/317127
- Mould, J., & Wyckoff, S. 1978a, *Monthly Notices of the Royal Astronomical Society*, 182, 63
- Mould, J. R., & Wyckoff, S. 1978b, *Monthly Notices of the Royal Astronomical Society*, 182, 63, doi: 10.1093/mnras/182.1.63
- Müller, H. S. P., Schlöder, F., Stutzki, J., & Winnewisser, G. 2005, *Journal of Molecular Structure*, 742, 215, doi: 10.1016/j.molstruc.2005.01.027
- Naraoka, H., Takano, Y., Dworkin, J. P., et al. 2023, *Science*, 379, abn9033, doi: 10.1126/science.abn9033
- Nemoto, M., Suzuki, A., Nakamura, H., Shibuya, K., & Obi, K. 1989, *Chemical Physics Letters*, 162, 467, doi: 10.1016/0009-2614(89)87009-5
- Neufeld, D. A., Zmuidzinas, J., Schilke, P., & Phillips, T. G. 1997, *Astrophysical Journal, Letters*, 488, L141, doi: 10.1086/310942
- Neufeld, D. A., Falgarone, E., Gerin, M., et al. 2012, *Astronomy and Astrophysics*, 542, L6, doi: 10.1051/0004-6361/201218870
- Nordh, H. L., Lindgren, B., & Wing, R. F. 1977, *Astronomy and Astrophysics*, 56, 1. <http://adsabs.harvard.edu/abs/1977A%26A...56...1N>

- Öberg, K. I., Facchini, S., & Anderson, D. E. 2023, *Annual Review of Astron and Astrophys*, 61, 287, doi: 10.1146/annurev-astro-022823-040820
- Ohnaka, K., Boboltz, D. A., Mulitz-Schimmel, G., Izumiura, H., & Wittkowski, M. 2013, *Astronomy and Astrophysics*, 559, A120, doi: 10.1051/0004-6361/201322425
- Olofsson, H., Khouri, T., Maercker, M., et al. 2019, *Astronomy and Astrophysics*, 623, A153, doi: 10.1051/0004-6361/201834897
- Ossenkopf, V., & Henning, T. 1994, *Astronomy and Astrophysics*, 291, 943
- Pardo, J. R., Cernicharo, J., Goicoechea, J. R., Guélin, M., & Asensio Ramos, A. 2007, *Astrophysical Journal*, 661, 250, doi: 10.1086/513734
- Pardo, J. R., Cernicharo, J., Goicoechea, J. R., & Phillips, T. G. 2004, *Astrophysical Journal*, 615, 495, doi: 10.1086/424379
- Pardo, J. R., Cernicharo, J., Velilla Prieto, L., et al. 2018, *Astronomy and Astrophysics*, 615, L4, doi: 10.1051/0004-6361/201833303
- Pardo, J. R., Bermúdez, C., Cabezas, C., et al. 2020, *Astronomy and Astrophysics*, 640, L13, doi: 10.1051/0004-6361/202038571
- Patel, N. A., Young, K. H., Gottlieb, C. A., et al. 2011, *Astrophysical Journal*, Supplement, 193, 17, doi: 10.1088/0067-0049/193/1/17
- Petrie, S. 1996a, *Monthly Notices of the RAS*, 282, 807, doi: 10.1093/mnras/282.3.807
- . 1996b, *Monthly Notices of the RAS*, 281, 666, doi: 10.1093/mnras/281.2.666
- Pickett, H., Poynter, R., Cohen, E., et al. 1998, *Journal of Quantitative Spectroscopy and Radiative Transfer*, 60, 883, doi: [https://doi.org/10.1016/S0022-4073\(98\)00091-0](https://doi.org/10.1016/S0022-4073(98)00091-0)
- Postberg, F., Khawaja, N., Abel, B., et al. 2018, *Nature*, 558, 564, doi: 10.1038/s41586-018-0246-4

- Quan, D., & Herbst, E. 2007, *Astronomy and Astrophysics*, 474, 521, doi: 10.1051/0004-6361:20078246
- Quintana-Lacaci, G., Cernicharo, J., Velilla Prieto, L., et al. 2017, *Astronomy and Astrophysics*, 607, L5, doi: 10.1051/0004-6361/201732015
- Ramstedt, S., Mohamed, S., Vlemmings, W. H. T., et al. 2017, *Astronomy and Astrophysics*, 605, A126, doi: 10.1051/0004-6361/201730934
- Remijan, A. J., Hollis, J. M., Snyder, L. E., Jewell, P. R., & Lovas, F. J. 2006, *Astrophysical Journal, Letters*, 643, L37, doi: 10.1086/504918
- Rogantini, D., Costantini, E., Zeegers, S. T., et al. 2019, *Astronomy and Astrophysics*, 630, A143, doi: 10.1051/0004-6361/201935883
- Ruaud, M., Wakelam, V., & Hersant, F. 2016, *Monthly Notice of the Royal Astronomical Society*, 459, 3756, doi: 10.1093/mnras/stw887
- Russell, R. W., Soifer, B. T., & Willner, S. P. 1977, *Astrophysical Journal, Letters*, 217, L149, doi: 10.1086/182559
- Sackmann, I. J., & Boothroyd, A. I. 1992, *Astrophysical Journal, Letters*, 392, L71, doi: 10.1086/186428
- Sahai, R., Claussen, M. J., Schnee, S., Morris, M. R., & Sánchez Contreras, C. 2011, *Astrophysical Journal, Letters*, 739, L3, doi: 10.1088/2041-8205/739/1/L3
- Sahai, R., Huang, P. S., Scibelli, S., et al. 2022, *Astrophysical Journal*, 929, 59, doi: 10.3847/1538-4357/ac568a
- Sahai, R., Lee, C.-F., Sánchez Contreras, C., et al. 2017, *Astrophysical Journal*, 850, 158, doi: 10.3847/1538-4357/aa9273
- Sahai, R., Morris, M., Sánchez Contreras, C., & Claussen, M. 2007, *Astronomical Journal*, 134, 2200, doi: 10.1086/522944
- Sahai, R., & Patel, N. A. 2015, *Astrophysical Journal, Letters*, 810, L8, doi: 10.1088/2041-8205/810/1/L8

- Sahai, R., Sánchez Contreras, C., Mangan, A. S., et al. 2018, *Astrophysical Journal*, 860, 105, doi: 10.3847/1538-4357/aac3d7
- Sahai, R., Scibelli, S., & Morris, M. R. 2016, *Astrophysical Journal*, 827, 92, doi: 10.3847/0004-637X/827/2/92
- Sahai, R., & Wannier, P. G. 1992, *Astrophysical Journal*, 394, 320, doi: 10.1086/171585
- Sahai, R., Young, K., Patel, N. A., Sánchez Contreras, C., & Morris, M. 2006, *Astrophysical Journal*, 653, 1241, doi: 10.1086/508507
- Samus', N. N., Kazarovets, E. V., Durlevich, O. V., Kireeva, N. N., & Pastukhova, E. N. 2017, *Astronomy Reports*, 61, 80, doi: 10.1134/S1063772917010085
- Santoro, G., Martínez, L., Lauwaet, K., et al. 2020, *Astrophysical Journal*, 895, 97, doi: 10.3847/1538-4357/ab9086
- Schilke, P., Walmsley, C. M., Pineau des Forets, G., & Flower, D. R. 1997, *Astronomy and Astrophysics*, 321, 293
- Scibelli, S., Sahai, R., & Morris, M. R. 2019, *Astrophysical Journal*, 870, 117, doi: 10.3847/1538-4357/aaf21b
- Shenoy, D., Humphreys, R. M., Jones, T. J., et al. 2016, *Astronomical Journal*, 151, 51, doi: 10.3847/0004-6256/151/3/51
- Shingledecker, C. N., Lee, K. L. K., Wandishin, J. T., et al. 2021, *Astronomy and Astrophysics*, 652, L12, doi: 10.1051/0004-6361/202140698
- Shirley, Y. L. 2015, *Publications of the Astronomical Society of the Pacific*, 127, 299
- Siebert, M. A., Van de Sande, M., Millar, T. J., & Remijan, A. J. 2022a, *Astrophysical Journal*, 941, 90, doi: 10.3847/1538-4357/ac9e52
- Siebert, M. A., Simon, I., Shingledecker, C. N., et al. 2020, *Astrophysical Journal*, 901, 22, doi: 10.3847/1538-4357/abac0e
- Siebert, M. A., Lee, K. L. K., Remijan, A. J., et al. 2022b, *Astrophysical Journal*, 924, 21, doi: 10.3847/1538-4357/ac3238

- Singh, A. P., Edwards, J. L., & Ziurys, L. M. 2022, *Astronomical Journal*, 164, 230, doi: 10.3847/1538-3881/ac8df0
- Smith, C. L., Zijlstra, A. A., & Fuller, G. A. 2015, *Monthly Notices of the RAS*, 454, 177, doi: 10.1093/mnras/stv1934
- Smith, I. W. M. 2011, *Annual Review of Astron and Astrophys*, 49, 29, doi: 10.1146/annurev-astro-081710-102533
- Smith, N., Humphreys, R. M., Davidson, K., et al. 2001, *Astronomical Journal*, 121, 1111, doi: 10.1086/318748
- Snyder, L. E., Hollis, J. M., Jewell, P. R., Lovas, F. J., & Remijan, A. 2006, *Astrophysical Journal*, 647, 412, doi: 10.1086/505323
- Sofia, U. J., Cardelli, J. A., & Savage, B. D. 1994, *The Astrophysical Journal*, 430, 650, doi: 10.1086/174438
- Soker, N., & Kashi, A. 2012, *Astrophysical Journal*, 746, 100, doi: 10.1088/0004-637X/746/1/100
- Solomon, P. M., Jefferts, K. B., Penzias, A. A., & Wilson, R. W. 1971, *Astrophysical Journal, Letters*, 168, L107, doi: 10.1086/180794
- Swings, P., & Rosenfeld, L. 1937, *Astrophysical Journal*, 86, 483, doi: 10.1086/143880
- Tabone, B., Bettoni, G., van Dishoeck, E. F., et al. 2023, *Nature Astronomy*, 7, 805, doi: 10.1038/s41550-023-01965-3
- Teague, R. 2019, *The Journal of Open Source Software*, 4, 1632, doi: 10.21105/joss.01632
- Tenenbaum, E. D., Dodd, J. L., Milam, S. N., Woolf, N. J., & Ziurys, L. M. 2010, *Astrophysical Journal, Supplement*, 190, 348, doi: 10.1088/0067-0049/190/2/348
- Teyssier, D., Hernandez, R., Bujarrabal, V., Yoshida, H., & Phillips, T. G. 2006, *Astronomy and Astrophysics*, 450, 167, doi: 10.1051/0004-6361:20053759

- Thaddeus, P., Gottlieb, C. A., Hjalmarson, A., et al. 1985, *Astrophysical Journal, Letters*, 294, L49, doi: 10.1086/184507
- Thompson, A. R., Moran, J. M., & Swenson, George W., J. 2001, *Interferometry and Synthesis in Radio Astronomy*, 2nd Edition
- Tielens, A. G. G. M. 2008, *Annual Review of Astron and Astrophys*, 46, 289, doi: 10.1146/annurev.astro.46.060407.145211
- . 2022, *Frontiers in Astronomy and Space Sciences*, 9, 908217, doi: 10.3389/fspas.2022.908217
- Tielens, A. G. G. M., McKee, C. F., Seab, C. G., & Hollenbach, D. J. 1994, *Astrophysical Journal*, 431, 321, doi: 10.1086/174488
- Tielens, A. G. G. M., Waters, L. B. F. M., & Bernatowicz, T. J. 2005, in *Astronomical Society of the Pacific Conference Series*, Vol. 341, *Chondrites and the Protoplanetary Disk*, ed. A. N. Krot, E. R. D. Scott, & B. Reipurth, 605
- Travers, M. J., Chen, W., Grabow, J. U., McCarthy, M. C., & Thaddeus, P. 1998, *Journal of Molecular Spectroscopy*, 192, 12, doi: 10.1006/jmsp.1998.7666
- Tuo, J., Li, X., Sun, J., et al. 2024, arXiv e-prints, arXiv:2401.16089, doi: 10.48550/arXiv.2401.16089
- Turner, B. E., Herbst, E., & Terzieva, R. 2000, *Astrophysical Journal, Supplement*, 126, 427, doi: 10.1086/313301
- Unnikrishnan, R., De Beck, E., Nyman, L. A., et al. 2023, arXiv e-prints, arXiv:2312.10014, doi: 10.48550/arXiv.2312.10014
- Van de Sande, M., & Millar, T. J. 2022, *Monthly Notices of the RAS*, 510, 1204, doi: 10.1093/mnras/stab3282
- Van de Sande, M., Sundqvist, J. O., Millar, T. J., et al. 2018, *Astronomy and Astrophysics*, 616, A106, doi: 10.1051/0004-6361/201732276
- van der Tak, F. F. S., Black, J. H., Schöier, F. L., Jansen, D. J., & van Dishoeck, E. F. 2007, *Astronomy and Astrophysics*, 468, 627, doi: 10.1051/0004-6361:20066820

- van der Tak, F. F. S., Lique, F., Faure, A., Black, J. H., & van Dishoeck, E. F. 2020, *Atoms*, 8, 15, doi: 10.3390/atoms8020015
- Vasyunin, A. I., & Herbst, E. 2013, *Astrophysical Journal*, 769, 34, doi: 10.1088/0004-637X/769/1/34
- Wakelam, V., Loison, J.-C., Herbst, E., et al. 2015, *The Astrophysical Journal Supplement Series*, 217, 20. <http://stacks.iop.org/0067-0049/217/i=2/a=20>
- Walch, S. P., & Dateo, C. E. 2001, *The Journal of Physical Chemistry A*, 105, 2015, doi: 10.1021/jp003559u
- Walmsley, C. M., Bachiller, R., Pineau des Forêts, G., & Schilke, P. 2002, *The Astrophysical Journal Letters*, 566, L109, doi: 10.1086/339694
- Walmsley, C. M., Jewell, P. R., Snyder, L. E., & Winnewisser, G. 1984, *Astronomy and Astrophysics*, 134, L11
- Wannier, P. G., Sahai, R., Andersson, B. G., & Johnson, H. R. 1990, *Astrophysical Journal*, 358, 251, doi: 10.1086/168980
- Waters, L. B. F. M., Beintema, D. A., Zijlstra, A. A., et al. 1998, *Astronomy and Astrophysics*, 331, L61. <https://arxiv.org/abs/astro-ph/9802289>
- Weiss, A., & Ferguson, J. W. 2009, *Astronomy and Astrophysics*, 508, 1343, doi: 10.1051/0004-6361/200912043
- Western, C. M. 2017, *Journal of Quantitative Spectroscopy and Radiative Transfer*, 186, 221, doi: 10.1016/j.jqsrt.2016.04.010
- Western, C. M., & Billinghurst, B. E. 2019, *Physical Chemistry Chemical Physics*, 21, 13986, doi: 10.1039/C8CP06493H
- Willacy, K., Williams, D. A., & Minh, Y. C. 1993, *Monthly Notices of the RAS*, 263, L40, doi: 10.1093/mnras/263.1.L40
- Wing, R. F., Cohen, J., & Brault, J. W. 1977, *The Astrophysical Journal*, 216, 659, doi: 10.1086/155507

- Wing, R. F., & Ford, Jr., W. K. 1969, *Publications of the Astronomical Society of the Pacific*, 81, 527, doi: 10.1086/128814
- Winters, J. M., Fleischer, A. J., Gauger, A., & Sedlmayr, E. 1994, *Astronomy and Astrophysics*, 290, 623
- Woods, P. M., Millar, T. J., Herbst, E., & Zijlstra, A. A. 2003, *Astronomy and Astrophysics*, 402, 189, doi: 10.1051/0004-6361:20030215
- Woon, D. E., & Herbst, E. 2009, *The Astrophysical Journal Supplement Series*, 185, 273, doi: 10.1088/0067-0049/185/2/273
- Xue, C., Willis, E. R., Loomis, R. A., et al. 2020, *Astrophysical Journal, Letters*, 900, L9, doi: 10.3847/2041-8213/aba631
- Yen, H.-W., Koch, P. M., Liu, H. B., et al. 2016, *Astrophysical Journal*, 832, 204, doi: 10.3847/0004-637X/832/2/204
- Zack, L. N., Halfen, D. T., & Ziurys, L. M. 2011, *The Astrophysical Journal*, 733, L36
- Zeichner, S. S., Aponte, J. C., Bhattacharjee, S., et al. 2023, *Science*, 382, 1411, doi: 10.1126/science.adg6304
- Zhang, X.-Y., Zhu, Q.-F., Li, J., et al. 2017, *Astronomy and Astrophysics*, 606, A74, doi: 10.1051/0004-6361/201730791
- Zhang, Y., Kwok, S., Nakashima, J.-i., Chau, W., & Dinh-V-Trung. 2013, *Astrophysical Journal*, 773, 71, doi: 10.1088/0004-637X/773/1/71
- Zhou, Y., Quan, D.-H., Zhang, X., & Qin, S.-L. 2020, *Research in Astronomy and Astrophysics*, 20, 125, doi: 10.1088/1674-4527/20/8/125
- Zhukovska, S., & Henning, T. 2013, *Astronomy and Astrophysics*, 555, A99, doi: 10.1051/0004-6361/201321368
- Zijlstra, A. A., Chapman, J. M., te Lintel Hekkert, P., et al. 2001, *Monthly Notices of the RAS*, 322, 280, doi: 10.1046/j.1365-8711.2001.04113.x

- Zinner, E. 1998, *Annual Review of Earth and Planetary Sciences*, 26, 147, doi: 10.1146/annurev.earth.26.1.147
- Ziurys, L. 2006, *PNAS*, 103, 12274
- Ziurys, L. M. 2006, *Proceedings of the National Academy of Science*, 103, 12274, doi: 10.1073/pnas.0602277103
- Ziurys, L. M., Milam, S. N., Apponi, A. J., & Woolf, N. J. 2007, *Nature*, 447, 1094, doi: 10.1038/nature05905
- Ziurys, L. M., Schmidt, D. R., & Bernal, J. J. 2018, *Astrophysical Journal*, 856, 169, doi: 10.3847/1538-4357/aaafc6